Estimating fatigue life of steel bridges using continuous response monitoring: Methodology and applications

Submitted by Jalil Eyada Kwad to

the University of Exeter as a thesis for the degree of

Doctor of Philosophy in Engineering

In November 2018

Signature: …………………………………………………………..

Abstract

The fatigue life of structural steel bridges is governed by the time-history of stresses generated in-situ in its fatigue-critical structural details under service conditions. However, these stresses are often not directly and accurately measurable due to the complex geometry of structural elements or access restrictions. Therefore, there is a need for an approach to infer stresses at a detail using measurements taken away from the detail. Another practical issue is that instrumenting all structural details is infeasible owing high cost. An approach to infer stresses across the bridge only a limited number of sensors is therefore essential.

This thesis aims to address the aforementioned two critical issues in monitoring-based fatigue life evaluation. It accomplishes this by investigating the following hypothesis: detailed finite element models of fatigue-critical connections and in-service strain measurements that capture the shear, flexure, and axial demands of the modelled connections can be combined to estimate accurately the in-situ hot spot/nominal stresses. This will enable much more reliable assessment of fatigue life than is possible by current methods. Proving this hypothesis will also permit expanding the approach to predicting hot spot/nominal stresses at uninstrumented connections by combining numerical models with real-time measurements from a few instrumented connections. This thesis focuses specifically on investigating this hypothesis on the fatigue-sensitive web-gap welded details in ladder-type bridge decks although the presented ideas are applicable to riveted/bolted connections in this type of bridges.

The proposed approaches are evaluated using measurements from three full-scale bridges. Results illustrate that the methodology accurately predicts fatigue

stress response. Results also confirm that the methodology can be utilised to infer stress time-histories at uninstrumented connections and to plan for retrofits. The study demonstrates that the proposed methodology is applicable for interpreting measurements from full-scale bridges, and can be integrated within a measurement interpretation platform for continuous bridge monitoring.

Acknowledgments

Dedication

For my father who I lost seven years ago, who I deeply feel his absences. For my Mother who I did not see five years ago, who always believed in me and support me through my life with unconditional love. For my wife, Hanan, who has always been there through the hard times, who gave me the best gift in my life, our kids, who without her patient and encouragement this work was impossible to accomplish. For my kids, Hamzah, Maali, Maher and Araz whom sparked in my life and brought me joy and happiness.

Contents

Contents

Contents

List of figures

14

21

List of tables

Notations

Acronyms		key
ASCE	-	American Society of Civil Engineers
SCF	-	Stress Concentration Factor
IIW	-	International Institute of Welding
FEM	-	Finite element models
S-N curve	-	Fatigue resistance curve
CAFL	-	Constant amplitude fatigue limit
SHM	-	Structural health monitoring
WIM	-	Weigh-in-motion
LSF	-	Load scaling factors
VSP	-	Proposed virtual sensing procedure
AASHTO	-	American Association of State Highway and Transportation Officials
NI	-	National Instruments
BDI	-	Bridge Diagnostics Inc.
cDAQ	-	Compact Data Acquisition
STS	-	Structural Testing System
SG	-	Strain gauges
SSI	-	Stochastic Subspace Identification
SSI-UPC	-	Stochastic Subspace Identification with Unweighted Principal Component
LabVIEW	-	Laboratory Virtual Instrument Engineering Workbench

Notations

Hz	-	Samples-per-second
CupDoF's	-	Coupling and constraint equations technique
APDL	-	Parametric design language
BC	-	Boundary condition
dof'	-	Degree of freedom
WSR	-	West Somerset Railway Inc
DMS	-	Imetrum Dynamic Monitoring Station

29

CHAPTER 1   Introduction

1.1   Motivation

Steel bridges of all ages, including those that are approaching or have exceeded their design service life and those built over the last few decades, are vulnerable to fatigue damage. Fatigue damage is progressive damage arising from cyclic loading and is a concern mainly at locations of high stresses such as connections in civil engineering structures. To understand the significance of fatigue for bridge structures, consider the study by Marques et al (2018) and Imam et al (2012) that analysed a database of metallic bridge failures from around the world as shown in Figure 1.1. Failures, according to their study, included both full bridge collapses as well as no-collapse scenarios. No-collapse scenarios cover cases that have resulted in loss of function (such as fatigue cracking which could result in collapse if left unchecked) leading to bridge closures, repairs or strengthening work. Their study found that over 50% of the bridge collapses occurred in the USA (36%) and the UK (20%), partly due to the large number of such bridges in these countries. Significantly they found that fatigue was responsible for over 13% of the bridge collapses.
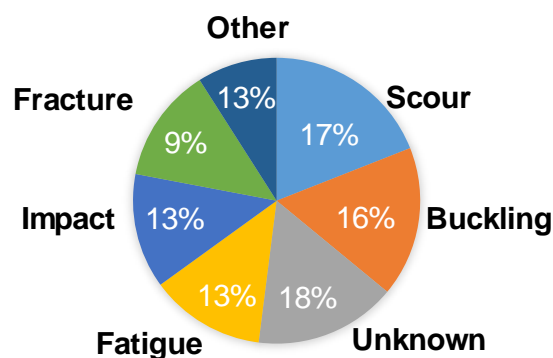
Figure 1.1Failure modes associated with metallic bridge collapses (Imam et al. 2012).

Fatigue risk is particularly high for old bridges owing to a combination of much greater traffic volumes in recent years and significant age-related deterioration (Zhou 2006). A comprehensive survey by Olofsson et al (2005) examining the age profile of existing steel railway bridges in Europe showed that more than 65% of them are over 50 years old, and about 30% of them are over 100 years old as shown in Figure 1.2. The UK has over 6,000 metallic bridges that are over 50 years old and have fatigue as the principal risk to their structural integrity (Adasooriya & Siriwardane 2014). In the USA, according to the 2017 Infrastructure Report Card prepared by the American Society of Civil Engineers, 39% of the all country's bridges were over 50 years (ASCE's 2017 Infrastructure Report Card, 2018).

A significant number of existing metallic bridges are assessed to be at or past the end of their design lives due to the conservativeness built into the fatigue assessment methods to account for the uncertainties in loading and structural behaviour. The development of more realistic and reliable assessment methods that are based on actual loading and the observed structural behaviour can provide a more accurate estimation of the remaining fatigue life, and this is the main aim of this research. The development of such methods can enable rational decision-making that keeps safe bridges in service and prioritizes at-risk structures for repair and replacement. Such methods are of great relevance to bridge operators nationally and internationally.
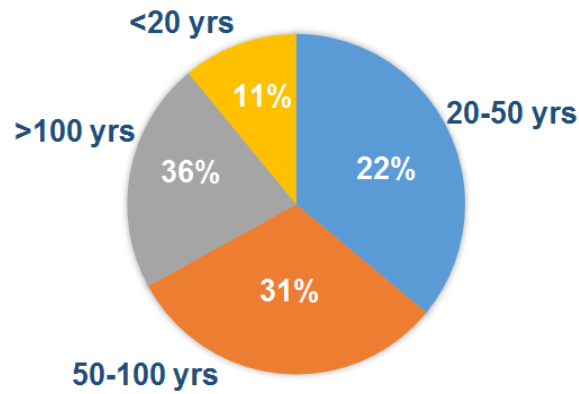
Figure 1.2 General age profile of European railway bridges based on the data collected from 17 European countries according to (Olausson et al. 2005).

1.2 Previous research

Significant research has gone towards evaluating effectively and accurately the remaining fatigue life of metallic bridges. Most of these have focused on evaluating the stress time history induced by code-specified loading (Zhou & Chan 2007), and then using it to determine the cumulative fatigue damage using an established damage model such as Miner's rule (Miner 1945) and relevant S-N curves derived from laboratory fatigue tests. Current approaches therefore have two key limitations. First, these approaches are based on nominal stress, which does not take into account the local stress concentration effects in a specific weld detail (Park & Kim 2014). These approaches can therefore be unreliable, particularly for large structures with complex details for which accurately estimating the nominal stress is often difficult (Tveiten et al. 2007; Ye et al. 2012). Second, current approaches exaggerate greatly the actual applied live loads and in turn the stress cycles, resulting in overly conservative estimates of the remaining fatigue life (Lee & Cho 2016; Zhou 2006; Kashefi et al. 2010).

32

For many bridges, these approaches even give a remaining fatigue life that is negative meaning that the bridge has no theoretical safety for a residual service or design life while in reality the structure is still in service without any visible evidence of fatigue cracking (Kwon et al. 2012). The unnecessary retrofits or repairs necessitated by such conservative assessment procedures significantly increase bridge maintenance costs (Rashidi & Gibson 2011).

With recent advances in sensing technology, in-situ strain measurements (Alampalli & Lund 2006; Zhou 2006; Chan et al. 2001) have been increasingly employed for assessing the remaining fatigue life of steel bridges. These have been shown to be more reliable than assessments based on stress predictions purely from numerical simulations (Brownjohn 2007; Ye et al. 2012; Lee & Cho 2016; Schumacher & Nussbaumer 2006). Strain sensors are usually installed further away from fatigue-critical locations to obtain the nominal strains and stresses (Ni et al. 2010). The nominal stresses are multiplied by a Stress Concentration Factor (SCF) to take into account the stress concentration and dimension effects. This approach, which is now widely used, is known as a modified hot spot stress method in many codes and standards such as the International Institute of Welding (IIW 2000) and Eurocodes (EN 1993-1-9 2005). The main weakness of this approach is that it requires knowledge of the SCF. The SCF is usually assumed based on the type of detail and may not reflect the in-situ stress concentration effects. A second weakness is that it will provide information on fatigue stresses only at the instrumented detail. Instrumenting all details of a bridge is practically difficult owing to the high cost associated with installing sensors.

This study proposes a novel methodology for evaluating in-situ hot spot stresses that overcomes the above-mentioned drawbacks of current methods. It integrates field measurements of strains taken from around the weld detail with a numerical model of the connection to evaluate the in-situ hot spot stresses. Unlike the modified hot spot stress method, knowledge of the SCF is not required but its effect is instead explicitly accounted for within the modelling process. The current study also aims to develop a stress response prediction method for short-span bridges that uses measurements from a limited number of sensors to predict the fatigue damage at uninstrumented locations. This method, which is based on a combination of direct measurement and calibrated numerical models, will enable monitoring a few bridge elements directly and the rest virtually. This concept can essentially enable tracking the fatigue life of all details within a structure using measurements from a few instrumented connections.

1.3   Research aim and objectives

The main aim of the project was to investigate the following hypothesis: detailed finite element models (FEM) of fatigue-critical connections and in-service strain measurements that capture the shear, flexure, and axial demands of the modelled connections can be combined to estimate accurately the in-situ hot spot stresses. This will enable much more reliable assessment of fatigue life than is possible by current methods. The thesis will investigate this hypothesis on the fatigue-sensitive web-gap details that exist at the connections between main beams and cross beams in ladder-type bridge decks. Proving this hypothesis will

also permit expanding the approach to predicting hot spot stresses at uninstrumented connections by combining numerical models with real-time measurements from a few instrumented connections. Accurate estimation of in-situ stresses also enables development of retrofit methods that extend the fatigue life of a detail. This research investigates this possibility for a specific metallic bridge.

The following objectives are formulated to fulfil the stated aim.

1. Review the state-of-the-art in research and the recommended approaches in practice for fatigue life assessment of bridges to identify drawbacks and weaknesses of current methods.

2. Devise and implement a hybrid approach that uses numerical models of structural details, and global measurements of deformations to estimate local stresses of importance to fatigue evaluation.

3. Integrate the developed global-local analysis approach for estimating fatigue stresses within a procedure for assessing the fatigue life of structural components in real-time.

4. Expand the developed approach to predict stresses at uninstrumented locations in real-time through numerical modelling, and thereby enabling using a limited number of sensors to assess fatigue performance of short span steel bridges.

5. Evaluate the performance of the developed methods using measurements from full-scale bridges during service and static/dynamic load tests.

6. Investigate, using a particular bridge, how retrofit methods to increase fatigue life can be designed for details that are assessed as vulnerable using the developed methods.

1.4   Structure of the thesis

This thesis consists of seven chapters. Chapter 1 introduces the subject of this research and underlines the motivation for the study as well as its aims and objectives. Chapter 2 presents a background of the process of fatigue damage and the parameters affecting fatigue life. Also this chapter presents a literature review that includes an overview of the following topics:

- Current state-of-the-art in the fatigue life assessment methods;

- Types of fatigue damage;

- Determination of stress histories.

Chapter 3 presents the proposed novel methodology and explains how it can support reliable evaluation of the hot spot stresses. Chapter 4 discusses the application of the novel methodology for a short span steel bridge - the Bascule Bridge. It describes the numerical modelling (global model and local model), the full-scale bridge monitoring, and the validation of the methodology with measured data. Chapter 5 discusses the application of the proposed research methodology to two short-span steel railway bridges: (i) the Mineral Line Bridge and (ii) the Williton up Bridge. Chapter 6 illustrates how the methodology proposed in Chapter 3 can support fatigue damage evaluation using the Bascule Bridge. It also presents a study on the secondary stresses induced by localized distortion

which plays an important role in the behaviour of vertical stiffeners that are welded to the web of main girders. Notably, for the Bascule bridge example, the study suggests a retrofit method to enhance the fatigue life of the detail with the numerical modelling for the evaluation of the retrofit benefiting from the measurements illustrated in Chapter 4. A summary of the research conducted in this thesis is provided in Chapter 7, which also includes key conclusions and recommendations for future research of this study.

CHAPTER 2   Background and literature review

The phenomenon of fatigue damage and current approaches for fatigue life assessment are reviewed in this chapter. The review starts by describing fatigue damage and then overviews the factors influencing fatigue life. It later focuses on the common fatigue life assessment methods that are currently employed. Particular attention is given to the process of determining stress histories, which is a key research challenge that this work aims to address.

2.1   Introduction

When a structure undergoes repeated dynamic stresses that result in damage, the process is referred to as fatigue. EN 1993-1-9 emphasises how fatigue is generally caused by fluctuating stresses (EN 1993-1-9 2005). In these instances, failure occurs when the amount of stress is substantially less than both the tensile and the yield strength of the material. Liao (2011) describes this phenomenon as "catastrophic and insidious" due to its sudden and unpredictable nature. However, it does not happen in all structures. Building frames are exempt given that they carry principally permanent loads (Liao 2011). As the stresses they undergo are not fluctuating and dynamic, fatigue damage is not a factor that is usually considered during their design. However, in structures like steel bridges, fatigue that results from fluctuating stresses is often a critical factor and must be taken into account for both design and maintenance.

The fatigue process occurs in three phases. The first phase, which is the initiation of cracks, happens long after the loading starts. Normally these cracks emerge at or near the surface, and particularly near surface defects where stress concentration effects are prevalent. Example of surface defects include scratches, pits, sharp corners caused by bad design or manufacturing, inclusions and grain boundaries. A fatigue crack following its initial emergence, grows and propagates due to the applied cyclic loads. Eventually, the material suddenly fractures because the area of cross-section that is un-cracked has become too small, incapable of supporting the applied stress. Because of the nature of this failure process, fatigue assessment must focus on the development of cracks and their rate of growth with applied loading cycles.

2.1.1 Factors influencing fatigue life

The fatigue life of a member or of a structural detail is described in terms of the number of stress cycles it can withstand before failure. Factors that influence fatigue life are those that affect fatigue crack initiation or propagation under applied stress cycles. The main factors that should be taken into account are the following (EN 1993-1-9):

- the geometry,

- the environment, and

- the loading.

The first two factors are discussed briefly below. Loading is a major factor influencing fatigue damage and is discussed in detail in the next section.

Geometry

Fatigue failures often happen due to the presence of specific geometrical features that are responsible for local stress concentration. The presence of these features is dependent on the fabrication method. For example, when bolts or rivets are used, flaws can be introduced in the process of creating the rivet or bolt holes. When fabricating using welding, defects such as a lack of penetration, porosity, misalignment or slag nucleation can occur. Yen and Dolan (2007) highlighted the fact that certain types of metal commonly contain welded defects and can be more susceptible to the emergence of localised stresses, namely notch and tensile residual stresses that are created by the welding process. Weld defects can be a source of fatigue cracks and rapidly grow in size to a critical level that significantly decrease fatigue life and increase the possibility of mechanical failure (Hobbacher 1996).

Welded details are in general more prone to fatigue damage than bolted details. Therefore, efforts to reduce stress concentration and increase the quality of weld geometric profile can dramatically improve fatigue life.

Environmental effects

Corrosion, which is a common problem in metallic bridges, is considered to be one of the most important causes of fatigue failure (Kreislova & Geiplova 2012). Zhang & Yuan (2014), in their investigation on corrosion-induced fatigue strength reduction, showed that the fatigue life may be reduced by as much as 40%

depending on corrosion levels. Another environmental factor that influences fatigue life is temperature. Structures in real-life environments are subject to a range of temperatures that may include extremes (Kossakowski 2016). Low temperatures, which cause steel to lose its ductility, can increase the risk of initiation and propagation of cracks, and reduce the creep rupture strength and the eventual fatigue life (Norman Edward Frost, Kenneth James Marsh 1974). Ambient temperature variations can influence structural response, which in turn can alter stiffness of the structure and stress distributions that determine fatigue damage. A fatigue damage analysis conducted for the Runyang Bridge by (Guo Tong et al. 2008) based on field monitored data showed that the deformation response of metallic bridges, especially cable-stayed bridges, can be affected significantly by variations in ambient temperatures. The cable system may deform and change the support conditions of girders, which in turn can affect fatigue damage accumulation.

Types of fatigue loading

Loading on real-life structures can be classified into two categories for the purpose of fatigue assessment: constant amplitude loading and variable amplitude loading. These are described below.

a) Constant amplitude loading

This term is used to refer to cyclic loading of a constant amplitude as exemplified in Figure 2.1. Generally laboratory tested specimens are more likely to experience this kind of loading. The stresses hence induced cycle between a

maximum (σ_{max}) and minimum (σ_{min}) value with the range $\Delta\sigma = \sigma_{\text{max}} - \sigma_{\text{min}}$ having a direct bearing on the fatigue life.

Until the early 1970s, fatigue design specifications used in many countries were based mainly on constant amplitude test data even though highway bridges are in reality subject to variable amplitude loading (Albrecht & Lenwari 2009).
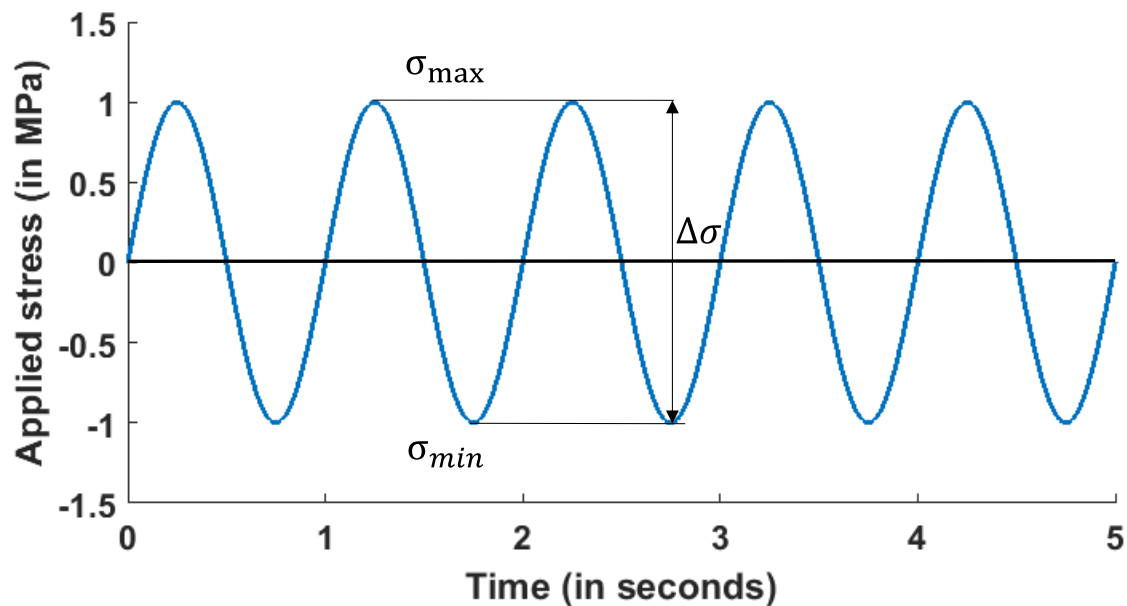
Figure 2.1 An example of stress due to constant amplitude loading.

b) Variable amplitude loading (real-traffic)

Engineering components and structures are generally subject to variable amplitude loading, i.e. the amplitudes of the loading and the induced stress-strain cycles keep varying. An example of such a scenario is shown in Figure 2.2. Many prior studies have investigated the effects of parameters of various amplitude loading on the fatigue strength of materials, particularly structural steel (Kim et al. 2017). An extensive review of this topic has been produced by (Albrecht & Lenwari 2009). They noted that certain combinations of parameters can

accelerate or retard fatigue crack growth. Importantly they also concluded that the variable-amplitude fatigue life was not dependent on the order in which stress cycles were applied but only on the full stress spectrum.
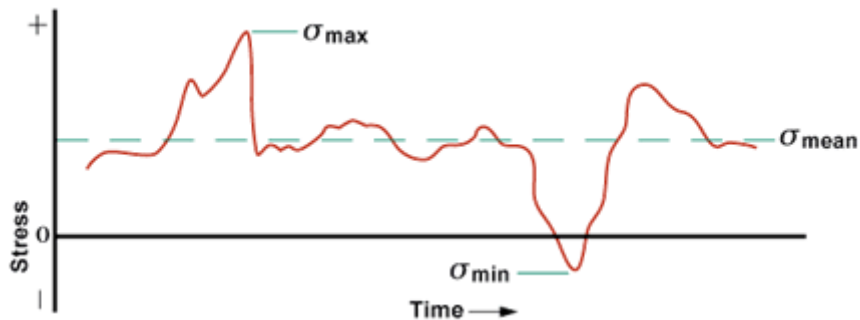
Figure 2.2 An example of stress due to constant amplitude loading

2.1.2 Characterizing fatigue resistance curve (S-N curve)

There are two main categories of methods for characterizing the fatigue resistance of metals and metallic components: stress-based approach (S-N curves) and fracture mechanics methods. The section below discusses only stress-based approaches (S-N curves) since these form the basis of fatigue design and assessment in structural engineering (Cremona et al. 2013).

a) Stress-based approach (S-N curves)

Two well established technical approaches for fatigue analysis and design of welded connection:

1. The nominal stress S-N curve approach

2. The hot spot stress S-N curve approach

These approaches are discussed briefly in the subsequent paragraphs.

Nominal stress S-N curve

The nominal stress S-N curve approach is based on fatigue test data. The major factors affecting fatigue resistance are the applied stress range, number of cycles and type of detail such as the presence of stress concentrations and discontinuity in the detail. In the nominal stress S-N curve approach, various details are separated into different categories with similar fatigue resistances. The resulting data consists of the magnitude of stress range (S) and number of cycle to failure (N) when subjected to a particular constant amplitude loading. Using the collected data, relationship between the number of cycles to failure and the cyclic stress range is assumed. The relationship which is typically exponential between N and S is plotted graphically as a piecewise linear curve between $\log N$ and $\log S$, which is referred to as a S-N curve.

Figure 2.3 presents the 14 S-N curves given in the Eurocode (EN 1993-1-9 2005) for various detail categories. Each detail category has a constant amplitude fatigue limit (CAFL) $\Delta\sigma_D$, which is defined as the stress range below which fatigue failures are not expected to occur during constant amplitude testing. These curves plot the mean minus two standard deviations of the data from constant amplitude testing, i.e. a 75% confidence level with which to predict 95% probability of survival for $\log N$, taking into account the standard deviation and the sample size and residual stress effects.

For stress ranges above $\Delta\sigma_D$, the reciprocal of slope of a S-N curve m is 3. m becomes 5 at 5 million cycles, which corresponds to the number of cycles for evaluating $\Delta\sigma_D$. m becomes zero from 100 million cycles, which is the cut-off

limit $\Delta\sigma_L$. Stress ranges that fall below $\Delta\sigma_L$ do not contribute to the calculated cumulative damage. $\Delta\sigma_D$ and $\Delta\sigma_L$ for each category can be calculated using

$$\Delta\sigma_D = \left(\frac{2}{5}\right)^{1/3} \Delta\sigma_c = 0.737\Delta\sigma_c \qquad\qquad (2.1)$$

$$\Delta\sigma_L = \left(\frac{5}{100}\right)^{1/5} \Delta\sigma_D = 0.549\Delta\sigma_D \qquad\qquad (2.2)$$

where $\Delta\sigma_c$ is the constant amplitude stress range, for a particular detail category for an endurance $N = 2\text{x}10^6$ cycles. N is the life to failure expressed in cycles, under the action of a constant amplitude stress history.

For a specific type of detail, the fatigue resistance (N_R), which is the estimated number of stress cycles to failure, is computed by comparing the stress range $\Delta\sigma_R$ of the nominal stress spectra with $\Delta\sigma_D$. If $\Delta\sigma_R > \Delta\sigma_D$, then N_R can be

$$N_R.(\Delta\sigma_R)^m = 2\text{x}10^6 .(\Delta\sigma_c)^m \text{ , with } m = 3 \text{ for } N \le 5\text{x}10^6 \qquad (2.3)$$

If $\Delta\sigma_R > \Delta\sigma_L$ but $\Delta\sigma_R < \Delta\sigma_D$, then N_R can be described by

$$N_R.(\Delta\sigma_R)^m = 5\text{x}10^6 .(\Delta\sigma_D)^m \text{ , with } m = 5 \text{ for } 5\times10^6 \le N \le 10^8 \qquad (2.4)$$
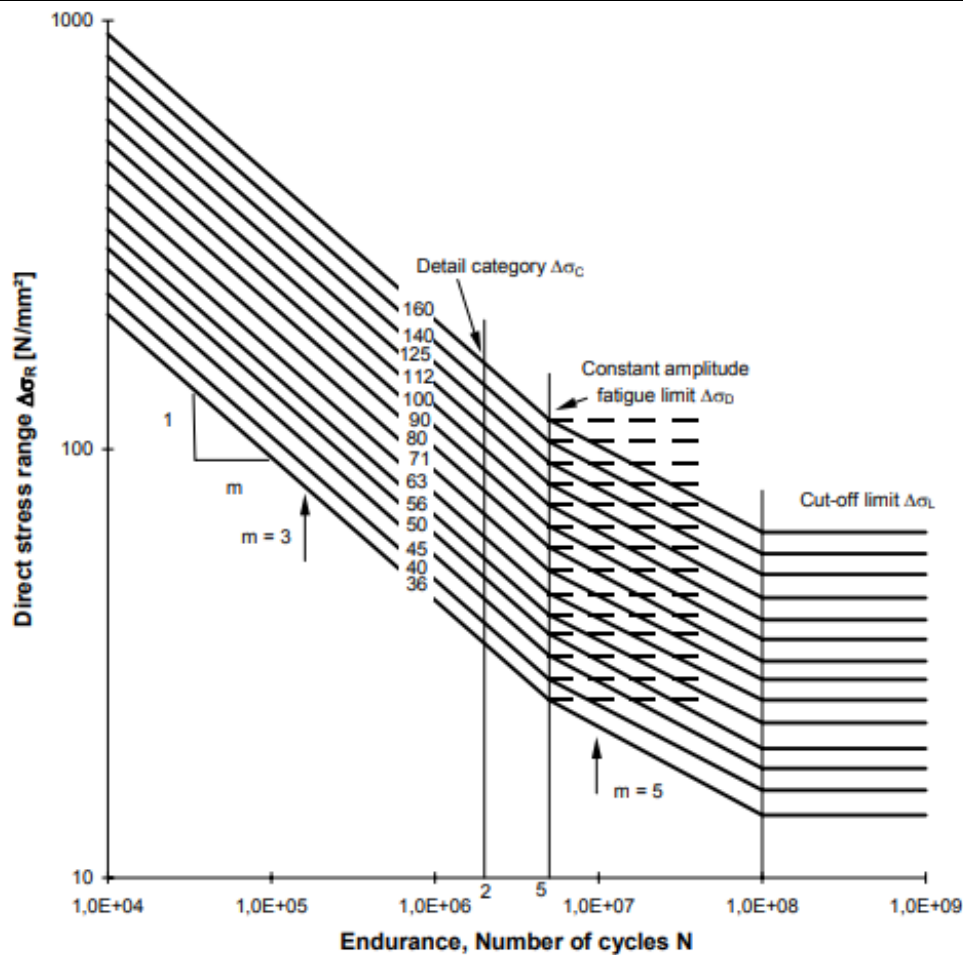
Figure 2.3 Fatigue strength curves for direct stress ranges in Eurocode (EN 1993-1-9 2005).

b) Hot spot stress S-N curve

Hot spot S-N curves are generally based on strains measured from various test specimens near the point of crack initiation. The strain ranges are measured with strain gauges at several points close to the weld toe and extrapolated to the weld toe. The hot spot S-N curves can be presented using stress or strain ranges. However hot spot fatigue analysis should be based on stress ranges (Niemi 1995).

The shape of fatigue strength S-N curves in IIW recommendations for the structural hot spot stress are similar to the direct nominal stress S-N curves. They

essentially consist of a single line with constant slope m = 3 (in a log-log scale)

and a cut-off limit for constant amplitude fatigue limit (CAFL) at 5 million cycles.

A schematic of the S-N curves is presented in Figure 2.4.
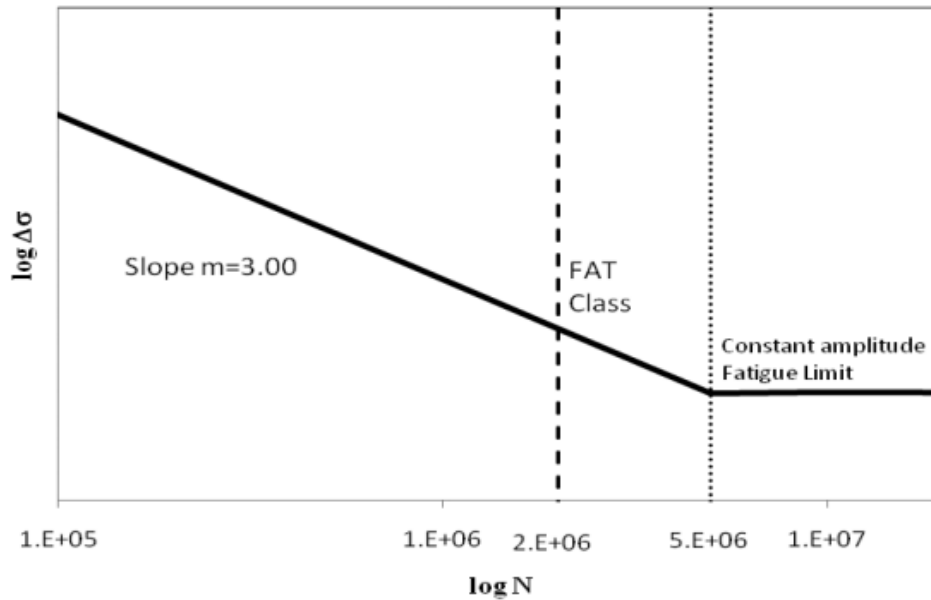
*Figure 2.4 Fatigue strength S-N curves for hot spot stress
in steel (Zamiri Akhlaghi 2009).*

Eurocode 3 (EN 1993-1-9 2005) recommends the same fatigue resistance S-N

curves as the IIW recommendations (Hobbacher 2016) which gives slightly

higher fatigue life for the components.

In contrast with nominal stress approach (See section *Nominal stress S-N curve*

Figure 2.3), no standard details are associated with the curves. Instead, 7 types

of welds are introduced and one S-N curve is recommended for each type. These

are shown in Table 2.1. Figure 2.5 shows the difference in the fatigue resistance

(endurance) between the nominal stress S-N and hot spot curves for connection

7 described in Table 8.4 in the Eurocode 3 (EN 1993-1-9 2005) as an example.

47

It shows that in the range between 5 and 100 million cycles, the slope of the hot

spot curve is zero while it is 5 for the nominal stress S-N curve at this range.

Outside this range both curves have the same slope. Hence, the nominal stress

S-N method is more conservative than the hot spot method, especially for number

of cycles higher than 100 million.
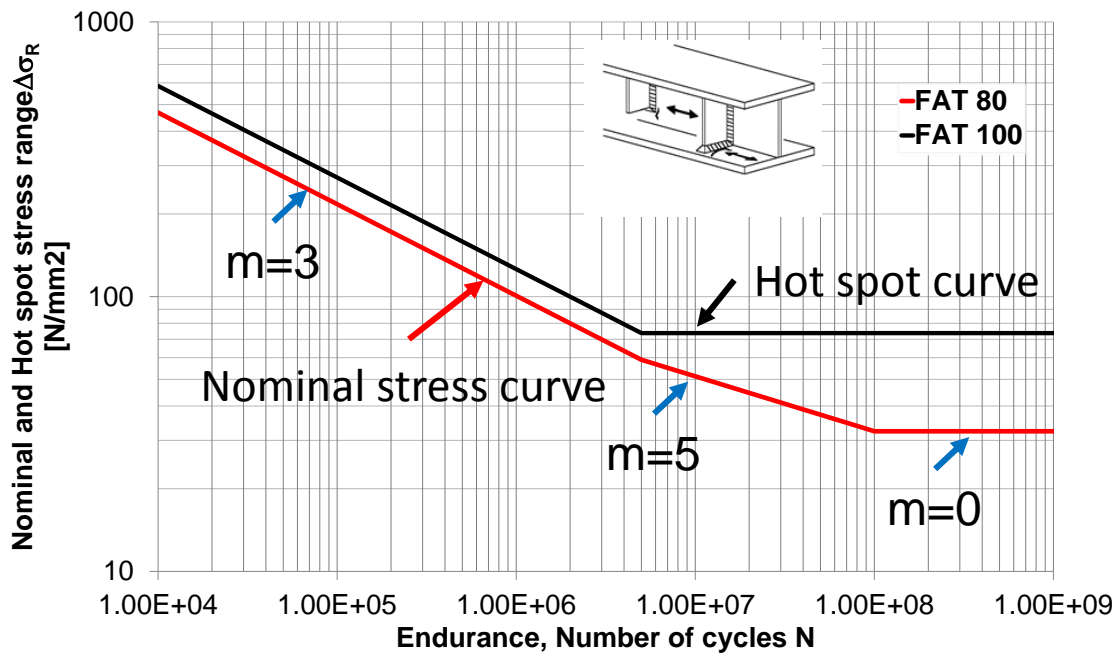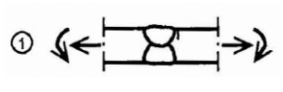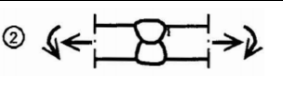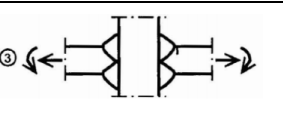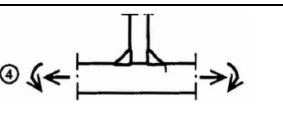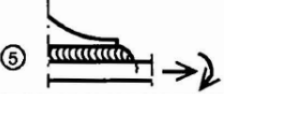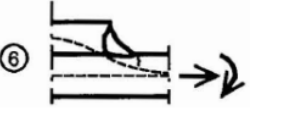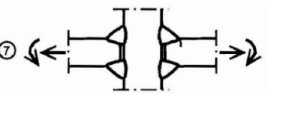
Figure 2.5 Comparison between the slope (m) of the nominal stress and hot spot stress curves for connection 7 as described in Table 8.4 in the Eurocode 3 (EN 1993-1-9 2005).

Table 2.1 Detail categories for the hot spot stress method
as recommended by Eurocode (EN 1993-1-9 2005)

Detail category	Constructional detail	Description	Requirements
112		Full penetration butt joint (Special quality).	All welds ground flush to plate surface parallel to direction of the arrow. - Weld run-on and run-off pieces to be used and subsequently removed, plate edges to be ground flush in direction of stress. -Welded from both sides, checked by NDT.
100		Full penetration butt joint (Normal quality).	Weld not ground flush - Weld run-on and run-off pieces to be used and subsequently removed, plate edges to be ground flush in direction of stress. - Welded from both sides.
100		Cruciform joint with full penetration K-butt welds.	Weld toe angle≤60º
100		Non load carrying fillet welds.	Weld toe angle≤60º
100		Bracket ends, ends of longitudinal stiffeners.	Weld toe angle≤60º
100		Cover plate ends and similar joints.	Weld toe angle≤60º
90		Cruciform joints with load-carrying fillet welds.	Weld toe angle≤60º

2.2 Cumulative fatigue damage theories

As noted before, real-life structures are subject to variable amplitude loading. Therefore the application of S-N curves, which are typically derived from testing under constant amplitude loading, to real-life structures requires cumulative fatigue damage theories that can integrate the damage induced by individual stress cycles.

For over seventy years, the most popular approaches to the assessment of fatigue damage were the Palmgren-Miner linear hypothesis or Miner's rule popularized by Miner (1945) and the double linear damage rule proposed by Manson & Halford in 1981. The latter was widely considered to be a credible alternative to Miner's rule although the former had the benefit of being relatively simpler (Manson & Halford 1981; Manson 1986).

More recent studies have however identified several shortcomings with Miner's rule and other older methods (Fatemi & Yang 1998) and (Cui 2002). A key shortcoming is the lack of an appropriate computationally and experimentally inexpensive uncertainty modelling technique to account for the stochastic nature of both material properties and external loadings (Liu & Mahadevan 2007). This has encouraged the development of more complex fatigue damage accumulation models such as non-linear continuum damage mechanics models (Aid et al. 2011), (Dai et al. 2013), (Luo et al. 2014) and (Zuo et al. 2015) that have been successfully illustrated for fatigue assessment of bridges (Zhang et al. 2013). However, our review finds that, despite the multitude of new cumulative damage models, there is no universally accepted model that accounts fully for all the phenomenological factors i.e. multiple damage stages, nonlinear damage

evolution, load sequence, overload effects, spectrum shape, small amplitude cycles below fatigue limit, and mean stress. The problem is simply too complex for any of the existing predictive models. Also the application of the new methods to real-life engineering design and assessment is extremely challenging. As a result, the Miner's rule remains the practitioner's choice for fatigue damage assessment and is also recommended by the current design codes and standards such as (EN 1993-1-9 2005). In the next section, the Miner's rule is briefly described.

2.2.1 Linear damage accumulation (The Palmgren–Miner rule)

Miner's rule, is probably the most widely used approach for fatigue life prediction. As previously discussed it was first published in 1945 by Miner (1945) based on the following three main assumptions (Zuo et al. 2015).

1. The rate of damage accumulation remains constant over each loading cycle.

2. Damage occurs and accumulates only when the stress is higher than the CAFL.

3. Fatigue failure is said to occur when fatigue damage accumulation D as evaluated using Equation 2.5 is equal to 1.0.

$$D = \frac{n_1}{N_1} + \frac{n_2}{N_2} + \frac{n_3}{N_3} \ldots = \sum_{n=1}^{k} \frac{n_i}{N_i} \leq 1.0 \qquad (2.5)$$

The same equation can also be used to arrive at an estimate of the remaining fatigue life of the component based on the current loading conditions. In the

above equation, n_i represents the number of applied cycles in the stress range S_i and is obtained from the stress time-history using one of the cycle counting methods as discussed in the next section. N_i represents the number of cycles until failure under constant amplitude loading with stress range S_i and is determined from the S-N curve. k is the number of stress ranges considered in the damage accumulation model.

2.3 Cycle- counting algorithms

A cycle-counting algorithm is an algorithm that transforms the stress history into a stress spectrum for the purposes of applying Miner's rule. Examples include level-crossing counting, peak counting, simple range counting, and Rainflow counting (Fasl 2013). A comprehensive and historical review of counting methods, in particular, the Rainflow method, is available in the work done by (Nijssen 2006) . In this study, the Rainflow method is used for stress cycle counting as recommended by ASTM E1049 (2011).

2.3.1 The Rainflow cycle-counting method

The Rainflow cycle-counting method was first proposed by Matsuishi and Endo in 1968 (Marsh et al. 2016). This method converts a stress time-history into a set of half cycles and reversal cycles that can then be analysed using Miner's rule. A half cycle is either the rising portion or a falling portion of a stress time-history (Rakoczy 2011). A reversal cycle, on the other hand, consists of both the rising (loading) and falling (unloading) portions with the start and end points having the

same stress value. (Rakoczy 2011) summarised the Rainflow counting method

in Figure 2.6.
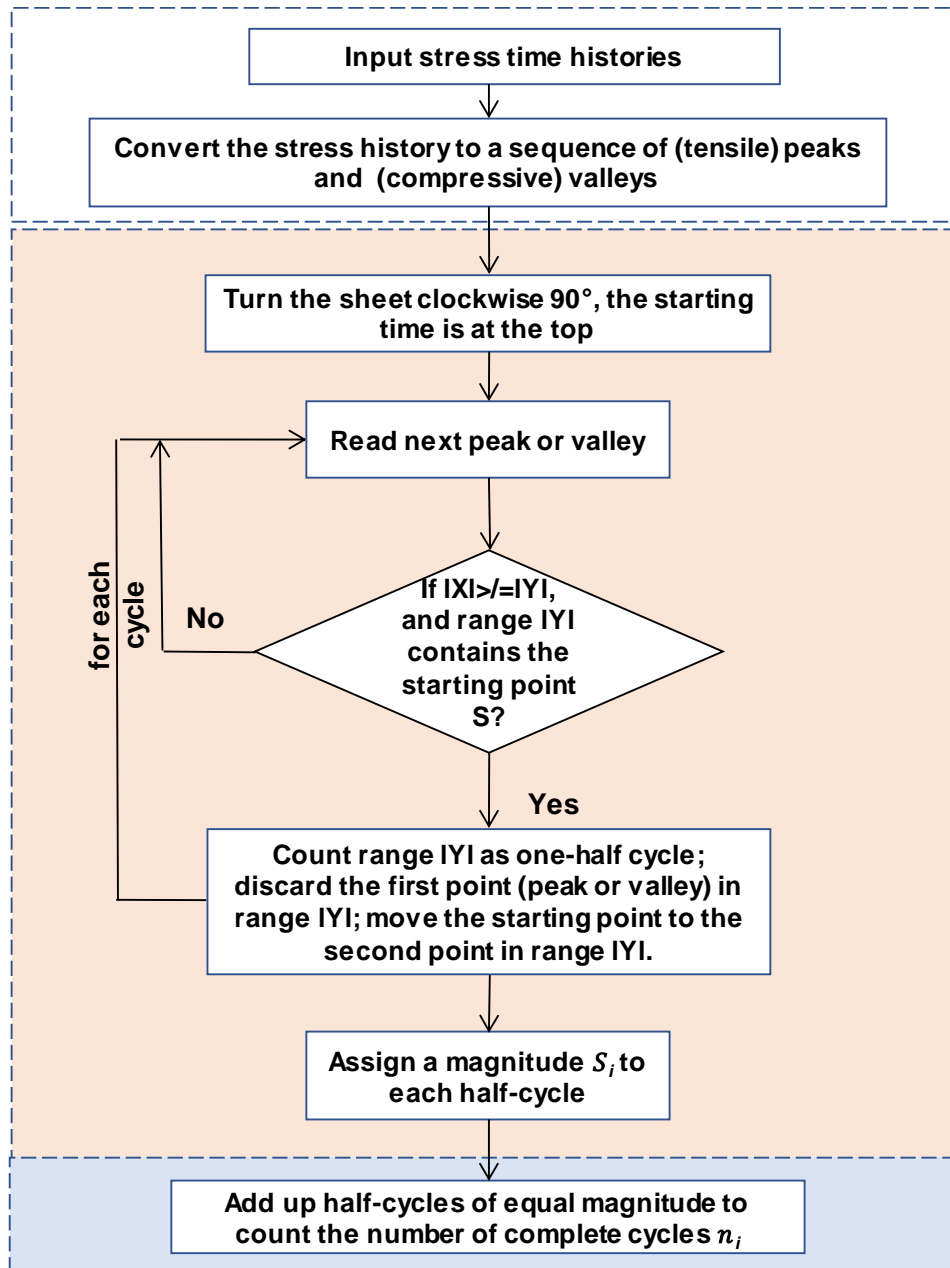
Figure 2.6 Rainflow counting method Flow chart. Where IXI denotes absolute stress range under consideration; IYI, previous absolute stress range adjacent to IXI; S, starting point in the time history.

An example is given using the ASTM implementation. A stress time history is

given in Figure 2.7 (a). The same time history is shown converted to a sequence

of (tensile) peaks and (compressive) valleys and rotated 90 degrees in

Figure 2.7(b) and Figure 2.8 along with the Rainflow lines, respectively.

(a)   (b)
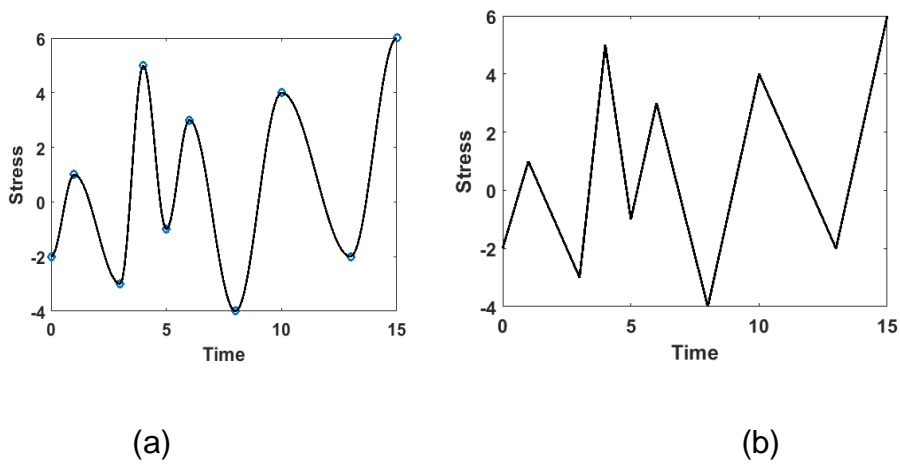
Figure 2.7 a) Original stress history and b) stress history reduced to turning points
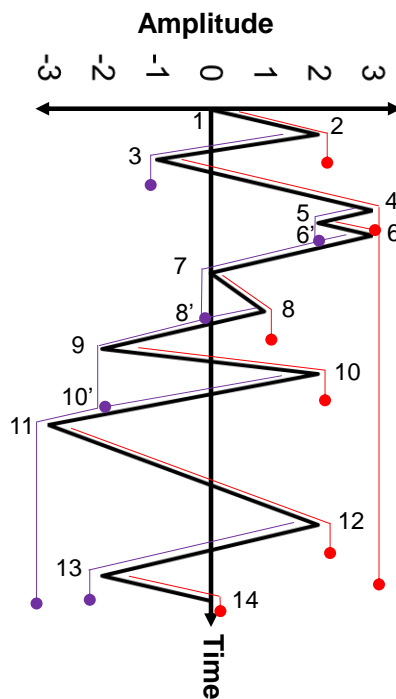
Figure 2.8 Rain-flow counting diagram (Rakoczy 2011).

Each peak and compressive valley are considered as a source of water from

which water drips down the pagoda. The number of half-cycles are counted by

looking for terminations in the flow occurring when either: (i) it reaches the end of the time-history (Figure 2.8 path 3-4-end or 4-5-7-9-11- end); (ii) it merges with a flow that started at an earlier tensile peak; or (iii) it flows opposite a tensile peak of greater magnitude (Figure 2.8, path: 5-6, 6- 6', 8-8', 10-10'). Each half-cycle is added to the stress range of corresponding S_i. The Rainflow data is summarized in Table 2.2 for the stress time history in Figure 2.8. Half-cycles of equal magnitude are paired up to count the number of complete cycles n_i (Table 2.3). Normally, this would still result in a few remaining half-cycles.

Table 2.2 Half cycles after Rainflow counting.

Half Cycles			
Positive direction		Negative direction	
Range	Amplitude (S_i)	Range	Amplitude (S_i)
1-2	2	2-3	3
3-4-end	4	4-5-7-9-11-end	6
5-6	1	6-6'	1
7-8	1	8-8'	1
9-10	4	10-10'	4
11-12	5	12-13	4
13-14	2	-	-

Table 2.3 Load cycles after Rainflow counting.

Amplitude (S_i)	Number of cycles (n_i)
1	2
2	1
3	0.5
4	2
5	0.5
6	0.5

2.4   Types of fatigue damage

Traditionally, fatigue damage is categorized as either load-induced fatigue cracking or out-of-plane displacement (distortion)-induced fatigue cracking (AASHTO, 2011; Bowman et al., 2012).

2.4.1 Load-Induced Fatigue

Load-induced fatigue refers to fatigue damage due to in-plane stresses (primary stresses). This is relevant for steel plates that comprise bridge member cross-sections. The in-plane stresses are typically calculated from numerical modelling (AASHTO LRFD 2017). For instance, flexural stress in the flange or web of a steel girder, or the stresses at a shear stud of a composite girder can be a cause of fatigue damage (Russo et al. 2016). In steel structures, load-induced fatigue cracking is often initiated in regions with residual stresses and other defects such as discontinuities that are caused by the manufacturing process.

2.4.2 Distortion-induced fatigue

Distortion-induced fatigue results from either out-of-plane distortion or secondary stress, and can subsequently result in major failure of bridge structural elements or of the structure in its entirety (Bowman et al. 2012; American Association of State Highway and Transportation Officials 2012). Distortion-induced fatigue cracking is a consequence of the cyclic manifestation of a small and local deformation that is normally out-of-plane (Okelo 2017; Lenwari & Chen 2013).

Distortion-induced fatigue is a major maintenance issue for steel bridges. In Japan, the majority of fatigue related cracks were attributed to distortion-induced stresses (Nishikawa et al. 1998). Connor & Fisher (2006) found that close to 90% of all fatigue cracking problems in steel bridges in the USA were due to out-of-plane distortion of fatigue sensitive details. Also Bowman et al (2012) did a survey of US state transportation officials to assess existing fatigue-related procedures and inspections and found that distortion-induced fatigue cracking was the most commonly encountered form of fatigue damage. In addition, the general consensus (Connor & Lloyd 2017) was that distortion-induced fatigue is not only a concern for steel girder bridges but also for trusses, suspension bridges, tied arch bridges and box girder bridges.

Cross beam - main girder connections

This section discusses a commonly used detail in steel girder bridges that is known to be susceptible to distortion-induced fatigue cracking. The detail is the transverse web stiffener which serves as an intermediate connection plate detail in old ladder type bridge decks. These connections are intended to distribute

traffic loading, resist lateral load, and stabilize the girders. The design of steel bridges before the mid-1980s did not align with the level of detail that is now acceptable according to today's industry standards (Dexter & Ocel 2013). Prior to the mid-1980s, steel girder bridges had cross beams that were adjoined to the main girder via transverse connection stiffeners. The stiffeners were welded to the main girder web but with a gap near the tension flange. As a result, a small length of the girder web, extending from the extreme edge of the stiffener to the tension flange, was left unsupported as illustrated in the Figure 2.9.
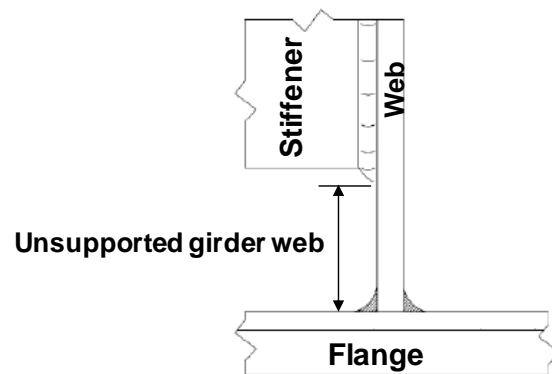
Figure 2.9 Schematic representation of web gap

Differential deflection between the main girders of the bridge under live loading results in cross frames either pulling or pushing the girder web. The consequence is a high level of cyclic secondary stress in the web gap area as illustrated in Figure 2.10. Fisher and Roy (2015) provide a more detailed discussion on the out-of-plane distortion manifesting in web-gap regions.
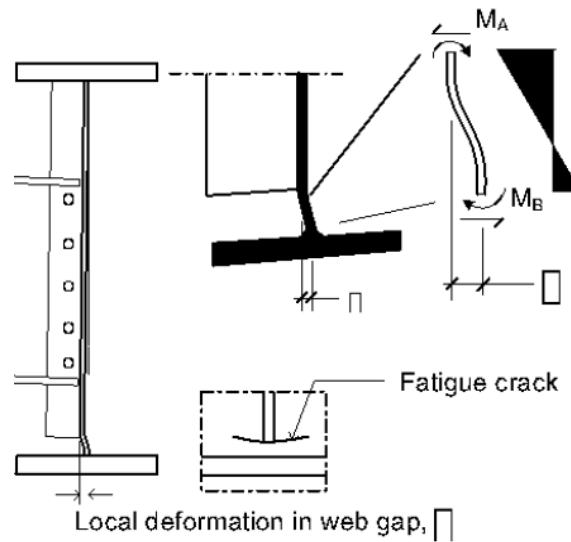
Figure 2.10 Differential deflection of bridge girders results in high local bending stresses in unstiffened web gaps (Haghani et al. 2012); the small rectangles represent the out-of-plane deformation.

There exist several practical examples where fatigue cracks have resulted directly due to out-of-plane distortion in the web-gaps (Dexter & Ocel 2013). One such example is shown in Figure 2.11. Even though modern design specifications give particular attention to structural details to ensure that these problems do not occur, thousands of older bridges nonetheless still exist and are vulnerable to cracking in this manner.

Figure 2.11 Example of web gap cracking resulting from distortion (Dexter & Ocel 2013).

2.5   Determination of stress time-histories

There are two main approaches for arriving at stress time-histories. The first uses numerical models such as finite element model (FEM) and the second relies on field measurements that may be collected as part of a structural health monitoring (SHM) system. Monitoring can refer to techniques ranging from those using measurements of structural response (e.g. strain-based methods) to those that employ other types of measurements such as non-destructive evaluation methods (e.g. acoustic monitoring). This research aims to utilise the former class of methods, specifically a combination of global and local response monitoring methods.

2.5.1 Numerical models

Stress histories for the fatigue assessment of steel bridges has traditionally been obtained through the use of a traffic load and a structural model (Hajializadeh et al. 2017). Modelling real traffic loads can be a challenge because of the unpredictability surrounding traffic parameters such as axle loads, their spacing and positions, and dynamic amplification effects. Therefore standard truck models recommended in the design codes are typically used. However better estimates may be obtained using a weigh-in-motion (WIM) system (Chotickai & Bowman 2006). The loading data must be combined with a numerical model of bridge structural behaviour to obtain stress histories. Relying on simple numerical models may cause errors as such models may ignore distortional and secondary deformations that are common at connections.

2.5.2 Field measurements based on Structural Health Monitoring (SHM)

SHM broadly refers to the process of using measurements from sensing to understand structural performance (Shen et al. 2016). Long-span bridges generally receive more focus in SHM applications. Ye et al (2014) asserted that this is because of larger investments and their more pivotal role economically, as well as the innovative methods employed for both designing and building these bridges in countries such as, but not limited to, the USA (D'Attilio et al. 2008), and (Jang et al. 2010), Japan (Fujino 2002), Korea (Yun et al. 2003), Hong Kong (Xu 2018) and (Wong 2007), Chinese mainland (Nie et al. 2018); (Shen et al. 2016); (Zhang & Zhou 2007); (Jinping Ou & Hui Li 2010) and (Yi et al. 2013), Turkey (D'Attilio et al. 2008) and Canada (Chowdhury et al. 2015) and (Mufti 2002) and (Desjardins et al. 2006). For a comprehensive description of SHM, readers are referred to (Ahlborn et al. 2010)(Worden & Dulieu-Barton 2004). This chapter focuses specifically on past research into application of SHM for fatigue assessment of short and medium-span metallic bridges, which is the focus of this study.

SHM is relevant for short and medium-span highway bridges and a number of applications exist in literature. However so far their applications have been limited due to the following two key factors. First, the time and cost of installing sensors can be a significant bottleneck. Attema et al (2017) mention that the time taken to install a full measurement system for a bridge may be more than 75% of the time needed for testing. The cost of installation can be over 25% of the total cost of the SHM system. In addition, both maintenance and data processing costs,

61

when factored in, can be significant. However all these costs depend on the types of sensors used. For strain gauges, which are the sensors needed for fatigue evaluation, these costs are relatively low. Moreover the savings in terms of extending the service life of a bridge may exceed the costs of sensors by a few orders of magnitude.

Second, SHM systems normally require sensors to be placed strategically on the structure. To be economical, the SHM system should provide meaningful information with a minimum number of sensors (Clarke 2009). However this may be difficult to achieve in practice. Complex bridge structures may require a large number of sensors in order accurately to obtain an understanding of their structural behaviour (Rodriguez et al. 2015). Furthermore, ascertaining the most conducive location for gauges can be challenging. For example, in the context of fatigue life assessment, care should be taken to avoid installing strain gauges at locations that have low stress ranges as the data may not prove useful. Zhou (2006) highlights the importance of analysing a bridge prior to monitoring as this allows for establishing areas that experience high stress levels. Nonetheless, due to site limitations, instrumenting these areas directly with strain gauges may be a challenge for many structures for reasons such as difficulties with access. This study will aim to alleviate these two issues by proposing a low-cost sensing-based fatigue assessment methodology.

The main reason to use SHM for fatigue assessment is to account for the environmental factors and the real structural behaviour, which together have a significant on fatigue damage development in steel bridges. Factors that influence the real loading on a bridge such as the distribution of vehicle types and

62

their speeds, road roughness and ambient conditions vary from one bridge to another. Fatigue analysis that uses code specified loads will hence have large safety factors to account for this uncertainty and typically end up overestimating loading. Large safety factors are also used with predictions obtained from numerical models of structural behaviour due to the uncertainties associated with modelling. Consequently fatigue damage estimates from modelling based approaches tend to be conservative. Monitoring can reduce the conservativeness by enabling a more accurate assessment of loading and/or structural behaviour. Stress ranges based on in-situ measurements are likely to be realistic and less conservative than stress range predictions obtained using design loads. This in turn can help in predicting reliably the remaining fatigue life (Saberi et al. 2016).

Mohammadi et al (1998) discuss the use of SHM for fatigue assessment through a case study involving fifteen highway bridges in Illinois. They employed field data to assess the stress ranges at fatigue-critical areas. This technique was also used by Alampalli & Lund (2006) and Zhou (2006) for evaluating fatigue life on the basis of the fatigue strength (S-N) curves of various bridges in the United States. Other examples are Saberi et al (2016) and Li et al (2009), who used field strain measurements and continuum damage mechanics methods to assess the fatigue damage of a bridge in Hong Kong. SHM data was also utilised for making predictions about the remaining fatigue life of bridge components (Zhao et al. 1994) and (Lee & Cho 2016). However all these studies suffer from one or more of the following limitations:

- Most studies rely on measurements of nominal stress in member rather than the local, concentrated stress at a weld detail (Saberi et al. 2016),

(Seo et al. 2013), (Alampalli & Lund 2006), (Tarries et al. 2002), (Kwon et al. 2012), (Phares et al. 2003), (Cardini & DeWolf 2009) and (Frangopol et al. 2008). The influence of local (i.e., concentrated) stresses is only indirectly taken into account by using S-N curves that are obtained via experimental testing for specific weld details. There is also the possibility of the structural detail and load type not falling under one of the design classes provided in the codes. In such a scenario, bespoke laboratory tests may be required to generate the S-N curves and this can be a challenge since the testing procedure is expensive and time consuming.

- Few studies have attempted to characterize accurately the loading. They often employ a combination of finite element modelling and measured loading data such as via a weigh-in-motion (WIM) system (Pasquier et al. 2016), (Attanayake & Aktan 2015), (Seo et al. 2013). Installation of WIM systems requires temporary roadway closures and pavement cuts for placing sensors. The condition of the existing pavement at the installation site may also create challenges for installation and for obtaining reliable truck weight measurements. The accuracy of WIM systems may also be low due to the interaction between pavement and vehicle and other factors such as the installation, calibration, and maintenance procedures of the sensor system. In fact, the stress computations based on the WIM data have previously been found to be much higher than those from actual in-situ monitoring (Attanayake & Aktan 2015).

- Other studies have attempted to evaluate in-situ hot spot stresses at welds using models that have been calibrated using measured data (Doornink et

al. 2006), (Schumacher 2003; Schumacher & Nussbaumer 2006). This is often done because placing a strain gauge at the point of highest stress is often impossible (Berglund & Schultz 2006), (Jajich et al. 2000) and (Connor et al. 2005). Also at details where cracking is driven by secondary (or local) bending of the connected elements, the measured stresses may not represent localized or "hot spot" stress due to the high stress gradients.

2.6   Fatigue life assessment methods

There are three main methods for estimating fatigue damage from stress time histories. These include the classical approach (stress-life S-N) method, local strain-life (Є-N) method and fatigue crack growth method. This literature focuses only on the stress-life method which is the most common method in the bridge sector.

2.6.1 Fatigue analysis using Stress-life (S-N) approach

Stress-life (S-N) is a technique applicable to scenarios where the relevant stress (or strain) quantity remains below yield limits. Such scenarios are also referred to as high-cycle fatigue scenarios since the number of cycles to failure is typically high. Structural metals and alloys usually fall in this category as they can withstand around 10^4 to 10^5 stress cycles to failure.

In the S-N approach, the elastic stress range is determined using a Wöhler S-N curve. Damage is amassed throughout history of operation and this is used to identify the total damage incurred. The method for establishing fatigue assessment is as follows:

65

1. Calculate linear elastic stress histories.

2. Extract fatigue cycles (generally using the Rainflow algorithm).

3. Assess damage caused using stress range and S-N curve.

4. Evaluate the cumulative damage (generally using Miner's rule).

Stress-life techniques are categorised into three main classes based on a stress analysis of structure-focused details. These include nominal stress method, hot spot stress method, and effective notch stress method (Ye et al. 2014)

Nominal stress method

One of the most widely used techniques for estimating the fatigue life of steel bridges is the nominal stress method. The current design standards in many countries, the IIW and the Eurocode (Fricke 2003) and (Cai et al. 2017) are based on this method. The method provides engineers a simple procedure for assessing the performance of welded details using global response data (Cai et al. 2017). It relies fundamentally on the average stress within the cross-section under consideration as computed using linear structural mechanics. The method excludes local stress and focuses on the relative large stress of macro-geometric shape of studied component in the vicinity of welded details, whilst disregarding the ignored attached welded effects (Vasudevan et al. 2016).

Nominal stress: Nominal stress can be computed based on simple linear elastic theory. For example, for elements subject to bending, the stress can be computed using

$$\sigma_{nom} = \frac{F}{A} + \frac{M}{Z} \tag{2.6}$$

66

where σ_{nom} is the nominal stress and A is the cross-sectional area of the detail. F and M are the axial force and bending moment respectively. Z is the elastic modulus of the cross section respectively. For complex structures, finite element analysis is often used to evaluate the nominal stress. Nominal stress can also be estimated via strain gauges, while taking care that the strain gauges are not placed too close to the regions with stress concentration.

After the calculation of nominal stress at a desired location, the S-N curve corresponding to the category of the given detail as defined in the design codes is identified (Heshmati 2012). The measured nominal stress and the S-N curve can be used to evaluate the fatigued damage and also predict the remaining service life.

However, the nominal stress method is not applicable to all situations. For example, a detail may be complex in geometry and not comparable to any of the categories listed in the design codes. Also, load distributions can be too complex for an accurate estimation of nominal stress (Mashiri & Zhao 2005). Additionally, even when nominal stress can be predicted, the method still excludes dimensional variations in individual structural details (Poutiainen et al. 2004). The method generally tends to overestimate stress ranges and when combined with conservative design curves leads to overestimation of fatigue damage or under-prediction of remaining service life (Chung et al. 2004).

Hot spot stress method

An alternative method proposed is hot spot stress developed to enable evaluating the fatigue strength of welded structures in cases where the nominal stress is

difficult to estimate because of geometric and/or loading complexities. This approach has traditionally been used for the fatigue design of pressure vessels and welded tubular connections. Over the last couple of decades, the method has been applied successfully to welded plated structures (Lotsberg 2006) and (Hobbacher 2009). The rapid development of the finite element software has enabled wider uptake of the hot spot stress method for the fatigue life evaluation of welded complex structures. The major advantage of the hot spot stress approach is that the stress raising effects of the joint members are taken into consideration in the fatigue stress calculations. Another advantage is that the number of S-N curves is significantly reduced with this approach. IIW and Eurocode 3 have defined only two S-N curves for fatigue evaluation based on the hot spot stress approach. Each S-N curve is identified by a fatigue class or detail class value (FAT) which is the characteristic strength at 2 million cycles in MPa.; FAT90 for load carrying and FAT100 for non-load carrying welded attachments. The fewer number of design classes irrespective of the joint geometry is consistent with the hot spot stress principle of including the macro-geometric stress raisers.

A comprehensive description of the hot spot stress approach is given in Lotsberg et al (2006), Hobbacher (2009), Lee et al (2010) and Hobbacher (2016). A brief description of this approach, as required to understand the methodology proposed by this research, is given below.

Hot spot stress: A location in a welded detail where fatigue cracking is most likely to initiate (e.g. due to abrupt structural discontinuity) is commonly called a hot spot. The stress at this location is referred to as the hot spot stress. The onset of

68

fatigue failure at a hot spot is determined by the time-history of hot spot stresses. In a welded connection, hot spots are usually at weld toes. The stress at the weld toe including the nonlinear notch effects is referred to as the notch stress. The notch stress, can be decomposed into three components: membrane stress σ_{mem}, shell bending stress σ_{ben}, and a nonlinear stress component σ_{nlp} due to the weld toe singularity as shown in Figure 2.12. The hot spot stress however includes only the linear stress components - σ_{mem} and σ_{ben}, and can be obtained from in-situ strain measurements or through numerical modelling. The nonlinear stress component σ_{nlp}, is included indirectly by using S-N curves that are obtained from laboratory fatigue tests (Radaj 1990) to estimate the fatigue life.
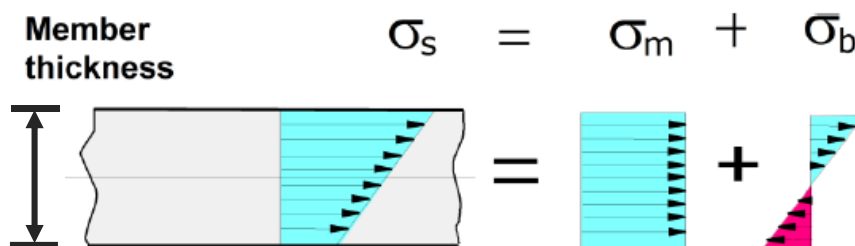
Figure 2.12 Stress distribution through plate thickness at a weld toe (Hobbacher 2009).

<u>Evaluation of hot spot stress:</u> If evaluated from measurements, the hot spot stress can be obtained using either surface stress extrapolation or linearization of stress in the through thickness direction (Dong 2001), (Xiao, Zhi-Gang and Yamada 2004), (Niemi et al. 2006) and (Hobbacher 2009). Owing the relative ease of application, the surface stress extrapolation methods are more popular in practice, and are also employed in this study. In surface stress extrapolation methods, the hot spot stress is evaluated using the strains measured at certain reference locations adjacent to the hot spot. To avoid nonlinearities, these

locations are located outside of the region affected by the weld toe notch singularity.

The IIW recommends consideration of stresses at two types of hot spots a and b. Figure 2.13 shows the two types of hot spots. Type a corresponds to hot spots on the plate surface, and b corresponds to those on the plate edge.
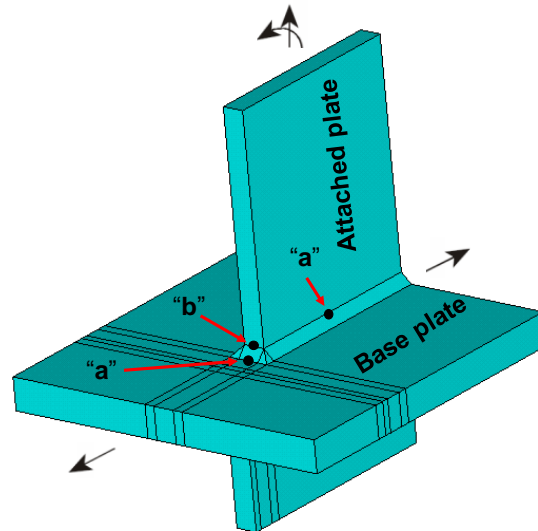
Figure 2.13 Hot spots of types a and b (Hobbacher 2009) with the arrows indicating the directions of the loads at the connection.

For hot spots of type a on a plate having thickness *t*, the hot spot stress is computed through linear extrapolation equation of the stresses, and, predicted at distances 0.4*t* and 1.0*t* away from the weld toe Figure 2.14, respectively as shown below.

$$\sigma_{hs} = 1.67\sigma_{0.4t} - 0.67\sigma_{1.0t} \qquad\qquad (2.7)$$
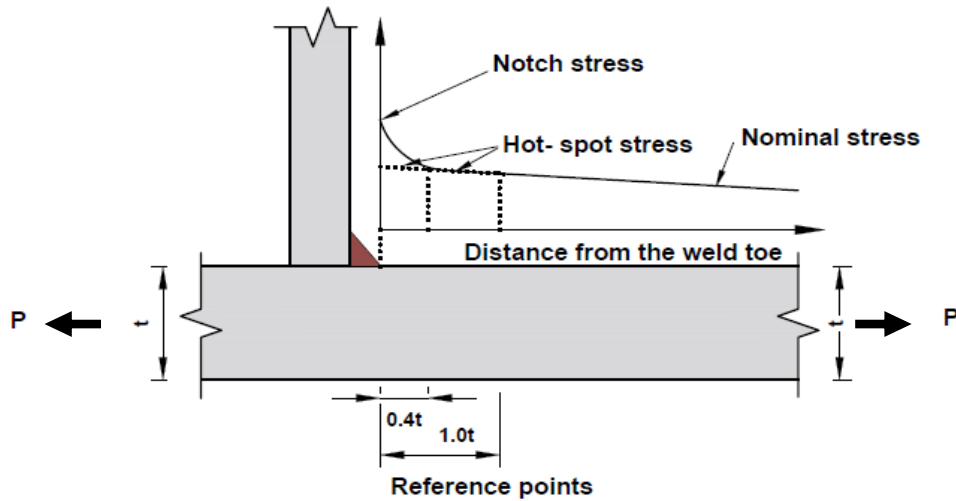
Figure 2.14 Evaluation of the hot spot stress at a hot spot of type a through linear extrapolation (Hobbacher 2009) with the arrows indicating loading directions.

The hot spot stress for locations of type b is computed using a linearized approximation of a quadratic stress profile σ_{4mm}, σ_{8mm} and σ_{12mm}, predicted on the plate at distances 4mm, 8mm and 12mm respectively from the weld toe as shown in Figure 2.15. The corresponding equation is as follows.

$$\sigma_{hs} = 3\sigma_{4\ mm} - \sigma_{8\ mm} + \sigma_{12\ mm} \tag{2.8}$$
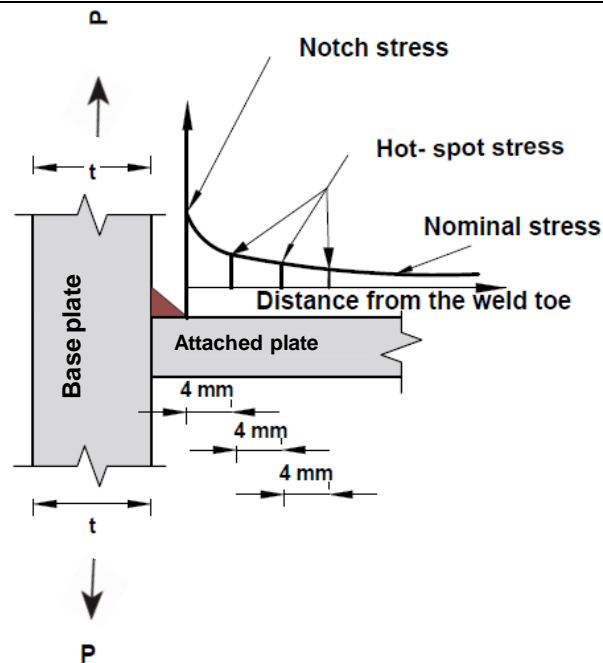
Figure 2.15 Evaluation of the hot spot stress at a hot spot of type b through quadratic linear extrapolation (Hobbacher 2009) with the arrows indicating loading directions.

For hot spots of type b, the stress profile near the weld toe is independent of the plate thickness *t* and hence Equation (2.8) does not have any terms related to *t*. This is in contrast to the stress profiles for hot spots of type a, which are functions of the plate thickness *t* (see Equation (2.7)).

If computing hot spot stress through numerical modelling, a finite element model of the welded connection is used to predict the stresses at reference locations as required to compute using Equations (2.7) or (2.8). The FEM needs to be set up carefully. This includes assigning suitable boundary conditions and loads, and utilizing appropriate element and analysis types to ensure reliable predictions. The IIW (Niemi et al. 2006) provides guidelines for this purpose. It permits the use of 8-noded shell or 20-noded solid elements, both of which allow for a linear stress distribution through the thickness. The element mesh in the area close to the hot spot must be refined to a degree such that the local stress gradients are

captured accurately. Also, the mesh should have nodes at locations where stresses are required according to Equations (2.7) or (2.8). If shell elements are used, the weld geometry is usually omitted from the model even though this simplification may underestimate the stiffness of the weld. The stress at a reference location as required for Equations (2.7) and (2.8) is either

1. the predicted maximum principal stress at the corresponding location in the model if the stress vector is oriented within 60º of the normal to a weld toe, or

2. the normal stress that is oriented in the direction normal to the weld toe.

Effective notch stress method

Another stress-life method that is classifiable as a 'local' approach is the effective notch stress method. This method was first introduced by (Radaj et al. 2006) and considers the highest computed elastic stress at the critical points, i.e. the weld toe and the weld root. Comprehensive guidelines and recommendations for fatigue assessment by notch stress analysis can be found in (Fricke 2013) and (Hobbacher 2016).

<u>Notch stress:</u> Areas of elevated stress, or notches, emanate from geometric discontinuities such as holes and sharp, local changes in geometry. They are extremely common and cannot be avoided in welded steel structures (Al-Emrani & Aygül 2014). These localized stress raisers influence the fatigue strength of welded details. Notch stress, which includes all of the effects of the stress raisers at the local notch, consists of the sum of geometrical stress and non-linear stress peak (Hobbacher 2016). The peak of a notch stress at the weld toe or root depends on the notch "sharpness", more frequently referred to as the "notch

radius" (Radaj et al. 2006). Additionally, the actual shape of the weld contour has to be replaced by an effective contour to account for the variation of the weld shape parameters as well as of the non-linear material behaviour at the notch root or toe Figure 2.16.
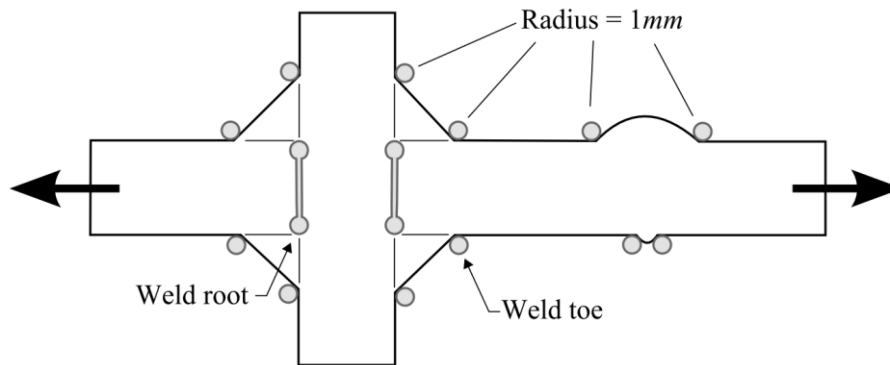
Figure 2.16 Fictitious rounding of weld toes and roots (Radaj et al. 2006).

Evaluation of effective notch stress based on IIW 2016: Effective notch stresses can be calculated by parametric formulae, taken from diagrams or calculated by finite or boundary element models. The effective notch radius is introduced such that the tip of the radius coincides with the root of the real notch, e.g. the end of an un-welded root gap.

The IIW's guideline for the determination of effective notch stress by FEA mentions that 3D solid elements and 2D planar elements can be used for calculating the total stress at the critical sections. However for accuracy with these calculations, a sufficient element density should be maintained. Element sizes of not more than 1/6 of the radius are recommended in the case of linear elements, and 1/4 of the radius in the case of higher order elements Figure 2.17 and Table 2.4. It should be noted that, for an analysis of this kind, only nodal stress values are applicable directly. In addition to that, the maximum principal

74

stress component should be used for all calculations. Fatigue assessment via the effective notch stress method has found that a fatigue strength of FAT225 can be used for all welded structural details irrespective of the loading type, IIW recommendations or geometry.
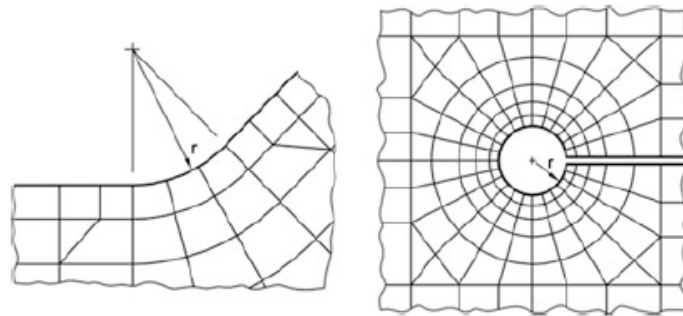
Figure 2.17 Recommended meshing at weld toes and roots (Radaj et al. 2006).

Table 2.4 Recommended size of elements on surface (Radaj et al. 2006).

Element type	Relative size	Absolute size (mm)	No. of elements In 45°	No. of elements in 360°
Quadratic with mid-side nodes	≤r/4	≤0.25	≥3	≥24
Linear	≤r/6	≤0.15	≥5	≥40

2.7   Conclusions

The following conclusions can be derived from the literature review on current fatigue damage evaluation procedures and the role of monitoring in these procedures, particularly on obtaining stress time-histories.

- The majority of the current approaches rely on fatigue design rules (Zhou & Chan 2007) to derive the stress time histories. These approaches are based on the nominal stress, which does not take into account the local stress concentration effects in a specific weld detail (Park & Kim 2014), (Tveiten et al. 2007; Ye et al. 2012).

- Current approaches exaggerate greatly the actual applied live loads and in turn the stress cycles, resulting in overly conservative estimates of the remaining fatigue life (Lee & Cho 2016; Zhou 2006; Kashefi et al. 2010).

- In-situ strain measurements are increasingly employed for assessing the remaining fatigue life of steel bridges (Alampalli & Lund 2006; Chan et al. 2001; Zhou 2006). These have been shown to be more reliable than assessments based on stress predictions (Brownjohn 2007; Schumacher & Nussbaumer 2006; Ye et al. 2012; Lee & Cho 2016).

- The majority of monitoring applications focus on measuring nominal stress in a member rather than local, concentrated stress at a weld detail. This is primarily due to the practical difficulty of measuring in-situ hot spot stresses due to site limitations and the steep stress gradients.

- Monitoring data are representative only of the locations where actual sensors are located (Hajializadeh et al., 2017). Methodologies that derive fatigue performance of uninstrumented details in a structure from a minimum number of strain gauges are therefore needed.

- The hot-spot stress approach, while widely used for fatigue assessment, has not been applied to distortion-induced fatigue problems, which are a major issue particularly in old steel railway bridges.

This thesis proposes a novel methodology for evaluating in-situ hot spot stresses that overcomes the above-mentioned drawbacks. It integrates field measurements of strains taken from around the weld detail with a numerical model of the connection to evaluate the in-situ hot spot stresses. The measured strains are used to compute the axial, shear and bending forces that are applied to the connection. By applying these forces to the model, it will capture the local effects such as dynamic amplification of load that play a major role in fatigue life. Also unlike the modified hot spot stress method, knowledge of the stress concentration factor is not required but its effect is instead explicitly accounted for within the modelling process. This thesis also proposes a novel procedure to use information from real sensors at one connection to estimate hot spot stress at other uninstrumented locations. The research methodology of this thesis is described in detail in Chapter 3.

CHAPTER 3   Research Methodology

3.1   Introduction

The literature review in Chapter 2 on fatigue life assessment clearly indicated the potential for fatigue assessment by combining field measurements with numerical models. This chapter aims to describe a methodology that exploits this potential. It will allow for the computation of hot spot stress time-history and thereby the fatigue damage at structural details instrumented with strain gauges. The methodology will also allow extrapolation of the measurements from one instrumented detail to other non-monitored details.

3.2   Methodology for hot spot stress evaluation

The methodology for deriving the hot stress time-history that is proposed in this study is illustrated in Figure 3.1 and is broadly as follows.

For a given steel bridge, the first step is to identify its fatigue-critical connections. In this study, this is done using a numerical model, i.e. a FEM of the bridge. Then local FE models are developed for the identified fatigue-critical connections. The local FE models are linear elastic FE models that comprise all the connection components (e.g. stiffener, weld) along with small portions of the structural elements that are part of the connection. For example, the local FEM of a main beam-stringer or a main beam-cross beam connection, which is the type of connection investigated in this paper, will include small portions of the intersecting beams in addition to the connection components. Simultaneously a field measurement plan is developed and implemented for the fatigue-critical

connections. The measurement plan will include installing strain gauges on the structural elements relevant to the connection in a manner that will enable evaluating the time-history of internal forces that are transferred via the connection. These force time-histories are then applied to the local FEM to evaluate the time-histories of stresses at relevant locations as necessary to compute the hot spot stress time-histories using Equations (2.7) and (2.8). These stress time-histories are then used for fatigue damage assessment using existing methods. Thus, in principle, if the strain gauges are left to collect measurements continuously, then the fatigue life of the critical details can be monitored continuously via this approach.
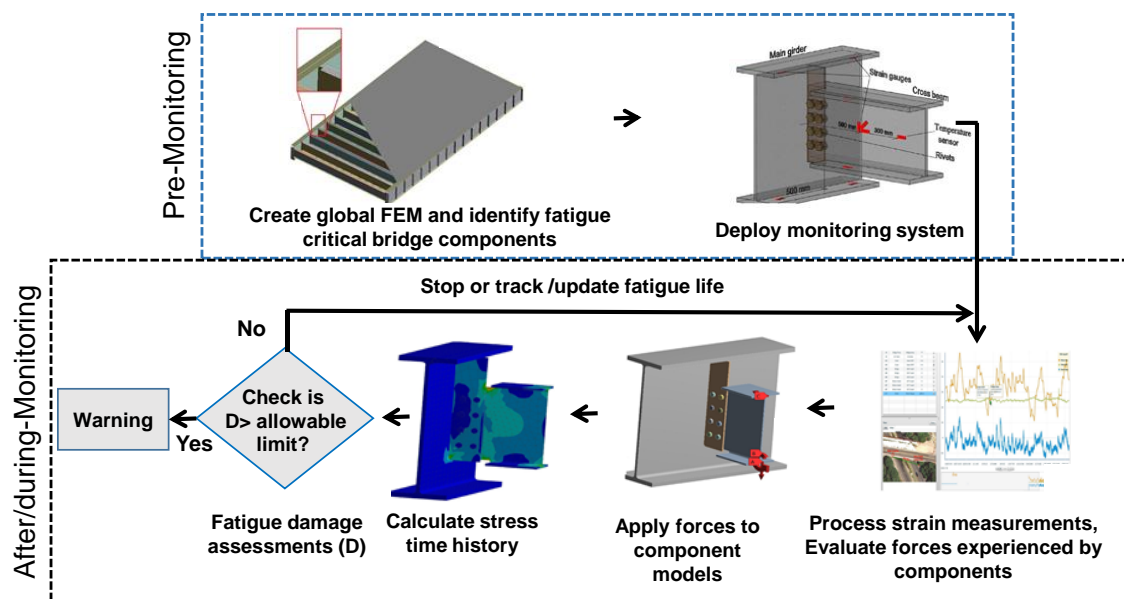
Figure 3.1 Overview of the proposed methodology for stress time history/fatigue damage evaluation at directly monitored details

The key elements in the methodology are now explained in detail.

Creation of global FEM: This is a numerical model of the entire structure.

Creation of local FEM: This model essentially simulates the structural behaviour of the connection and includes the connection and the structural elements that intersect at the connection. In this thesis, the structural elements are main beams and cross beams. These are not modelled fully but only a short length as required to ensure stress concentration effects from the connection are absent at the boundaries. The local FEM is created based on the IIW recommendations (Niemi et al. 2006) currently used to set up a FEM to apply the hot spot stress approach. The IIW recommends the types of critical hot spots to be considered as well as the element type and the stress extrapolation techniques to be adopted. Defining suitable boundary conditions for the local FEM is critical to ensure model predictions are reliable. This study evaluates three different boundary conditions and their influence on the performance of the overall methodology (see Section 4.5.2).

Deployment of monitoring system: This step needs to consider several factors including strain gauge locations and sampling rates for data collection and processing. Measuring strain histories for fatigue life assessment require a modern data acquisition system with sufficient data storage and a high sampling rate (~100 Hz) to capture dynamic effects of loading. Strain gauges are installed in a manner that will allow evaluating the internal forces at locations corresponding to the boundary of the local FEM. For each beam intersecting at the connection, sufficient strain gauges are installed to enable computing the three main internal forces – stress resultant (about its major axis), axial force and shear force. The assumption is that torsion and bending effects about the minor axis are negligible. Typically, this will require installing strain gauges at the top

and bottom of the cross-section to capture bending effects, and a rosette near the neutral axis to capture shear effects. Measurements from these gauges when taken together will enable computing the exact location of the neutral axis, and subsequently the bending moment, shear force and axial force through simple Euler-Bernoulli beam bending assumptions.

Updating and validation of the Global FEM: This is achieved by performing a preliminary experimental modal identification on the bridge and using results of ambient vibration tests to record the bridge responding. Defining suitable boundary conditions for the global FEM to ensure model predictions are reliable. Conducting a controlled load test on the bridge for collecting data to validate the finite element models of the bridge. This is achieved by using readings from installed strain sensors at several locations on the bridge.

Hot spot stress evaluation: The internal forces computed for each measurement time-step are applied as loading to the local FEM of the connection. The local FEM is used to predict the stresses at the reference locations as required to compute the hot spot stress σ_{hs} using Equations (2.7) and (2.8). Since the local FEM is a linear elastic model with stresses related linearly to the applied loads, individual FEM runs are not required for determining the stresses due to internal forces evaluated from each measurement time-step. This can be accomplished simply through the use of load scaling factors (LSF) – $S_{M,i}$, $S_{V,i}$, $S_{A,i}$, which are essentially the stresses produced at a reference location i by an internal moment and force – namely a bending moment M, a shear force V or an axial force A of unit magnitude U_M, U_V and U_A, respectively. The stress $\sigma_{i,j}$ at a reference location i due to the internal forces - M_j, V_j and A_j, evaluated for a measurement time step

81

j is therefore computed by superposing together the individual stresses - $\sigma_{M,i,j}$, $\sigma_{V,i,j}$ and $\sigma_{A,i,j}$, produced by the three internal forces as shown using the following equations.

$$\sigma_{M,i,j} = \frac{M_j S_{M,i}}{U_M} \tag{3.1}$$

$$\sigma_{V,i,j} = \frac{V_j S_{V,i}}{U_V} \tag{3.2}$$

$$\sigma_{A,i,j} = \frac{A_j S_{A,i}}{U_A} \tag{3.3}$$

$$\sigma_{i,j} = \sigma_{M,i,j} + \sigma_{V,i,j} + \sigma_{A,i,j} \tag{3.4}$$

$\sigma_{i,j}$ computed at reference locations i for a time step j are used in Equations (2.8) and (2.9) to determine the corresponding hot spot stress $\sigma_{hs,j}$. The time-history of hot spot stresses is then used to assess fatigue damage using Miner's rule (Miner M 1945) and appropriate S-N curves. The methodology for hot stress time-history and fatigue damage assessment for monitored details proposed in this study is illustrated in Figure 3.2.

Phase I

Create a global FEM using design drawings and/or site measurements

Choose appropriate boundary conditions

Perform transient analysis

Evaluate (LSF) – $S_{M,i}$, $S_{V,i}$, and $S_{A,i}$

Apply unit load U_M, U_M and U_M

Identify fatigue critical connection/s

Validate the local FEM

Create local FEM for critical connection/s

Extract stress time-history
$$\sigma_{i,j} = \sigma_{M,i,j} + \sigma_{V,i,j} + \sigma_{A,i,j}$$

Deploy monitoring system

Obtain stress time history at monitored location/s
$$\sigma_{hs,j}$$

Rain flow counting method

Collect and process strain data

Assess fatigue damage using Miner's rule D=$\sum {}^{n_i}/{}_{N_i}$

Classify fatigue category

Evaluate force time-histories experienced by connections: M_j, V_j and A_j

Check is D> allowable limit? — Yes → **Warning**

Continue monitoring? — Yes / No

No → **Stop**

Figure 3.2 The proposed methodology for hot spot stress time history/fatigue damage evaluation at directly monitored details

83

3.3 Stress extrapolation using global FEM

This study aims to develop a methodology to predict hot spot stresses and nominal stresses at locations where there are no sensors by using measurements from an instrumented connection and calibrated FE models. This methodology is referred to as a virtual sensing procedure (VSP).

The VSP can be divided into two consecutive parts. The first step utilises the in-service monitoring data along with the local finite element model to estimate the stress at a specific hot spot location (i.e. web gap region) around an instrumented connection. This will use the methodology described earlier in Section 3.2. In the second step, the hot spot stress evaluated at the instrumented connection and FE models (both local and global) are combined to estimate hot spot stress at uninstrumented locations. A summary of this research methodology is shown in Figure 3.3.

The key elements of the VSP are now explained in detail.

‘Hot spot’ location at the instrumented connection: If a connection is instrumented with a limited number of strain sensors, following steps of section 3.1, strain measurements from these sensors can be used to predict stresses at this connection. It should be noted that the physical gauges are referred to as reference gauges and the remaining uninstrumented locations are denoted as virtual sensing locations.

‘Hot spot’ location at uninstrumented connections: This part of the methodology is proposed to estimate the stresses at the weld toe of uninstrumented connections (i.e. virtual sensing locations) using data from instrumented

connections. The main requirement is a calibrated global FEM of the bridge. The global FEM is used to extract influence lines of the hot spot stress (σ_{hs}) at the hot spot near the reference sensors and also of the hot spot stress at the virtual sensing locations (σ_{Vhs}). Since fatigue damage is determined by the peak-to-peak stress cycles, the ratio R_i between the peak magnitude of σ_{hs} and σ_{Vhs} is computed. R_i is assumed to remain constant across different load values, and this assumption is generally true for short-span bridges. Finally, hot spot stress time-history at a virtual sensing locations (σ_{Vhs}) is determined by multiplying the hot spot stress (σ_{hs}) at the reference locations (i.e. at weld toe of web gap region) computed using measurements by R_i. This procedure is described in detail below.

First, use strain measurements from reference gauges locations to derive the time-history of hot spot stress (σ_{hs}) at instrumented hot spot locations.

Second, adapt the global FEM to simulate reliably the structural behaviour of uninstrumented locations. This is achieved by refining the calibrated global FEM at the virtual sensing locations to a mesh resolution similar to that of the local FEM. The global FEM is then loaded with axle loads corresponding to lorries from Fatigue Load Model 4 (FLM4) in the Eurocode (BS NA EN 1991-2 2003). The hot spot stress peaks at the virtual sensing locations (σ_{VSi}) and the reference locations σ_{phs} are evaluated. The peaks are used to compute R_i according to

$$R_i = \sigma_{VSi}/\sigma_{phs} \tag{3.5}$$

Finally, the hot spot stress time-history at a virtual sensing location (σ_{Vhsi}) is obtained using

$$\sigma_{Vhsi} = \sigma_{mhs} \cdot R_i \tag{3.6}$$

'Nominal' stresses at uninstrumented locations: Although this thesis focuses on the evaluation of the time-history of hot spot stresses, the developed methodology can also be adapted to estimate the nominal stresses at any desired global location (e.g. top/bottom flange of a steel bridge girder) using data collected from an instrumented connection. The idea is based on one key assumption: each vehicle produces one load cycle on the bridge, regardless of the traffic flow conditions. This is based on findings by Baptista (Baptista 2016) who showed that the effect of the traffic flow conditions on stress influence lines is negligible in bridges with spans shorter than 40 m. This is because of the span length being in the range of the vehicle length plus a minimum distance between lorries as recommended by (BS NA EN 1991-2 2003). The proposed procedure is essentially similar to that for deriving hot spot stresses at uninstrumented locations. In this case, the calibrated global FEM is used to compute the ratio between the peak nominal stress at the instrumented location and that at the uninstrumented location.

Phase II

Calibrate and validate the global FEM

Fatigue Load Model (FLM4)

Obtain stress peak ratios (R_i) between un-instrumented locations and monitored location/s

Use stress hot spot stress time-history at monitored location/s σ_{hsi} from Phase I

Multiply

$$\sigma_{Vhsi} = R_i \times \sigma_{hsi}$$

Predict stress time history at un-instrumented location/s σ_{Vhsi}

Rain flow counting method

Assess fatigue damage using Miner's rule D=$\sum {n_i}/{N_i}$

Classify fatigue category

Check is D> allowable limit?

Yes

Warning

No

Continue monitoring?

Yes

No

Stop

Figure 3.3 Developed a hot spot stress response prediction method for locations where there are in sufficient sensors (flow chart).

87

3.4   Summary

This thesis proposes a comprehensive, experimentally supported stress evaluation procedure dedicated to short span steel bridges. The most significant contribution of this research is the methodology for evaluating in-situ hot spot stresses. It integrates field measurements of strains taken from around the weld detail with a numerical model of the connection to evaluate the in-situ hot spot stresses. The measured strains are used to compute the axial, shear and bending forces that are applied to the connection. By applying these forces to the model, it will capture the local effects such as dynamic amplification of load that play a major role in fatigue life. Other novel contributions are in the individual steps of the methodology, in how the methodology is evaluated on full-scale bridges and in the use of the results from this methodology to design retrofits. Specifically these include: (i) the development of a procedure to use information from real sensors at one connection to estimate hot spot stress/nominal stress at other uninstrumented locations/connections and (ii) a study on repair measures to extend fatigue life of details vulnerable to distortion induced fatigue. The latter is not discussed in this chapter but presented in Chapter 6. The methodology presented in this chapter is investigated in detail in Chapters 4 and 5 using full-scale bridges as case studies.

CHAPTER 4   Field testing and finite element modelling of Bascule Bridge

4.1   Introduction

A steel bridge (Bascule Bridge) is employed to address the study objectives (2-5) stated previously in Chapter 1. This bridge is representative of many old bridges having fatigue concerns. In this chapter, a detailed description of the structure is first presented. Then, the bridge instrumentation (i.e. sensors deployment) is discussed including equipment set up and description. This is followed by a description of the global finite element model (global FEM) of the bridge, which is used to simulate the bridge response under different conditions. The local finite element model (local FEM) is then presented. This is an FE model of a selected welded connection used for hot spot stress estimation. Then, field measurements are presented, which is used to calibrate the FE models and validate the proposed methodology. This starts with a detailed description of the sensors and data acquisition system used to measure and record the bridge response due to different types of excitation. Sensor layout and installation procedures are discussed in detail, along with in-situ loading methods used to excite the bridge. Signal processing and modal analysis methods are also explained in detail. The study of the global and local bridge FEM modelling including defined loads and boundary conditions is explained. The validation of these models is also discussed. A sensitivity analysis is conducted to identify the most suitable finite element mesh configuration for local FEM application is detailed. Finally, a sensor-free stress estimation model validation is presented.

4.2   The Bascule Bridge

The Bascule Bridge in Exeter, UK is selected as the main case study to illustrate the proposed research methodology described in Chapter 3. It is a structural system that is commonly used in short span steel girder bridges within the U.K. roadway transportation network. The bridge was built in 1972, and carries the northbound carriageway of A379, a major trunk road, over the Exeter Canal. The map in Figure 4.1 delineates the location of the bridge and Figure 4.2 shows a picture of the bridge.
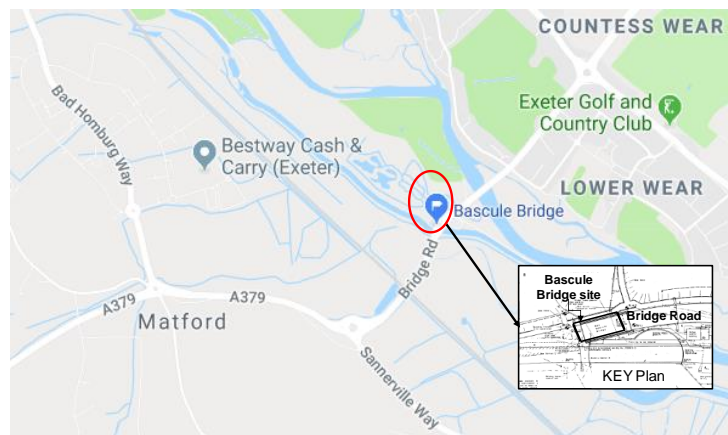
Figure 4.1 Location of Bascule Bridge on Google Maps (Latitude: 50.694626, Longitude: -3.502002).

Figure 4.2 The Bascule Bridge.

The Bascule Bridge is a movable bridge with lifting hangers, a counterweight and hydraulic cylinders on both sides of the bridge that enable it to be raised and lowered to allow boats to pass through (Figure 4.3). The bridge supports one-way traffic of significant volume with a posted maximum speed limit of 64 km/h (40 mph). The bridge uses a twin-main beam system that is classified as fracture critical by AASHTO (American Association of State Highway and Transportation Officials 2010) as the fatigue failure of a single connection can lead to bridge collapse or closure of the bridge for repair.
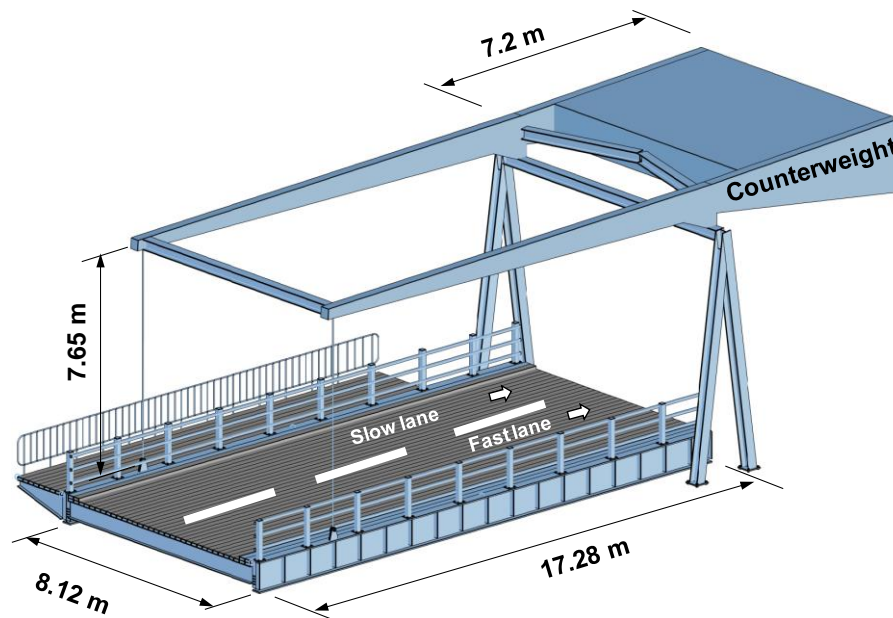
Figure 4.3 Schematic of the Bascule Bridge.

4.2.1 Structural Components:

The bridge has a simply supported span of length 17.28 m. It consists of two rolled main girders, 17 cross beams and a composite aluminium deck. The cross beams are 8.12 m long and spaced at 970 mm intervals as shown in Figure 4.4.

The functions of the cross beams are to provide resistance against lateral forces and to distribute loads from the aluminium deck to main girders. The cross-beams are attached to vertical web-stiffeners welded to the web of the main girders by bolts as shown in Figure 4.5.
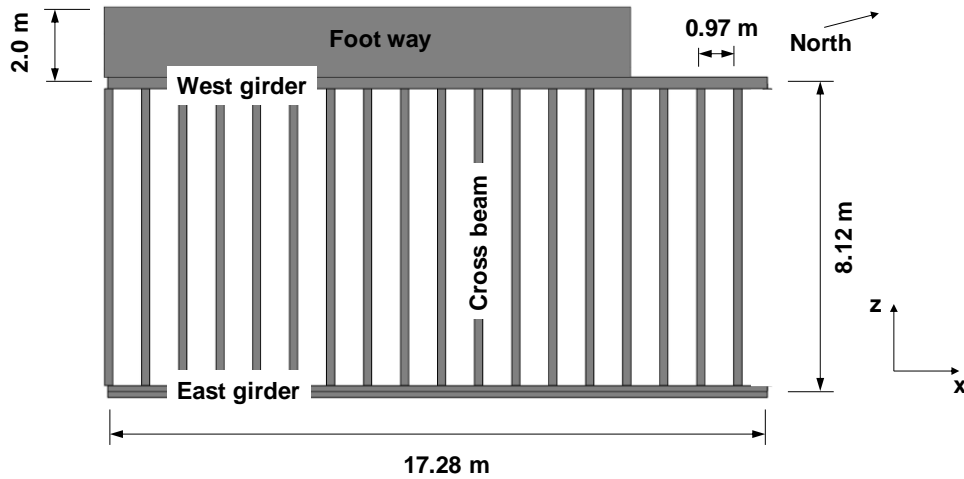
Figure 4.4 Plan schematic of the Bascule Bridge (lengths in metres).

Figure 4.5 Picture of a main girder - cross beam connection.

A typical cross section of the bridge is shown in Figure 4.6. The clear carriageway width of the bridge is 6.7 m and includes two lanes of 3.35 m width each. There is also a 2.0 m wide footway on one side of the bridge. The longitudinal beams and cross beams are steel rolled sections type S355 having the cross-section geometries detailed in Table 4. The longitudinal beams are spaced 8.12 m apart.
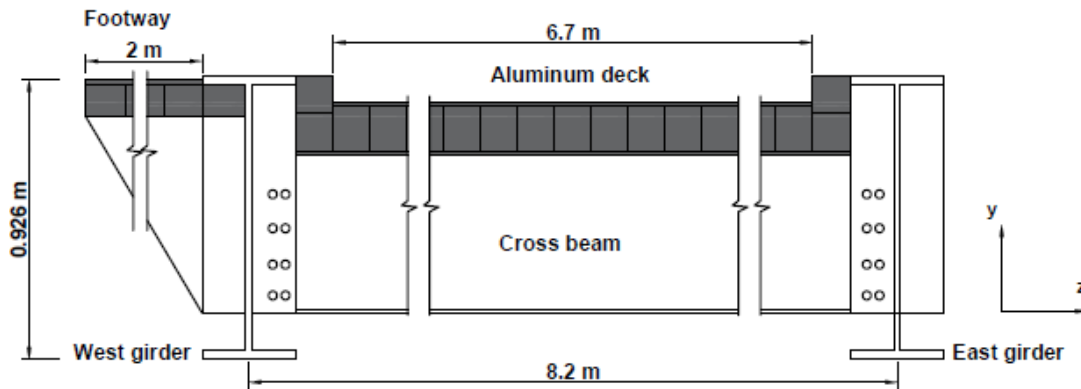
Figure 4.6 Bridge cross section (units in metres).

Table 4.1 Geometrical characteristics of the main girders and cross beams.

Structural element	Depth (mm)	Top flange width (mm)	Top flange thickness (mm)	Bottom flange width (mm)	Bottom flange thickness (mm)	Web thickness (mm)
Main girder	926.6	307.7	32	307.7	32	19.5
Cross beam	528.3	208.8	13.2	208.8	13.2	9.6

The deck of this bridge consists of cross beams supporting aluminium deck planks. The depth of an aluminium plank is 140 mm. The aluminium planks are

held down onto steel cross beams with bolts as shown in Figure 4.7 and Figure 4.8.
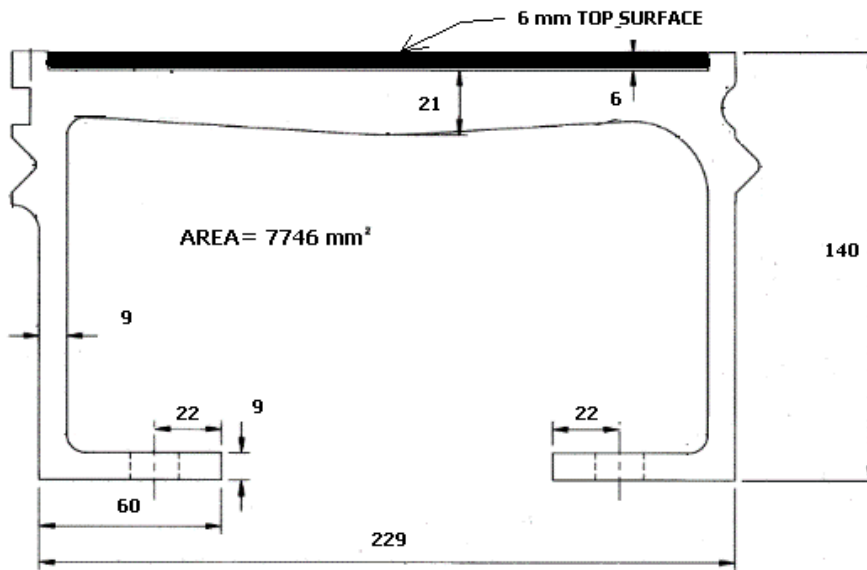
Figure 4.7 Schematic of deck plank cross-section (units in millimetres). "Courtesy: Devon County Council".
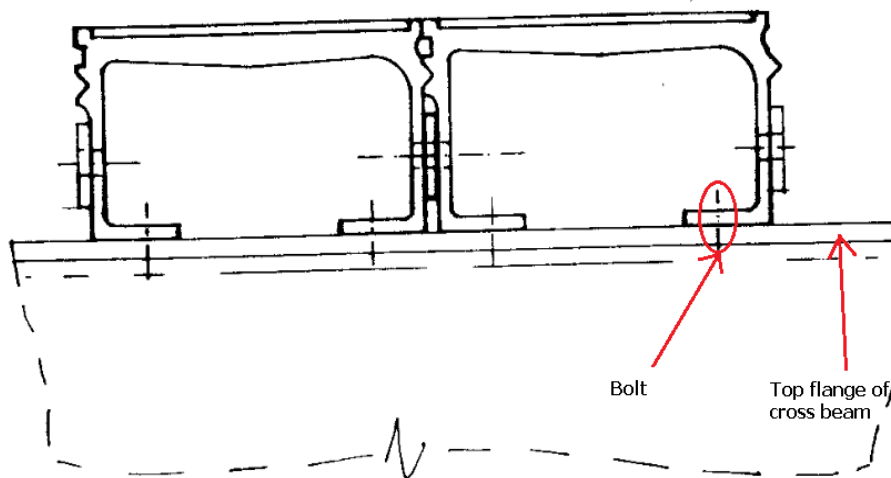
Figure 4.8 Schematic of deck planks and top flange of cross beam connection "Devon County Council".

94

4.2.2 Lifting and stabilization system and bridge support:

Figure 4.9 shows the key elements of the lifting and stabilization system (counterweight, lifting suspension rods, and hydraulic cylinders) and also identifies the support conditions.
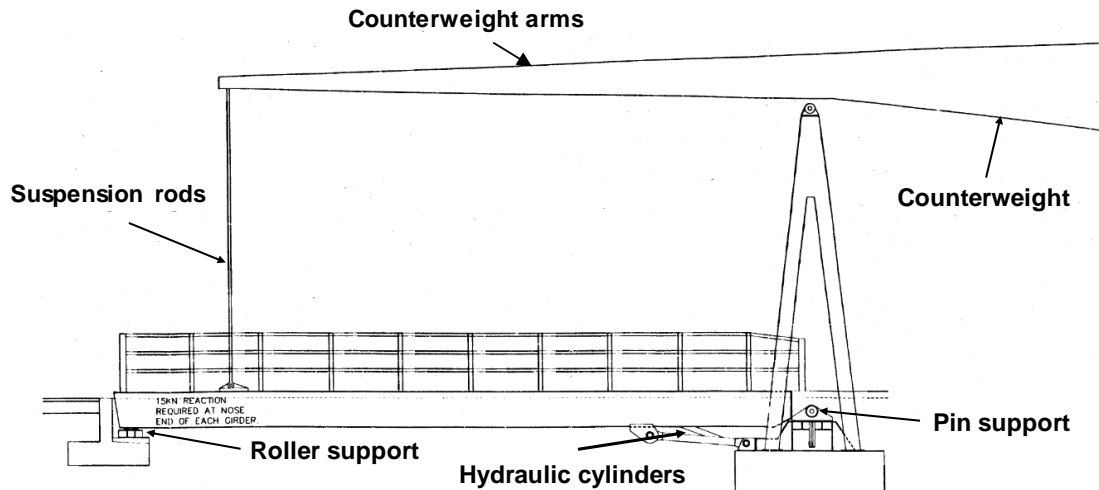
Figure 4.9 Schematic of the support conditions and lifting and stabilization system of the Bascule Bridge.

Steel counterweight

The 70 tons mass produces a 15 kN reaction at the other end of each longitudinal main girder when the bridge is open for traffic. This ensures that minimal power is needed to lift the bridge. The 15 kN reaction is transferred via 60 mm diameter cylindrical rods (referred to as suspension rods in Figure 4.9) that connect each of the bridge main girders with the counterweight arms.

Hydraulic cylinders

The bridge is raised and lowered using a pair of hydraulic jacks. The jacks are operated from a control room located next to the bridge.

Supports (Bridge Ends)

The main girders are simply supported, i.e. with a roller and a pin support as outlined below. The roller support is at the end furthest from the counterweight. Figure 4.10 shows one of the roller supports. A hydraulic shock absorber that is present to dampen the impact caused when the bridge is lowered and to reduce vehicle-induced vibration is also partially visible in the figure.
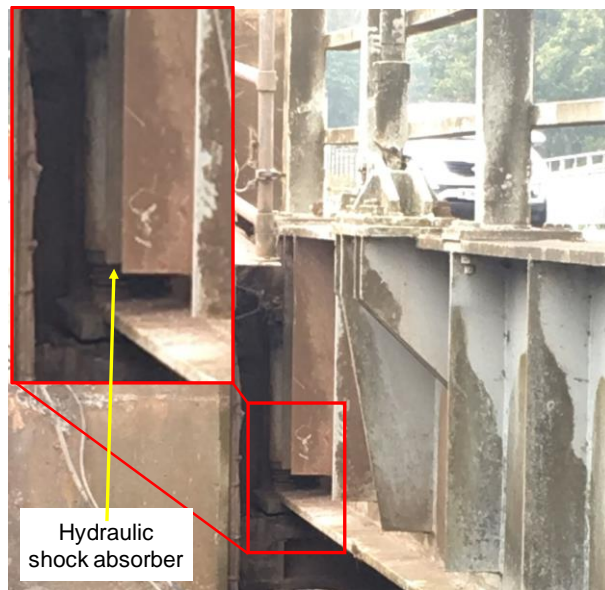
Figure 4.10 Picture for the roller support furthest from the counterweight end of the

The pin support is at the end closer to the counterweight (see Figure 4.11). The bridge rotates freely about this support when raised or lowered.

Figure 4.11 The pin support of the bridge.

4.3   Instrumentation plan and equipment

This section discusses the process of selecting the structural connection for instrumentation along with the instrumentation scheme of the selected fatigue-detail. A detailed description of the sensors and data acquisition system used to measure the bridge response due to different types of excitation is also given.

4.3.1 Fatigue-critical connections

The Bascule Bridge has 34 beam – beam connections corresponding to where the 17 cross beams are connected to the two main girders. These connections are identical in assembly and are as shown in Figure 4.12.
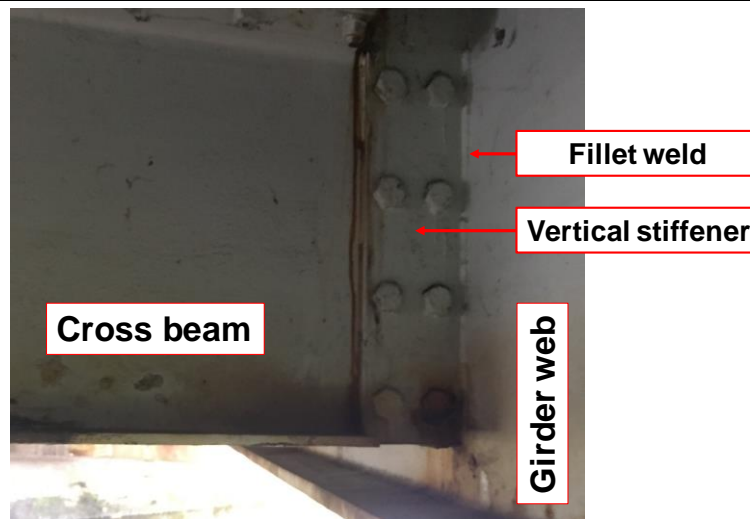
Figure 4.12 The cross beam is attached to the vertical web-stiffener of the girder by bolts.

As discussed in part one of chapter 3, the development of the proposed research methodology requires field measurements around welded connection/s. This connection could be any accessible detail, i.e. either fatigue critical (where fatigue damage is expected to be a major concern) or any other connection. For the Bascule Bridge, the fatigue-critical connection was identified as a first step. In this thesis, this is done by using the developed global FEM of the bridge along with the equivalent Lorries for Fatigue Load Model 4 NA to BS EN 1991-2-3 (BS NA EN 1991-2 2003), which is discussed in more detail in chapter 6. The location of the critical connection is close to the bridge support as shown in Figure 4.13. However, accessing this connection is difficult on site due to it being located over river stream, and hence it was not instrumented. Instead a similar connection but one that was easily accessible was instrumented as shown in Figure 4.13.
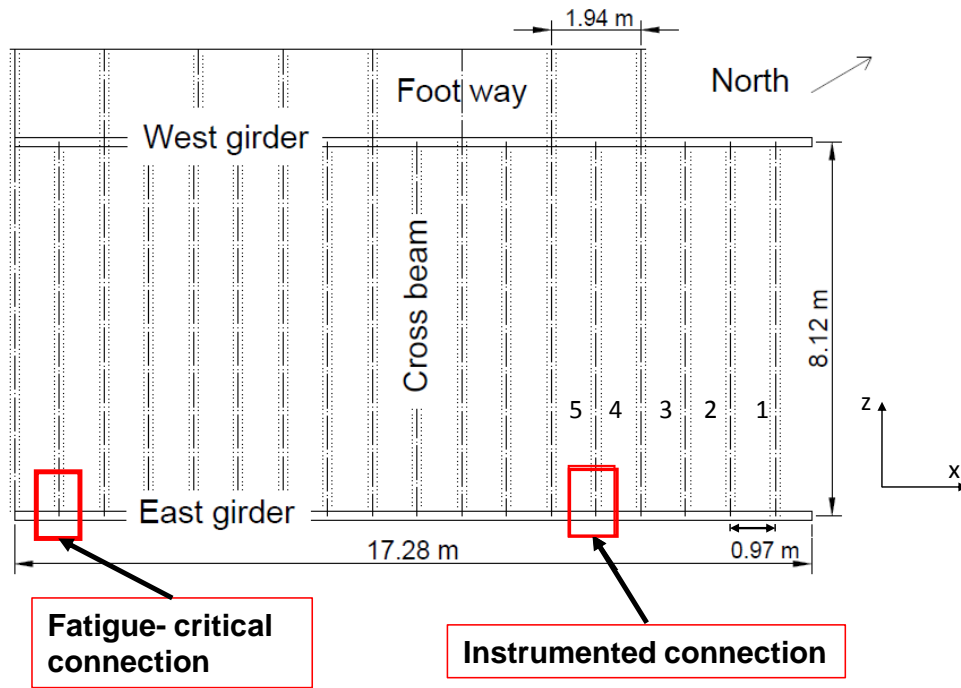
Figure 4.13 The critical and instrumented connections locations.

4.3.2 Instrumentation equipment and sensor layout

Strain gages were the primary type of sensor used and these were of two types: standard weldable strain gauges from Micro-Measurements (Division of Vishay Precision Group) and Strain Transducer 350 (ST 350) from BDI. The locations of these gauges on the schematic of the full-scale bridge are shown in Figure 4.14. In addition to the strain sensors, the bridge was instrumented with accelerometers which were used to measure acceleration responses of the bridge. These responses were used to calibrate the numerical model of the bridge.
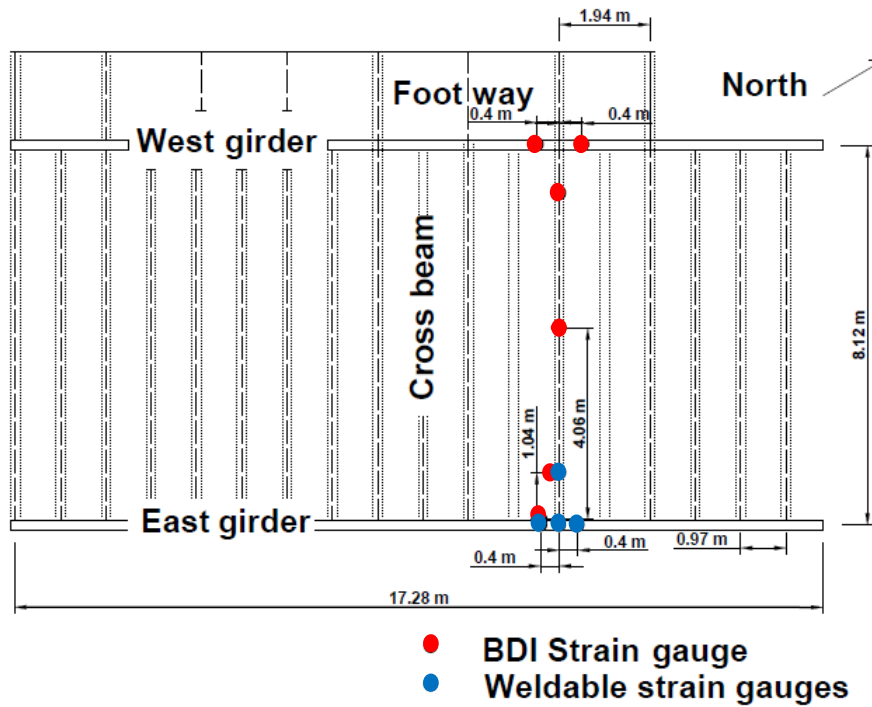
Figure 4.14 Instrumentation layout on the bridge.

Weldable strain gauges: Weldable strain gauges measure strain in one principal direction; along the long axis of the shim. The gauges were 5.84 mm (0.72") active grid long with a resistance of 120 Ω. For the application, the gauge wires were spliced to a thicker, insulated wire to minimize possible electrical interference. A total of 11 weldable strain gauges were applied to the steel surfaces of the bridge. Gauges were attached using spot welder model 700 (Vishay Micro-Measurements) by adding spot welds around the surface of the gauge as shown in Figure 4.15. Rubber tape and foil tape were applied over the gauge to protect it from moisture. Vishay (2017) provides a detail discussion on the application and protection techniques for this kind of strain gauge.

Figure 4.15 Picture of a weldable strain gauge being installed on the bridge.

The sensors were installed at locations corresponding to the boundary of the local FEM described in the section 4.5.2. The locations of the strain gauges in the connection are indicated in Figure 4.16 and Figure 4.17, in which the rivets are not sketched for clarity.
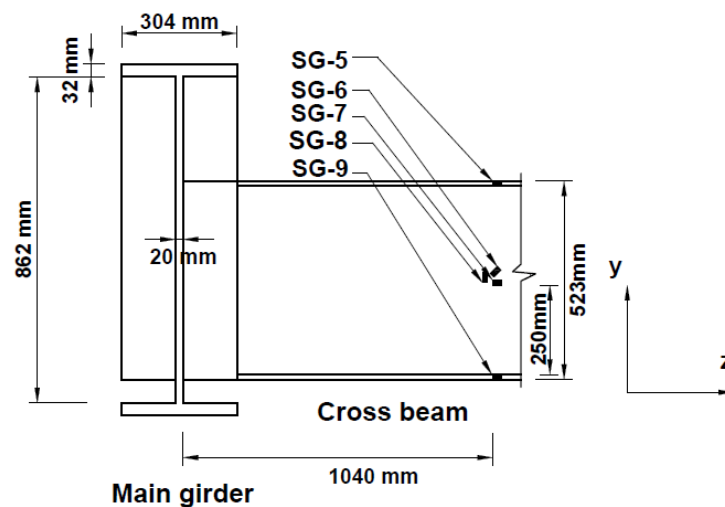
Figure 4.16 Schematic of weldable strain gauges installed to top, bottom flanges and mid web of cross beam (front view).
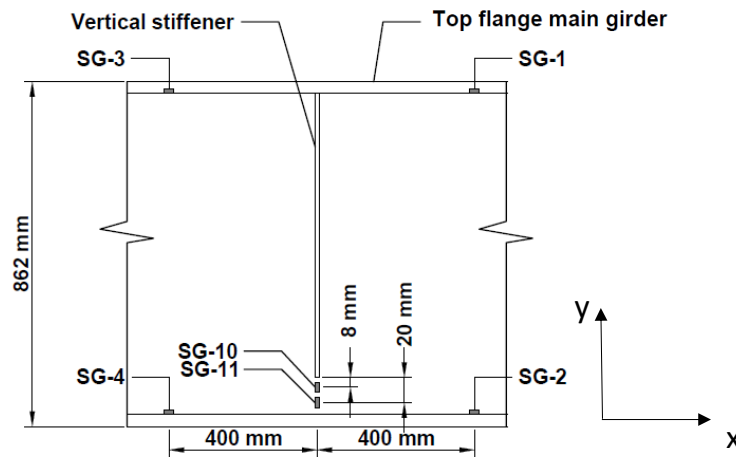
Figure 4.17 Schematic showing locations of weldable strain gauges in web gap near weld region of main girder (side view).

SG-5 to SG-9 represent the location of the strain gauges installed on the cross beam. These are installed to evaluate the internal forces transferred by the weld. SG- 1 to SG-4 are the gauges located on the main beam at distances 400 mm from the vertical stiffener to capture strains developed in the main girder. SG-10 and SG-11 are the gauges placed at distances $0.4t$ (8 mm) and $1t$ (20 mm) from the weld toe at the end of the vertical stiffener. These are the reference locations at which stresses are required to compute the stress at a hot spot of type a according to the IIW recommendations. Figure 4.18 shows a photograph of the weldable strain gauges installed in the web gap region.

The NI 9174 Compact Data Acquisition device (NI cDAQ-9174) was used to measure the strains captured by these gauges. It provides a flexible, expandable platform for sensor measurement system. The NI Compact DAQ system consists of a chassis of 4 - Slot, NI C Series I/O modules, and software. The chassis can connect to a host computer over USB or Ethernet. NI 9237 simultaneous bridge module (NI 9237) was combined with the NI cDAQ-9174 for strain measurement.
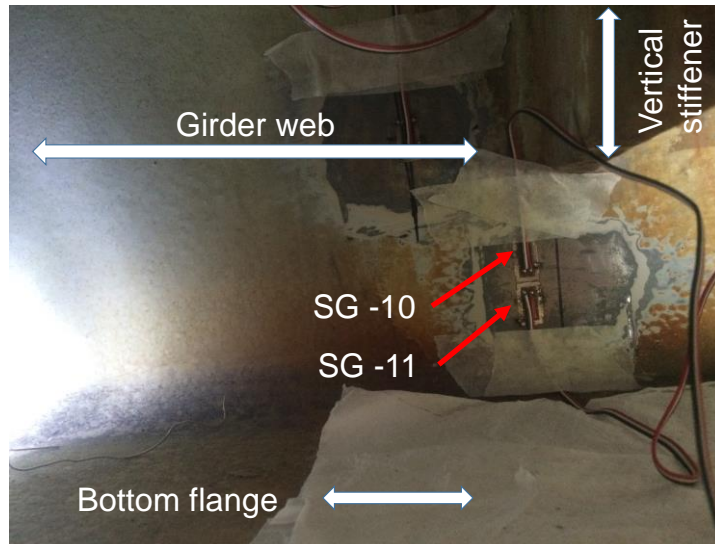
Figure 4.18 Weldable strain gauges installed in web gap near the stiffener (see Figure 4.17).

The NI 9237 contains all the signal conditioning required to power and measure up to four bridge-based sensors simultaneously with 24-bit resolution. The module supports sampling rates between 1,613 Hz and 50,000 Hz per channel with built-in anti- aliasing filters. The signal from the strain gauges were carried to the datalogger via a wire type 326-DFV, 3-conductor lead wire. Figure 4.19 shows the wired NI cDAQ-9174 system with NI 9237 module.
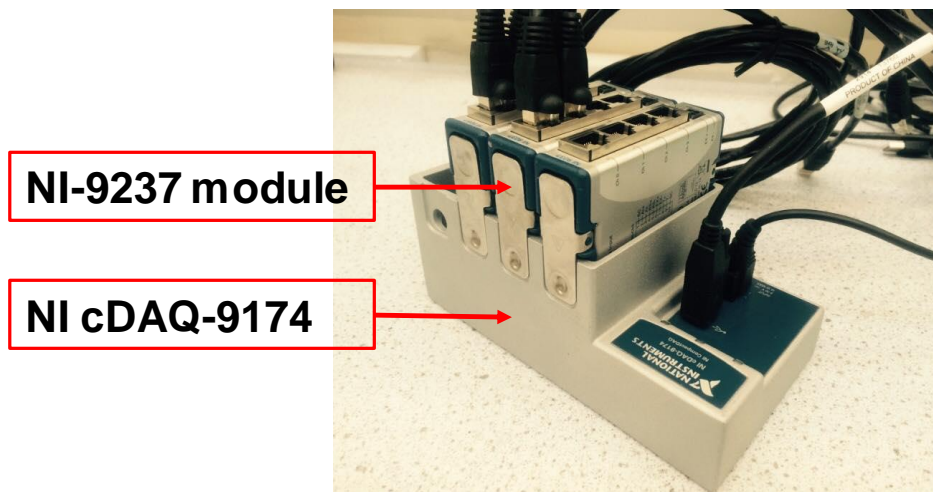
Figure 4.19 Datalogger type NI cDAQ-9174 with NI 9237 modules.

BDI Sensor: The BDI sensor is a strain transducer used with the BDI system for measuring bridge response as shown in Figure 4.20.

Figure 4.20 Picture for BDI transducers in use on top of a cross beam.

The sensor has a dimension of 110 mm x 31 mm x 13 mm with 76.2 mm long active grid and a resistance of 350 Ω. BDI strain transducers are prewired with 6 m long wires and are identified by the system with a unique number (i.e., 5985, 5986, etc.). From this unique number, the system has the ability to calibrate and zero the gauge using a pre-stored gauge calibration factor. Transducers may be used on many different surfaces, including, but not limited to, steel, concrete (reinforced and pre-stressed), and timber. Two holes (76 mm on centre) in the transducer are for the 'tabs', which are bonded to the testing surface using lactic adhesive after appropriately preparing the surface of the element being tested.

The BDI system was used mainly because the NI cDAQ-9174 supports only 11 strain gauges and as the BDI system was readily available within the team, it was used to record strains at other proposed locations on the bridge. Figure 4.21shows the locations of 6 BDI transducers installed on the longitudinal

girders and cross beam of the bridge. This cross beam is the same beam that is instrumented with weldable strain gauges.
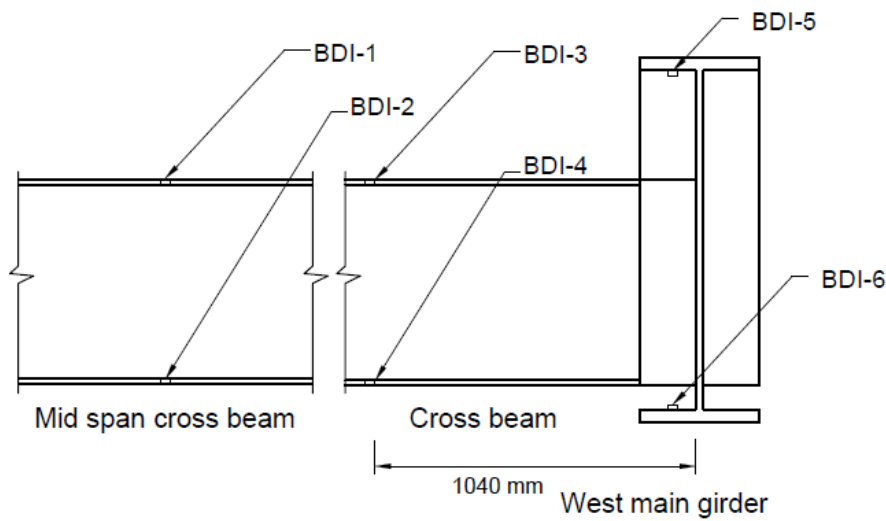
Figure 4.21 Location of BDI gauges.

Gauges BDI-1 and BDI-2 represent those installed on the cross beam at mid span to capture strains developed in the cross beam. Gauges BDI-5 and BDI-6 are placed on the main beam at distances 400 mm from the vertical stiffener to capture strains developed in the west main girder. BDI-3 and BDI-4 are installed on the top and bottom flange of the cross beam. These are installed to capture strains developed in the cross beam closer to its connections with the main girders. Data from BDI-1 to BDI-6 were used alongside those from the weldable strain gauges to calibrate the FE models of the bridge described in the section 4.

The BDI system consists of four main elements: the BDI Sensor, the BDI STS Units, the BDI Node, and the BDI Power Unit (STS4) (see Figure 4.22). The BDI sensors are connected to nodes that acquire data and send the data wirelessly to a BDI STS unit connected to a computer where it can be stored. The nodes

are capable of acquiring data from 4-channels and support sampling rates up to 1,000 Hz per channel with real-time filtering options.
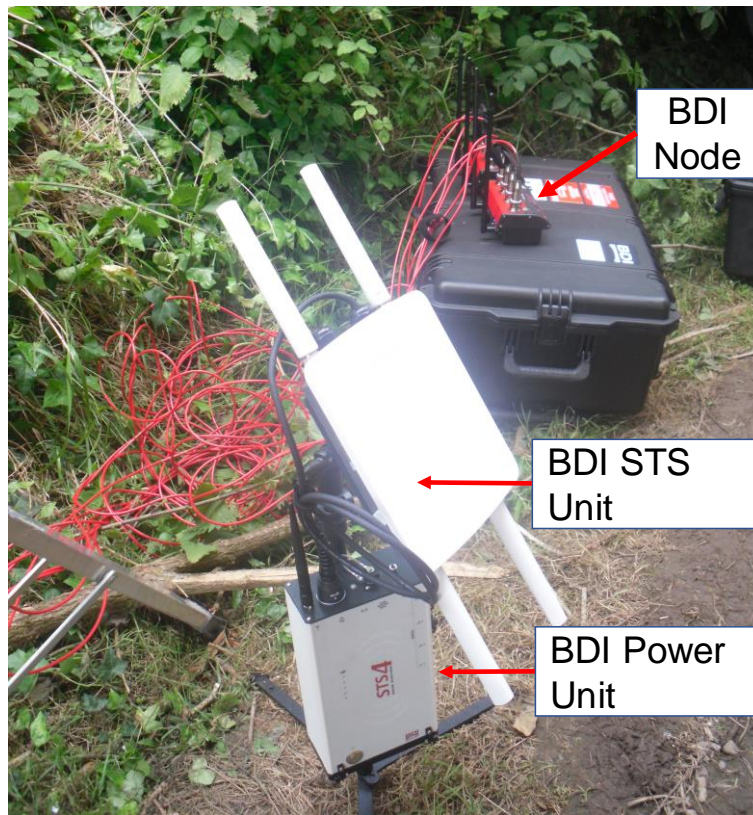
Figure 4.22 BDI STS4 units in use during a load test.

4.3.3 Sensor for acceleration measurements

Accelerometers are required to measure acceleration response of the bridge, in order to update the global FEM of the bridge. Four force-balance accelerometers (QA700 and QA750) were installed to measure the vertical responses during loading tests conducted on the bridge. Figure 4.23 shows a typical accelerometer located on the top flange of the main girder. The signals of the acceleration responses were recorded using a Data Physics SignalCalc Quattro analyser as shown in Figure 4.24. The data was sampled at 128 Hz.

Figure 4.23 QA in use during a load test.

The limited number of accelerometers available at the time of the testing determined the sensor configurations shown in Figure 4.25 and Figure 4.26. A total of four accelerometers were installed on the bridge girders for the two swipes taken during the ambient and loading tests respectively. In the first swipe, the 4 accelerometers are installed on the west girder of bridge as shown in Figure 4.25 Schematics of the QSs locations (swipe one) during an ambient vibration test. This configuration captures bridge bending mode shapes at mid and quarter span.
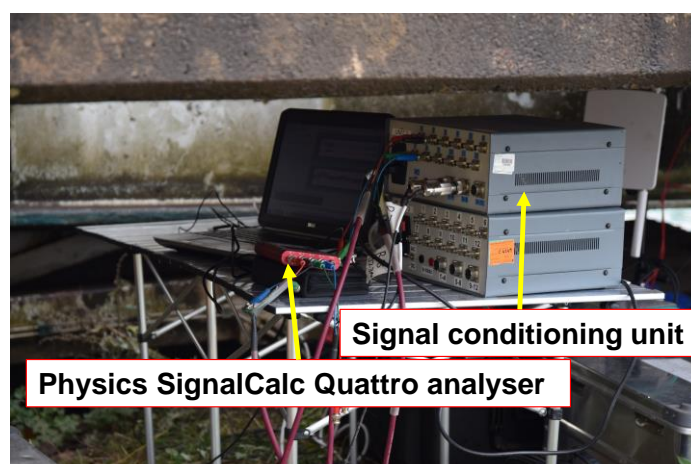
Figure 4.24 Accelerometers data logger units in use during a load test.
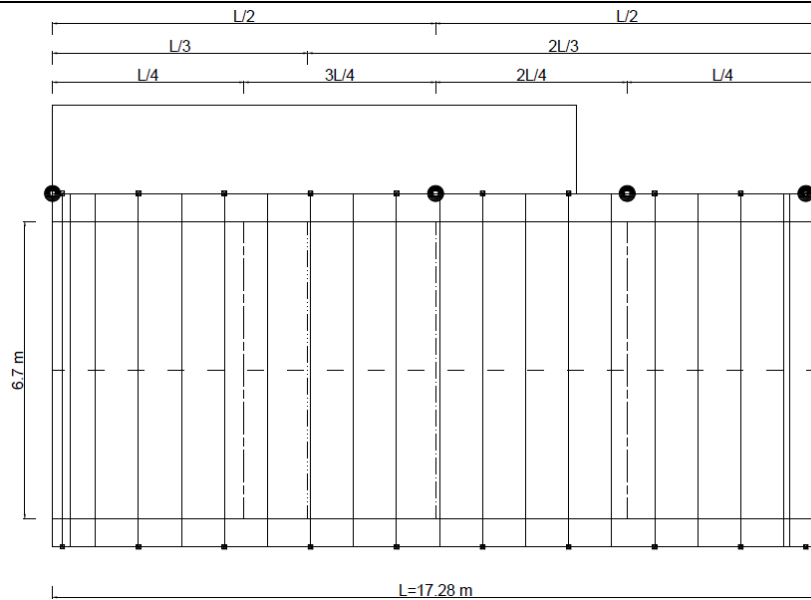
Figure 4.25 Schematics of the QSs locations (swipe one) during an ambient vibration test.

In the second swipe the 4 accelerometers are distributed on both sides of the bridge at quarter and mid span as shown in Figure 4.26 Schematics of the QSs locations (swipe two) during the first loading test. The aim of the second swipe is to identify global bending and torsion modes of the bridge.
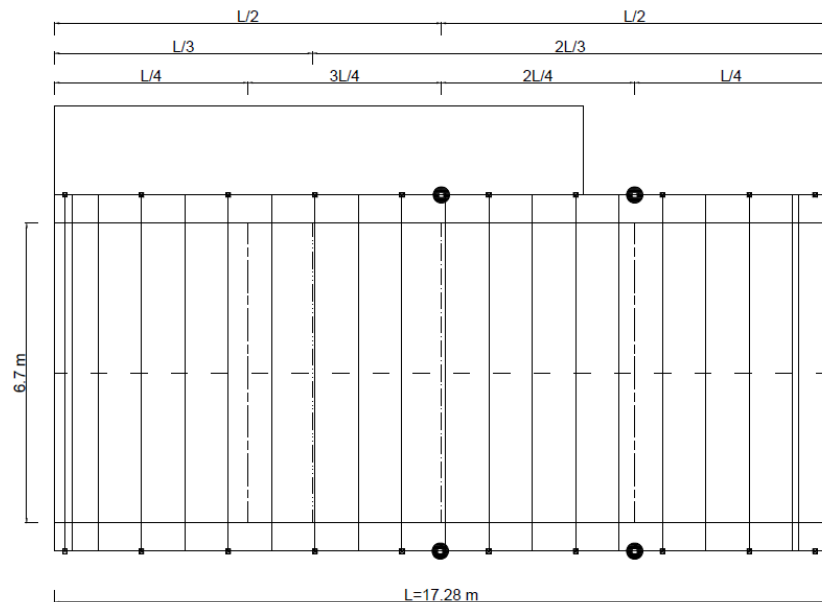
Figure 4.26 Schematics of the QSs locations (swipe two) during the first loading test.

4.4　　　Field measurements

Field measurements were performed for two purposes: first, to provide an objective basis to calibrate the global and local FEM models; and second, to investigate the proposed research methodology.

One ambient vibration test, one controlled quasi static loading test and two in-service monitoring sessions are conducted on the Bascule Bridge. The ambient vibration test is conducted to identify the dynamic properties, namely the natural frequencies and mode shapes, of the bridge. The controlled load test was conducted on November 19, 2016 for the purpose of validating the global FEM model of the bridge and the proposed methodology. In-service monitoring is conducted for the purpose of demonstrating that the methodology is capable of measuring the actual effective stress near an instrumented connection due to uncontrolled, real-time traffic. The two in-service monitoring events took place on July 12, 2016 and August 12, 2016, respectively. Each event continued around the clock and lasted for seven hours. These tests are described in the next sections along with some key results. The description starts with ambient vibration test, then moving to the controlled load tests and then finishing with the in-service monitoring.

4.4.1 Vibration tests

A preliminary experimental modal identification was performed using two different accelerometers setups (see Figure 4.25 and Figure 4.26) – the first was used for an ambient vibration test and the second was for a dynamic test under the passage of a truck. Time domain modal analysis was performed via ARTeMIS

Modal 5.1 software. Stochastic Subspace Identification (SSI) with Unweighted Principal Component (SSI-UPC) was used for modal identification.

The modelling technique used in ARTeMIS is not complex and detailed (Han 2009) . It uses lines, nodes and surfaces to roughly define the geometry of the bridge. Figure 4.27 and Figure 4.28 show the models for the two swipes of measurements.
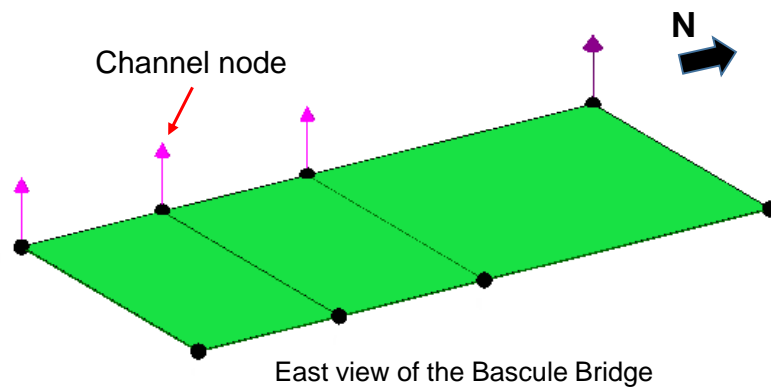
Figure 4.27 Bascule Bridge ARTeMIS Model - the first swipe setup.
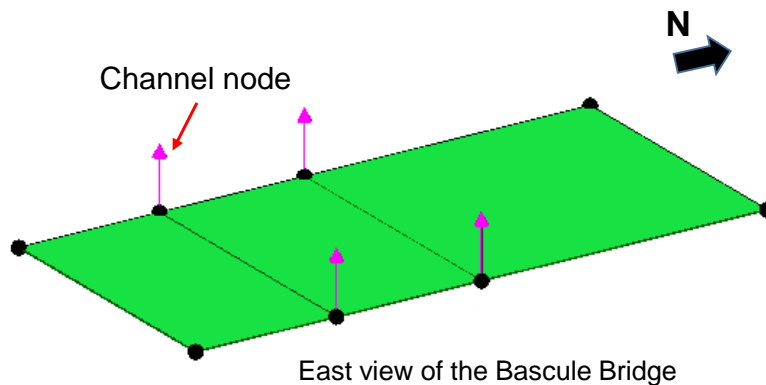
Figure 4.28 Bascule Bridge ARTeMIS Model - the second setup.

Artemis uses the following process. A low-pass filter is first applied on the data. It then converts the vibration data from time series to frequency domain using Fourier transformation. It estimates spectral density matrices and then using

singular value decomposition identifies the modal frequencies. Figure 4.29 shows the results from singular value decomposition for the data from the second accelerometers setup. Stochastic subspace identification was used to identify the mode shapes. Data from the ambient vibration test helped define the first global bending mode even though the data was limited to one side of the bridge. The first global bending mode and a torsion mode were identified from the second setup. Additionally, Figure 4.30 and Figure 4.31 show the mode shapes obtained for these frequencies.
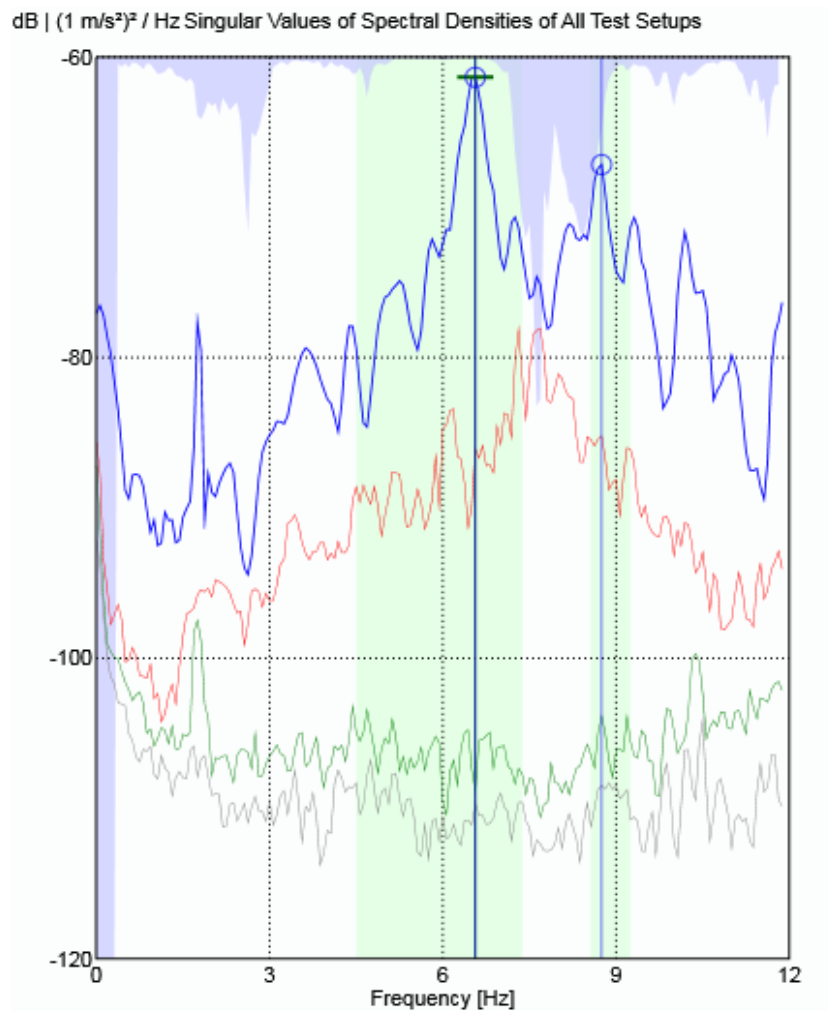
Figure 4.29 Singular Values of Spectral Densities Matrix for Bascule Bridge.
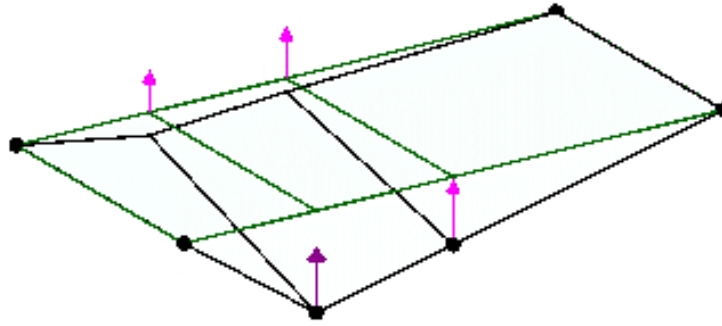
Figure 4.30 1st experimental vibration mode shape (first global bending mode) 6.53Hz
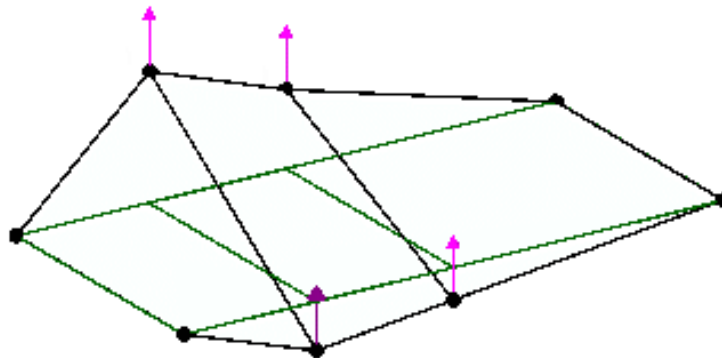
Figure 4.31 2nd experimental vibration mode shape (a torsion mode) 8.68Hz.

4.4.2 Controlled load tests

A quasi static loading test was performed to validate the FE models in terms of stresses near the target fatigue detail using a loading truck shown in *Figure 4.32*. The total weight of 4-axle truck used in the load test was 314.2 kN. During the test the speed of the truck was estimated between 5-17 km/h. During the test, the bridge was closed for local traffic. For weldable strain gauges, strain readings were recorded at a rate of 2000 samples-per-second (Hz). 2000 Hz is a much higher sampling rate than required for this task but this was used as the instrumentation offered this capability. For BDI gauges, strain readings were taken at a rate of 100 Hz.

(a)   (b)

(c)
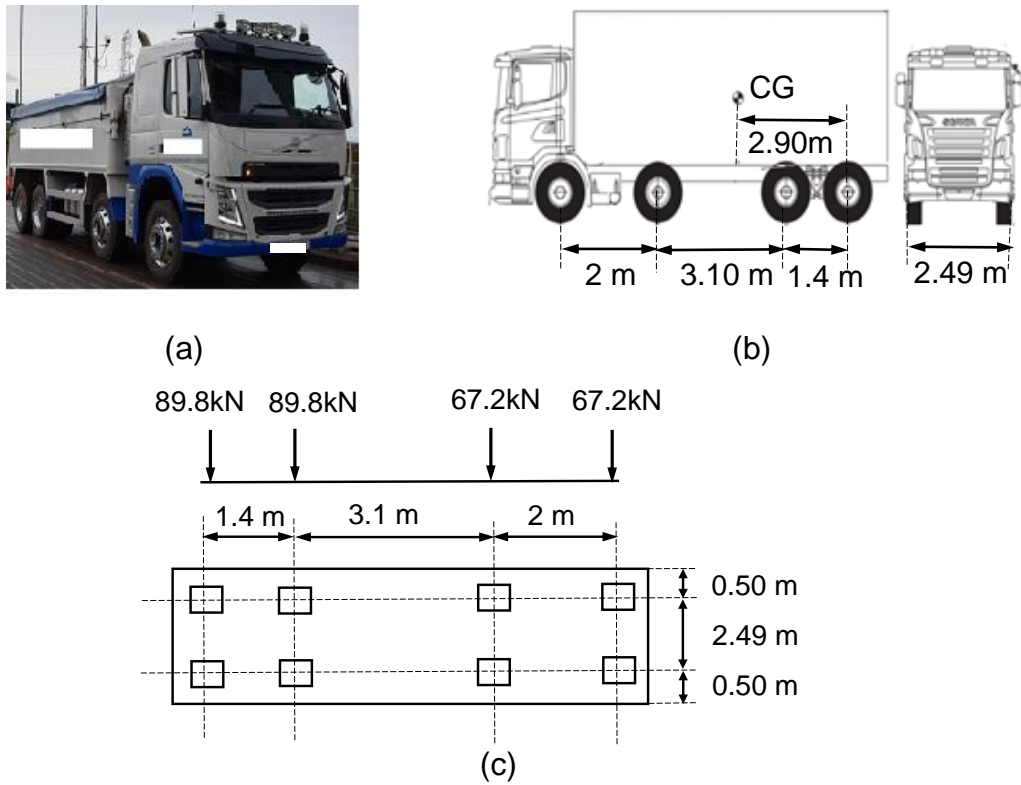
Figure 4.32 (a) A picture of the truck used in the test load,
(b) Truck scheme dimensions and (c) Axle configurations
and axle loads for trucks.

A total of four truck positions were used as shown in Figure 4.33 and Figure 4.34.
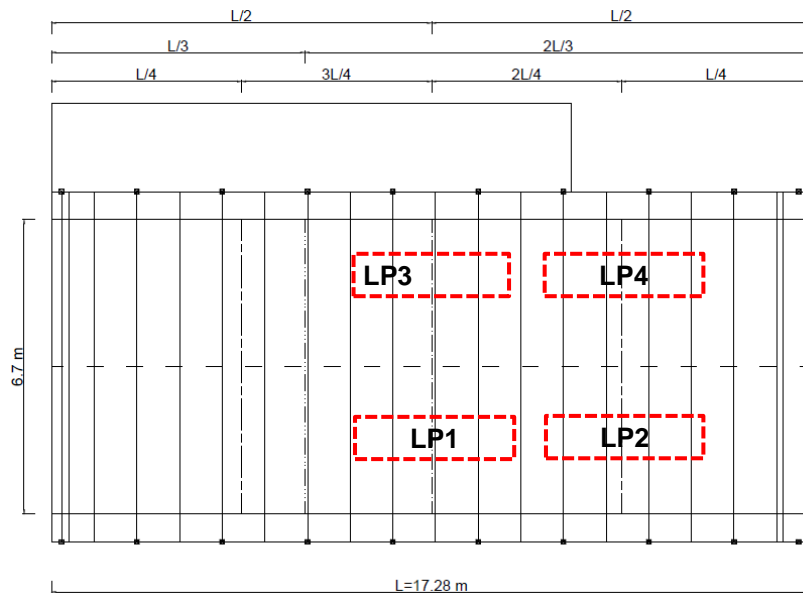
Figure 4.33 A schematic of the truck positions during the
load test.

Figure 4.34 Picture for truck load test on the bridge (LP4).

Presented in Table 4.2 are the maximum recorded strains for SG-1, SG-2, BDI-5 and BDI-6 locations, for LP1 and LP3. The transverse distribution of strain is also apparent from the table. For LP1, the east girder is likely to carry approximately 60% of the load due to proximity and thus the strains are highest in that girder.

Table 4.2 Maximum strains (Micro) for selected sensors and truck stops (negative denotes compression).

Truck position	SG-1	BDI-6	SG-2	BDI-5	SG-5	BDI-3	SG-7	BDI-4
LP1	-73.5	-38	116.5	60	-22	-6.4	31	12
LP3	-46	-59	67	116	-6.3	-12.5	12	26.5

A total of five truck passes were made on the roadway closer to the east girder. Figure 4.35 shows the strain history for gauge (SG-2) on the east main girder at bottom flange for the five truck runs. In this figure, five large peaks can be observed, each of which corresponds to one of the five aforementioned passes. A small peak can also be seen between the third and fourth large peaks. This

114

peak is due to roadworks vehicle passing over the bridge after the third truck

pass.
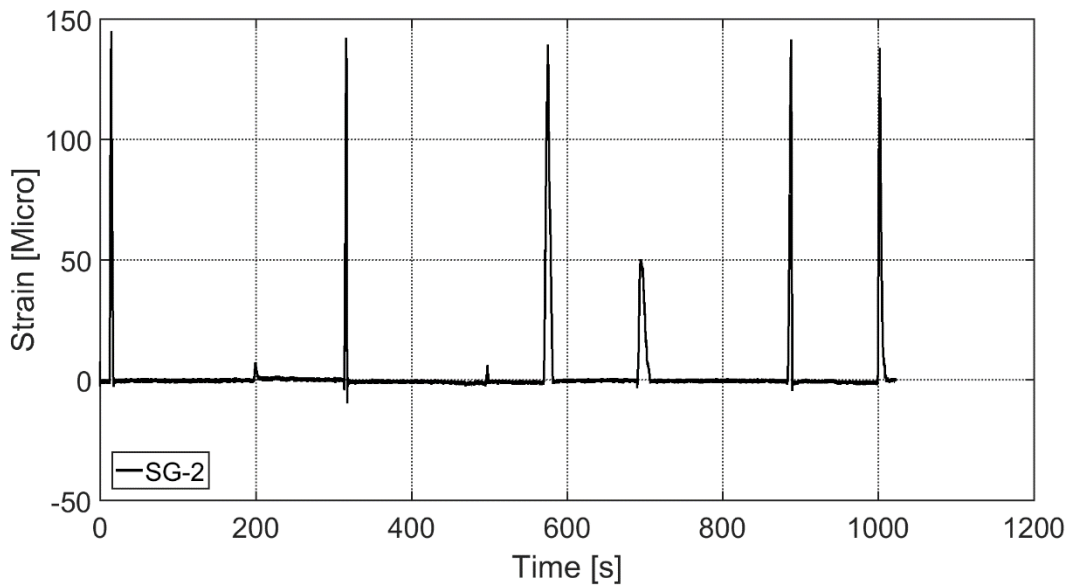
Figure 4.35 Raw strains measured by sensor SG-2 for five truck runs.

Figure 4.36 shows typical time history plots of the recorded strain from SG-1 to

SG-4 on the east main girder at top and bottom flanges for the truck run 1.
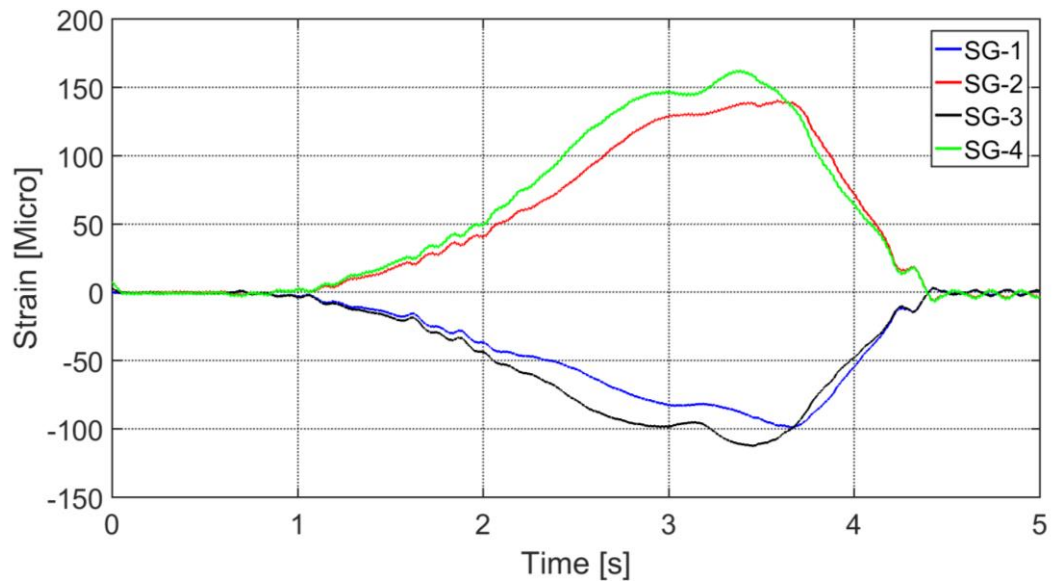
Figure 4.36 Raw strains measured by sensor SG-1to SG-4 for truck run 1.

Figure 4.37 presents typical plots of the recorded strain from SG-5 to SG-9 in the web and top and bottom flanges cross beam for the truck run 1.
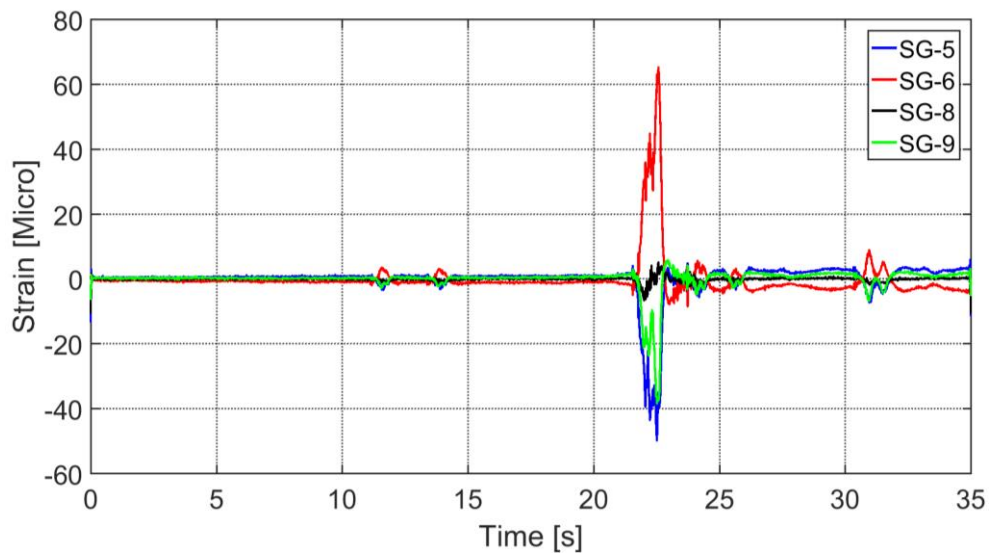
Figure 4.37 Raw strains measured by sensor SG-5 to SG-9 for truck run 1.

Figure 4.38 presents typical plots of the recorded strain in the top and bottom flanges cross beam at mid span for the truck run 1.
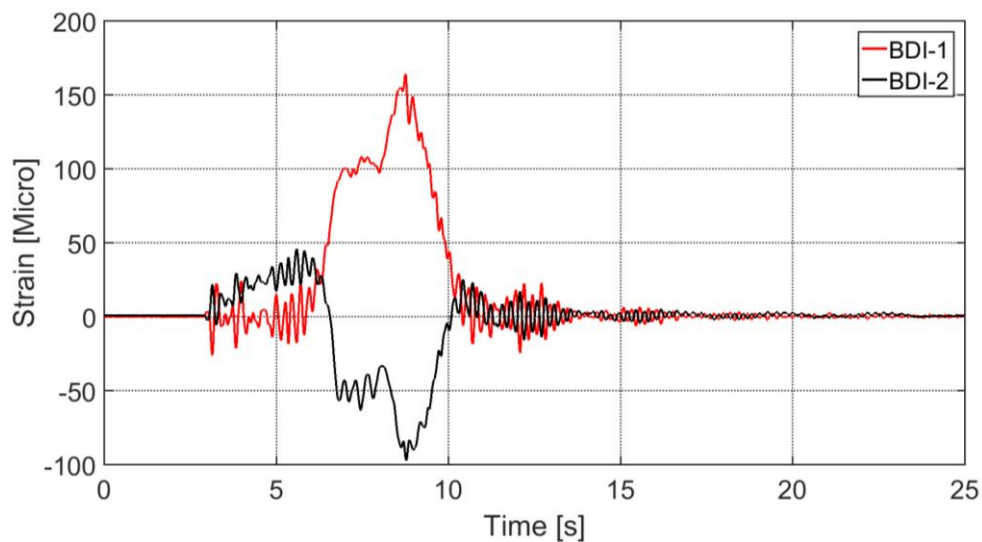
Figure 4.38 Raw strains measured at top and bottom flange of the cross beam at mid span.

Field measurements are utilized to make inferences regarding the structural behaviour of the bridge. From Figure 4.34, the test results from different cycles of the same truck path are identical. The bridge behaviour is found to be elastic (i.e. all strain gauges returned to zero when the truck drove off the bridge). These results (Figure 4.36, 4.37 and 4.38) illustrate the characteristic behaviour of the main girder and cross beam connection, i.e. that the load develops compression in the top flange.

4.4.3 In service monitoring

Strains were recorded at 2000 Hz sampling rate for a period of 7 hours during the following times: 8am-4pm and 9am-5pm respectively for the first and second monitoring event. Figure 4.39 shows typical time history plot of the recorded strain in the east main girder at bottom flange gauge (SG-1) for over a 70 second duration when heavy trucks passed over the bridge.
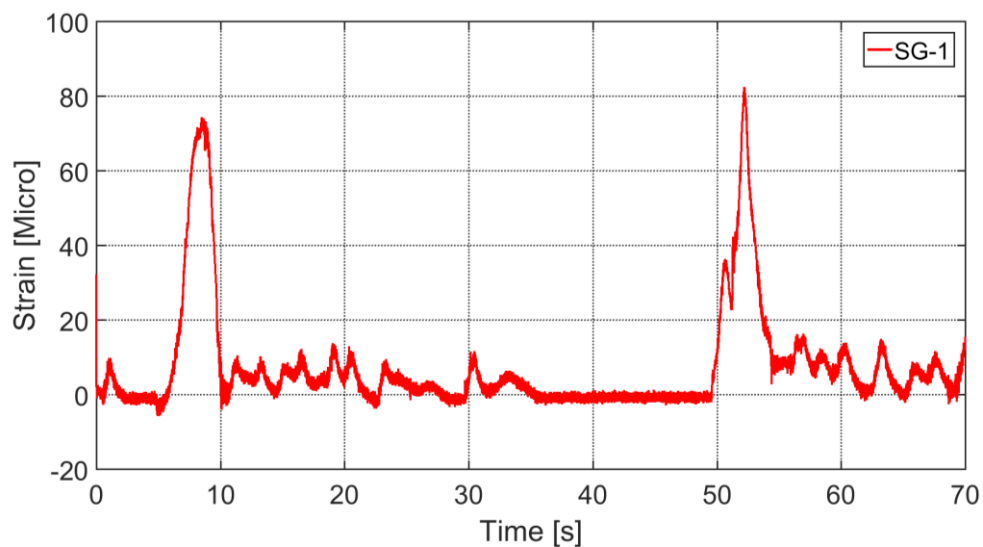
Figure 4.39 Raw strains measured over a 70 second duration by sensor SG-1.

4.5   Global-local FEM

Two types of finite element models were developed for the fatigue assessment of the investigated fatigue detail. One is a global FEM with three-dimensional shell elements, which allows for the computation of stress time history and thereby the fatigue damage at non-monitored details. The other numerical model is a local FEM of the selected connection. The local FEM can allow for computation of hot spot stress time history and fatigue damage at the instrumented details.

4.5.1 Global FEM

A FE model of the bridge is constructed according to the original design drawings provided by the owner and operator - Devon county council. The main focus during the modelling process was to represent the actual geometry as accurately as possible with careful placement of elements according to drawings, proper simulation and quantification of element mass and stiffness, and boundary conditions that represent real conditions. The commercial finite element code ANSYS® was used to perform numerical analyses. The ANSYS® APDL was used to build the model of the bridge. There were a total of 247,286 elements and 556,211 nodes in the model. The quad-shaped shell element is used with size 150 mm. This mesh size was adopted after solving the FE model with different mesh sizes. Adopting a mesh size smaller than 150 mm only increased computational cost and offered negligible improvement in the calculated stresses. MASS21 element is used to simulate the mass of non-structural elements. Young

modulus of 205 GPa and 69 GPa reported by (Devon county council), and a

Poisson's ratio of 0.3 were used for rolled-iron steel and aluminium, respectively.

Steel details: In this section, three-dimensional (3D) 8-noded shell elements are

used to model the cross beams, main girders, and vertical stiffeners. Beam

elements are used to model suspension rods and rails, which together with other

modelling strategies were crucial to obtain the correct calibrated frequencies.

Figure 4.40 shows all steel details described above.
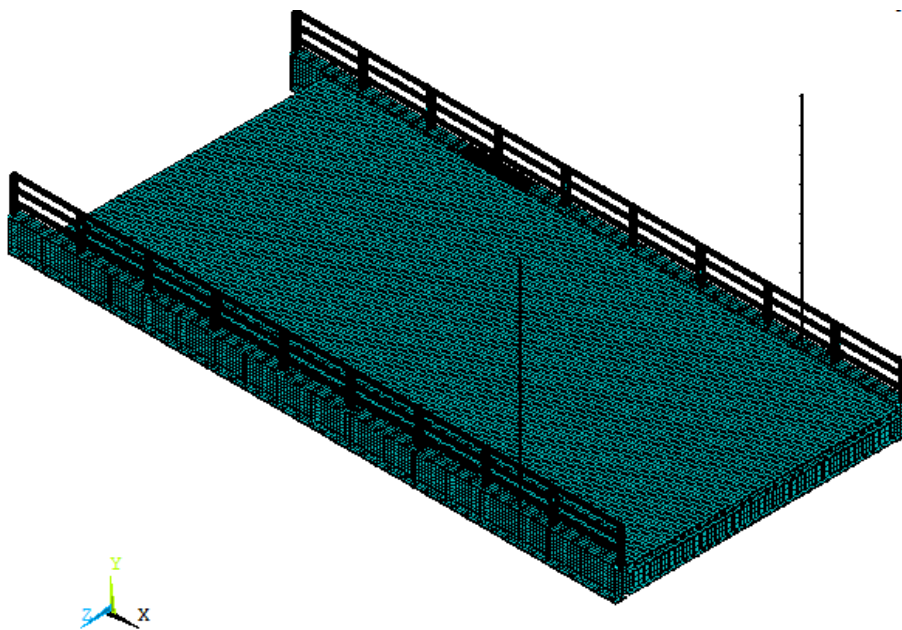
Figure 4.40 Steel details of the bridge model.

The deck: Three-dimensional 3D 8-noded shell elements are used to model

aluminium deck of the bridge with an appropriate number of aluminium deck

planks along the deck width as shown in Figure 4.41. Deck planks are modelled

with an equal width and height and the dimensions were obtained from the

drawings. Surfacing part is considered by considering an additional thickness

added to the top part of the deck planks.
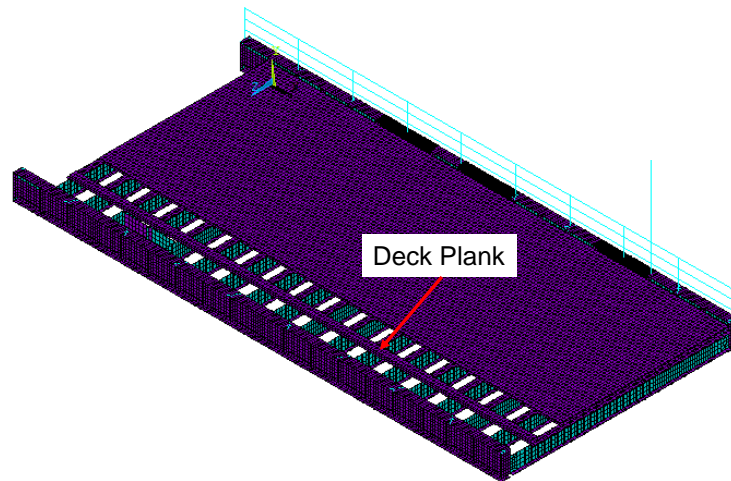
Figure 4.41 The bridge deck planks.

Connections between the aluminium deck and top flanges of cross beams: In

Bascule Bridge, composite action between deck and cross beam is developed

using shear bolts bolted to the top flange of the cross beam. In the model the

composite action between the aluminium deck and the cross beam was modelled

by connecting the top flange nodes to the deck nodes by using coupling and

constraint equations technique (CupDoF's) in ANSYS (see Figure 4.42). The

coupling connection assumes perfect interaction; it neglects relative movement

between adjacent deck surfaces and studs elongation due to uplifting force. The

coupling technique is assumed to have negligible effect in the global analysis.
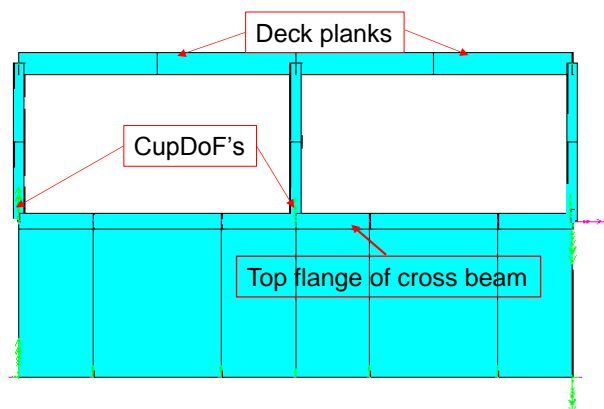
*Figure 4.42 The aluminium deck planks and top flange of
cross beam connection.*

The connection between cross beams-main girders*:* In the Bascule Bridge the cross beams are attached to the vertical web stiffener with bolts, as shown in the Figure 4.4. In the global FEM, the edge of the web in the end of the cross beam is attached to the edge of the vertical web stiffener of the main girders. The connections are assumed to be fully fixed in a finite element perspective, i.e. within the global FEM this is achieved by tying all the members together at the locations of the connections fixed as shown in Figure 4.43. This is a reasonable approximation given the large number of heavy bolts in this connection.
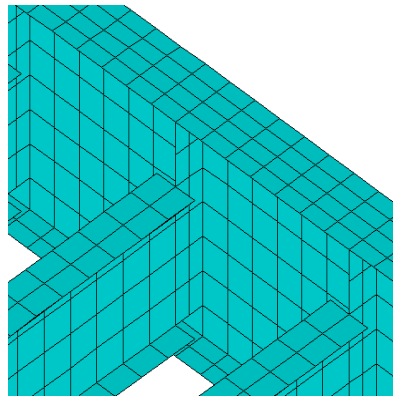
Figure 4.43 The connection between cross beams and main girders.

Boundary conditions*:* In this study, the bridge substructure such as abutments were assumed to be perfectly rigid. The supports at the ends of the main girders were modelled by restraining the appropriate degrees of freedom. Pivot ends are considered as pin supports, and lifting ends are assumed as roller supports.

4.5.2 Local FEM

In this section, a local FEM of the connection is presented. This model (Figure 4.44) is created following the IIW recommendations (Hobbacher 2009). It consists of an assembly of a main girder, cross beam and vertical web stiffener.
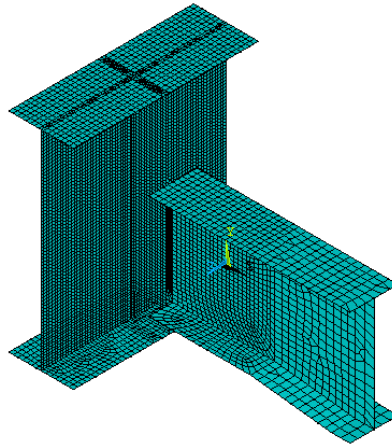
Figure 4.44 The Local FEM of the fatigue sensitive connection.

The ANSYS® parametric design language (APDL) is used to build the model of the connection. 8-noded shell elements are used instead of 20-noded solid elements, since they require relatively less modelling effort and computational power, to model the cross beams, main beams and vertical stiffener. A relatively fine mesh is adopted, and weld geometry is not modelled. The welded connection is assumed to be fully rigid within the local FEM. This assumption is acceptable as the large number of heavy bolts and weld in this connection are likely to make the connection behave in a rigid manner (Zamiri Akhlaghi 2009). To comply with the IIW recommendations, the size of the elements is 8 mm x 8 mm (i.e. $0.4t \times 0.4t$) at type a hotspots and 20 mm x 20 mm (i.e. $t \times t$) for adjacent elements where *t* represents the base plate thickness and is equal to 20 mm. Materials are assumed linear elastic and isotropic (Elastic modulus of steel = 205 GPa and Poisson's ratio = 0.3). The local FEM mesh consists of 29,400 elements with a total of 31,659 nodes. The running time for a typical analysis is approximately 1 minute on a PC with 8 GB of RAM.

As explained in Chapter 3, the monitoring plan is decided considering the structural purpose of the connection. The connection is designed to transfer forces from the cross beam, which are created by the vehicles traveling on the bridge deck, to the main (longitudinal) girder. These forces are the key determinant of the stresses at the weld in this connection, and the monitoring system, described in section 4.3.2, is designed to capture these forces. The measured forces – A, V and M, namely, the axial force, shear force and bending moment, will be applied as loading to the local FEM.

Defining the boundary conditions for the local FEM can be challenging. The level of flexibility or stiffness offered by the rest of the bridge is not readily known. Therefore three different boundary conditions are attempted to evaluate which one can be used to simulate the real conditions and provides satisfactory balance between accuracy and computing resources. In *BC1,* the relative vertical displacement between the two modelled ends of the main girder is assumed to be minimal. Also there is no constraint on the free end of the cross beam. *BC2*, a boundary condition with translational and rotational stiffness corresponding to that of the rest of the bridge is introduced. The main difference between *BC1* and *BC2* is in the level of rotational fixity provided at the ends of the main girder. In the case of *BC3*, a sub modelling technique is employed, in order to transfer the boundary conditions from the global model to the local model. This concept is more realistic than others and can also be extended to other bridges.

BC1: All translational and rotational degrees of freedom at a node at the neutral axis on the two ends of the main beam on either side of the connection with cross-beam are fixed. This is equivalent to a pin connection.

_BC2_: The supports at the cut ends of the main girder are assumed to offer partial

fixity. This is modelled using 3 translational and 3 rotational springs at each end.

The spring element (combine 14) available in ANSYS is used to simulate this

concept. A coupling technique available in ANSYS is adopted for connecting shell

elements at the cut ends and spring elements.   Zero point-mass elements

MASS21 provided in ANSYS are used as master nodes to translate applied

boundary conditions to the nodes along the three cut edges of the local FEM.

Figure 4.45 shows a schematic of these spring elements applied to the local FEM.
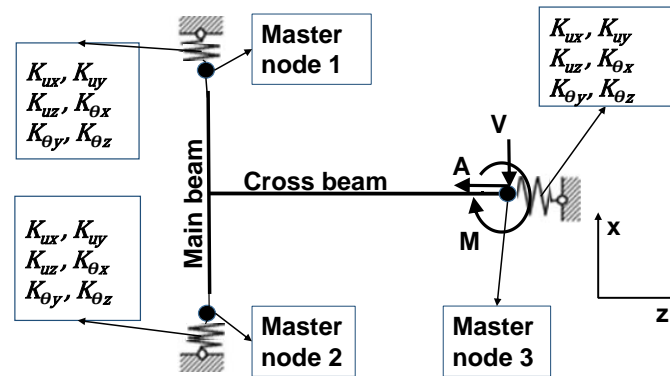
Figure 4.45 Schematic of spring elements applied to the local FEM, $K_{ux}, K_{uy}, K_{uz}, K_{\theta x}, K_{\theta y}, K_{\theta z}$ are the stiffness constants of the translational and rotational springs, which are assumed to behave in a linear manner.

To find the spring stiffnesses, a stiffness approach is used. Basically, stiffness is

the relationship between an applied load (force or moment) and the displacement

or rotation the load produces. For translational springs, the applied force (F) is

assumed to be linearly related to the displacement (x). This type of spring obeys

Hooke's Law:

$K = F/x$ (4.1)

For rotational springs too, the applied moment (M) is assumed to be linearly related to the rotation (θ), giving

$$K = M/\theta \tag{4.2}$$

The full global FEM is used to calibrate the spring stiffnesses, comparing deformations and reactions at boundaries *BC2* of the local FEM with those at corresponding locations in the full structure model.

BC3: A shell-to-solid sub modelling technique available in ANSYS is employed, in order to transfer the boundary conditions from the global model to the local model.

The finite element mesh of the sub model adopts solid elements with quadratic shape functions (20-noded SOLID186 element) and it follows the rules indicated in IIW (2016) for a fine mesh and a linear extrapolation with two extrapolation points.

Load scaling factors (LSF):

As described in Chapter 3, stress responses are computed for individual unit internal forces, i.e. 1 kNm, 1 kN and 1 kN. The predicted values of the normal stress component (inner side of the web gap of the main beam) oriented in the normal direction to the weld toe at the reference locations for each of the applied forces, are the LSFs. These forces are applied separately at the end of the modelled cross beam at a distance of 1040 mm from the connection, which coincides with the physical location of strain gauges on the full-scale bridge. Figure 4.46 shows the local FEM under a shear force of unit magnitude.
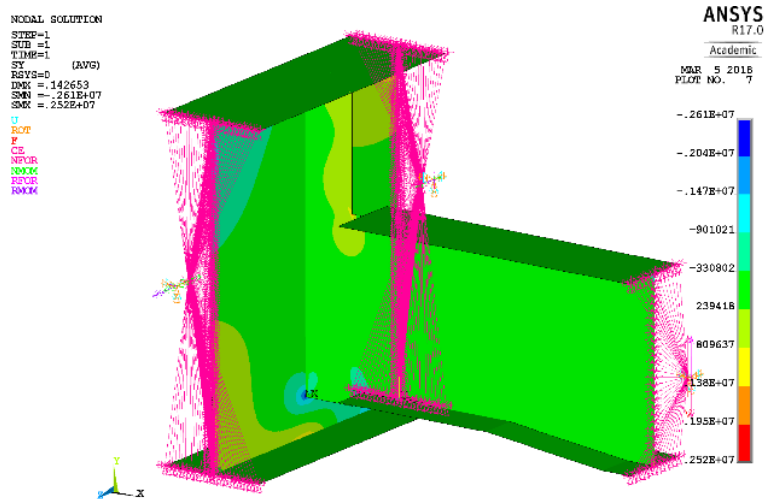
Figure 4.46 Normal stress component (SY) from local FEM for boundary condition BC3.

Figure 4.47 shows the web gap region of the investigated connection showing the extrapolation path of the considered stresses. Table 4.3 presents magnitudes of LSFs of the main girder-cross beam connection for the three types of boundary conditions.
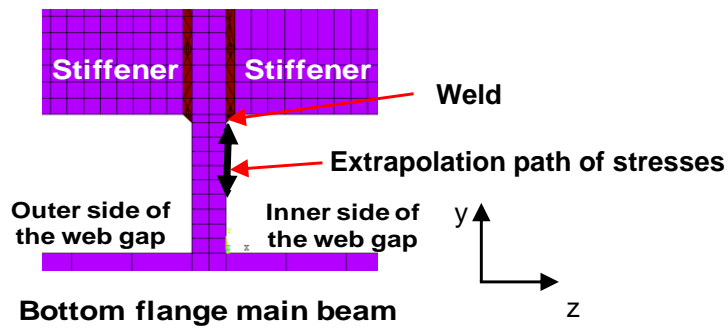
Figure 4.47 Extrapolation path of considered stresses at web gap region (y-axis represents the vertical direction).

Table 4.3 Computation of load scale factors (LSF) for the main girder-cross beam connection for the three types of boundary conditions.

Boundary condition type	Load scale factor (LSF)	Stress (SY) at 8 mm from weld toe $\sigma_{0.4t}$ (MPa)	Stress (SY) at 20 mm from weld toe $\sigma_{1.0t}$ (MPa)
BC1	$S_{M,i}$	0.0649	0.0654
	$S_{V,i}$	-1.1480	-0.4720
	$S_{A,i}$	0.1030	0.1640
BC2	$S_{M,i}$	0.067	0.075
	$S_{V,i}$	-1.41	-0.93
	$S_{A,i}$	-1.69	-0.94
BC3	$S_{M,i}$	0.101	0.22
	$S_{V,i}$	-1.48	-0.98
	$S_{A,i}$	-3.99	-3.2

4.6   Validation of FE models

For a numerical analysis to accurately reproduce the real response of a bridge, it must be calibrated and updated based on data gathered from field testing. (Rahbari et al. 2015) and (Goulet et al. 2010) asserted that field measurements from static and dynamic load tests can be used effectively to update parameters of numerical models of bridges. A FEM calibrated or updated using modal properties (Rahbari *et al*, 2015) and identified through system identification

provides the best tool for interpreting and understanding the causes and effects of the various loading conditions.

This section describes how the global FEM and local FEM are updated and validated using field measurements. It also addresses the uncertainties in defining connection and boundary condition fixities.

4.6.1 Validation of the Global FEM

The global FEM is updated using load tests described in section 4.4.2. This is performed in two stages. In the first stage, results from the vibration testing and the truck passing are employed.

Modal analysis: A modal analysis of the developed global FEM is performed using ANSYS to determine the vibration characteristics (natural frequencies and mode shapes) of the bridge and compare it with its measured counterpart to validate the model. A finite element model of the bridge was developed to help decide the location of the accelerometers needed to measure the 1st few dominant modes of vibration. The general equation of motion related to structural dynamic problems is given by Equation 4.1:

$$m\ddot{x} + c\dot{x} + kx = f(t) \tag{4.1}$$

where, m, c and k are the mass, damping and stiffness matrices and $\ddot{x}$, $\dot{x}$ and x are the acceleration, velocity and displacement vectors and $f(t)$ is the external modal force vector acting at time t.

In modal analysis, the external force $f(t)$ and damping c can be considered to be zero. The corresponding harmonic function becomes:

$$\{u\} = \{\varphi_i\} \cos \omega_i t \tag{4.2}$$

where, φ_i is the eigenvector corresponding to mode i. By combining the previous

equations, modal analysis can be performed using the following equation:

$$(-\omega_i^2 [m] + [k])\{\varphi_i\} = \{0\} \tag{4.3}$$

By solving the previous equation, natural frequencies $\omega_{1,2,...,n}$ and mode shapes

$\{\varphi_{1,2,...,n}\}$ are computed for n number of modes.

In short span bridges, only the most structurally significant modes, i.e. the first

global bending and torsion modes are responsible for almost all the stress range

in the main girders of the bridge (Museros 2002). Hence, they are used in the

comparison process in this study. The correlation between the predicted and

measured modal parameters is evaluated quantitatively by comparing the

corresponding frequencies, and qualitatively by comparing visually the obtained

mode shapes (see Figure 4.48). The discrepancy in frequencies is only 2%. The

asymmetric behaviour observed in the first bending mode (see Figure 4.48) is

due to the excessive mass one side of the bridge due to the existence of a

footway.

f_{01exp} = 6.53 Hz f_{01num} = 6.50 Hz

(a)

f_{02exp} = 8.68 Hz f_{02num} = 8.87 Hz

(b)
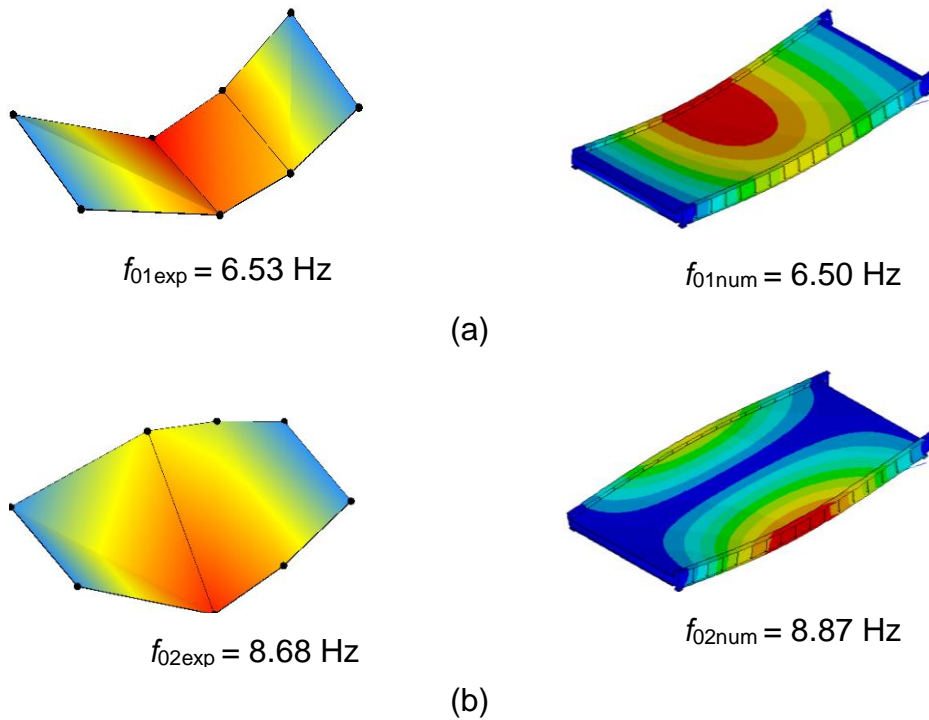
Figure 4.48 (a) Comparison between 1st numerical and experimental vibration mode shape and (b) Comparison between 2nd numerical and experimental vibration mode shape

Analysis of strain data

The global FEM is also validated using bending strain measurements from the strain gauge (SG-2) collected when the truck described in section 4.4.2 crossed over the bridge. As stated earlier, SG-2 was installed within 7 cm of the exterior edge of the bottom flange as shown in Figure 4.15. To avoid any notch effect induced by the welded connection near to the weld toe, the sensor was offset a distance of 400 mm to the left of the cross beam. Using the FE models, the field test run using the truck was simulated. To simulate the truck pass, the two wheel loads were applied as nodal forces on the deck with load spacing as shown in *Figure 4.32* and *Figure 4.32*. The predicted strains were multiplied by the elastic modulus E = 205 GPa to get the stress-history response, which is in very good agreement with the stresses computed from the measured strains (Figure 4.49).

.
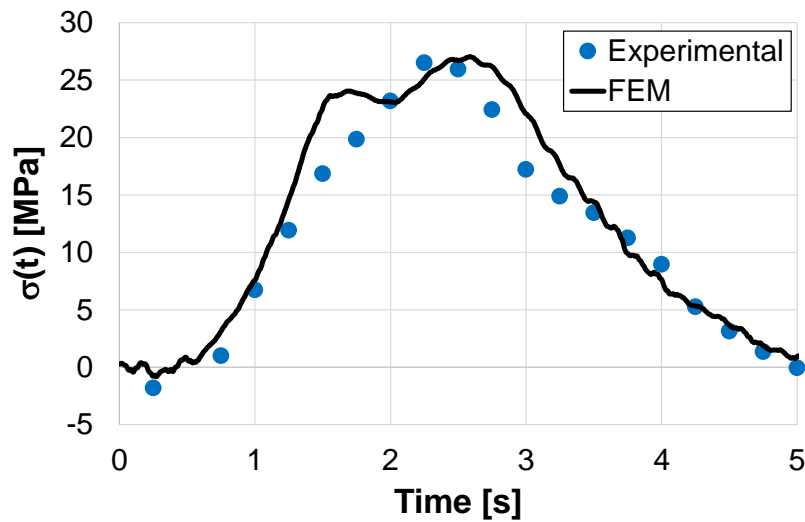
Figure 4.49 The stress predicted by global FEM vs the stress computed from measured strain at SG-2.

While the global FEM predicted well the modal properties and the longitudinal strain data as shown above, a significant discrepancy is observed with respect to the structural behaviour in the web-gap region as shown in Figure 4.50 and Figure 4.51.
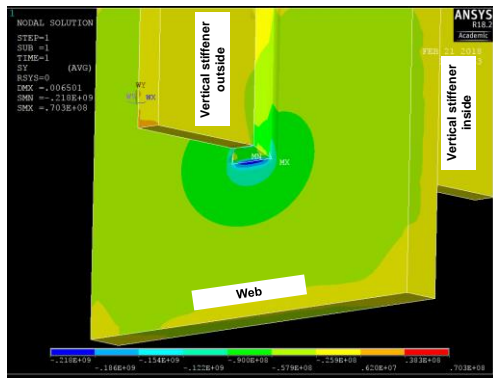
Figure 4.50 The stress predicted by global FEM on the outside face of the web gap of the girder (compression).
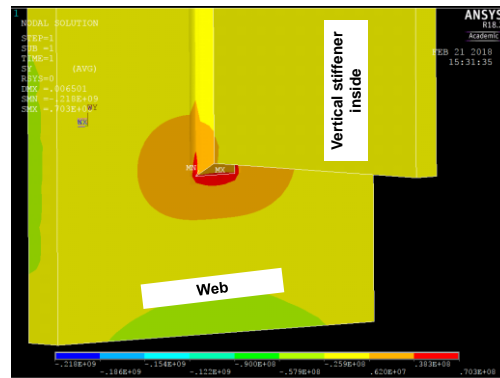
Figure 4.51 The stress predicted by global FEM on the inside face of the web gap of the girder (tension).

For the kind of detail analysed in this study, the vertical load (shear) from the cross-beam should typically cause compression on both sides of the girder web. However, the strain measurements showed that there is compression on the inside face and tension on the outside face of the web gap of the girder This is potentially due to the distortion effects outlined in Section 1.7.2. To address this issue, the global FEM is further updated by systematically examining uncertainties in structural behaviour due to the following model parameters:

a) the lifting system (hinges and hydraulic cylinders),

b) the connection between main beam and cross beam,

c) the connection between deck and cross beams,

d) the connection between deck and main beams,

e) the connection between deck planks,

f) the bridge deck, and

g) the hand rail.

The cross beam-main beam connection, initially assumed to be entirely fixed, is modified to a pin connection. Consequently only vertical displacements are transferred from the cross beam to the main beam; rotations are allowed freely. This assumption is valid since the main beam-cross beam connection in the full-scale bridge is designed to act as a pure shear connection to transfer mostly shear forces through the bolts. This change brings the behaviour of the global FEM in the web gap regions closer to reality. It produces tension at the outer face of the web gap and compression in the inner side.

An improvement to the model is also made by modelling the actual geometry of the deck rather than assuming an equivalent cross section. The connection between the bridge deck and cross beam is also modified to ensure the deck behaves as an orthotropic deck (i.e. the distribution of loads is mainly in one direction rather than bi-directional). This modification has a significant effect on the magnitude of the stress peaks at the web gap region. Lastly, the lifting system (hanger) and the rail guards are also modelled, which improved the accuracy of the calibrated frequencies. Figure 4.52 shows the complete bridge model with the deck, suspension rods and hand rails.
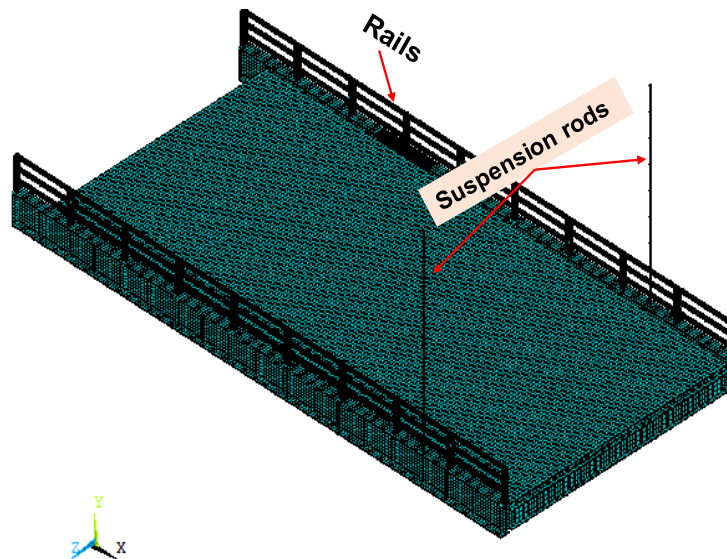
Figure 4.52 Overview of the Global FEM of the bridge, Y-axis refer to the vertical direction.

Validation of the global FEM created after performing the aforementioned modifications can be based on either static or dynamic analysis. However, due to vehicles not crossing the bridge at very high speeds (due to an imposed speed limit of 64 km/h) and the driving surface of the road on the bridge being in a

relatively good condition, it is assumed that the dynamic analysis would not be necessary and static analysis can be used.

Static analysis: A total of 8 weldable and BDI strain gauges are installed on the bridge; however, only two of them were placed directly in a region where fatigue cracks may occur. The location of these strain gauges – SG-10 and SG-11, are presented in section 4.3.2. These record the local strain response, i.e. in the web gap. Strain measurements from SG-3, SG-4, SG-9, BDI-2 and BDI-6 are used to record the global response of the bridge to live loads. Noise in strain measurements is first eliminated using a low-pass filter with a cut-off frequency of 150 Hz. Filtered strain measurements from these sensors are multiplied by modulus of elasticity of steel (E = 205 GPa) to get the stress response.

A linear static analysis is performed to evaluate the bridge response for the passing of a truck. The two-wheel loads for the truck are applied as nodal loads. The movement of the truck along the bridge is simulated in time-steps with each time-step moving the loads by 150 mm. Figure 4.53 presents the time history of measured stresses as computed using strain measurements from sensor SG-3 and SG-4. The figure also shows the stresses predicted by the global FEM at the locations of SG-3 and SG-4. The stresses predicted by the global FEM are in good match with the measured stresses with mean errors over 5.5% and 1% respectively.
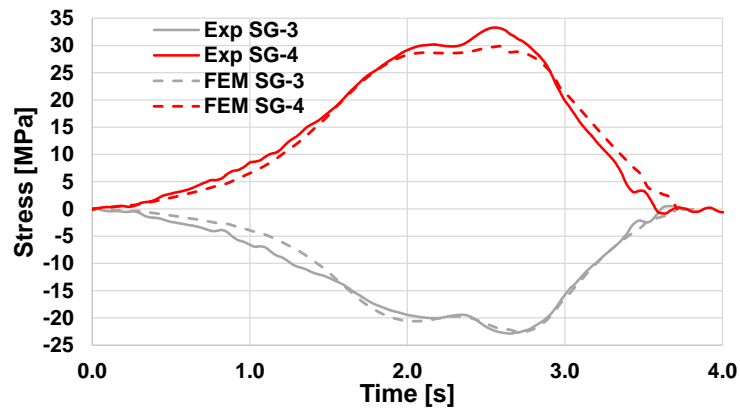
Figure 4.53 The time history of computed and measured stresses using strain measurements from sensor SG-3 and SG-4.

The time history of measured stresses as computed using strain measurements from sensor SG-9, BDI-7 and BDI-11 are presented in Figure 4.54, Figure 4.55 and Figure 4.56. The figures also show the stresses predicted by the global FEM at the same locations.
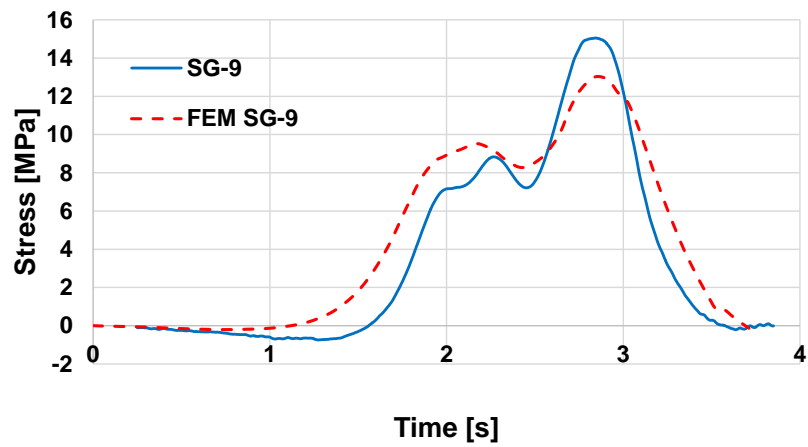
Figure 4.54 The time history of computed and measured stresses using strain measurements from sensor SG-9.
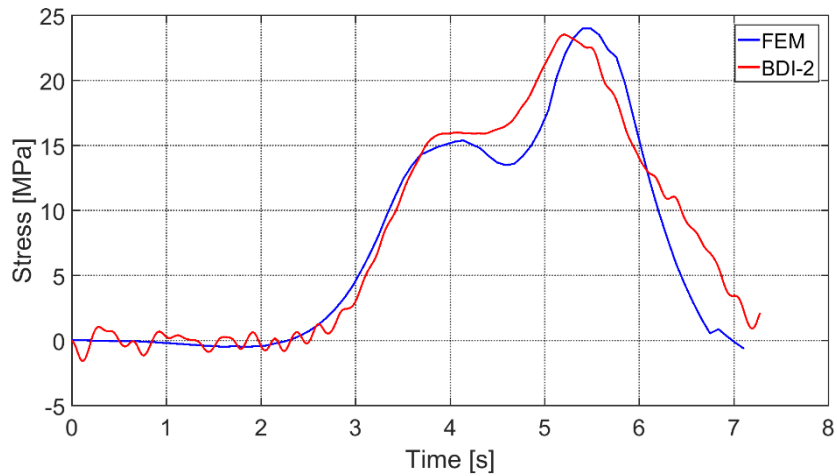
Figure 4.55 The time history of computed and measured stresses using strain measurements from sensor BDI-2 (at mid span of the cross beam).
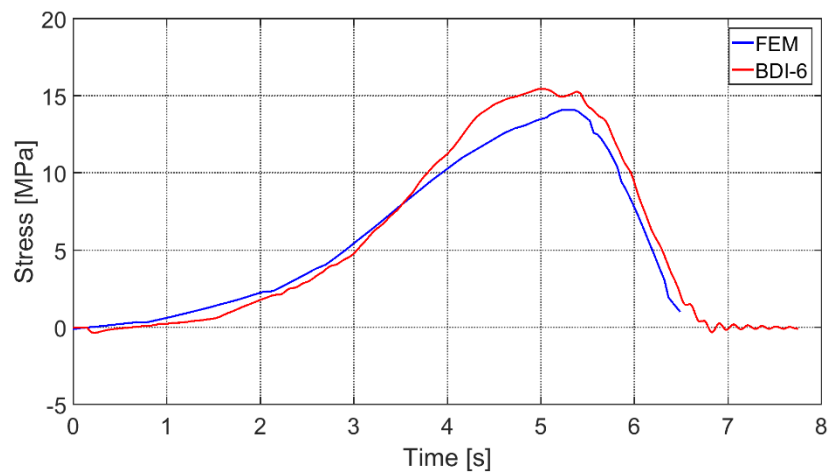
Figure 4.56 The time history of computed and measured stresses using strain measurements from sensor BDI-6

The global FEM, as created with a mesh size of 150mm, fails to produce the measured stress time-history at sensor SG-11. This is expected as SG-11 is very close to the weld toe and will likely experience large stress gradients. To come close to the measured results, the mesh in the global FEM is further refined at the cross beam-main girder connection to a size of 10mmx10mm as shown in Figure 4.57. For this mesh resolution, the global FEM predicts accurately the stress $\sigma_{20\ mm}$ measured at SG-11 (Figure 4.58), which also happens to be the

reference location (i.e. 20 mm from the weld toe) for hot spot stress calculation.

However this level of refinement is still insufficient to predict the stress $\sigma_{8\,mm}$ at

SG-10, which is the reference location at 8mm from the weld toe, as the stress

concentration effects are much stronger here than SG-11.
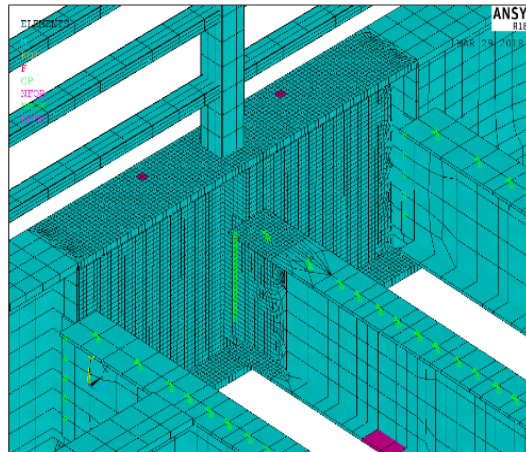
Figure 4.57 The refined zone at the investigated connection (10x10 mm).
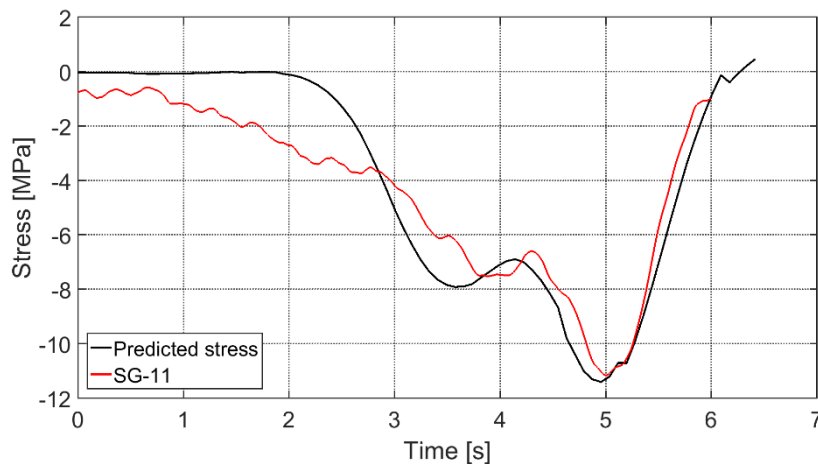
Figure 4.58 The time history of computed and measured stresses using strain measurements from sensor SG-11.

Validation of the Local FEM

This section discusses validation of the local FEM of the bridge using the results

of the field measurements. Moreover, it addresses the uncertainties in defining

boundary conditions for the local FEM. This section also presents a validation of

137

the virtual sensing procedure wherein measurements from selected locations are combined with a global FEM to calculate the stresses at uninstrumented fatigue sensitive details.

Noise in strain measurements is first eliminated using a low-pass filter with a cut-off frequency of 150 Hz as shown in Figure 4.59. This frequency was, through a trial and error process, identified as the minimum frequency below which filtering would adversely affect the stress peaks caused by the traffic. In Figure 4.59, the trough in the measurements is due to the passage of a heavy vehicle. Filtered strain measurements from sensors SG-10, SG-5 to SG-9 and SG-1 are multiplied by modulus of elasticity of steel (E = 205 GPa) to get the stress response. The calculated stresses from sensors SG-5 to SG-9 are converted into time history of internal forces using the equations from linear, elastic beam theory.
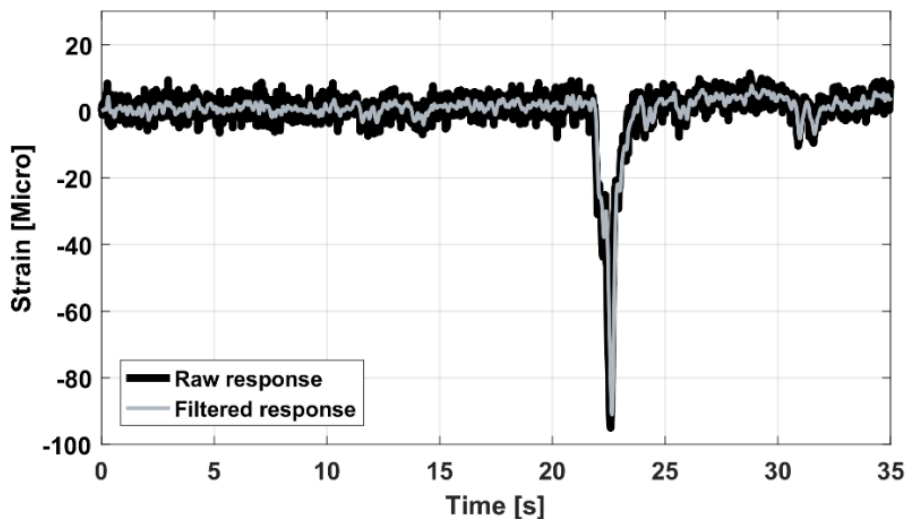
Figure 4.59 Raw strains measured over a 35 second duration by sensor SG-10, and after filtering using a lowpass filter with a cut-off frequency of 150 Hz.

Figure 4.60 shows the magnitudes of computed internal forces, namely bending moments, axial and shear forces for the considered 35 second duration of the in-

service monitoring. All three internal forces are used in conjunction with the local

FEM discussed in section *Local FEM* to determine the stress time-history at

reference locations that are 8 mm and 20 mm from the weld toe of the connection.
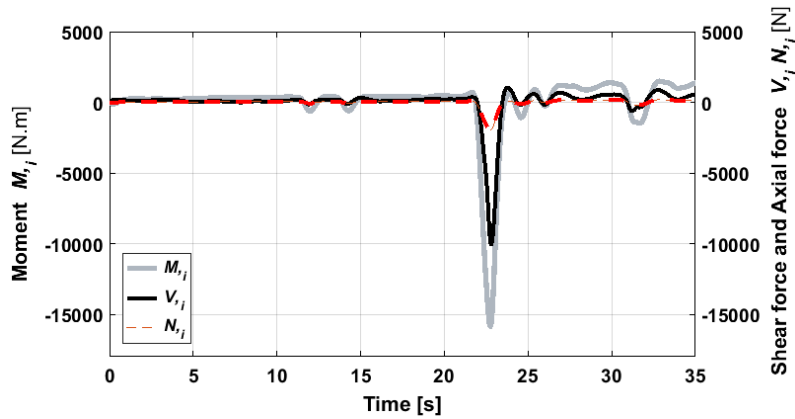
Figure 4.60 Internal moments and shear forces computed over a 35 second duration using strains from sensors SG-5 to SG-9.

These force time histories and the LSFs, discussed in section 4.5.2, are used in

Equations 3.1 to 3.4 to predict individual stresses at the two reference locations

and main beam location (i.e. location of the SG-1). Figure 4.61 shows the time

history of predicted $\sigma_{8\,mm}$, the stress at the reference location at a distance of 8

mm from the weld toe, when using boundary conditions *BC1*, *BC2* and *BC3* in

the local FEM. The figure also presents the time history of measured stresses at

this location as computed using strain measurements from sensor SG-10.
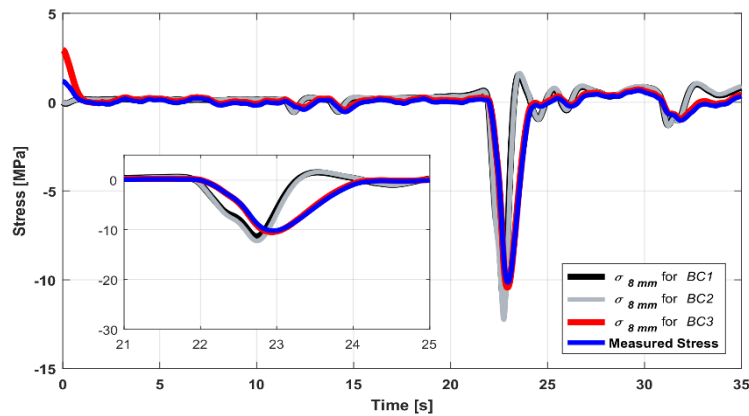
Figure 4.61 Comparison of the time history (35 sec) of stresses measured by sensor SG-10 with that of stresses predicted by local FEM with boundary condition BC1, BC2 and BC3.

The plots show that the local FEM is very sensitive to the chosen boundary conditions. This sensitivity can be captured by examining the difference between the predicted stresses for the duration when the bridge is crossed by a heavy vehicle. The peak compressive stress obtained using *BC2* in the local FEM is more realistic than predicted using *BC1* and *BC2*. The stresses predicted by the local FEM using *BC1* and *BC2* is partially agreed with the experimental measurements with a mean error of only 3.5% and 5.9% over the 35 second period, respectively. However, when using *BC2* the mean error is over 2.6%. Figure 4.62 shows the time history of predicted stresses- $S_{M, 8\ mm}$, $S_{V, 8\ mm}$, and $S_{A, 8\ mm}$, at the reference location that is 8 mm from the weld toe using the measured internal forces.
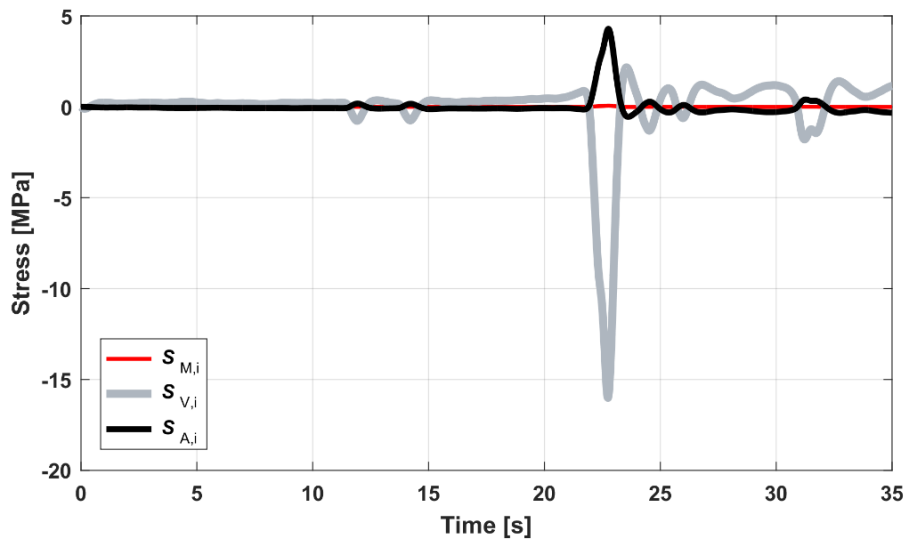
Figure 4.62 Stresses predicted at 8 mm from the weld toe using measured internal moments, shear and axial forces with local FEM using boundary conditions BC2.

Strain measurements from sensor SG-1 are also used to resolve the uncertainty in boundary conditions in the local FEM. Figure 4.63 presents the time history of measured stresses at this location as computed using strain measurements from sensor SG-1. The figure also shows the stresses predicted by the local FEM using *BC1*, *BC2* and *BC3* at the location of the SG-1. The stresses predicted by the local FEM using *BC3* is almost the same as the measured stresses with a mean error of only 2.5% over the 35 second period. From the same figure, however, when using *BC1* and *BC2* the mean error are over 59% and 3.8%, respectively.
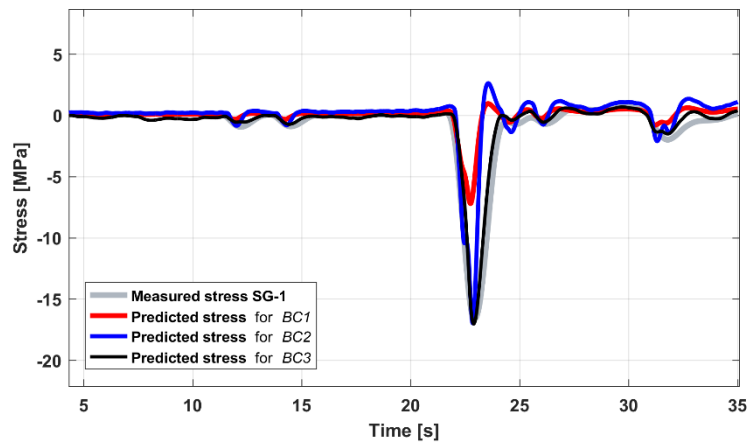
Figure 4.63 Comparison of the stress time-histories measured by sensor SG-1 with those predicted by local FEM for boundary conditions BC1, BC2 and BC3.

From Figures 4.61, 4.62 and 4.63, it can be concluded that the predicted stress at the weld region is mainly due to shear in the cross beam. Stresses induced by moment in the cross beam are very small and can be neglected for this connection. Also, the local FEM using boundary condition *BC3* is found to be appropriate for simulating the local stresses induced by real traffic. Using the local FEM with boundary conditions *BC3*, the time history of hot spot stress σ_{hs} is computed for the duration of the monitoring. Strain measurements from sensors SG-10 and SG-11 are used to derive the measured time history of the hot spot stress at the weld toe. The measured and predicted hot spot stress are compared for a 35-second duration when a heavy vehicle passes over the bridge causing significant stress in the connection. These stresses are given in Table 4.4.

Table 4.4 The measured and predicted hot spot stress of the connection when a heavy vehicle passed over the bridge.

Connection type	σ_{8mm} from local FEM (MPa)	σ_{20mm} from local FEM (MPa)	Hot spot stress σ_{hs} based on strain measurements (MPa)	Hot spot stress σ_{hs} based on proposed methodology (MPa)
Vertical stiffener to the beam web	7.96	12	14.71	14.1

The results reveal that there is a good agreement between the hot spot stresses obtained using the proposed methodology and its counterpart from the measured strain under real-life loading. The mean percentage error in the predicted stress relative to the measured hot spot stress values is calculated, for the chosen 35 seconds as well as the full duration of monitoring (6 hours). It is observed to be less than 4.1% for the selected 35 seconds, and less than 6.96% for the whole monitoring period. The range of these errors is less than the $\mp 10\%$ error ranges given for hot spot stresses obtained based solely on finite element analysis (Heshmati 2012). Although these errors are in an acceptable range, a sensitivity analysis is conducted and described in the next section to identify the most suitable finite element mesh and element type configuration for this application.

Effects of mesh size and element types: The hot spot stress may be sensitive to the mesh size of the finite element model. IIW (Hobcher, 2016) suggests that the element size should be no more than $0.4t$ and $t \times t$ for relatively fine and

coarse meshed models respectively. The mesh sensitivity varies with the object

weld detail, the stress analysis model and the hot spot stress calculation method.

Therefore to enhance confidence in the hot spot stress results, a convergence

study on the reference stresses with respect to its dependence on mesh size and

the stress analysis method is warranted. In this research, only the stresses on

the inside web gap have been considered as shown in Figure 4.47.

The hot spot for this analysis is the weld toe. The distances of reference locations

are specified relative to the weld toe. The mesh-size is selected relative to web

plate thickness t (i.e. 20 mm) and ranges from t to $0.1t$ using 8-noded shell and

8-noded solid brick elements. To keep a small mesh density (8, 4 and 2 mm), the

web gap is meshed with a fine mesh but the rest of local model is meshed using

$0.5t$ i.e. 10 mm mesh size. The result of mesh sensitivity analysis is presented in

Figure 4.64.

It can be observed that the behaviour close to weld toe is influenced slightly by

the mesh-size. Also, the peak stress increases with mesh refinement and occurs

at the element edge closest to the weld toe. However, away from the weld, the

stresses predicted are nearly the same for mesh sizes less than $0.4t$.
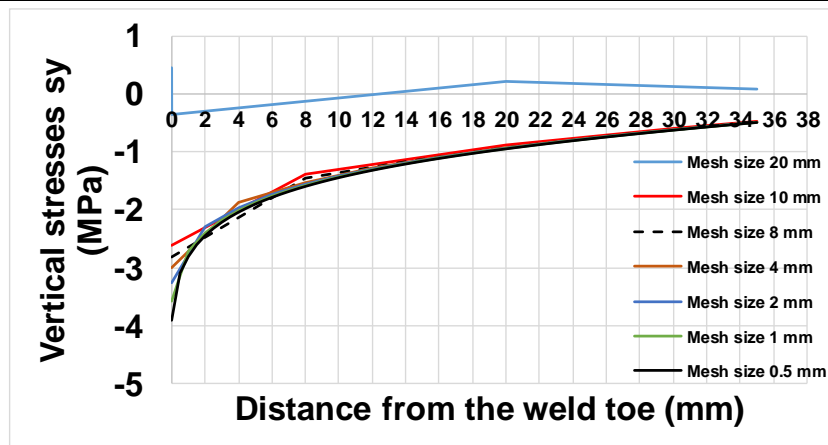
Figure 4.64 Vertical stress vs distance from weld toe for various mesh sizes (shell model).

For a local FEM with linear 8-noded solid brick elements, the element size in the region of interest is varied from t to $0.1t$. In contrast to the shell model, behaviour close to weld toe is influenced significantly by mesh-size as shown in Figure 4.65. Also, general outline of the curve differs if mesh-size is larger than t/5 (equals 4 mm). However, the stresses away from the weld toe for mesh sizes less than $0.4t$ are nearly the same as observed in the shell model.
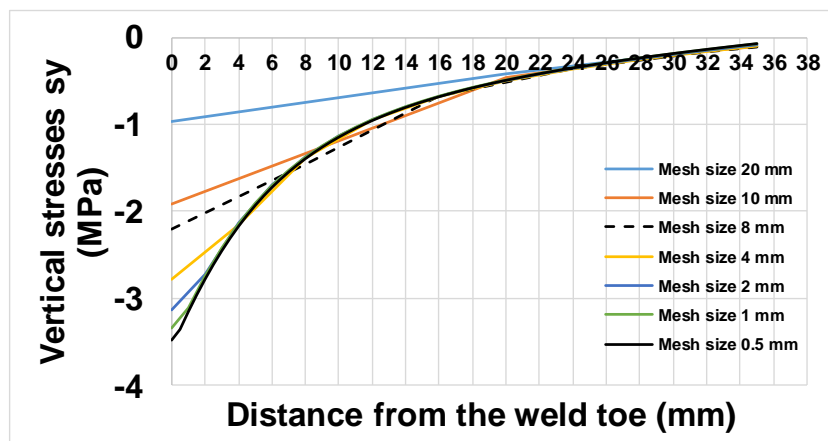
Figure 4.65 Vertical stress vs. distance from weld toe for various mesh sizes (solid model).

The effect of mesh size can also be inferred from computing the hot spot stress as recommended by the BSI standards (BSI, 2014), i.e. using Equation 2.7. For

stress analysis based on measured strains or finite element models of relatively

fine mesh model, the BSI standards recommend the use of a leaner extrapolation

from stresses on plate at distances $0.4t$ (i.e. 8 mm) and $1.0t$ (i.e. 20 mm) from the

weld toe. Using this equation, hot spot stress for different mesh sizes are

calculated and compared in Figure 4.68 and Table 4.5. It is found that the model

with shell elements computes the stress in the weld toe more accurately. The

model with solid elements when using a fine mesh also provides acceptable

results. Figure 4.66 also shows clearly that the plate surface stresses in the web

gap region near the stiffener plate are underestimated with a coarse mesh for

both shell and solid elements. The plot shows that a mesh composed of 4 mm

shell or 8 mm solid elements can be adopted to obtain a reasonable solution to

avoid unnecessary complexity and computational effort. Consequently, the

local FEM developed in this research successfully evaluates the hot spot stress

at the weld toe and is appropriate for simulating the local stress values induced

by the real traffic.
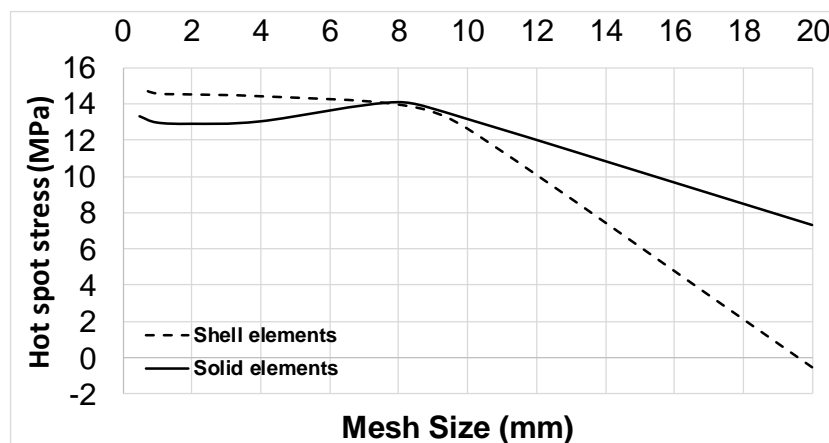
Figure 4.66 Comparison of the hot spot stress obtained at web plate weld toe for the solid element model and shell element model with different mesh sizes.

Table 4.5 Measured and predicted hot spot stress of the connection when a heavy vehicle passed over the bridge.

Mesh size	Predicted hot spot stress/ Shell elements (MPa)	Error (%)	Predicted hot spot stress/ Solid elements (MPa)	Error (%)
20	6.52	53	7.315	50
10	12.66	14	13.19	10
8	13.98	4.9	14.12	4
4	14.44	1.8	13.05	11
2	14.54	1.2	12.92	12
1	14.59	1	12.99	11
0.5	14.90	-1.3	13.34	9

4.7   Stress   predictions   at   uninstrumented locations

The virtual sensing procedure (VSP) proposed in Chapter 3 is validated in this section. The discussion is divided into three consecutive parts. First, the instrumented connection used for validating the developed VSP is discussed in detail. Also, this part presents the utilisation of the in-service monitoring data along with the local FEM to estimate virtually the stress at a specific hot spot point on the instrumented connection (i.e. web gap region). Second, the combination of field measurements and FE models (both local and global) that facilitates monitoring virtually the fatigue critical detail is explained. Finally, this combination of measurements and FEM is used to evaluate the stress at global, fatigue sensitive, locations.

4.7.1 The instrumented connection

The structural description of the instrumented connection and the instrumentation plan used for field measurements were given in sections 4.3 and 4.4.2 respectively. It should be noted that the outer face of the web gap region was not instrumented due to bridge owner restrictions. Figure 4.67 shows a schematic of the instrumented connection with sensor locations and their labels.
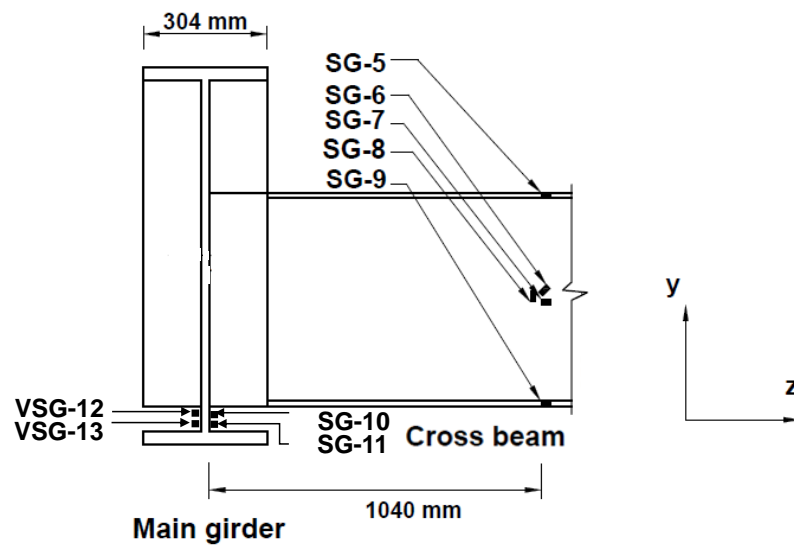
Figure 4.67 Schematic of the virtual sensing gauges locations.

SG-1, SG-5 to SG-9, SG10, and SG11 are locations of physical gauges. These sensors are referred to as reference sensors. The remaining locations - VSG-12 and VSG-13, are denoted as virtual sensing locations. Using the VSP described in Chapter 3 of this thesis, strain measurements from reference sensors are used to predict individual stresses at these virtual sensing locations. The accuracy of the VSP is determined by comparing the predicted stress time history with the measured response time history from sensors placed at the virtual sensing locations.

As discussed in section 4.4, results show that there is a good agreement between the hot spot stresses obtained from the local FEM and from the measured strain at sensor locations SG-10, SG-11 and SG-1 under real-life loading. Here to further illustrate this, strain measurement from SG-10 is compared with that from the local FEM for the scenario when the truck passes over the bridge during the loading test as shown in Figure 4.68. The local FEM achieves an adequate response to the stress time-history with a mean percentage error of less than 2%.
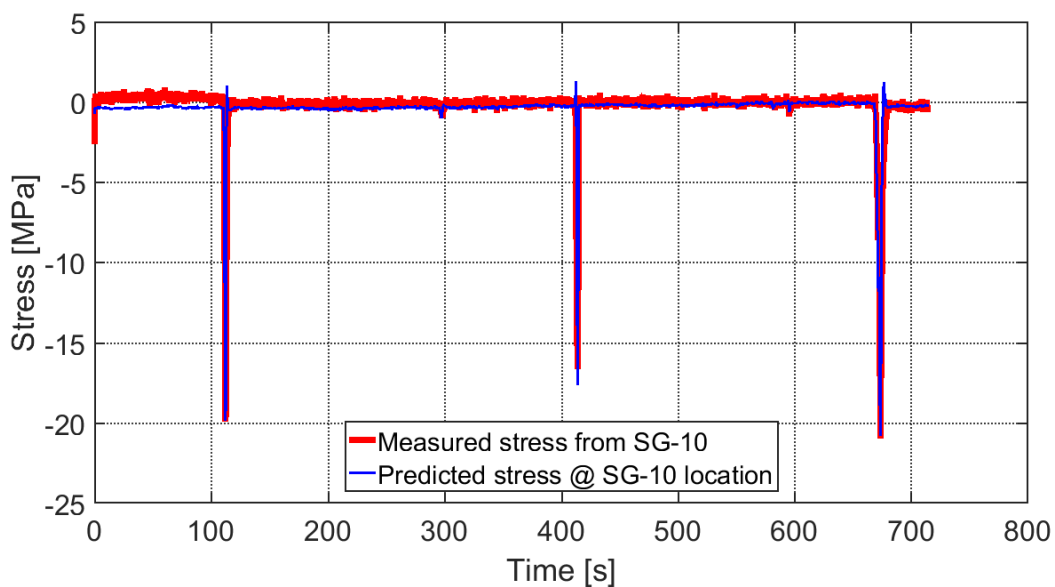
Figure 4.68 Comparison of the time history of stresses (800 sec) measured by sensor SG 10 with that of stresses predicted by VSP when the loading vehicle test passes over the bridge.

The prediction accuracy of the VSP at VSG-12 and VSG-13 is not experimentally verified since there are no sensors here. For this purpose, the calibrated global model is used to predict stress time histories at VSG-12 and VSG-13. The predicted hot spot stresses from the global FEM, and the VSP are both compared for approximately 2.5-seconds duration when the test vehicle passes over the bridge. Figure 4.69 shows the time history of predicted stress at a distance of 8

mm from the weld toe $\sigma_{8\,mm}$, (at the VSG-12 location) when using strain measurements from reference gauges. The figure also presents the time history of predicted stress at the VSG-12 location $\sigma_{8\,mm}$, when using global FEM.
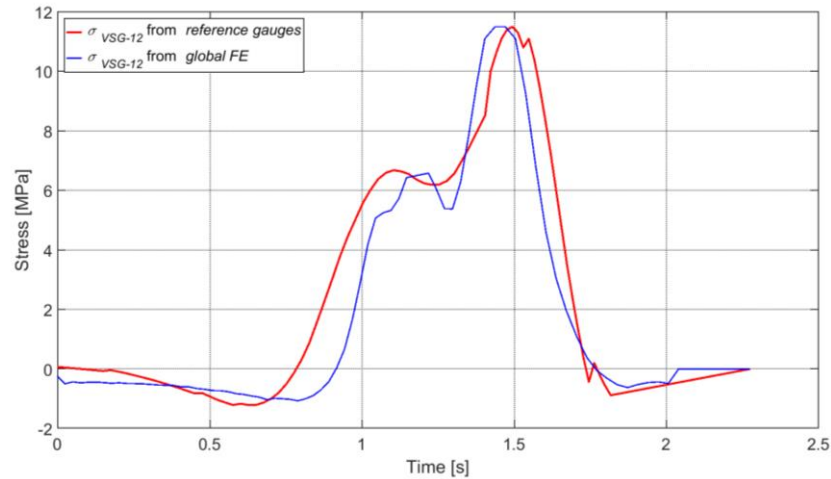
Figure 4.69 Comparison of the time history of stresses predicted at VSG-12 location by global FEM with that of stresses predicted by VSP.

As seen in Figure 4.69, the stresses predicted by the VSP is similar to the stresses predicted by the global FEM with a mean error of 2.84% over the 2.5-seconds period. The stress time-histories (σ_{8mm} and σ_{20mm}) near the weld toe (VSG-12 and VSG-13) are then used to derive the stress time-history at the hot spot σ_{Vhs} as shown in Figure 4.70. From Figures 4.69, and 4.70, it can be concluded that the predicted stress at the weld region by the VSP using gauges SG5-SG-9 as reference gauges is sufficient for fatigue evaluation at the studied virtual sensing locations. Hence, the virtual sensing procedure can be generalised to estimate the stresses/strains at uninstrumented connections using data from instrumented connections and it will numerically be verified in the next section.
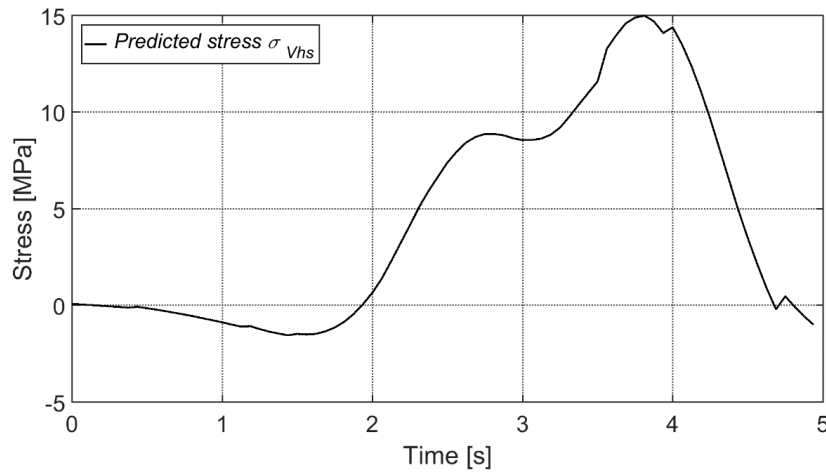
Figure 4.70 The predicted hot spot stress of the connection (outer side of the web gap) when the load test vehicle passed over the bridge.

4.7.2 Uninstrumented 'hotspot' locations on the bridge

As described in section 4.3.1, the Bascule Bridge has 33 beam – beam connections, where the 17 cross beams were connected to main girders. These connections are similar to the instrumented one in terms of connection assembly. One of these uninstrumented connections is considered as a fatigue critical detail (see Chapter 6). The location of the critical connection is close to the bridge support as shown in Figure 4.71. The figure also shows virtual sensing locations VSG-14 and VSG-15 which are at - 8 mm and 20 mm from the weld toe at the outer face of its web gap region.
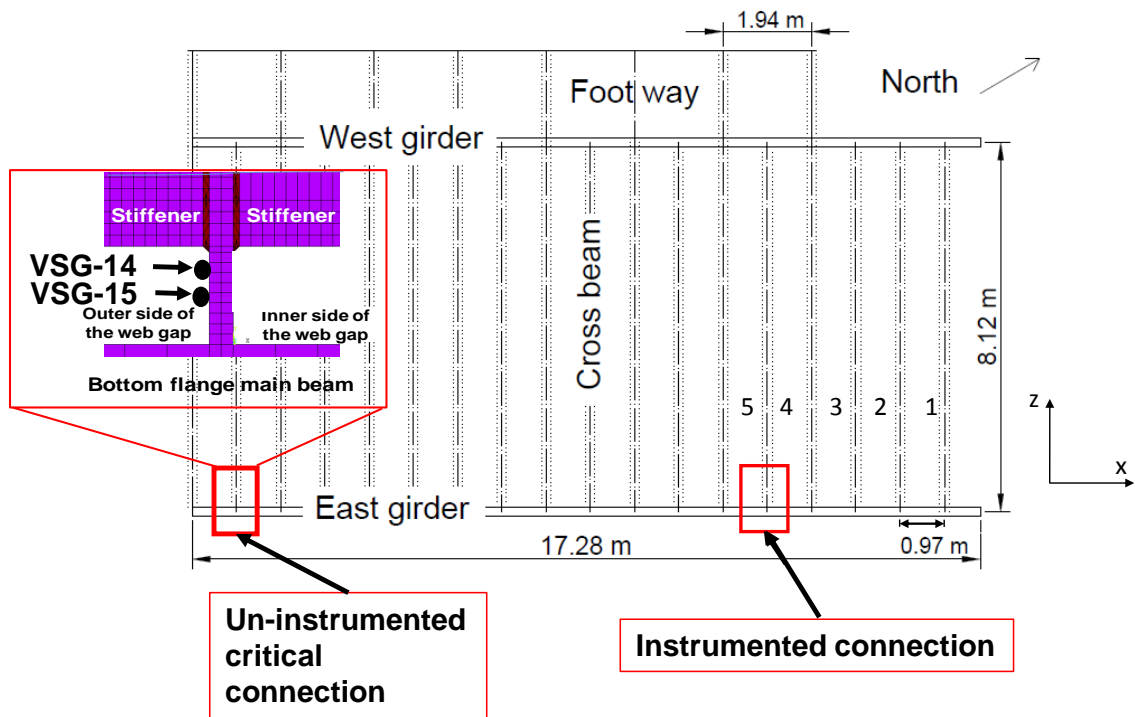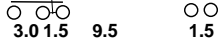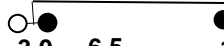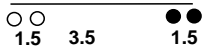
Figure 4.71 Location of critical connection.

The VSP is used to estimate the hot spot stress at the weld toe of the critical connection using data from the instrumented connection. As described in Chapter 3, the virtual sensing procedure requires a relation between the peak magnitude of the stress at the hot spot of the instrumented connection and the stress at the virtual sensing location. This is derived using the global FEM as follows.

The global FEM is refined at the defined virtual sensing locations to the level of resolution as the local FEM with respect to element type and mesh size (shell element and 4 mm mesh size). The global FEM is loaded using five equivalent lorries of the FLM4 (BS NA EN 1991-2 2003). Characteristics of these lorries are summarized in Table 4.6.

Table 4.6 Set of equivalent lorries for FLM4 (BS NA EN 1991-2, 2003).

Chassis type	Average Spacing (m)	Loading Group	Total Weight kN	Axle Loads kN
Articulated	3.0 1.5 9.5 1.5	H2	630	70 130 130 150 150
Articulated	3.5 5.5 1.5 1.5	H	380	70 100 70 70 70
Articulated	3.0 6.5 1.5	H	240	40 80 60 60
Rigid	1.5 3.5 1.5	H	280	50 50 90 90
Rigid	4.0 1.5	H	240	60 90 90
Rigid	4.0	H	135	50 85

Hot spot stresses peaks (V_{VSi}) at the virtual sensing location (i.e. VGS-14 and VGS-15) are calculated. Also the ratio of the peak hot spot stresses (R_i), between the reference location and virtual sensing location (σ_{hspi}) on the bridge, are established according to Equation 3.5 and are presented in Table 4.7. Hot spot stress time history at a virtual sensing location (σ_{Vhsi}) is extracted using Equation 3.6.

Table 4.7 The ratio of hot spot stresses (R_i) between the reference location and virtual sensing locations on the bridge for selected equivalent lorries for FLM4 (BS NA EN 1991-2, 2003).

Axle number	Hot spot at reference location σ_{hspi} (MPa)	Hot spot at virtual sensing locations V_{VSi} (MPa)	(R_i) %
2	46.27	31.1	148.8
3	87.14	60.02	145.2
4	58.73	40.01	146.8
4	83.16	59.18	140.5
5	147	100	147
		Mean	145

Figure 4.72 illustrates the predicted hot spot time stress history responses of the investigated detail (critical location) of the bridge for the passage of the selected standard fatigue lorries. These are obtained by combining results in Figure 4.70 with the R_i evaluated above. Figure 4.72 also shows the hot spot stress time history predicted at the critical location by VSP using Equation 4.5.

Figure 4.72 show that the peak values of the hot spot stresses predicted by the VSP are generally in good agreement with the measured stresses with peak error of 2%.
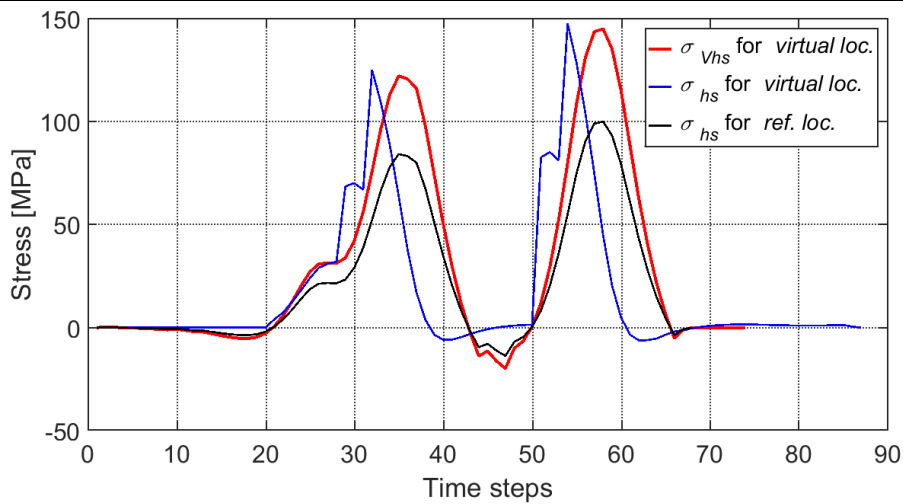
Figure 4.72 Comparison of the hot spot time histories of stresses predicted at critical location by global FEM with that of stresses predicted by VSP.

Prediction of 'nominal' stress at uninstrumented locations

As mentioned in Chapter 1: section 1.7, load-Induced fatigue cracking occurs in primary elements of a bridge due to in-plane stresses. These elements are usually flanges of steel girders, particularly, if they have welded details such as connections between girder splices and welded cover-plates. At such details, the primary stresses are of interest for fatigue damage assessment.

The aim here is to show that the VSP can be used to estimate the primary stresses at any desired location in a short-span steel bridge using data collected from instrumented connections. This is particularly relevant for flanges of the main longitudinal girders that according to beam theory will be subject to the maximum nominal stresses in bending. The VSP is predicated on the knowledge that each vehicle produces one load cycle on the bridge, regardless of the flow conditions. This is based on observations discussed by Baptista (2016) who showed that the stress peaks for bridges shorter than 40 m can be determined essentially by the influence line and the knowledge of the truck load. Specifically

Baptista (2016) showed that the effect of the flow conditions on the stress is negligible. This is due to the bridge span length being of the same range as the vehicle length (plus a minimum distance between lorries).

The proposed procedure is used to extract nominal stress time history at SG-4 location. First, strain measurements from sensors SG-5 and SG-9 are used to derive the measured nominal time history (σ_{nom}) at bottom flange of the main girder (SG-2) as described in chapter 3: part 2.

Second, the global FEM is loaded using the geometrical characteristics and loads of the vehicles used during the load test to extract an influence line of the longitudinal bending nominal stresses at mid span of the bridge (bottom flange) as shown in Figure 4.73.
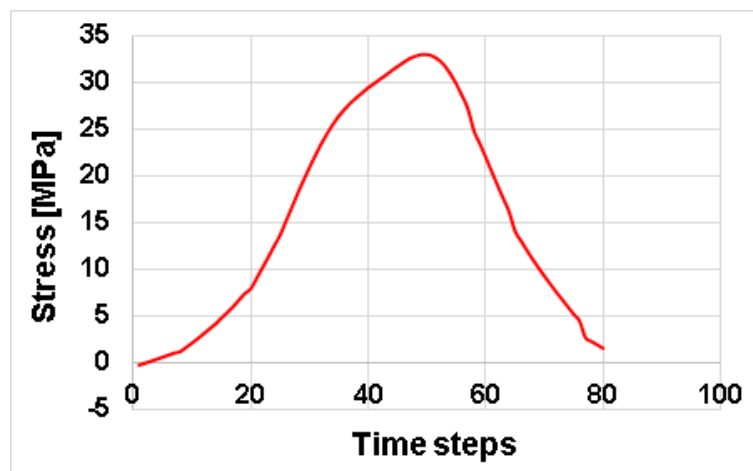
Figure 4.73 The predicted influence line for bending stresses at mid span of the bridge under truck loading test.

Finally, from the influence line peak relation of nominal stresses (R_{nom}), between the stress (σ_{SG-2}) from SG-2 and stress (σ_{SG-4}) from SG-4 on the bridge is established according to Equation 3.7 and Table 4.8.

Table 4.8 Ratio of the peak nominal stress (R_{inom}) at the reference location and the virtual sensing location on the bridge as computed from truck load test.

Nominal stress at reference location SG-2 (MPa)	Nominal at virtual sensing locations SG-4 (MPa)	(R_{nom}) %
28.6	29.9	104.5

Nominal stress time history (σ_{Vnom}) at location of SG-4 is extracted using Equation 3.8. Figure 4.74 shows the predicted time history at SG-4 obtained using VSP when the bridge was under the truck loading test and the corresponding measured stresses from SG-2 placed on the bottom flange of east girder.
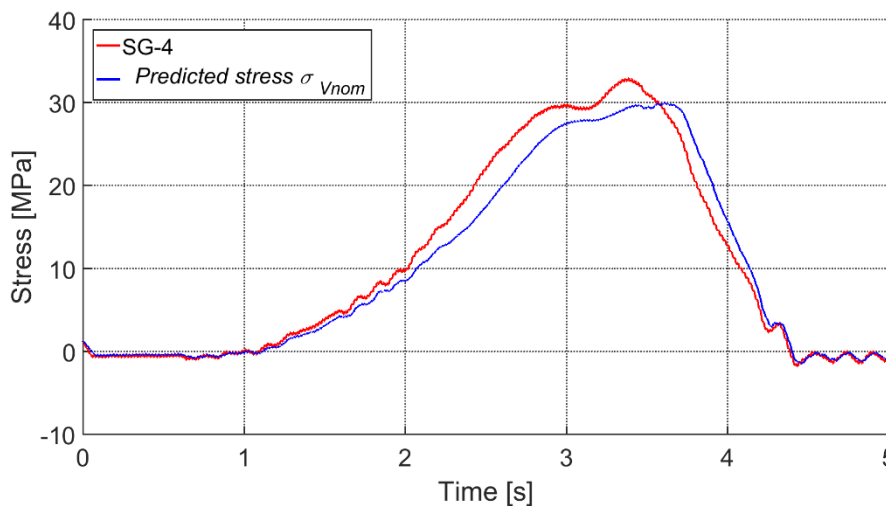
Figure 4.74 Comparison of the nominal time histories of stresses predicted at SG-4 location with that of stresses measured by SG-4 when the bridge was under the truck loading test.

The calculated peaks relations presented in Table 4.9 are used for representing the behaviour of the bridge under real-time traffic. Figure 4.75 shows the predicted stress by VSP and measured stress response at SG-4 location of east girder.
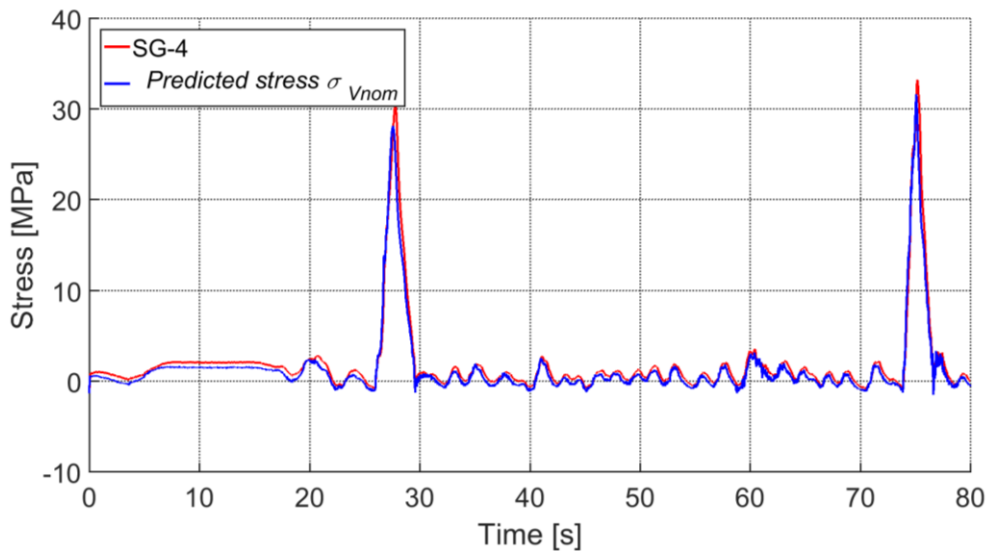
Figure 4.75 Comparison of measured stress and predicted stress according to the VSP at location of SG-4 when the bridge was under real time traffic (80 second duration

As can be seen from Figure 4.74 and Figure 4.75, the peaks can be predicted accurately with mean error percentage of only 6% and 4.34% respectively.

4.8   Summary & conclusions

A steel bridge (Bascule Bridge) is employed to address the study objectives (2-5) stated previously in Chapter 1. This bridge is representative of many old bridges having fatigue concerns. The bridge is investigated to characterize the fatigue response of critical connections due to vehicles crossing the bridge. The instrumentation and the data acquisition equipment used at the bridge are summarized. Strain data from the bascule bridge are analysed using the techniques presented in Chapter 3. The virtual sensing procedure presented in

Chapter 3 is also investigated to characterize the fatigue response of uninstrumented critical connections to vehicles crossing the bridge.

From this study, the following conclusions can be drawn on the monitoring of the bridge and the research methodology.

Monitoring:

- Based on the conducted field measurements, the maximum measured hot spot stress range (78 MPa) exceeds the CAFL at instrumented location. Therefore, the longitudinal girder of the bridge must be considered to have a finite fatigue life and the remaining fatigue life of the bridge have to be estimated.

- Results illustrate that the proposed monitoring strategy can provide accurate in-situ stress information to support an approach for real-time fatigue damage assessment.

Research methodology:

- The proposed methodology successfully evaluates the hot spot stress at the weld toe, which can be used to simulate the local stress values induced by the real traffic.

- Strains predicted by the local FEM of the connection upon using internal forces computed from measured strains is within 3% of the field measured strains. This demonstrates that the real stresses at fatigue critical details can be evaluated using the proposed methodology.

- Results show that the proposed methodology provides a valuable tool to calculate the hot spot stress at complicated locations (e.g. web gap region) using measured strains and a calibrated local FEM model.

- The hot spot stresses evaluated using the local FEM with boundary condition *BC3*, which corresponds to supports with partial fixity, matches the in-situ measured stresses to within 1.8%.

- For the studied connections, the predicted stress at the weld region are mainly due to internal shear forces in the cross beam. The internal moment is found to have a negligible effect on the hot spot stress.

- The results show that the virtual sensing procedure can be used to characterize the fatigue response of uninstrumented critical connections due to vehicles crossing the bridge.

- The results show that shell elements of size $0.2t$ (4 mm) or solid elements of size $0.4t$ (8 mm) elements can be adopted in the local FEM to obtain a reliable solution while avoiding unnecessary complexity and computational effort.

- Although nonlinear behaviour is expected in the web-gap region due to the nature of the connections, the global FEM is still able to accurately predict strain response in this region using only a linear elastic model.

CHAPTER 5   Field testing and monitoring of railway steel bridges

5.1   Introduction

Data from two steel railway bridges (Mineral Line Bridge and Williton Up Bridge) are used to validate the proposed methodology (chapter 3). The discussion for the two bridges is structured similarly. A detailed description of the structure is first presented. The instrumentation plan and the field measurement campaigns are then discussed. This is followed by a description of the global finite element model (global FEM) of the bridge, which is used to simulate the bridge response under different loading conditions. The local finite element model (local FEM) is then presented, which is an FE model of a selected riveted connection used for stress estimation. However, for Williton Up Bridge, no FE models are created due to time constraints and the reasons detailed in section 5.6.

5.2   Mineral Line Bridge

The Mineral Line Bridge (Figure 5.) is part of the West Somerset Railway, a heritage railway line with 20 miles of track in South West England. This line is owned and operated by West Somerset Railway Inc (WSR) https://www.west-somerset-railway.co.uk/.

Figure 5.1 Elevation of the Mineral Line Bridge.

The Mineral Line Bridge is located on the outskirts of Watchet and was originally constructed to carry the Minehead route over the West Somerset Mineral Railway (see Figure 5.2). The bridge, which was built in the 1870s, has a single span of 14.7 m between brick abutment faces and is constructed skewed to the pathway beneath with a skew angle of 57° as shown in Figure 5.2.

Figure 5.2 Location of Mineral Line Bridge on satellite map (51°10'47.3"N 3°20'06.2"W)

.

The original bridge construction was of wrought iron plate girders carrying a timber deck supporting the ballasted track bed. Inspection had indicated significant corrosion of internal cross beams and the secondary wrought ironwork, with even rivets missing in places. The main girders appeared in reasonable condition but with some plating and rivet replacement required. Consequently repairs were carried out in 2004 when the timber deck was replaced with a steel open mesh grid, overlain with a porous geo-textile sheeting (WSR). This supports the ballast but permits water to drain through quickly, allowing the supporting structure to dry out. The bridge supports a single track, which is subject to relatively low speed passenger trains. The bridge design is typical of many railway steel bridges in the UK and has easy access.

The bridge is simply supported and consists of two wrought iron plate girders located on either side of the railway. 21 cross beams are placed transversely and support a steel sheet plate deck as shown in Figure 5.3.

Figure 5.3 Superstructure of Mineral Line Bridge.

The longitudinal girders were built-up plate girders and geometrically fabricated like steel I-beam sections (labelled G1 and G2). The top and bottom flanges were riveted to stiffened web panels (10 mm thickness). Upper and lower cover plates (87 mm x 87 mm x 9.5 mm) have a L shape and run longitudinally along the girders. These cover plates are riveted to the top and bottom flanges and web of plate girders. Increased flexural stiffness is provided using steel plates added to the top and bottom flanges of the girders. As a result, the thickness of top and bottom flanges varies from 40 mm at mid span to 10 mm close to bridge supports as shown in Figure 5.4.

Figure 5.4 The varying thickness of bottom flanges of the main girder.

Web girders are reinforced with transverse intermediate stiffeners at approximately (1.78 m) intervals as shown in Figure 5.5 to increase the buckling strength.

Figure 5.5 Transverse intermediate stiffeners riveted to web girder.

A typical cross section for the bridge is shown in Figure 5.6. The width of the bridge is 5.04 m centre-to-centre. Cross beams are steel rolled sections of type 406 x 178 x 74 kg/m UB (S255). The length of cross beams vary from 1.4 m to 5.04 m due to the skew of the bridge and are spaced at 890 mm intervals as shown in Figure 5.7. The functions of the cross beams are to distribute loads from the steel plate deck to the main girders and to provide resistance against lateral forces. 20 mm thick steel plates span over the top flange of cross beams. Track system (rails, rails tie and crushed stone) lay directly on the steel deck plates. The deck plate is fastened to the top flange of the cross beams using M20 bolts at 160 mm intervals. Concrete ballast curbs are placed along the edges of the deck to ensure that the ballast remains in place.
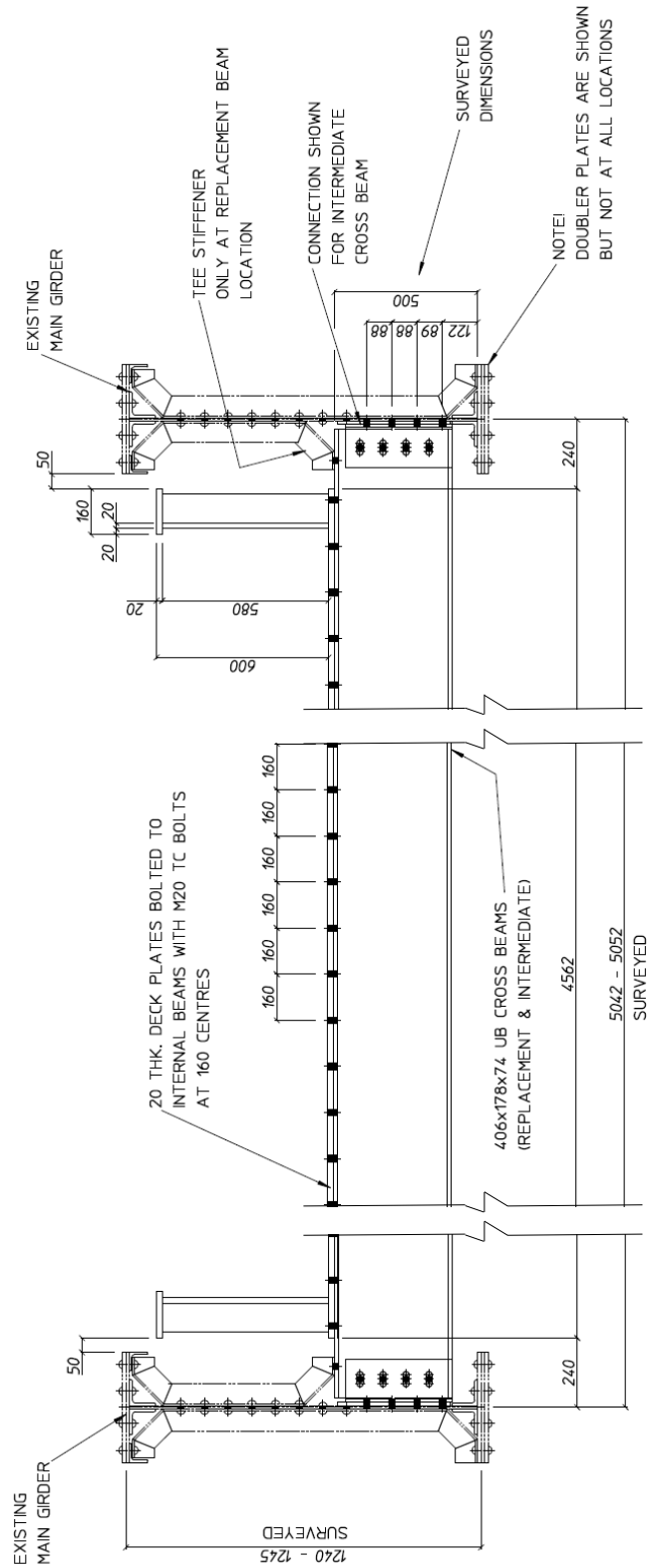
Figure 5.6 Bridge cross section (units in millimetres) (WSR).
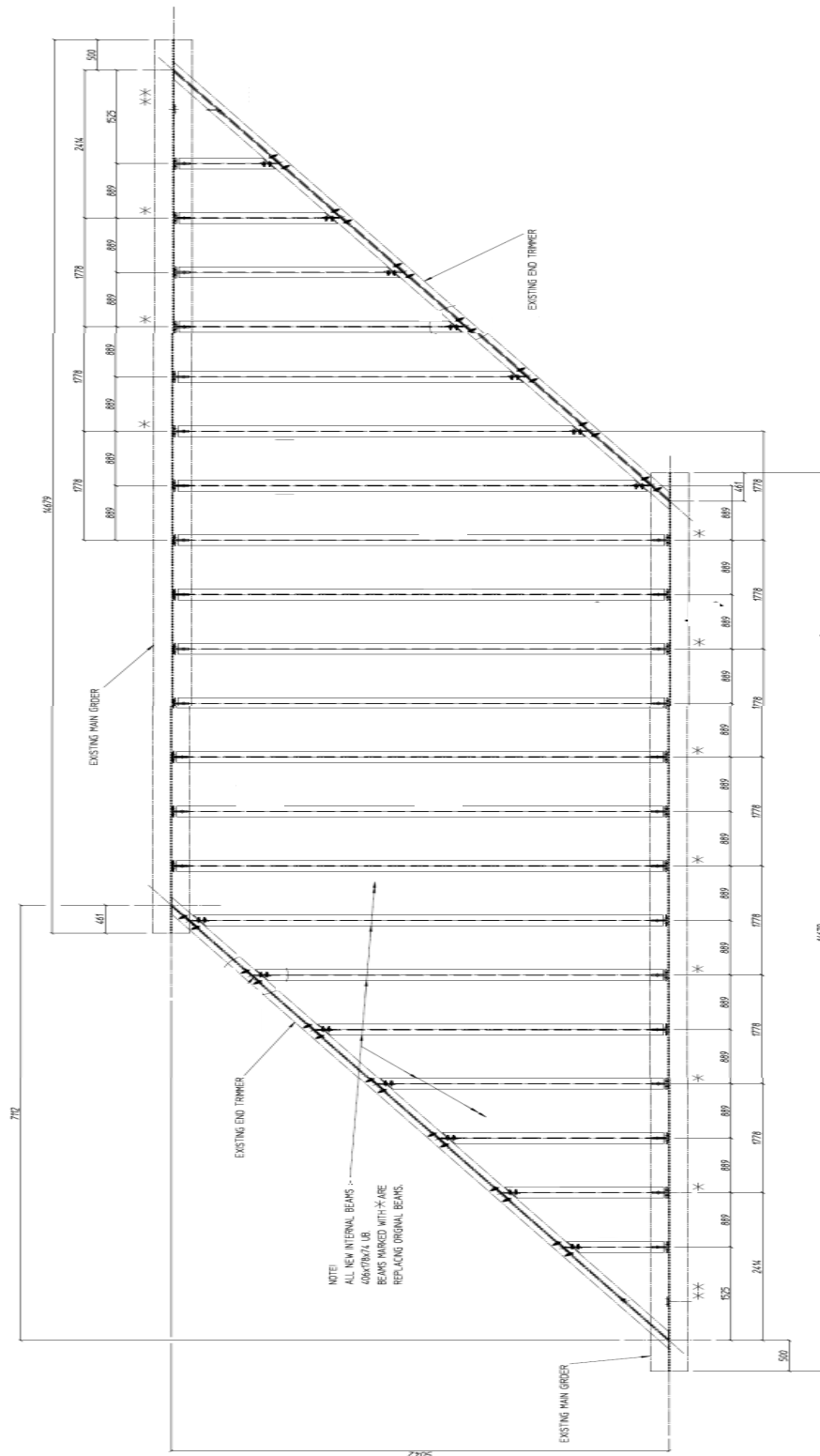
Figure 5.7 Plan schematic of the Mineral Line Bridge (units in millimetres) (WSR).

Table 5.1 gives the cross-section geometries of the longitudinal girders and cross

beams.

Table 5.1 Dimensions of the main girder and cross beam sections.

Structural element	Depth (mm)	Top flange width (mm)	Top flange thickness (mm)	Bottom flange width (mm)	Bottom flange thickness (mm)	Web thickness (mm)
Main girder	1300	380	10-40	380	10-40	10-30
Cross beam	380	179	16	179	16	9.7

All connections between members within the structure are made using rivets with

a shank diameter of 22 to 24 mm. The girder-to-cross beam connection is made

using 150 × 90 mm × 12 mm double angles riveted to cross beam and main girder

webs. The connections are shown in Figure 5.8 and Figure 5.9.
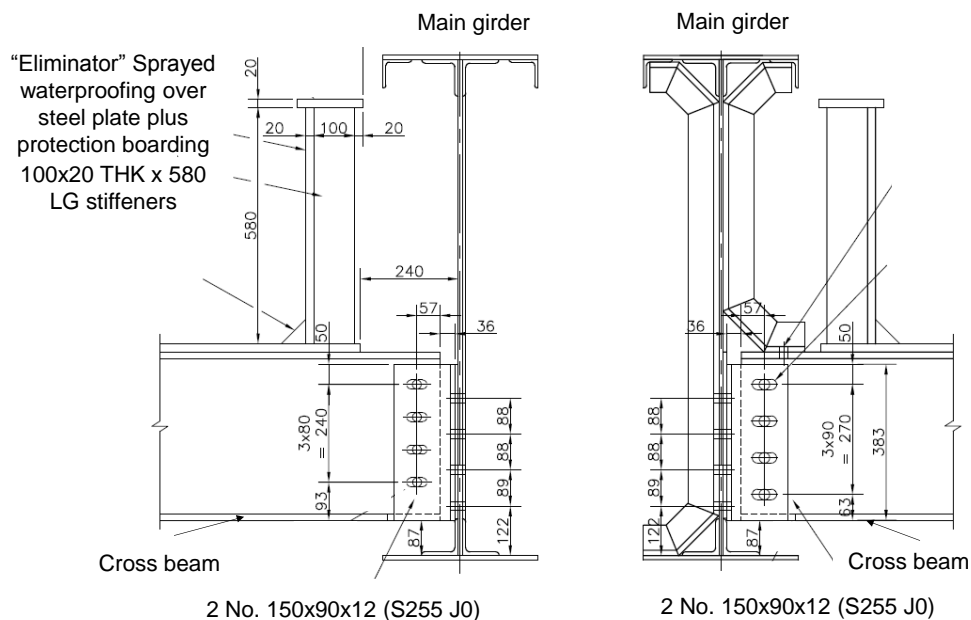
Figure 5.8 Main girder to cross beam connection details (units in millimetres) (WSR).

Figure 5.9 Photo of connecting main girder to cross beams using double L angles (WSR).

The connections between cross beams and end trimmer beams (Figure 5.10 and Figure 5.11), which are used to adjust for the skew, is made using 285 mm × 175 mm × 12 mm single angles as shown in Figure 5.10.
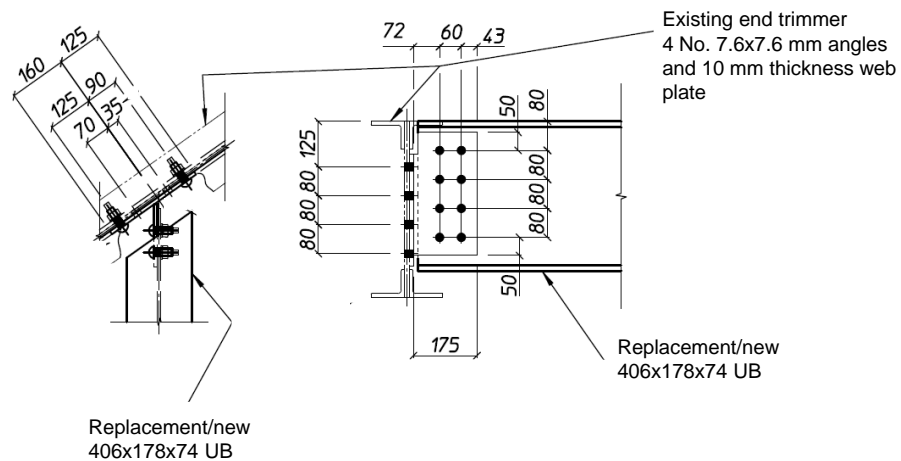
Figure 5.10 Cross beam to End trimmer connection details (units in millimetres) (WSR).
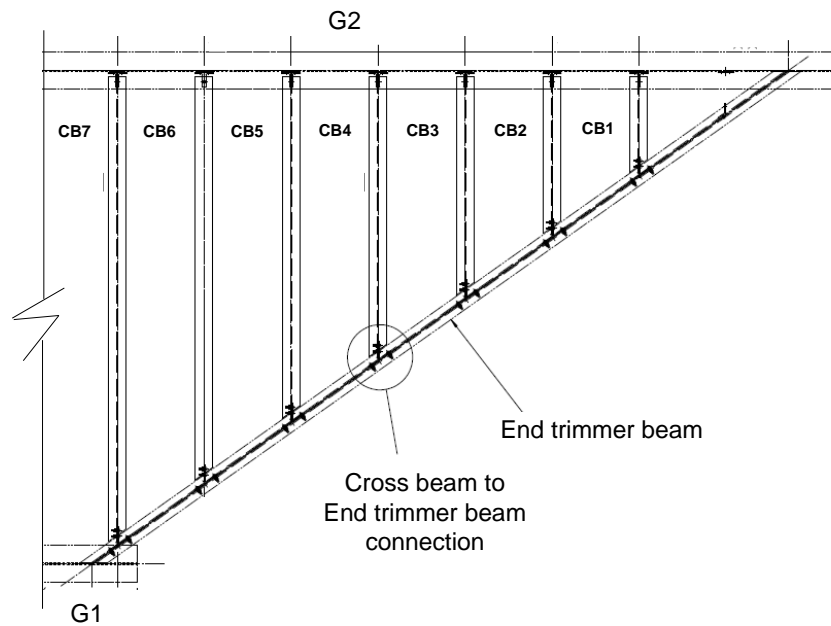
Figure 5.11 Schematic of right side of the bridge showing the cross beams to End trimmer beam connections (WSR).

The bridge deck and main girders are connected to stone abutments at each end which provide vertical and lateral support for the bridge. In addition to translation support, the abutments act as retaining walls to resist lateral movement of the earthen fill of the bridge approach as shown in Figure 5.12. This arrangement eliminates the need for expansion joints and bearings.

South side   North side

Figure 5.12 Photos for the stone abutments at each end of the bridge.

5.2.1 Fatigue-critical connections

Skewed supports significantly complicate the behaviour of steel girder bridges by introducing alternate load paths and causing greater interaction between the main girders and cross beams. The effects of the skew are more pronounced in the case of the Mineral Line Bridge and have led the bridge operator to specifically consider damage due to distortion induced fatigue introduced as described below. In the Mineral Line Bridge, the ends of any cross beam undergo significant differential deformation due to the skewed geometry of the bridge deck. The deflecting girders force a racking distortion of the cross beams, but the in-plane racking stiffness of the cross beams is quite large and so the cross beams rotate and force the girders to twist about the longitudinal axis of the bridge. These twisting deformations, which induce torsion in the girders, are different at different points along the span since they are a function of the vertical displacement of the girders. In addition, significant forces occur within the cross beams as it resists the racking deformation the girders are trying to apply (Coletti et al. 2011).

Figure 5.13 shows two intermediate cross beam connections noted as MG2C and MG1C. At MG2C location, girder G2 will vertically displace more than girder G1 since the location of MG2C along G2 is closer to mid span than the connected location of G1. Thus, the bridge cross section rotates out-of-plane, and forces are developed in the cross beams. However in G1, at intermediate cross beam connection MG1C, the bridge rotates out-of-plane in the opposite direction of the rotation experienced along cross beam connection MG2C.
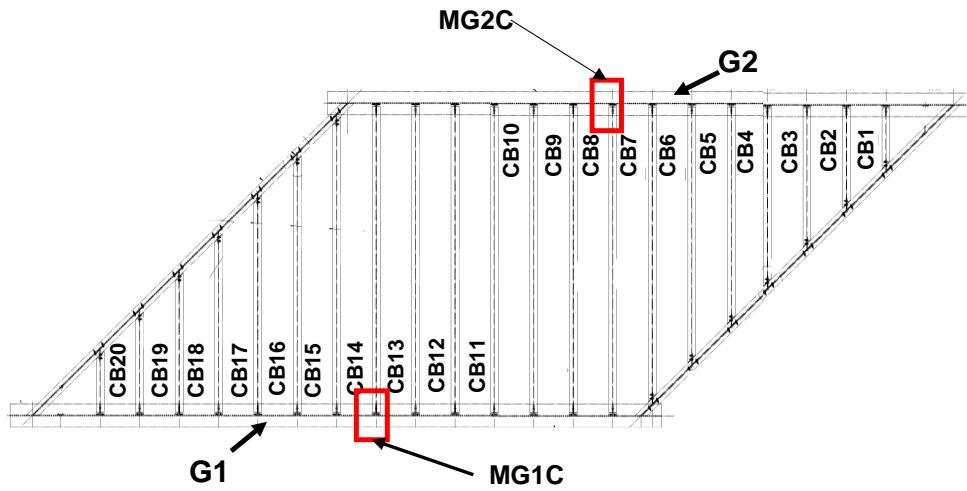
Figure 5.13 Location of connection to be instrumented at the Mineral Line Bridge.

To add to the effects of the skew, the rail track system is not at the centre width of the bridge. It is closer to G2 than G1. The author has chosen the MG2C location to be instrumented rather than MG1C because the MG2C is expected to carry high load due to the eccentricity of the track as shown in Figure 5.14.

Figure 5.14 Photo of the track system of the Mineral Line Bridge.

5.3   Instrumentation

Field measurements were performed for two purposes: first, to calibrate the global and local FEM models; second, to investigate the proposed research methodology and ensure it is applicable for riveted/bolted steel bridges. BDI strain sensors and the Imetrum dynamic monitoring systems were used to measure the structural response.

5.3.1 Strain sensors

A total of ten BDI strain transducers were installed on the bridge to monitor the live-load response. Figure 5.15 and Figure 5.16 were taken during the fieldwork undertaken to install the sensors. Eight sensors were installed around the connection between cross beam CB8 and the main beam. These will enable evaluating the time history of internal forces that are transferred via the connection. BDI-1, BDI-2, BDI-3 and BDI-4 represent those installed on the cross beam CB8, as shown in Figure 5.17. BDI-7 and BDI-8 are the sensors placed on top and bottom flanges of the main girder at distances 20 mm from the vertical stiffener to capture strains developed in the girder G1.

Figure 5.15 Equipment used during the monitoring event.

Figure 5.16 A team member installing strain sensors on the girder G2 of the bridge.
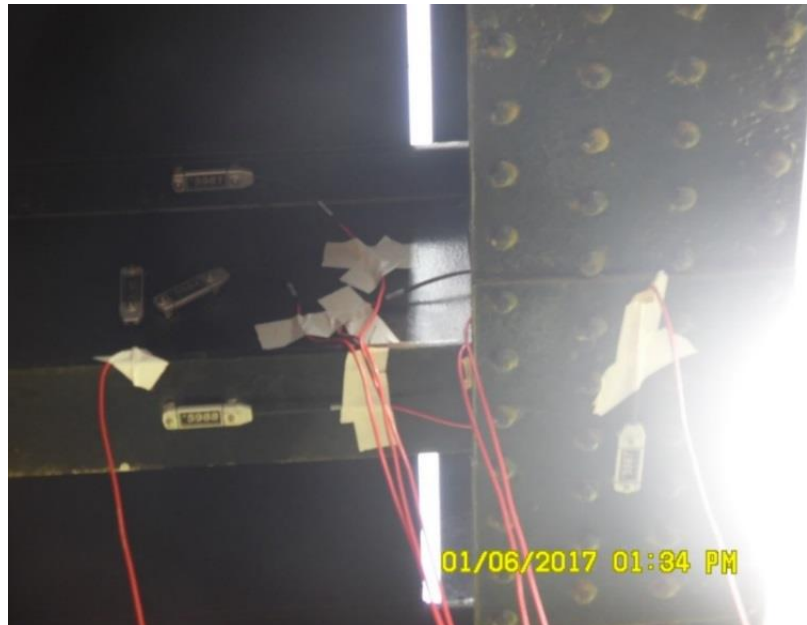
Figure 5.17 Photo showing BDI-1 to BDI-4 and BDI-8 installed on the bridge.

An additional two sensors are installed at mid span and quarter span of the longitudinal girder G2 and cross beam CB3, respectively. BDI-9 is on cross beam CB3, which is the cross beam at quarter span of the bridge. BDI-10 was placed

on bottom flange of the main girder at distances 20 mm from the vertical stiffener to capture strains developed in the girder G1. These are installed to capture strains developed in the cross beam closer to its connections with the main girder G1. The locations of all strain sensors are summarised in Table 5.2 and Figure 5.18. Strains were sampled at 100 Hz when trains passed over the bridge (see Figure 5.19).

Table 5.2 Summary of the locations of BDI gauges installed along the G1 and G2 longitudinal girders and cross beams.

Girder	BDI sensor	Position	Location in cross-section
Girder G2	BDI-7 & BDI-8	20 mm west north of cross beam	West side of the top and bottom flange
Girder G1	BDI-10	20 mm east north of cross beam	West side of the bottom flange
Cross-beam CB8	BDI-1 & BDI-4	500 mm west of main girder	Underside of the top and bottom flanges
Cross-beam CB3	BDI-9	500 mm west of main girder	Upper side of the bottom flange
Cross-beam CB8	BDI-2 & BDI-3	500 mm west of main girder	Mid web
Girder G2	BDI-6	100 mm and	400 mm above the bottom flange
Cross-beam CB8	BDI-5	30 mm west of main girder	L-angle that connected G1 with CB8
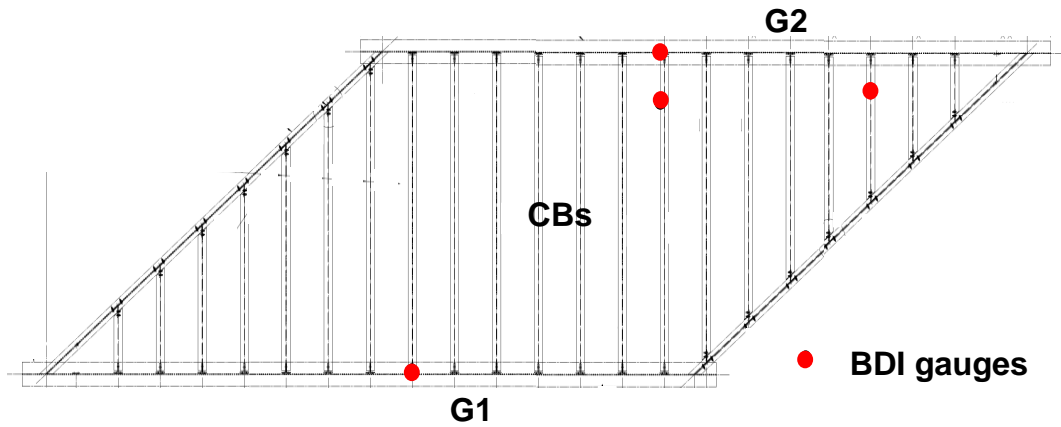
Figure 5.18 Layout of BDI transducers Locations.

Figure 5.19 Locomotive passes over the Mineral Line Bridge.

5.3.2 Imetrum Dynamic Monitoring Station (DMS)

The Imetrum system is a commercial vision-based system that originated from research at the University of Bristol (Brownjohn et al. 2017). The system supports 2D structural displacement measurement using a GigE high performance camera (see Figure 5.20). For the field monitoring, a GigE high-performance camera was connected to a computer via Ethernet cables for time-synchronised recording and

real-time video processing. Target tracking algorithms based on correlation-based template matching and super-resolution techniques which enable better than 1/100 pixel resolution at sample rates beyond 100 Hz in field applications were utilised.

Figure 5.21 shows the artificial target that was mounted on the bridge. The DMS recorded vertical deflections of the west girder with the artificial target placed at point B as shown in Figure 5.22.

Figure 5.20 Photo for a GigE high-performance camera.

Figure 5.21 Photo for an artificial target.
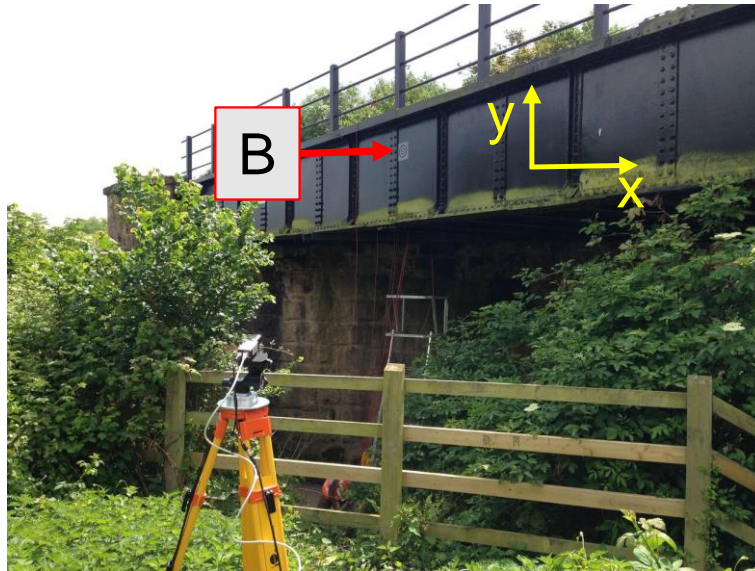
Figure 5.22 A high-resolution camera in use during the monitoring event (y-axis represents the vertical direction).

5.4 Field measurements

The in-service monitoring event took place on June 01, 2017. Measurements from the monitoring are described in the following sections along with key results.

Figure 5.23– 5.25 show the stress time-histories recorded at various BDI sensors during the passing of a train with six coaches plus the engine (Figure 5.19). Figure 5.23 shows the stresses computed from the strains measured by sensors BDI-7 and BDI-8, which are attached to the top and bottom flanges of the main girder G2. Figure 5.24 compares the stress time histories from the sensors on the bottom flange of the main girder G2. Figure 5.25 shows typical time history plot of the recorded stress in the bottom flange of the cross beam at sensors BDI-1 and BDI-4.
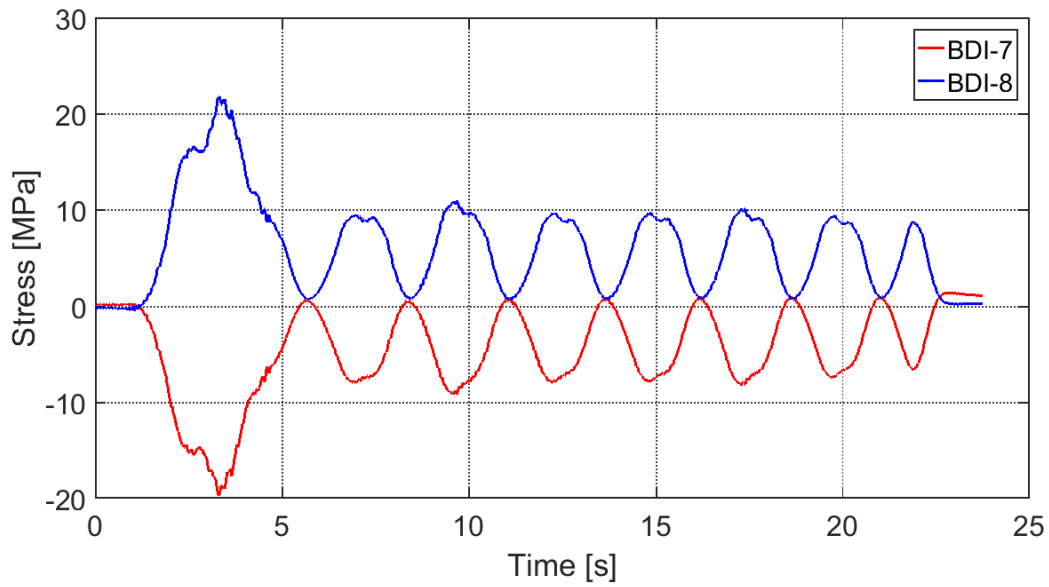
Figure 5.23 Stresses computed using strains from sensors BDI 7 and BDI-8 when a train passes over the bridge.
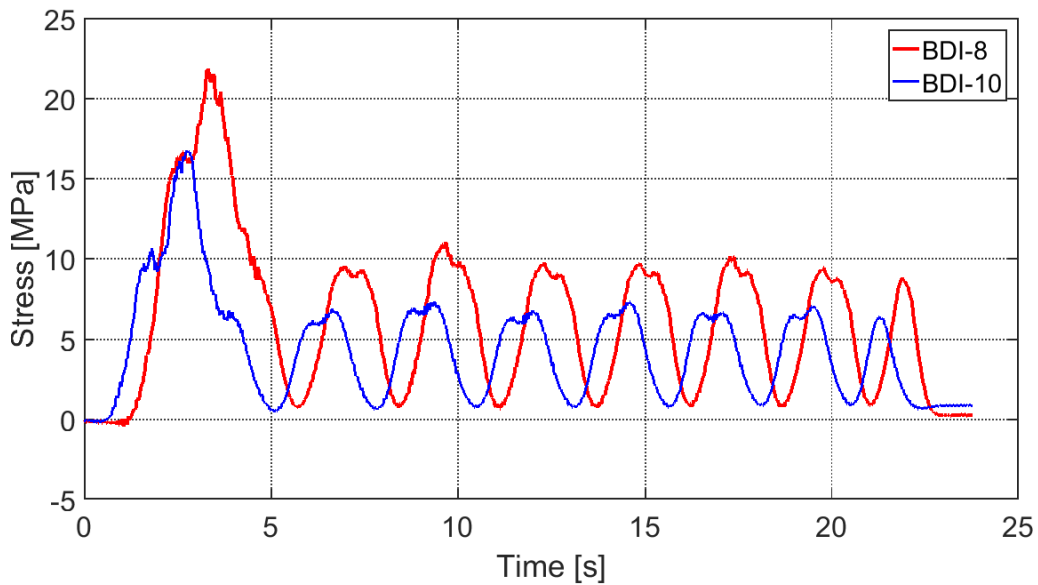
Figure 5.24 Measured stresses by sensor BDI 8 and BDI-10, when train passes over the bridge.
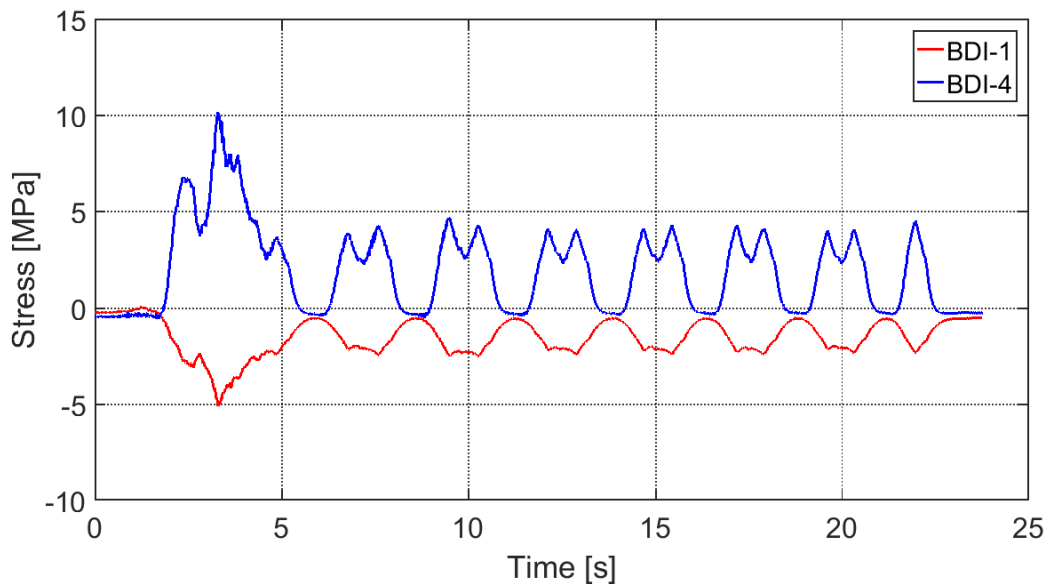
Figure 5.25 Measured stresses by sensor BDI 1 and BDI-4, when train passes over the bridge.

Strain measurements in Figure 5.24 and Figure 5.25 provide indications of the utilisation of the girders in the bridge. The maximum stress from the loading of a steam locomotive in the main girder was 21 MPa and in the cross beam was 10 MPa. As expected, when the train was crossing the bridge, girder G2 experienced a larger stress peak (21 MPa) than G1 (16 MPa). The maximum stress range from the loading of a steam locomotive in the G2 was 22 MPa and in the cross beam was 10.67 MPa, which are both below cut-off limit (28.3 MPa), as proposed by Network Rail (2001).

The deflection of the main beam was relatively small, with the maximum deflection being just over 6 mm as shown in Figure 5.26. The plot also shows that the DMS can measure reliably the dynamic response of the bridge.
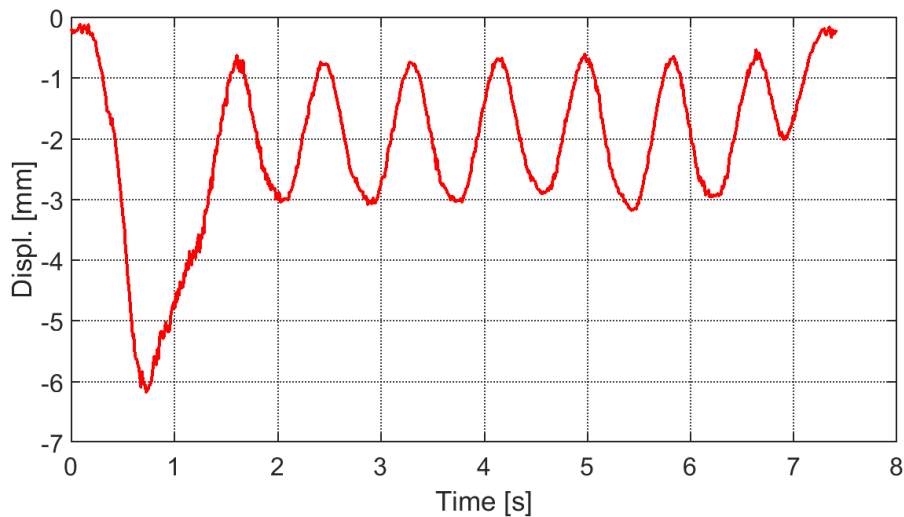
Figure 5.26 Vertical displacement time history of the point B when train passes over the bridge.

5.5　Finite element models of Mineral Line Bridge

Two finite element models – a global FEM and a local FEM, were developed for the stress assessment of the investigated fatigue detail. The global FEM allows the computation of stress/fatigue damage at non-monitored details. The local FEM models the selected connection (local FEM) at a high resolution allowing for estimation of the stress/fatigue damage at the details instrumented with strain sensors.

FE models for the bridge were developed using ANSYS V18.0 software utilizing the Mechanical APDL scripting option (ANSYS, 2018). Available drawings coupled with information obtained following a site survey were used to develop the initial model which was later calibrated using the strains obtained from the monitoring results performed on the bridge (see section 5.4).

181

5.5.1 The global FEM

The main focus during the modelling process was to represent the actual geometry as accurately as possible with careful placement of elements according to drawings, proper quantification of element mass and stiffness, and choice of boundary conditions that represent real conditions. The model consists of 7,128 brick elements and 25,715 shell elements. Figure 5.27 shows the created global FEM model for the Mineral Line Bridge.
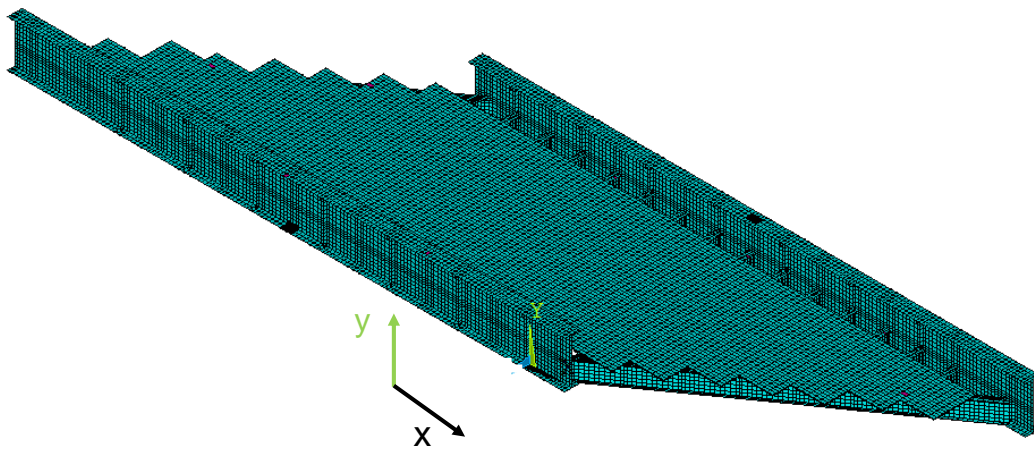
Figure 5.27 Global FEM model of Mineral Line Bridge.

For the purposes of the global FEM analysis, all built-up members are transformed into equivalent I-sections having the same depth and the same second moment of area. All the beams and vertical stiffeners are then modelled using 8-noded shell elements (SHELL181 of ANSYS® library). A Young's modulus of 200 GPa and a Poisson's ratio of 0.3 that correspond to typical UK wrought iron (Moy et al. 2004) are used. The main girders and cross beams are modelled with a relatively fine mesh of shell elements, with maximum dimension of 150 mm in order to facilitate the comparison of the numerical results with the strain gauge measurements captured by the monitoring system.

182

The connections in the real bridge are made up of angle cleats riveted to the webs of the members (cross beams and main girders), as shown in Figure 5.28. Such connections have generally been divided in to three groups, flexible, semi rigid or rigid depending on the degree of restraint they provide (Larsson 2009).
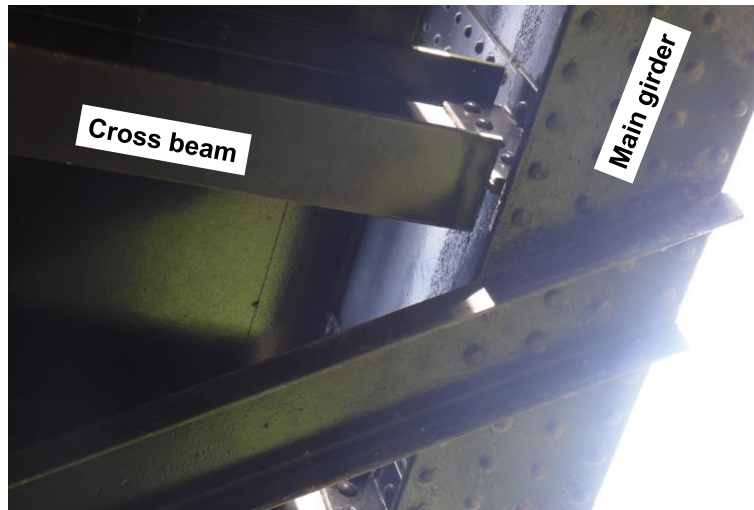
Figure 5.28 Photo for cross beam and main girder connection.

The connections are assumed to be fully fixed in the global FEM. This is achieved by tying all the members together at the locations of the connections (Vičan et al. 2014) and (Imam & Righiniotis 2010) as shown in Figure 5.29. This approximation makes this connection stiffer but is likely to be correct given the large number of heavy rivets in this connection. Furthermore, previous studies have demonstrated that this assumption results in stress histories, which are in better agreement with field measurements in similar bridges (Terrence et al. 1995).
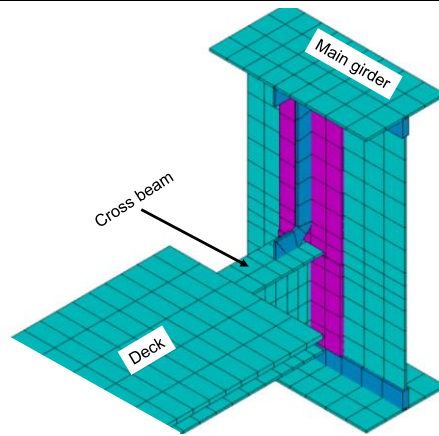
Figure 5.29 Coloured sketch of the connection (using volumes of the regions drawn in ANSYS.

The deck: 8-noded solid brick elements (Solid brick 8 node 185 of ANSYS® library) are used to model deck plates. In the real structure, composite action between deck and cross beam is developed using shear bolts bolted to the top flange of the cross beam. In the model the composite action between the steel deck and the cross beams is modelled by connecting the top flange nodes to the deck nodes by using coupling and constraint equations technique (CupDoF's) in ANSYS (see Figure 5.30). The coupling connection assumes perfect interaction; it neglects any relative movement between adjacent deck surfaces and the elongation of studs due to uplifting force.
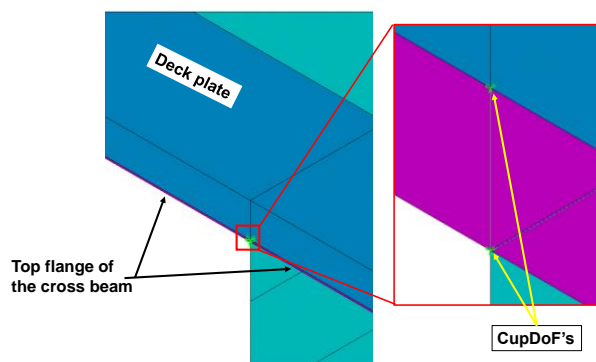
Figure 5.30 Plate deck connected by cross beam using CupDoF's.

The bridge is assumed to be simply supported at the ends of the two main girders. One end of the bridge is assigned a pinned support – rotations about the transverse direction are allowed but all other translations and rotations are restrained. The other end has a roller support – longitudinal translation and rotation about the transverse axis are allowed and all other translations and rotations are restrained.

5.5.2 Global FEM validation

The model is validated by comparing the strains and displacements predicted by the FE model with in situ measurements taken during the passing of a train coach and not a locomotive. The locomotive was not used for the purpose of model validation as the weight of a steam locomotive axle could not be established accurately.

A typical train coach is shown in Figure 5.31. The axle loads and dimensions of the train coach can be estimated from available documentation. Figure 5.32 shows a schematic representation of the load model adopted in performing the numerical simulations. The coach with a total of 8 axles weights weighs approximately 34 tonnes (Auran.com., 2017).This provides an axle load of 42.5 kN. The coach is moved in 150 mm steps over the bridge deck. Axle loads are applied directly on the top surface of bridge deck neglecting the beneficial effect of any load distribution due to the rails and sleepers. The loads are applied quasi-statically and no dynamic amplification is included. 98 load steps are needed in total, starting from the entering of the first axle of the coach onto the bridge to the departure of the last axle from the bridge. The loads are ramped linearly over the steps so that the bridge is never unloaded between steps.

Figure 5.31 A picture of a coach passed during the monitoring event (01/06/2017).
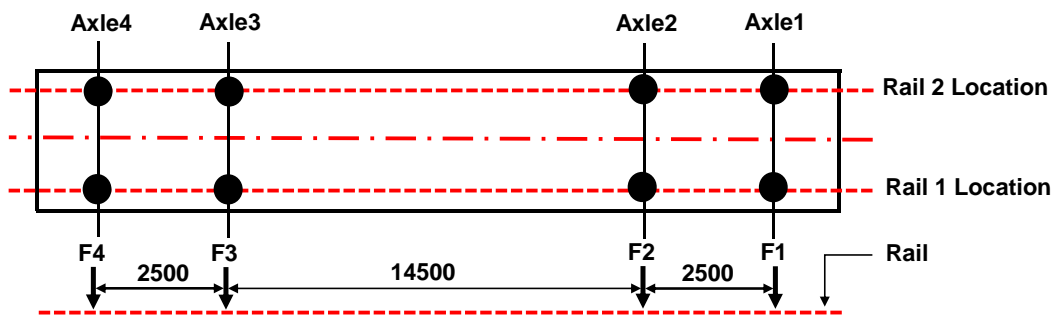
Figure 5.32 Load model adopted for the numerical simulations.

The developed global FEM was calibrated against the results of the monitoring event so that the live load distribution and cross sectional strain profiles matched the monitoring results as closely as possible (to within 5%). This was performed by choosing appropriate boundary condition type and modulus of elasticity. The bridge was considered to be made of wrought iron, a material that was extensively used in the mid- to latter part of the 19th century. The value of Young's modulus for wrought iron can be between 170 and 220 GPa (Moy et al 2004) with 200 GPa being the typical value. The updating process varied iteratively the

modulus of elasticity within this range. Two types of boundary conditions were also tested. A Young's modulus of 200 GPa and simply supported boundary conditions produced the best match with measured strains and displacements. It is however noted that the model is not very sensitive to the Young's modulus and any value within the range of 170 and 220 GPa still produces reasonable results.

Predictions from the FE model for the aforementioned scenario are compared with the stresses obtained from the strain measurements of sensors BDI-4, BDI-7, BDI-8 and BDI-10 for a coach crossing the bridge, as shown in Figure 5.33.
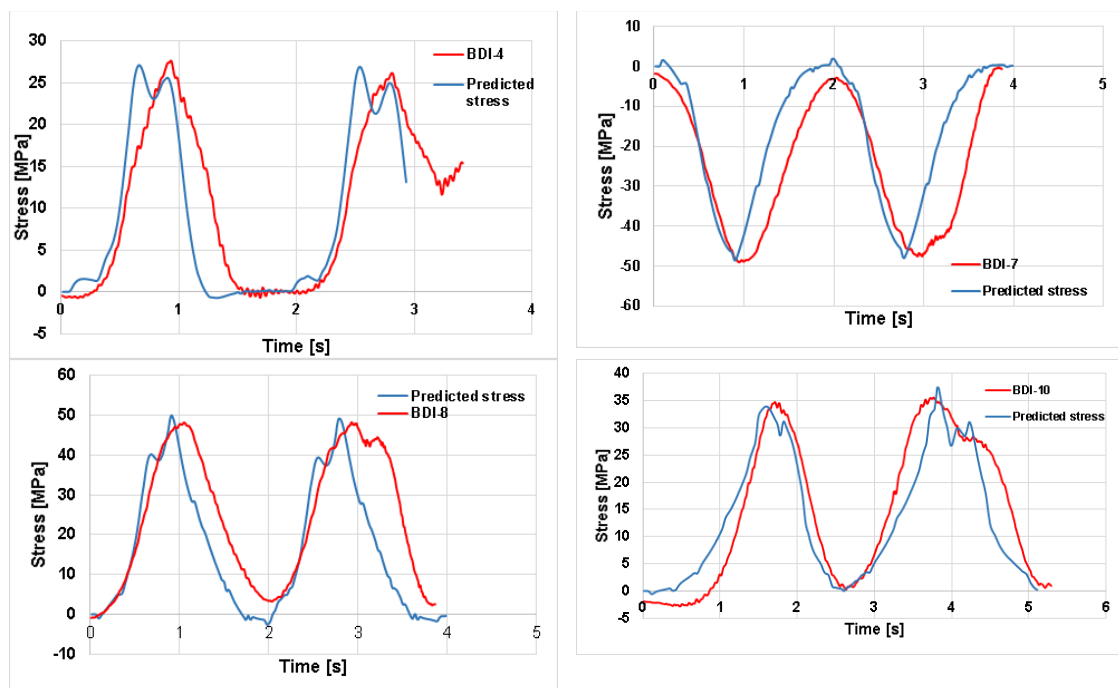
Figure 5.33 Comparison of the time history of stresses measured by sensor BDI 4, BDI-7, BDI-8 and BDI-10 with that of stresses predicted by global FEM.

These results show that the stresses predicted by the FE model are generally in good agreement with the measured stresses with peak errors of 0.9%, 4.4%,

2.5% and 0.3% respectively. This is significant given the following assumptions were made in the modelling.

- The model assumed a constant coach speed while the real speed may have had some variation. This is potentially the reason for the slight but noticeable time lag in the stress histories from the simulation and the measurements, particularly for BDI-4, BDI-7 and BDI-8.

- The axle loads were not measured but were based on literature.

The global FEM model is also validated using the vertical deflection measured at point B on the bridge. The comparison between the measured and predicted deflection under double set axle loads is given in Figure 5.34.
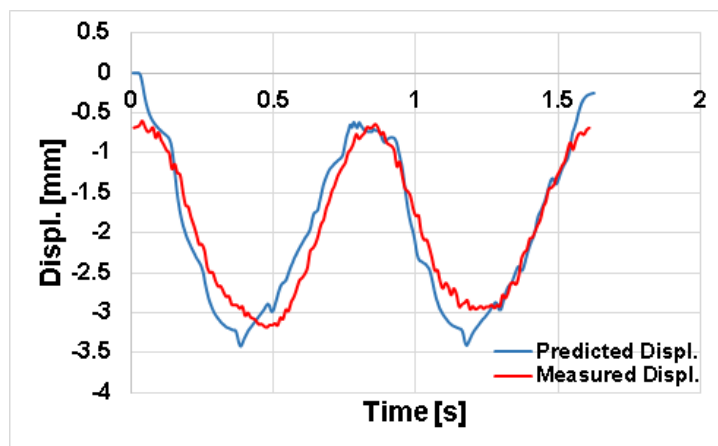
Figure 5.34 Measured deflection in the middle of the bridge compared to FE-prediction.

The predicted maximum deflection at the mid span of the bridge agrees well with the measured values with the prediction having a percentage error less than 7%. The difference can be attributed to a greater flexibility in the global FEM due to the model used for the main girder and cross beam connection.

5.5.3 The local FEM model

A local FEM of a selected riveted detail is created using the finite element software ANSYS®. All the properties of the finite element model are defined in a parametric format, using ANSYS® APDL language (see Figure 5.35). The modelled connection comprises of two 150mm×90mm×12mm angle cleats, each riveted to the cross beam and girder webs using eight 24 mm rivets. The connection components (angles, rivets) and part of the cross beam and the main girder are modelled with brick elements (Solid brick 8 node 185 of ANSYS® library).
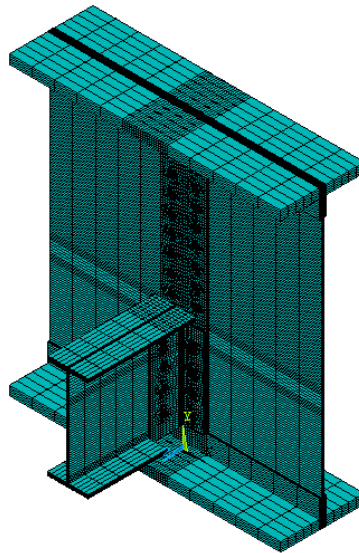
Figure 5.35 Local FEM model for a riveted connection of the Mineral Line Bridge.

A relatively fine mesh is adopted with element size ranging between 10 mm and 100 mm. Multi Point Constraints elements (available in ANSYS) are used to model the riveted connections (contact between rivets with angles and rivets with web plates). Materials are assumed linear elastic and isotropic (Elastic modulus = 200 GPa and Poisson's ratio = 0.3) for main girder plates, cross beam and

angles (Moy et al. 2004). The local FEM mesh consists of 112,320 elements with a total of 508,181 nodes.

The connection is designed to transfer forces from the cross beams, which are developed by trains traveling on the bridge deck, to the main (longitudinal) girders. These forces, which are the key determinant of the stresses at the riveted/bolted connection, are inferred from the monitoring data and applied as loading to the local FEM model.

The boundary condition *BC3* (as defined in Section 4.5.2) is used for the two ends of the main girder in order to transfer the boundary conditions from the global model to the local one.

Load scaling factors (LSF) are computed as described in Section 3.2. These are basically the stress responses at desired locations for unit internal forces, i.e. 1 kNm, 1 kN and 1 kN. Table 5.3 presents magnitudes of LSFs of the main girder-cross beam connection for the *BC3* boundary conditions.

Table 5.3 Computation of load scale factors (LSF) for the main girder-cross beam connection for the considered boundary condition.

Boundary condition type	Load scale factor (LSF)	Stress (SX) at BDI-7 location (MPa)	Stress (SX) at BDI-8 location (MPa)
BC3	$S_{M,i}$	0.067	0.065
	$S_{V,i}$	-1.41	1.875
	$S_{A,i}$	-0.11	0.125

5.5.4 Validation of the Local FEM

This section presents the validation of the local FEM model of the bridge and the predicted stresses using the field measurements. Strain measurements from sensors BDI-1 to BDI-8 are multiplied by the modulus of elasticity (E = 200 GPa) to get the stress response. The calculated stresses from sensors BDI-1 to BDI-4 are converted into time histories of internal forces using the equations described in Section 3.2. All three internal forces are used in conjunction with the local FEM model to determine the stress time history at of the locations of BDI-7 and BDI-8 of the connection. Figure 5.36 and Figure 5.37 present the time history of measured stresses at these locations as computed using strain measurements from sensors BDI-7 and BDI-8. It can be seen that the stresses predicted by the local FEM model are almost the same as the measured stresses with a mean error of only 5% and 1%, respectively over the 25 second period.
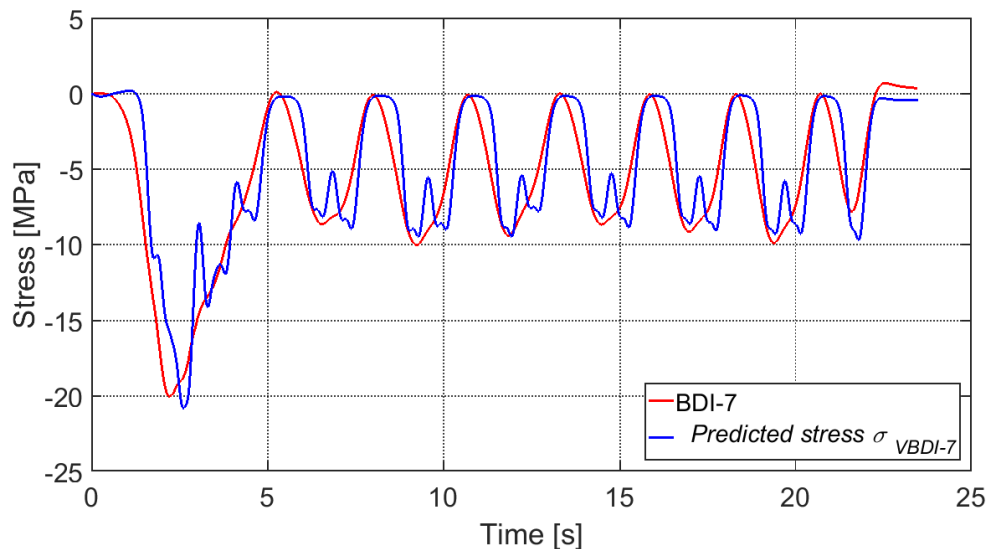
Figure 5.36 Comparison of the time history (25 sec) of stresses measured by sensor BDI-7 with that of stresses predicted by local FEM.
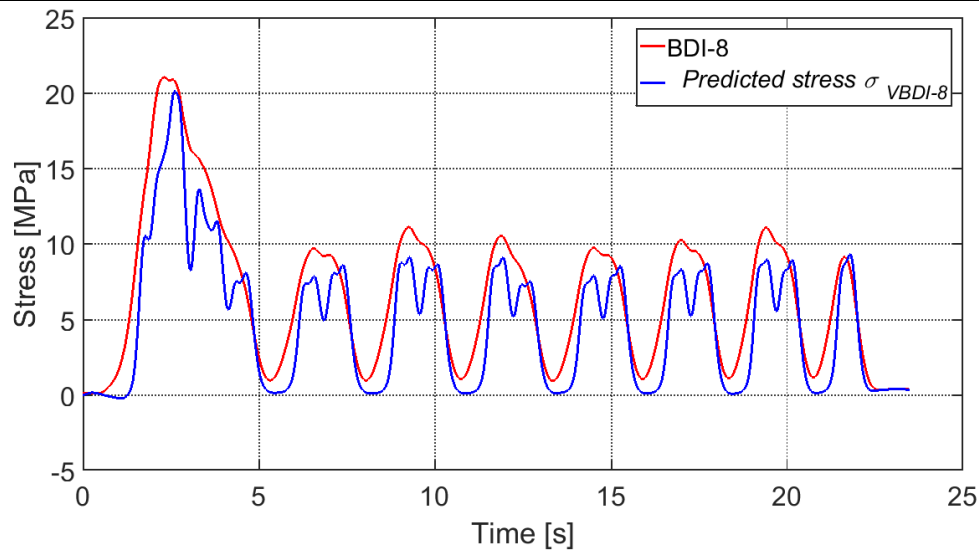
Figure 5.37 Comparison of the time history (25 sec) of stresses measured by sensor BDI 8 with that of stresses predicted by local FEM.

The Mineral Line Bridge being relatively short (17.7 m in length) is subject to relatively more major cycles than larger spans (Sorrenson 2003); the bridge experiences a stress cycle for nearly each axle of the train. Figure 5.36 and Figure 5.37 confirms this observation; bridge experiences a stress cycle for each pair of the seven 4-axle coaches. The figures also show the effect of the relatively long 76mm gage length of the BDI sensor. The measurements don't include the smaller peaks since it tends to take an average of the strains over the full gage length.

The comparison between experimental and numerical results illustrated above provides ample evidence to conclude that the developed FE models for Mineral Line Bridge can be relied on in understanding its structural behaviour.

5.5.5 Stress prediction at uninstrumented locations

As discussed in 5.5.1, for BDI-7 and BDI-8 locations, the results reveal that there is a good agreement between the stresses obtained using the local FEM and its counterpart from the measured strain under real-life loading. In this section, the strain measurements from reference gauges (BDI-1 to BDI-4) are used to predict the stresses at BDI-6, which is located on main girder G2 and is treated as an uninstrumented location. The accuracy of the virtual sensing procedure is proven by comparing the predicted stress time history with the measured response time history as shown in Figure 5.38.
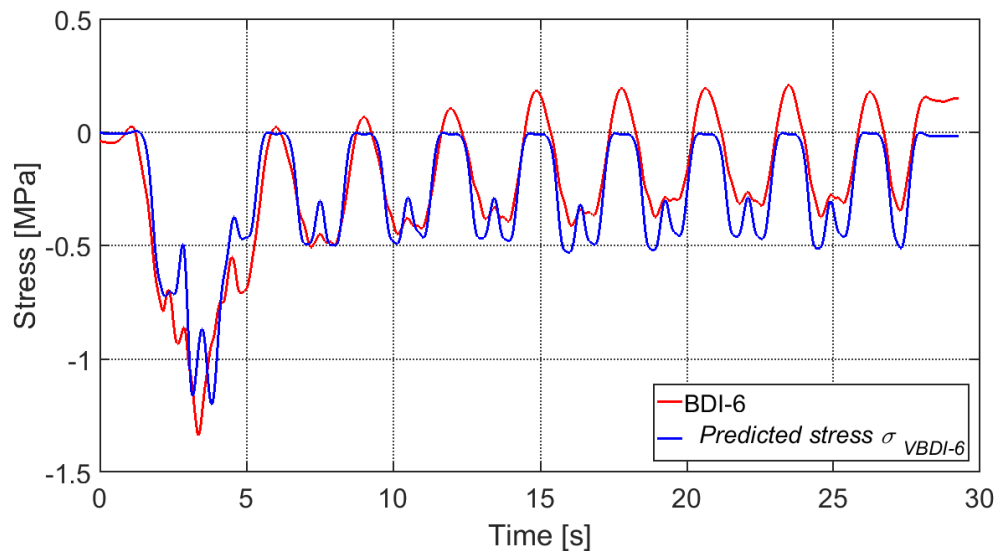
Figure 5.38 Comparison of the time history (25 sec) of stresses measured by sensor BDI 6 with that of stresses predicted by local FEM.

Also, strain measurement from BDI-8 is compared with that predicted using the virtual sensing procedure for a period when a diesel train with one engine and three coaches passes over the bridge as shown in Figure 5.39. The proposed procedure is seen to produce an adequate stress time-history with a mean percentage error of less than 3%.

193
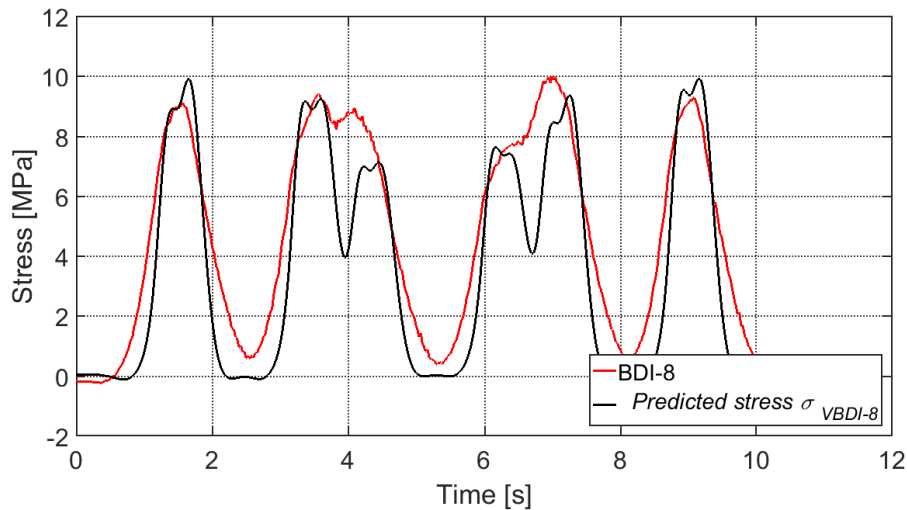
Figure 5.39 Comparison of the time history (12 sec) of stresses measured by sensor BDI 8 with that of stresses predicted by local FEM.

5.6 Williton Up Bridge

The Williton Up Bridge is located on the Minehead-Taunton Railway line. This line is owned and operated by WSR. The bridge links Minehead and Taunton of Williton Station and is located at a distance of 28.65 km from Minehead. The line was opened in 1862 by WSR, closed in early 1971 by the British Rail and again reopened in 1976 by the present WSR. The railway is considered a heritage line and is single-track between subsequent stations but double-track near the respective stations to facilitate passage of the trains in the two opposing directions. The line and by extension the bridge, completed in 2015, is used majorly by passenger steam trains. Figure 5.40 shows the bridge's general location.

Figure 5.40 Location of Williton Up Bridge on satellite map (51°09'55.7"N 3°18'31.8"W).

5.6.1 Structural Components

The bridge is a steel I-girder bridge with no deck. The rails are mounted directly onto the top flange of the two main girders as shown in Figure 5.41. The two girders are I-beam section with 356 mm x 406 mm x 235 kg/m UB (S355). The bridge is a single span with total length of 5.1 m. There are 5 cross beams running between the two main girders and are referred to as CB1. Distance between main girder beams is 1.505 m. Cross beams between the main girders are standard I-beam sections of type 254 mm x 254 mm x 73 kg/m British Universal Columns (S275).

The connections between main girders and cross beams are achieved through end plates welded to their ends. The external sides of the main girders are connected to secondary steel cross beams (I-beam section 203 mm x 203 mm x 46 kg/m British Universal Columns), herein referred to as CB2.

Figure 5.41 Photo of the track -line shown the Williton Up Bridge.

The bridge is considered as a simply supported with lateral restraints in all directions using anchor bolts. Plan and cross-sectional views of the bridge are presented in Figure 5.42 and Figure 5.43.
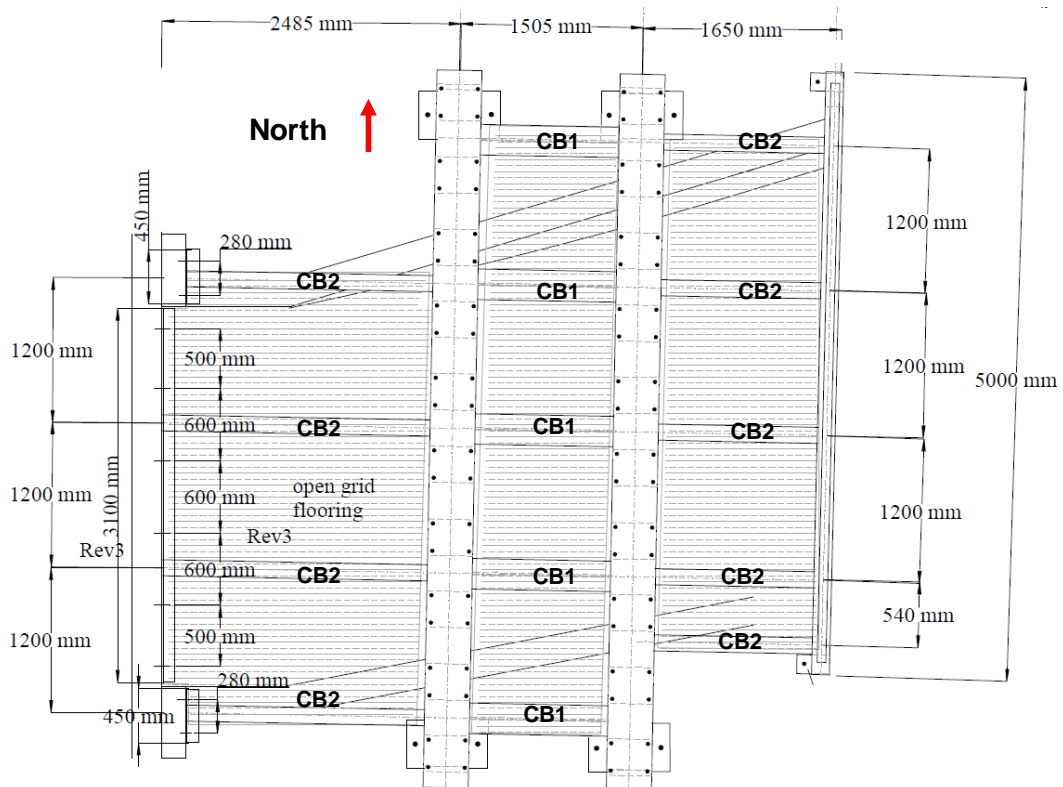
Figure 5.42 Plan view of the Williton Up Bridge.
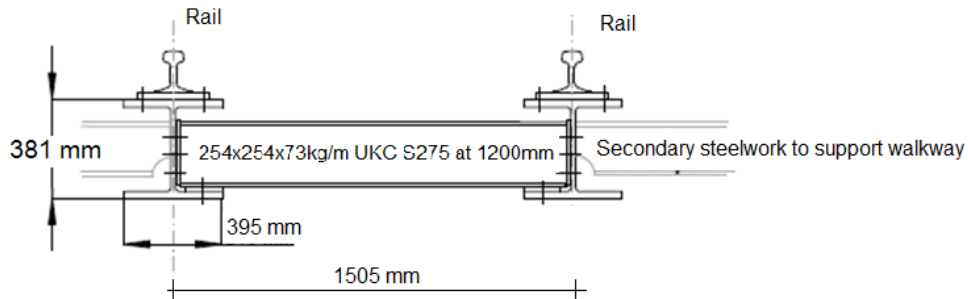
Figure 5.43 Cross sectional view.

The cross beams - CB1, have welded stiffeners at their ends. The stiffeners are connected with webs of the main girders by bolts. A layout of the main girder and CB1 connection is presented in Figure 5.44.
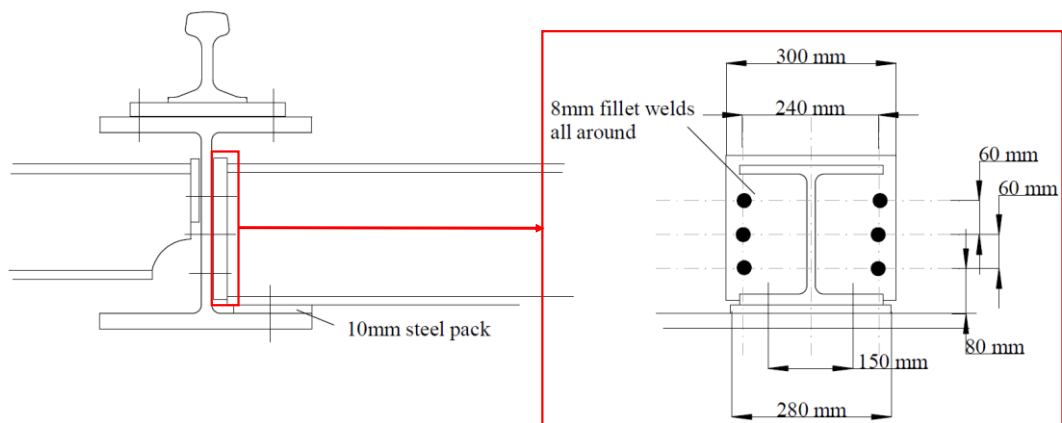
Figure 5.44 Connection of cross beam CB1 with main girder.

5.6.2 Instrumentation equipment and sensors layout

The Williton Up Bridge was instrumented with BDI sensors, shown in Figure 4.22, to capture the bridge strain response to trains crossing the bridge. The fieldwork was done in two phases. Data from the first phase offered evidence that the cross beams acted primarily as bracing, i.e. lateral restraints and was not involved in

transferring the loading to the main girders. This information on the bridge behaviour indicates that the stresses at the cross beam-main girder connection are potentially insignificant and that the bending stresses in the main girder due to applied loading may be more relevant from a fatigue perspective. Consequently, in the second phase, the instrumentation focused on the main girder, and only results from this phase are shown here for brevity.

Instrumentation

A total of ten BDI sensors were installed along the longitudinal main girders of the bridge to monitor the live-load response as shown in Figure 5.45 and Figure 5.46. All of the BDI sensors are applied to the steel at locations as summarised in Table 5.4. Signals from the BDI sensors were transmitted to the data logger using BDI STS4 data acquisition system. Response from all the BDI strain transducers response under moving trains are used to validate the part three of the proposed research methodology (described in Chapter 3).
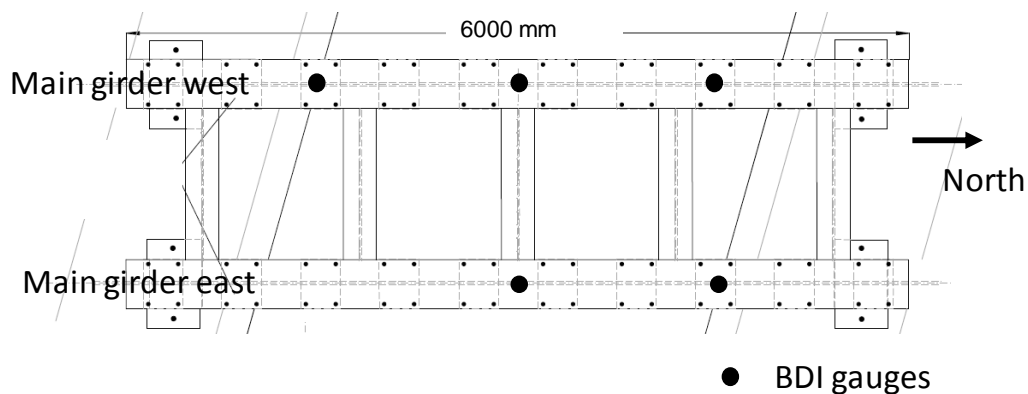
Figure 5.45 Location of BDI strain gauges.

Figure 5.46 Photo showing typical installation of BDI sensors at mid span.

Table 5.4 Summary of the locations of BDI strain gauges installed along the east and west longitudinal main girders.

Sensor Location	Number of Sensors
1/4-span of the east main girder on the top and bottom flanges	BDI-7 & BDI-8
East main girder mid span both on the top and bottom flanges	BDI-9 & BDI-10
1/4-span of the west main girder on the top and bottom flanges	BDI-1 & BDI-2
West main girder mid span both on the top and bottom flanges	BDI-3 & BDI-4
3/4-span of the West main beam on the top and bottom flanges	BDI-5 & BDI-6

5.6.3 Field measurements

In-service monitoring was conducted on the Williton Up Bridge for the purpose of measuring the actual stresses in the bridge due to uncontrolled, real-time traffic. The in-service monitoring event took place on July 13, 2017. This in-service monitoring is described in the next sections along with some key results.

Strain measurements

 As mentioned before strain measurements were collected with BDI strain gauges. Their number and the positions differed between the main beams and the cross beams. The train was passing over the railway bridge with crawling speed of approximately 5 km/h, as shown in Figure 5.47. Strains were recorded at 100 Hz sampling rate during each passing train. Figure 5.48 presents the time history of measured strains distributed along the top and bottom flanges of east girder from sensors BDI-5 to BDI-10.

Figure 5.47 Locomotive passes over the Williton Up Bridge.
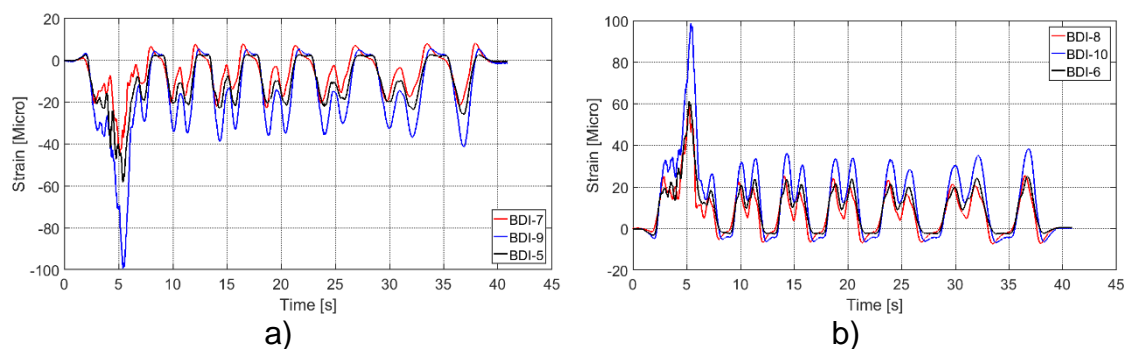
Figure 5.48 Time history of measured strains along: a) top flange and b) bottom flange (1/4L, 1/2L and 3/4L) of east girder as computed using strain measurements.

Figure 5.48, which plots the measurements for the top and bottom flanges of main girder (east girder), indicates that the girder exhibits similar amplitudes of bending stresses at 1/4L and 3/4L, where L is the span length of the bridge. At mid span, whilst the pattern of the time-history is similar, the amplitudes are larger. The flexural stress history measured at the top and bottom flanges at mid span of both longitudinal main girders (east and west girders) are shown in Figure 5.49. The bending stresses measured for the top and bottom flanges exhibit similar amplitudes and are in fact mirror images of each other.
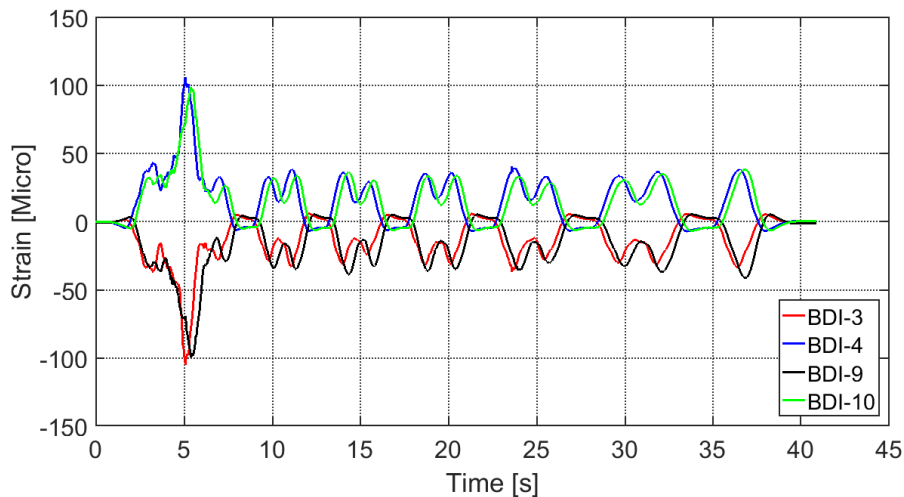
Figure 5.49 Measured strains at top and bottom of both east and west girders.

5.6.4 Stress predictions at uninstrumented locations

In Williton Up Bridge, the primary stresses responsible for load-induced fatigue cracking are of interest for fatigue damage assessment. This section aims to demonstrate that the virtual sensing procedure can be used to estimate such stresses at any desired location (possibly along the top/bottom flanges of a main girder) in a short-span steel bridge using data collected from one instrumented connection.

The virtual sensing procedure is illustrated by predicting the nominal stress time history at the locations of BDI-4, BDI-6 and BDI-8 during the passing of a steam train. The process is as follows. First, strain measurements from sensor BDI-10 are used to extract the stress time-history of the nominal longitudinal bending stress at mid span of the bridge (bottom flange) as shown in Figure 5.50.
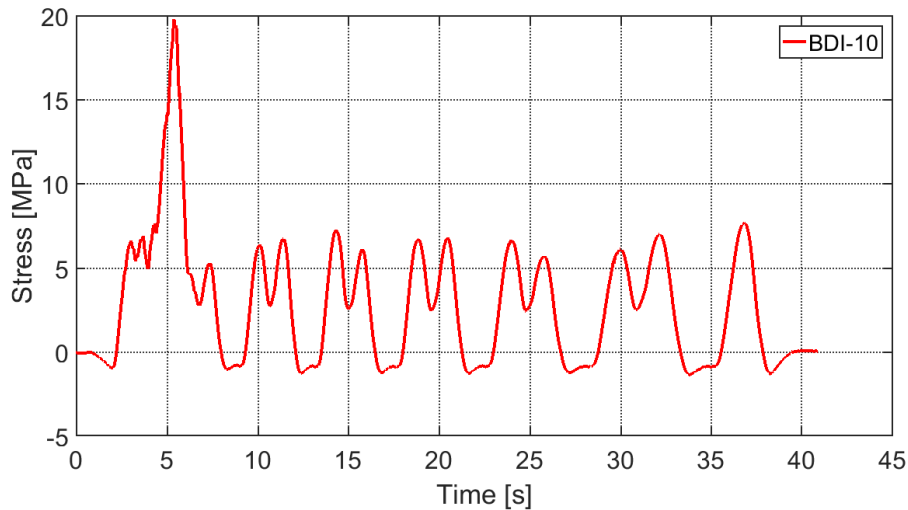
Figure 5.50 The time-history of bending stress at mid span of the bridge during the passing of a train.

Second, strain measurements from sensors BDI-4, BDI-6 and BDI-8 are used to derive the measured nominal stress time histories (σ_{nomi}) at their respective locations. Finally, the ratio (R_{nom}) between the peaks on the influence line of the nominal stress at BDI-10 and the nominal stresses at BDI-8, BDI-4 and BDI-6 are established according to Equation 3.5 and the results are presented in Table 5.5. Here a global FEM is not used as the strain measurements themselves provide for evaluating the R_{nom} values.

Then, nominal stress time histories at the locations of the BDI gauges (σ_{Vnom}) (virtual sensing location) are extracted by multiplying the stress time-history at BDI-10 by the respective R_{inom} as per Equation 3.7. Figure 5.51 displays the

comparison between the measured stresses from sensors BDI-8, BDI-4 and

BDI-6 and the predicted stress at the same locations computed using the virtual

sensing procedure.

Table 5.5 R_{inom} computed between the reference location and sensing locations on the bridge under a steam train load

Sensor number	Peak nominal longitudinal stress at reference location (MPa)	Peak nominal longitudinal stress at sensing locations (MPa)	(R_{nom}) %
BDI-10	20.1		
BDI-8		12.1	0.602
BDI-4		21.7	1.078
BDI-6		12.6	0.627
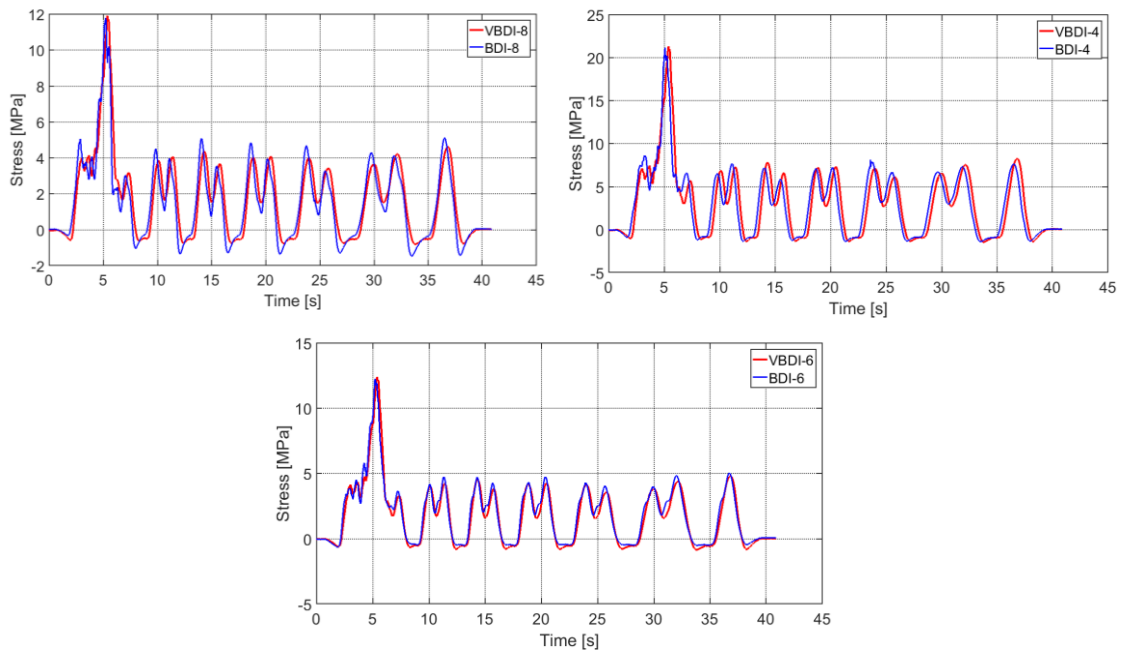
Figure 5.51 Comparison of the time history of stresses measured by BDI-8, BDI-4 and BDI-6 sensors with that of stresses predicted by proposed virtual sensing procedure.

Figure 5.51 shows that the proposed virtual sensing procedure based on the ratio of peaks generated by the strain measurements can predict stress responses accurately. The R_{inom} presented in Table 5.5 are also used for evaluating the stress response of the bridge when loaded by a different train. Figure 5.52 shows the measured and predicted stress response at 1/4L, 1/2L and 3/4L of east girder.
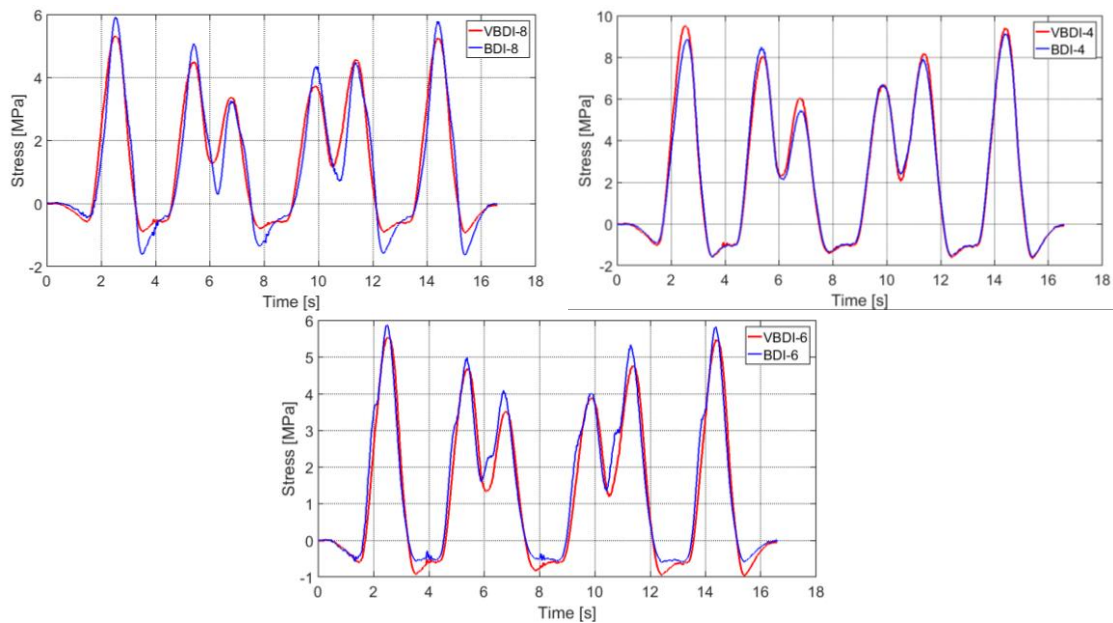
Figure 5.52 Measured and computed time histories of stresses at 1/4L, 1/2L and 3/4L of east girder considering one train run.

Some measured stress peaks are not captured exactly (Figure 5.52). This is potentially due to the R_{inom} being derived from the stress time-histories obtained for one train run. A better approach may be to obtain R_{inom} values for a number of different loading scenarios and then take an average. Figure 5.53 shows the results obtained following such an approach and the difference from Figure 5.52 is visually evident.
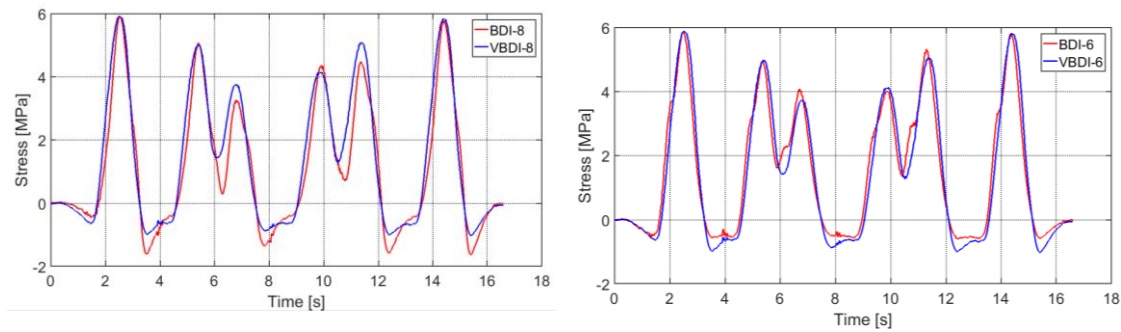
Figure 5.53 Measured and predicted bridge response at 1/4L and 3/4L based on the calibrated peak relation considering different runs.

5.7   Conclusions

Data from two steel railway bridges (Mineral Line Bridge and Williton Up Bridge) are used to validate the methodology proposed in chapter 3. Results support the following conclusions on the research methodology.

- The strains predicted by the local FEM of the connection using internal forces computed from measured strains are within 3% of the field measured strains. This demonstrates that the real stresses at fatigue critical details can be evaluated using the proposed methodology.

- Results show that the local FEM can capture the stress cycles due to each axle of a train, a factor of significant importance for stress range counting.

- Results show that the proposed methodology can be used to predict stress histories at uninstrumented locations from strain measurements taken at only a few locations on a bridge.

205

- The agreement between measured and predicted bridge responses for the Williton up Bridge demonstrates that the presented virtual sensing procedure is effective at finding the stress peak ratio directly from strain measurements.

- When deriving the stress peak ratio from a calibrated global FEM, there is a need to average all the peak ratio over a number of load scenarios to adjust for any loading related variations.

CHAPTER 6   Assessment of fatigue damage and retrofit

6.1   Introduction

In this chapter, the fatigue damage calculations for the connections in the Bascule Bridge that were discussed in chapter 4 are presented. It also presents a retrofit measure for the critical connection in the bridge. A numerical assessment of the retrofit is carried out through sub-models of the critical connection, considering conventional local approaches such as the hot-spot stress method and the notch stress method. A novelty of this research is the calibration of the sub-model using measurements from the full-scale structure that in this case were collected for a moving truck load. Fatigue life of the retrofitted connection is evaluated considering roadway traffic according to current European standards EN 1993-1-9 2005.

6.2   Fatigue damage based on field measurement

This section demonstrates that the proposed procedure for fatigue stress evaluation can become part of a fatigue damage assessment method. The instrumented fatigue detail of Bascule Bridge (see Chapter 4) is employed for that purpose.

6.2.1 Identification of fatigue detail category

Table B.1 of Eurocode 3 (EN 1993-1-9 2005) gives the detail categories to be considered for the application of the hot spot stress method to cracks initiating

from toes of fillet welded attachments. Figure 6. shows the S-N curve for the fatigue detail category 100 (FAT 100) listed in Table B.1. This category includes non load-carrying fillet welds such as those of the instrumented connection in the Bascule Bridge.
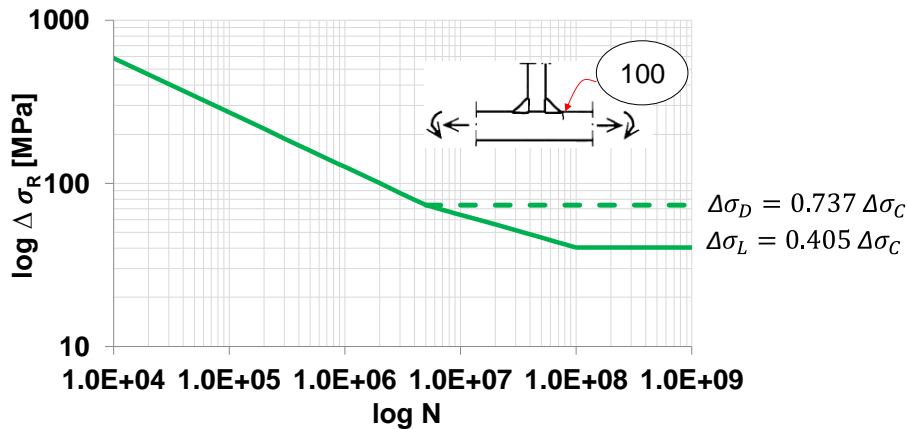
Figure 6.1 SN characteristic curve Detail 100 ($\Delta\sigma_c$ = 100 MPa).

The threshold stress range, which is the stress range above which fatigue damage is introduced, is 29.9 MPa for detail category FAT 100 according to Equation 2.4. The measured stress ranges for the instrumented connection are between 2.6 MPa and 78 MPa (Table 6.1), and the maximum measured stress range exceeds the threshold stress range. Therefore, the longitudinal girder must be considered to have a finite fatigue life.

The calculated fatigue damage at uninstrumented connection (critical connection) at the east longitudinal girder of the Bascule Bridge is described in Section 6.2.3.

6.2.2 Fatigue damage calculation

As described in section 4.6.1, strain measurements from sensors SG-5 and SG-9, collected during the in-service monitoring sessions on July 12, 2016 and August

12, 2016, are used to derive the virtual hot spot stress time-history (σ_{Vhs}) at the weld toe. Figure 6.2 shows the time-history of hot spot stresses for the entire 6-hour duration on August 12, 2016.
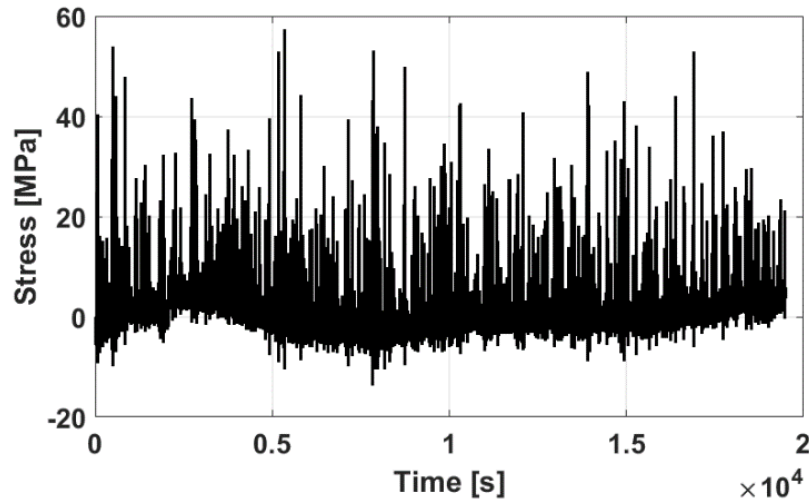
Figure 6.2 Hot spot stress time history (6 h)

The strain measurements are corrected for an offset error using Equation 6.1 (Leander 2008).

$$\sigma = E\left(\varepsilon_g - \varepsilon_{g0}\right) \tag{6.1}$$

where E is the Young's modulus of the material (steel), ε_g is the measured strain and ε_{g0} is a factor for baseline correction.

Hot spot stress cycles are then counted using the Rainflow counting algorithm (ASTM E1049 - 85 2005). A sample of the Rainflow results for each of the monitoring days are presented in Table 6.1. The number of stress cycles within each of the stress ranges considered is given in the table. Each stress range is presented in terms of its median stress. The first bin records any cycles between 0 and 4 MPa, the second bin records any cycles between 4 and 8 MPa, and so on. Only those stress cycles whose range exceed the measurement noise

209

threshold, which is 6 microstrain (or 1.2 MPa) in this case, are included. Consequently, the first bin or stress range spans between 1.2 MPa and 4 MPa. The rightmost column in Table 6.1contains the total number of cycles during the total time of in-service monitoring (i.e. 13hrs over two days).

Table 6.1 Rainflow totals for the two in-service monitoring sessions.

	Number of cycles above noise threshold		**Two-Day**
Date:	12/07/2016	12/08/2016	**Total**
Bin Median (MPa):			n_i
2.6	9311	11998	21309
6	2911	1630	4541
10	1228	189	1417
14	306	46	352
18	106	78	184
22	71	80	151
26	41	37	78
30	36	28	64
34	28	21	49
38	31	16	47
42	23	6	29
46	32	6.5	38.5
50	40	5.5	45.5
54	31	2	33
58	23	2.5	25.5
62	17	4	21
66	11	0	11
70	3	1.5	4.5
74	10	0	10
78	5	0	5
Total Number of Cycles			**28415**

Figure 6.3 shows the stress range histograms for the two monitoring sessions as obtained after using the Rainflow algorithm.
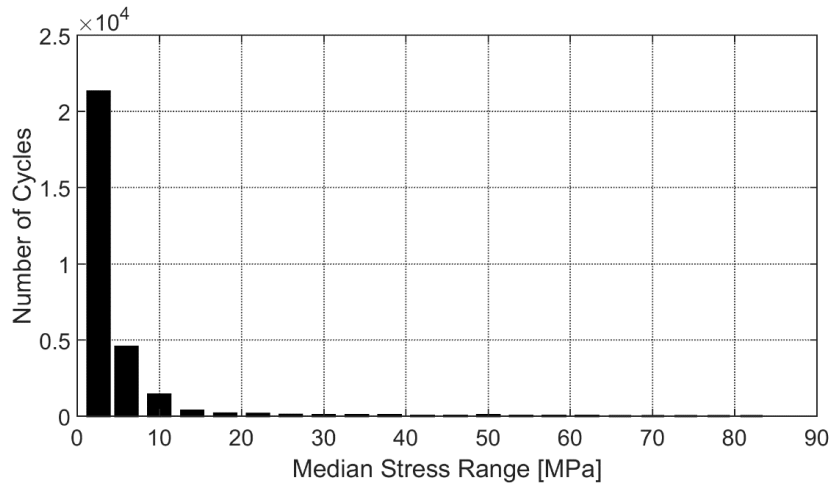
Figure 6.3 Histogram of measured data - 13 total hours 8am to 3 pm July 12, 2016 and 10am to 4pm August 12, 2016

The consolidated data over two days from Table 6.1 is used for evaluating fatigue damage and is replicated for this purpose in Table 6.2. The total number of cycles to failure is calculated using the stress range, the values given in Eurocode 3 (EN 1993-1-9 2005) for the detail category and Equations 6.5 and 6.6. The fatigue life within a specific stress range, N_R, is calculated using Miner's linear damage accumulation model (Miner M 1945) as expressed in Equation 6.2.

$$D = \frac{n_1}{N_1} + \frac{n_2}{N_2} + \frac{n_3}{N_3}... = \sum_{n=1}^{k} \frac{n_i}{N_R} \leq 1.0 \qquad (6.2)$$

The following example demonstrates the principles of damage accumulation: Detail category 100 (described in section 6.2.1) has constant amplitude stress range $\Delta\sigma_C$=100 MPa for an endurance $N = 2\times10^6$ cycles. The constant amplitude fatigue limit (CAFL) $\Delta\sigma_D$ and the cut-off limit $\Delta\sigma_L$ for this category can be calculated using Equation 6.3 and Equation 6.4.

$$\Delta\sigma_D = \left(\frac{2}{5}\right)^{1/3} \Delta\sigma_c = 0.737\Delta\sigma_c \qquad (6.3)$$

211

$\Delta\sigma_D$= 0.737*100= 73.7 MPa

$$\Delta\sigma_L = \left(\frac{5}{100}\right)^{1/5} \Delta\sigma_D = 0.549\Delta\sigma_D \tag{6.4}$$

$\Delta\sigma_L$= 0.549*73.7= 40.46 MPa

For the mentioned type of detail, the fatigue resistance (N_R), which is the estimated number of stress cycles to failure, is computed by comparing the first and last stress ranges $\Delta\sigma_R$ of the nominal stress spectra in Table 6.2 with $\Delta\sigma_D$. If $\Delta\sigma_R > \Delta\sigma_D$, then N_R can be described by Equation 6.5.

$$N_R.(\Delta\sigma_R)^m = 2x10^6 .(\Delta\sigma_c)^m \quad \text{, with} \quad m = 3 \text{ for} \quad N \leq 5x10^6 \tag{6.5}$$

$$N_R.(78)^3 = 2x10^6 .(100)^3$$

N_R =4214501 cycles

If $\Delta\sigma_R > \Delta\sigma_L$ but $\Delta\sigma_R < \Delta\sigma_D$, then N_R can be described by Equation 6.6.

$$N_R.(\Delta\sigma_R)^m = 5x10^6 .(\Delta\sigma_D)^m \quad \text{, with} \quad m = 5 \text{ for} \quad 5 \times 10^6 \leq N \leq 10^8 \tag{6.6}$$

$$N_R.(42)^5 = 5x10^6 .(73.7)^5$$

N_R =83188059 cycles

The cumulative fatigue damage is then evaluated using N_i and $\boldsymbol{n_i}$ (from the histogram). Table 6.2 contains the damage ratios obtained for each stress range and also the cumulative fatigue damage - 1.316×10^{-5}, for the considered monitoring period.

Table 6.2 Cumulative fatigue damage (D) evaluated over a two days (13 h period).

$\Delta \sigma_{ri}$ [MPa]	n_i	N_{Ri}	$D = \dfrac{n_i}{N_{Ri}}$
42	29	8.32E+07	3.4861E-07
46	38.5	5.28E+07	7.2936E-07
50	45.5	3.48E+07	1.3078E-06
54	33	2.37E+07	1.3937E-06
58	25.5	1.66E+07	1.5395E-06
62	21	1.19E+07	1.7696E-06
66	11	8.68E+06	1.2671E-06
70	4.5	6.47E+06	6.9566E-07
74	10	4.90E+06	2.0410E-06
78	5	4.21E+06	1.1864E-06
Total Cumulative fatigue damage			1.23E-5

6.2.3 Fatigue damage for uninstrumented connection

As explained in section 4.3.1, the fatigue-critical detail of the Bascule Bridge was not instrumented due to access issues. The fatigue damage at this detail is evaluated from the time-history of hot spot stress obtained using the virtual sensing procedure (discussed in section 5.6.2). Following a similar procedure as outlined in the previous section, the critical detail is observed to experience a cumulative fatigue damage of $1.95{\times}10^{-5}$ during the monitoring period.

Based on the field measurements, the maximum range of hot spot stress – 78 MPa (Table 6.1), exceeds the CAFL at the instrumented location. Therefore, the longitudinal girder of the bridge must be considered to have a finite fatigue life and the remaining fatigue life of the bridge have to be estimated. As the bridge has been monitored only for a short duration (13hrs in total), the author acknowledges that the derived stress histogram is not sufficient to evaluate the remaining fatigue life of the bridge (R. J. . Connor & Fisher 2006); this requires

data from a much longer monitoring duration (at least a week with 24hrs per day). However, the goal here is only to illustrate that the proposed fatigue stress evaluation method can support an approach for fatigue damage assessment, and the measured data is sufficient for this purpose.

6.3   Fatigue damage based on design load

As discussed in the previous section, measurements from long-term monitoring are not available for the Bascule Bridge. Therefore this study uses the standard traffic loads from Eurocode 3 (EN 1993-1-9 2005) as given in the UK National Annex (BS NA EN 1991-2 2003) to estimate the remaining fatigue life of the connection, which will then enable proposing interventions.

The linear damage accumulation method, described in Chapter 2, is used to analyse the critical detail. The application of the damage accumulation method in the context of steel roadway bridges involves the following steps as suggested by (Nussbaumer et al. 2011).

1. Define the traffic scenarios (vehicle types, annual traffic volume) for consideration;

2. Calculate the stress time-histories in critical structural details that include dynamic effects by using the nominal stress, the structural hot spot or the effective notch stress approach.

3. Compute the stress histograms, i.e. the number of cycles versus the stress ranges, by using a cycle counting algorithm such as the Rainflow algorithm (ASTM E1049 - 85 2005).

4. Adopt suitable S-N curves to describe the fatigue resistance of the detail. Curves proposed by the Eurocode 3 (EN 1993-1-9 2005) are used in this work. Moreover, as stated in the UK National Annex (BS NA EN 1993-1-9 2005), the fatigue strength reduction factor, γ_{Mf}, is taken as 1.35 since the eventual failure of the bridge can have significant consequences in terms of loss of human's lives and economic resources.

5. Compute the fatigue damage by using a linear damage accumulation model as proposed by Miner (Miner M 1945) using Equations 2.4 and 2.5. Fatigue failure is reached when the cumulative damage $D = 1$ according to the original Miner's rule (EN 1993-1-9 2005). However, according to Niemi et al. (Niemi et al. 2006), many tests have shown that failure may occur at a computed damage $D_d = 0.5$. The fatigue life calculated by assuming fatigue failure for a cumulative damage $D_d = 0.5$ is likely to be a lower bound estimate (Gurney 2006). This work however uses this assumption for safety purposes.

6.3.1 Definition of the traffic scenario

The fatigue load model that is adopted consists of sets of idealized standard trucks, which are typical of the traffic in UK. There are 23 typical types of truck. The axle load and the axle span are listed in Table 6.3. According to the UK NA to BS EN 1991-2, the fatigue damage can be assumed to have arisen from 80%

of the number of observed heavy vehicles N_{obs} crossing the bridge as single vehicles and 20% of N_{obs} considered as all trucks passing one after the other with distance between the last axle of a vehicle and the front axle of the next vehicle being 40m.

Table 6.3 Set of equivalent lorries for Fatigue Load Model 4 (FLM4) according to UK National Annex to BS EN 1991-2-3 (BS NA EN 1991-2 2003).

	Vehicle number	Average Spacing (m)	Loading Group	Total Weight kN	Axle Loads kN
Girder trailer and 2 tractors	23 (18GH)	1.5 4.5 4 1.5 [No.5] 13.5 1.5 [No.5] 4 1.5 4.5	H	3680	80 160 160 240(6no.) 240(6no.) 80 160 160
	22 (18GM)		M	1520	80 160 160 60(6no.) 6(6no.) 80 160 160
Girder trailer and tractor	21 (9GH)	4.5 1.5 4.0 1.5 [No.5]	H	1610	70 140 140 210 210 210 210 210 210
	20 (9GM)		M	750	50 110 110 80 80 80 80 80 80
Girder trailer and 2 tractors	19 (7GH)	4.5 1.5 4.0 2.0 10.0 2.0	H	1310	70 140 140 240 240 240 240
	18 (7GM)		M	680	60 130 130 90 90 90 90
Articulated	17 (7AH)	3.0 1.5 9.5 1.5 1.5 1.5	H	790	70 100 100 130 130 130 130
Articulated	16 (5AH2)	3.0 1.5 9.5 1.5	H2	630	70 130 130 150 150
Articulated	15 (5AH)	3.5 5.5 1.5 1.5	H	380	70 100 70 70 70
	14 (5AM)		M	300	50 70 60 60 60
	13 (5AL)		L	190	40 60 30 30 30
Articulated	12 (4AH)	3.0 6.5 1.5	H	240	40 80 60 60
	11 (4AH)		M	175	40 55 40 40
	10 (4AH)		L	145	35 50 30 30
Rigid	9 (4RH)	1.5 3.5 1.5	H	280	50 50 90 90
	8 (4RM)		M	240	40 40 80 80
	7 (4RL)		L	120	20 20 40 40
Rigid	6 (3RH)	4.0 1.5	H	240	60 90 90
	5 (3RM)		M	195	45 75 75
	4 (3RL)		L	120	60 45 45
Rigid	3 (2RH)	4.0	H	135	50 85
	2 (2RM)		M	65	30 35
	1 (2RL)		L	30	15 15

However Baptista (2016) asserted that for influence lines shorter than 40 m, the effect of the flow conditions is not important. This is because the span length is in the range of the vehicle length (plus a minimum distance between lorries) so that each vehicle produces only one load cycle on the bridge, regardless of the flow conditions. Therefore, in this study, 100% of N_{obs} is treated as single vehicles to ensure evaluated damage is realistic. Baptista (2016) also observed that the traffic density assumed in the development of the Eurocode fatigue load models is high and conservative and close to the maximum motorway capacity. In this study, therefore no traffic growth tendency is included. Instead only a traffic density of 2×10^6 lorries/year (8000 lorries/day) is assumed.

6.3.2 Calculation of the stress history

Stress histories of concerned details are generated based on two types of S-N curve methods: nominal stress method and hot spot stress method.

Nominal stress method

According to Eurocode 3 (EN 1993-1-9 2005), the fatigue assessment for the investigated detail (i.e. transverse attachment) should use the nominal stress assessed in the longitudinal direction to the weld toe. Therefore, longitudinal nominal stresses are evaluated for all the bridge connections (i.e. 34 transverse attachments). The location with the highest stress was the fillet weld that attaches the vertical stiffener to the web of the east main girder at mid span. This detail falls within the FAT80 class in Eurocode 3 (EN 1993-1-9 2005) and the resistance curve for load-induced fatigue cracking for this class is as shown in Figure 6.4. As discussed in section 6.3.1, the bridge model was loaded in both lanes with the

FLM4 using 23 lorries. The annual frequency of the vehicles was assumed to be constant for the period between 1973 (the year of opening) to 2018. This assumption is conservative as the loading has increased gradually over time. Figure 6.5 illustrates the stress histories of the investigated detail for the passage of the 10 heaviest standard fatigue lorries.
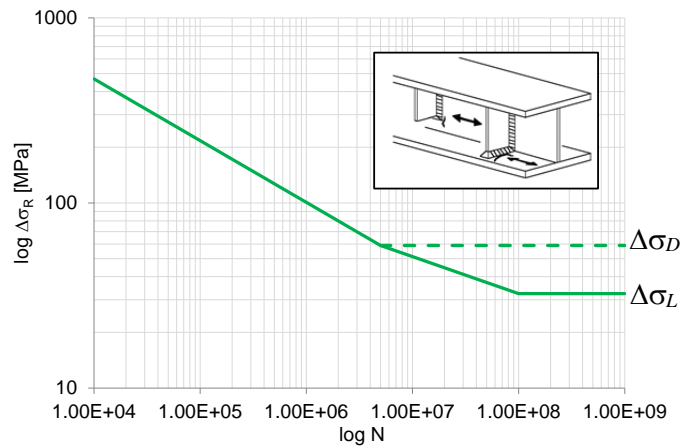
Figure 6.4 S-N characteristic curve Detail 80 ($\Delta\sigma_c = 80$ MPa).
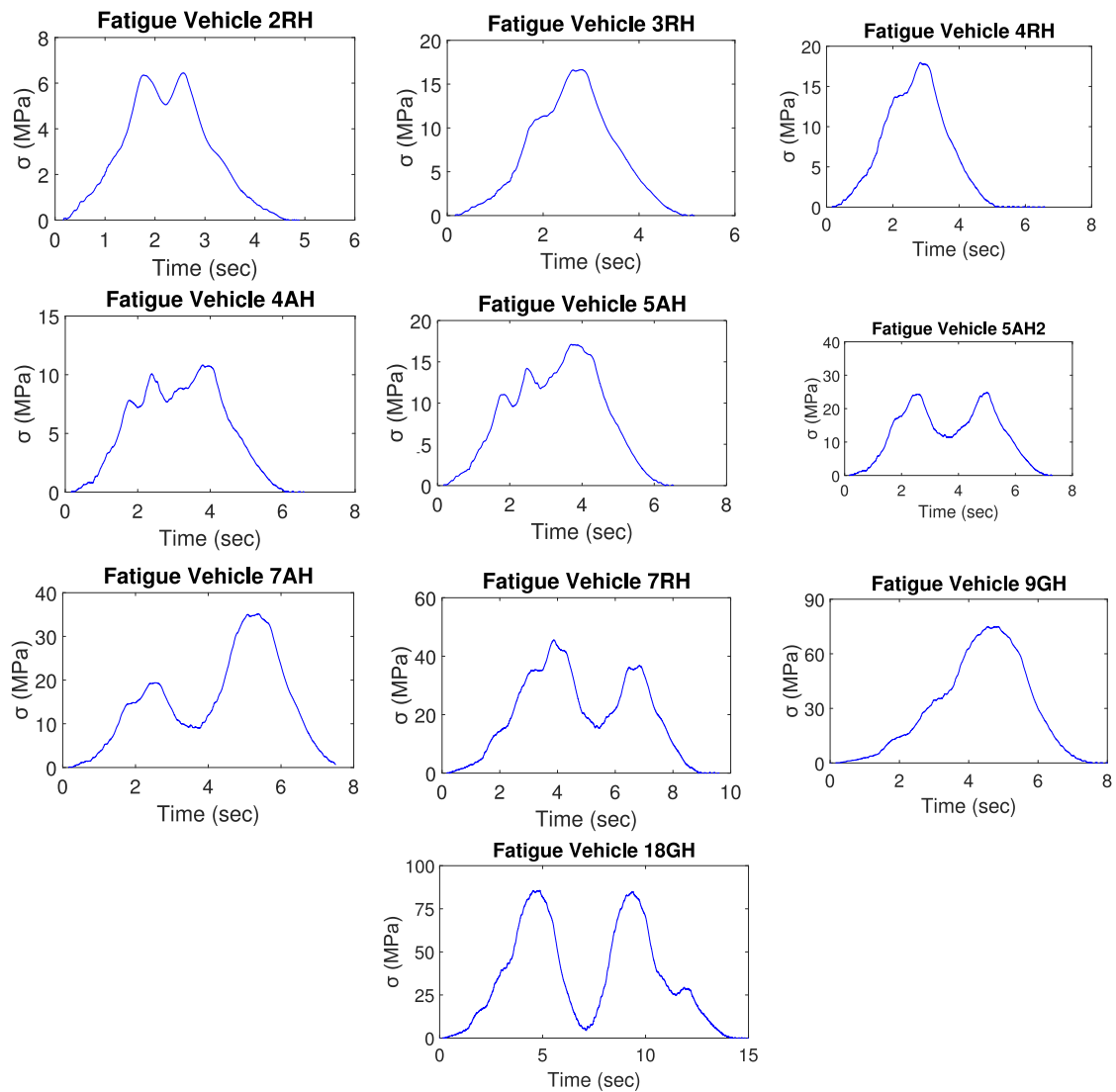
Figure 6.5 Stress histories for the investigated detail for standard fatigue vehicles.

ANSYS and MATLAB (MATLAB 2017) are employed for the dynamic analyses that are performed using the dynamic superposition method (Clough & Penzien 1995) considering the fatigue vehicles to have a crowd speed of 17 km/h. A sensitivity analysis showed that varying the speed between 10 and 120 km/h did not worsen the dynamic effects in the output stress time histories just as it did not affect the process of calibration of the FE model. Therefore, a conventional static influence line approach based only on transient static analyses is used to perform

the remaining fatigue life assessment using all three methods - nominal stress method, hot-spot stress method and notch stress method.

Results show that the bridge deformation response is dominated by axle loads and that the stresses vary between 6.5 and 86 MPa (Figure 6.5). The vehicle causing the most damage is vehicle 15 (see Figure 6.5- Fatigue Vehicle 5AH) described in Table 6.3. This vehicle does not result in the highest stress, but when factoring in the traffic frequency, it results in the highest fatigue damage ratio. Fatigue damaging stress cycles in the investigated detail are counted using the Rainflow algorithm (ASTM E1049 - 85 2005).

Hot spot stress method

 According to IIW (2016), for the kind of detail (i.e. weld toe in web gap region), the fatigue assessment should be based on normal stresses assessed in the direction perpendicular to the weld toe. The location of the highest hot spot stress is on the outside surface of the web gap region of the bridge main girder. This position is on the east main girder at 970 mm distance from the bridge support. Figure 6.6 shows the location of the concerned detail.
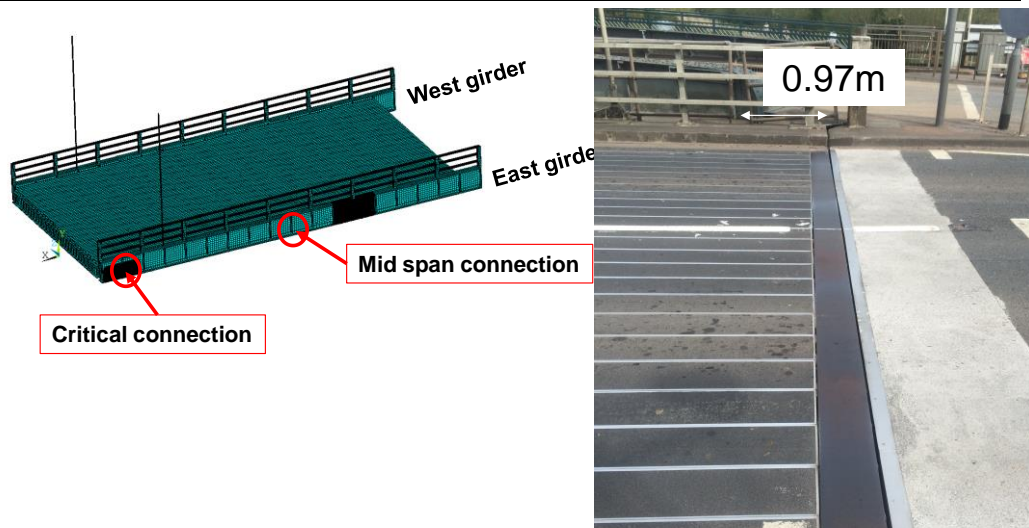
Figure 6.6 Position of the considered fatigue connections.

The dynamic amplification factor $\Delta\varphi_{fat}$ at the mentioned location is calculated according to Equation 6.7 and Figure 6.7.

$$\Delta\varphi_{fat} = 1.30\left(1 - \frac{d}{26}\right); \quad \Delta\varphi_{fat} \geq 1 \tag{6.7}$$

where: d is the distance (m) of the cross-section under consideration from the expansion joint.
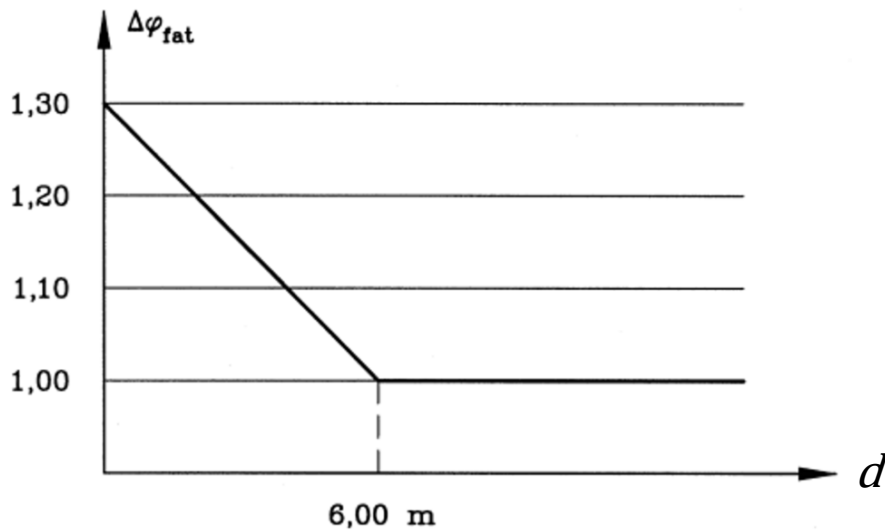
Figure 6.7 Representation of the additional amplification factor.

Table 6.4 gives the computed dynamic amplification factors. These show that the cross beams closer to the support have a higher dynamic amplification factor than the intermediary crossbeams.

Table 6.4 Computed dynamic amplification factors.

The distance between cross beam and the expansion joint (Dis) (m)	Dynamic amplification factor ($\Delta\varphi_{fat}$)
0.97	1.25
8.64	1

The global FEM is used to derive the influence lines for the forces transmitted from the cross-beam to the main beam for each of the intermediary cross beams and the end cross beams. Figure 6.8 shows the calculated reaction influence line of cross beams (CBs) as assessed at the 17 connections of the east girder.
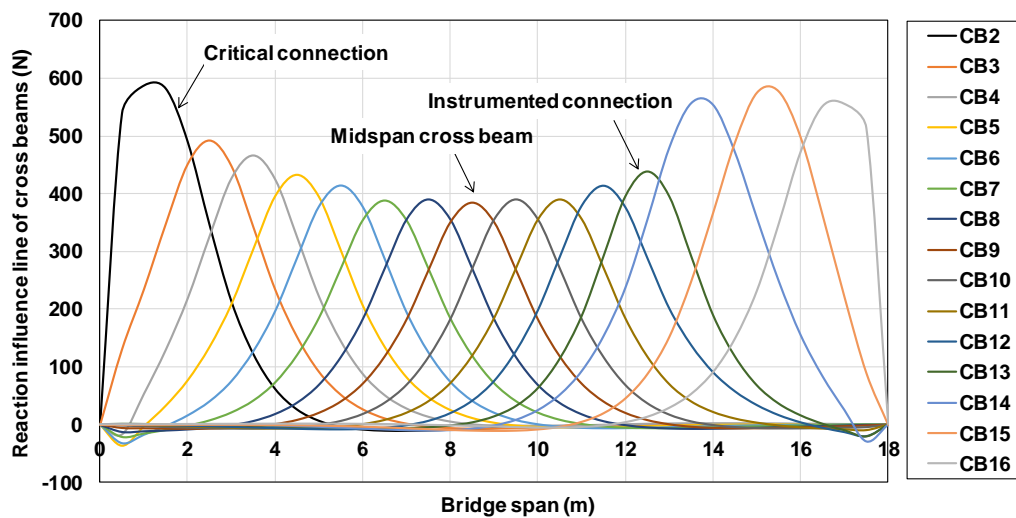
Figure 6.8 Comparison between reaction forces.

Figure 6.8 shows that connection CB2 has the highest reaction (600 N) among the connections. Therefore, it is taken as the most critical location with respect to fatigue life.

As indicated in the previous section, fatigue damage assessment requires a S-N curve for the studied connection. In Eurocode 3 (EN 1993-1-9 2005), the fatigue strength of a hot spot stress range is represented by two curves for typical weld detail categories. Figure 6. shows the S-N curve provided in Table B.1 of Eurocode 3 (EN 1993-1-9 2005) for the detail category FAT100, which covers connections such as non-load-carrying fillet welds in the Bascule Bridge.

6.3.3 Stress influence line approach

As referred to in Chapter 4, herein a static influence line approach is used to derive the stress time histories for the all standard traffic events for fatigue assessment. This acceptable given the low dynamic effects observed due to low vehicle speeds. The calibrated global FE model of the bridge is used to extract a reference stress influence line for the concerned details. The bridge model is loaded in both lanes with the Fatigue Load Model 4 (FLM4) as shown in Table 6.3. These lanes are the two notional lanes that individually cause the most theoretical fatigue damage in the component under consideration.

Following the FLM4 in UK NA to BS EN 1991-2-3, the scenario of a single axle in contact with the bridge deck is considered. The axle force is assumed to be 2 kN so that the wheel load of both tires is 1 kN. There are 121 loading steps in total. The axle moves by a distance of 0.15 m between each consecutive loading step. The wheel load is moved along the centre of the bridge deck. The stress influence line of the detail is derived for this scenario first. The relevant analysis is performed in ANSYS. The derived influence line is then scaled suitably to derive the stress response to any of the truck loads in Table 6.3. This essentially saves computational resources by eliminating the need for a large number of numerical

simulations. The scaling and load combination is done using a MATLAB routine that uses the stress influence line from ANSYS to extract stress influence lines for each fatigue standard truck. This routine is also used in Chapter 4 for the test truck in order to obtain the calibrated response with the experimental measurements.

6.3.4 FE Sub-models

Stresses at the weld toe and weld root for the studied connection are computed using the sub-modelling technique because a fine mesh is required around the critical points to capture the maximum elastic stress. Displacements from the coarsely meshed global model are transferred to the finely meshed local sub-model. Two sub-models are created: a local sub-model for hot spot stress and one for effective notch stress.

Sub-model for hot spot stress

A local sub model of the web gap region is created. Solid elements with quadratic shape functions (i.e. 20-noded SOLID186 element in ANSYS) are used to model this region following the rules indicated in IIW (Hobbacher 2016), as shown in Figure 6.9. To take into account the local stiffness at the critical points of the sub-model, the fillet welds are fully modelled. Structural imperfections or misalignments are not considered since all stress concentrations corresponding to them are already included in the hot spot stress determination.

As can be seen in Figure 6.9, the sub-model of the investigated detail has more nodes and elements than the global FE model of the bridge. By having a fine mesh for only the region around the critical location, the sub-modelling technique

reduces computation costs and yet obtains reliable estimations of the stress gradient at the weld toe.
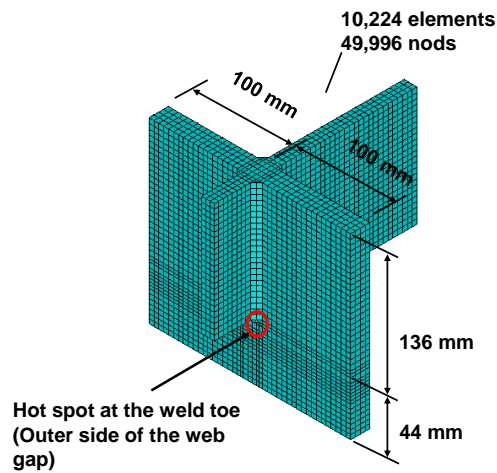
Figure 6.9 Web gap detail in the local sub-model (solid elements).

The nodes of the sub-model that are expected to be in connection with other structural elements of the structure are subject to the deformations caused by the global model as shown in Figure 6.10.
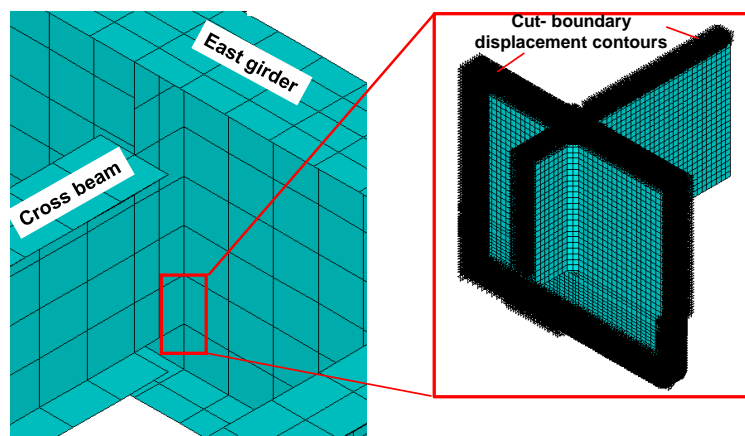
Figure 6.10 Boundary conditions of the local sub model.

The girder's strains at the web gap region location were recorded during the load tests conducted as part of the field measurement campaign (as shown previously

in Figure 4.20). These measurements support validation of the generated local sub-model. The local sub-model is calibrated at the reference point that is at a distance of 20 mm from the weld toe (Figure 6.11(a)) since it experiences less stress concentration effects than the reference point at a distance of 8 mm from the weld toe. Figure 6.11 (b) shows the time history of predicted stress ($\sigma_{20\ mm}$) at the reference location. The figure also presents the time history of measured stresses using strain measurements from sensor SG-12. There is good agreement between results from the numerical analysis and the measurements.

a)   b)
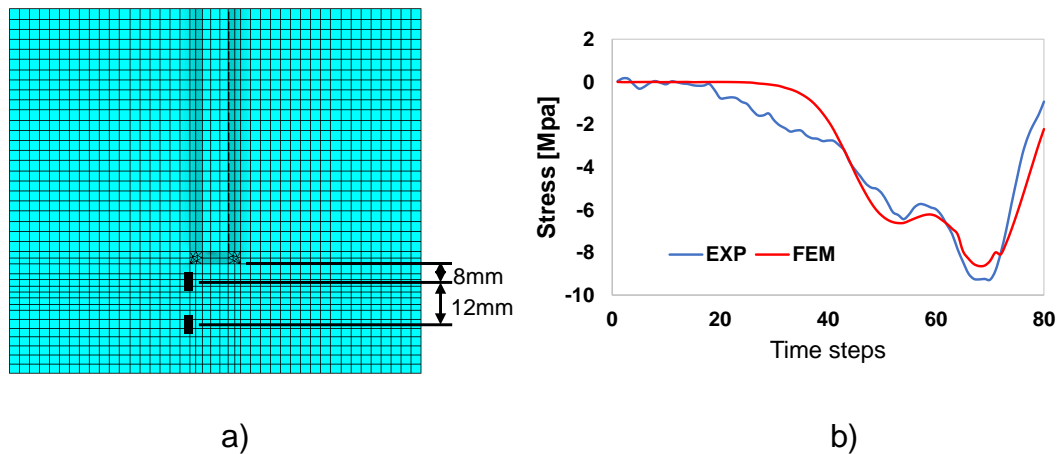
Figure 6.11 a) The FEM reference locations-point-8 mm and point-20 mm, and b) The time history of computed and measured stresses using strain measurements from sensor SG-12.

As discussed in section 6.3.1, the global FEM is used for simulating the structural behaviour of the critical connection. The global FEM is loaded using 23 equivalent Lorries for FLM4 according to BS NA EN 1991-2-3 (2003). Time histories at location VSG-14 and VSG-15, discussed in section 5.6.2, are used in Equation 3.7 to predict hot spot stresses at weld toe of the web gap region. Figure 6.12 illustrates the hot spot stress histories of the investigated detail of the bridge for the passage of the 10 heaviest standard fatigue lorries.
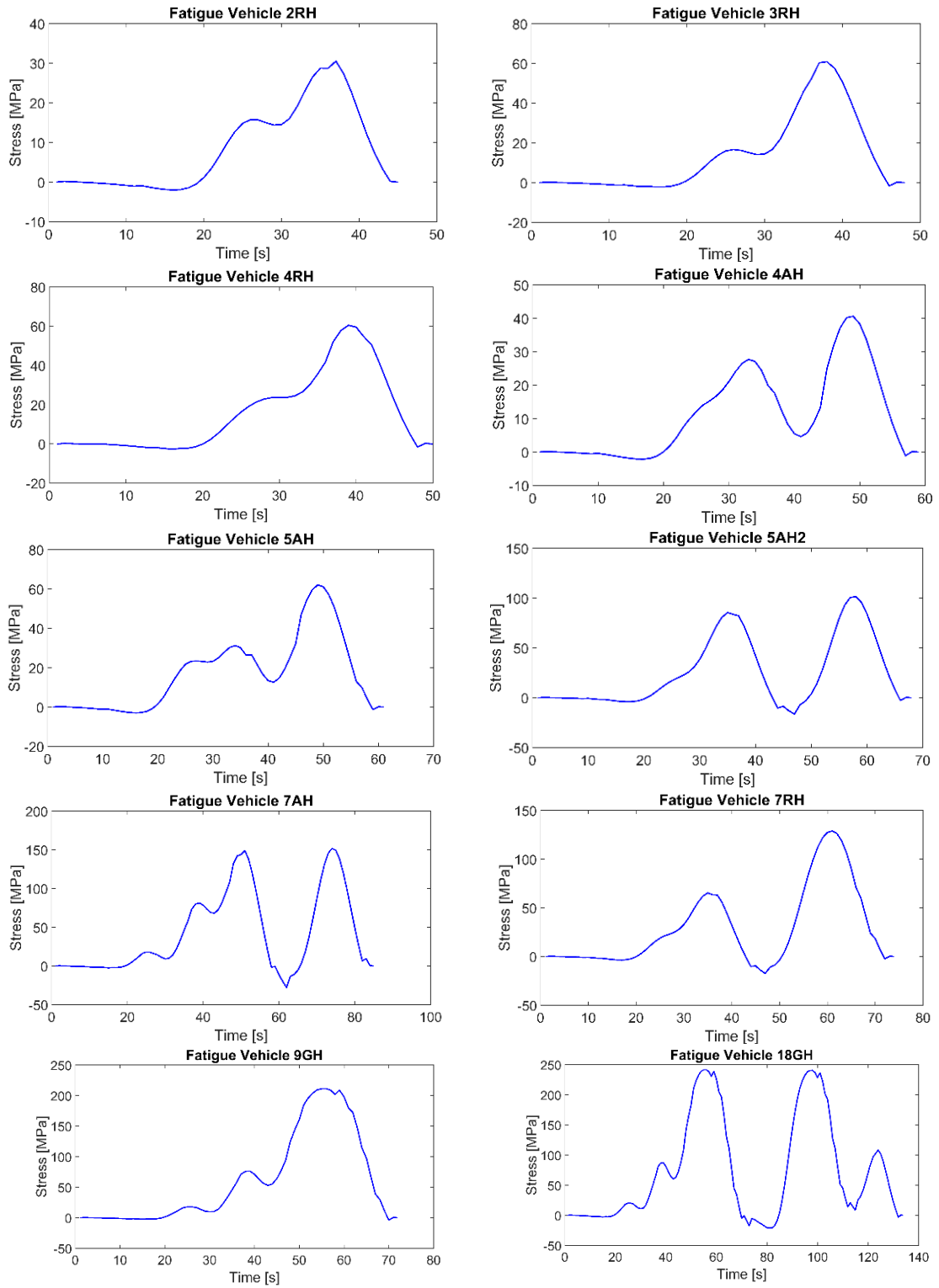
Figure 6.12 Hot spot stress histories in the investigated connection, due to FLM4.

Local sub model for effective notch stress method

A second local sub model is developed using the calibrated sub-model described in section 6.3.4 to evaluate the effective notch stresses at the weld toe and the root of the web gap region. Solid elements with quadratic shape functions (20-noded SOLID186 element) are used to model this sub model following the rules indicated in IIW (Hobbacher 2016). The weld toe and the weld root are rounded off with a fictitious radius q_{ref} = 1 mm according to Radaj and Neuber (Radaj et al. 2006). Figure 6.13 shows the developed local sub model and its mesh in the regions around the weld toe and the weld root. Boundary conditions of the sub model are similar to the local sub model for hot spot stress method.
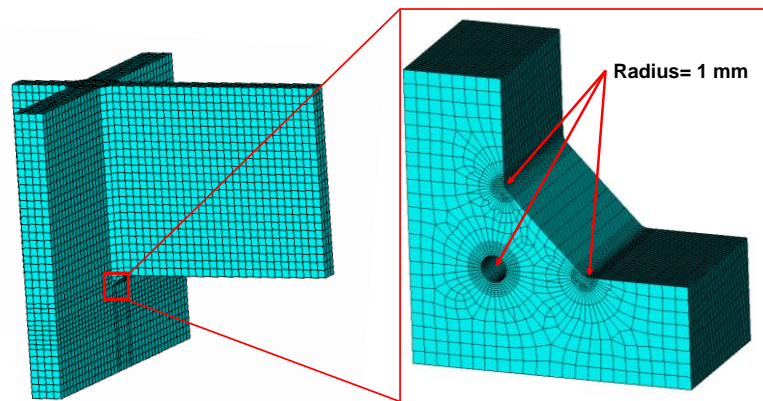
Figure 6.13 Fictitious notch at weld toe and the weld root.

6.3.5 Fatigue damage calculation

Fatigue damage based on Nominal stress method: Total damage D_d is obtained by adding contributions from the traffic on the two lanes as given in

$$D_d = D_1 + D_2 \tag{6.8}$$

D_1, D_2 are the damage from the 1st and 2nd traffic lanes respectively. The effect of vehicles travelling side-by-side is allowed as recommended in UK NA to BS EN 1991-2-3 (BS NA EN 1991-2 2003). This is computed using

$$D_d = K_b \cdot Z$$ (6.9)

K_b is the ratio of the maximum stress range caused by single vehicles in lane 2 to the maximum stress range caused by single vehicles in Lane 1, and Z varies linearly with the logarithm of the loaded length from 1.0 to 1.5 for loaded lengths between 3.0 m and 20.0 m. K_b and Z are calculated as 1 and 1.448, respectively. Figure 6.14 shows the total damage corresponding to each individual fatigue vehicle type considered in this study. The total annual damage for all vehicles is 1.214×10^{-4}, considering 1 million vehicles per year per lane.
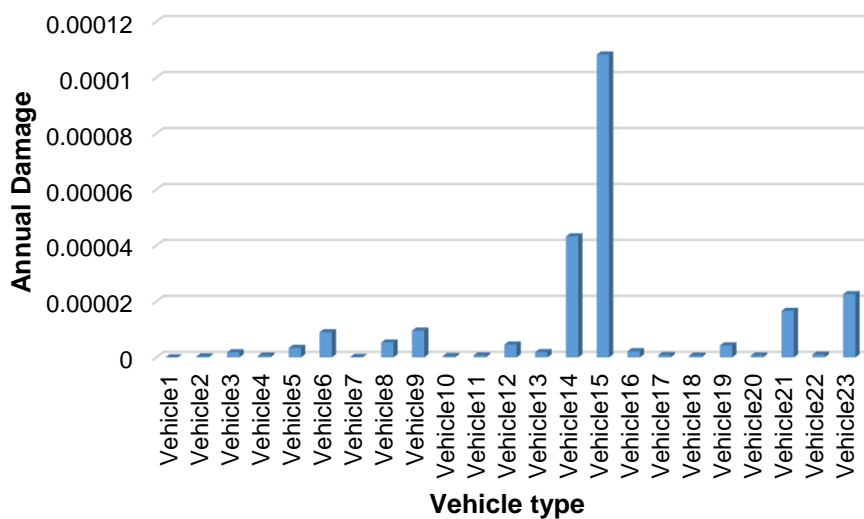
Figure 6.14 Fatigue damage in the critical detail, due to standard fatigue vehicles.

Finally, the total damage for the critical connection for a 46-year period is 5.6×10^{-3}. The remaining fatigue life, in years, for the total annual damage for all vehicles was calculated as presented in Table 6.5.

Table 6.5 Remaining fatigue life of the bridge.

Total Damage year	Bridge's life (years)	Total fatigue damage	Remaining fatigue life (years) considering $D_d = 0.5$
$1.22×10^{-3}$	46	0.056	410

Fatigue damage based on hot spot stress method: Total damage, D_d, is obtained by adding contributions from the Lane 1 and Lane 2 traffic as given in Equation 6.1. This damage was based on N_{obs} = 2.1 million vehicles. The effect of vehicles travelling side-by-side is allowed as recommended in NA to BS EN 1991-2-3 (BS NA EN 1991-2 2003) and given by Equation 6.8. The calculated values of K_b and Z corresponding to the critical connection were 0.45 and 1.448, respectively.

The total annual damage for all vehicles per year for fast and slow lanes were $6×10^{-3}$ and $1.94×10^{-4}$, respectively. The total annual damage for all vehicles per year was $8.36×10^{-3}$. Given this, the remaining fatigue life, in years, of the bridge is less than 14 years (Table 6.6).

Table 6.6 Remaining fatigue life of the bridge.

Total Damage year	Bridge's life (years)	Total fatigue damage	Remaining fatigue life (years) considering $D_d = 0.5$
$8.36×10^{-3}$	46	0.38	13.8

6.4   Preventive retrofit measure

Field measurement of strains in the cross beam-main girder connection was performed in August 2016 under normal traffic. Based on the stress range histograms measured over a 13 hours period, the hot spot stress ranges are determined at the instrumented location.

- The measured stress range is 78 MPa, which exceeds the CAFL of 74 MPa (i.e. the limiting stress range for infinite safe life of FAT 100 class fatigue details). Consequently, the remaining fatigue life of the instrumented connection is expected to be finite.

- The proposed procedure for evaluating hot spot stress is appropriate for distortion-induced fatigue, and can be used by transportation officials to determine the fatigue life.

- Based on the assessment of fatigue performance for the investigated connection, it is observed that the nominal stress method is not able to perform reliable fatigue life estimations.

A numerical fatigue evaluation of the critical detail using the standard procedure in the NA to BS EN 1991-2-3 shows that it has insufficient remaining fatigue life for their continuing service. Hot spot stress and nominal stress time histories at considered locations are calculated by means of finite element analysis. The corresponding fatigue lives are determined numerically.

- The remaining fatigue life of the bridge at mid span connection is determined according to the nominal stress method to be finite with more than 400 years.

- The remaining fatigue life of the bridge at the critical connection is determined to be finite with less than 14 years for of N_{OBS} = 1.5 million vehicles. These findings emphasize the importance of treating distortion-induced fatigue in localized regions in a bridge rather than focusing on the global structure.

231

It is worthwhile noting that in this study, the fatigue damage assessment for this bridge is limited to only the aforementioned detail (i.e. the fillet weld connecting the vertical stiffener to the web of the main girder of the bridge). However, the fatigue life estimation can be extended to other transverse stiffeners too since they are very similar to the instrumented connection.

The previous discussion shows that the Bascule Bridge has a limited fatigue life for the investigated connections. This is due to out-of-plane bending at the connections between the transverse element (i.e. cross beam) and the main longitudinal girder. To avoid damage, fracture or failure caused by fatigue, preventive maintenance on this connection is necessary.

Many repair and retrofit methods exist to extend fatigue life of steel bridges that are at risk to failure due to distortional fatigue damage. Each repair method has its advantages and limitations. One class of retrofit methods eliminate secondary stresses in web gap regions by removal of cross beam (Hassel 2011). Bascule Bridge being a ladder bridge, this is not advisable since cross beams are needed to transfer vertical loads from the bridge deck to the main girders. A second retrofit option is to stiffen the web gap by attaching a connection plate to the girder flange. This has been shown to be a good solution to reduce the stresses in the web gap region (Ghahremani 2015). However, bolting or welding an attachment to the girder flange usually requires the removal of the deck and the closure of the bridge to traffic during the repair. Softening techniques such as cut back of a portion of the transverse stiffener plate offer another retrofit option and have been attracting more attention as low-cost and reliable means to extend the fatigue lives of steel bridges. The primary mechanism by which these techniques achieve

life extension is through lengthening the web gap to enhance the connection's

flexibility which serves to reduce stress concentration.

According to AASHTO (AASHTO 2012), the minimum web gap length to resist

shear buckling of the web is $4t_w$ (where t_w, is thickness of the web girder plate)

and the maximum is $6t_w$. For the aforementioned detail described in Chapter 4,

vertical transverse web stiffeners are typically plates welded to the web girder as

shown in Figure 6.15. These plates were applied to both sides of the web. The

transverse stiffeners are used to prevent buckling of the web and to add rotational

stiffness.
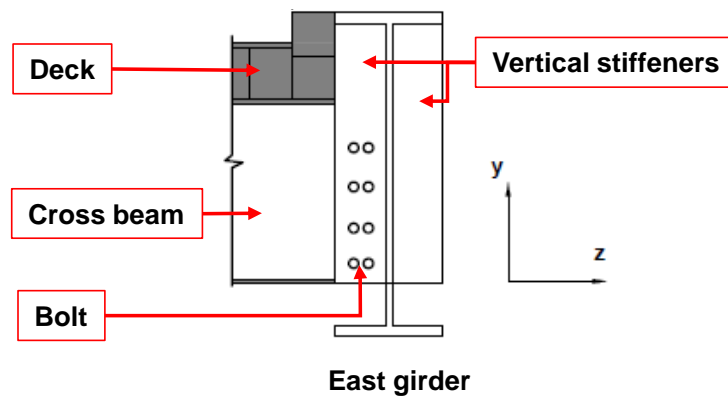
Figure 6.15 Schematic of vertical transverse web stiffeners welded to east web girder.

In this study, the cut back retrofit method is adopted. Although the application of

cut back retrofits to web-gap fatigue problems is not new, the numerical

application of such retrofit on the full-scale model of a real structure is new. The

proposed repair measure focuses on ease of implementation compared to more

conventional options. As the bridge girders are both external, tensile stresses are

expected to be at the outside of web gaps of each girder. From field

measurements, compression stresses at inside of the web gap are observed.

Therefore, the cut back retrofit is proposed only on the outside stiffener. The cut back of an outside stiffener can vary between t_w and $4t_w$ (where $t_w = 20$ mm) as stated earlier. The length of the web gap at the outside stiffener is 80 mm (as built). This study evaluates the consequence of increasing the web-gap length to 100, 120, 140 and 160 mm as shown in Figure 6.16.
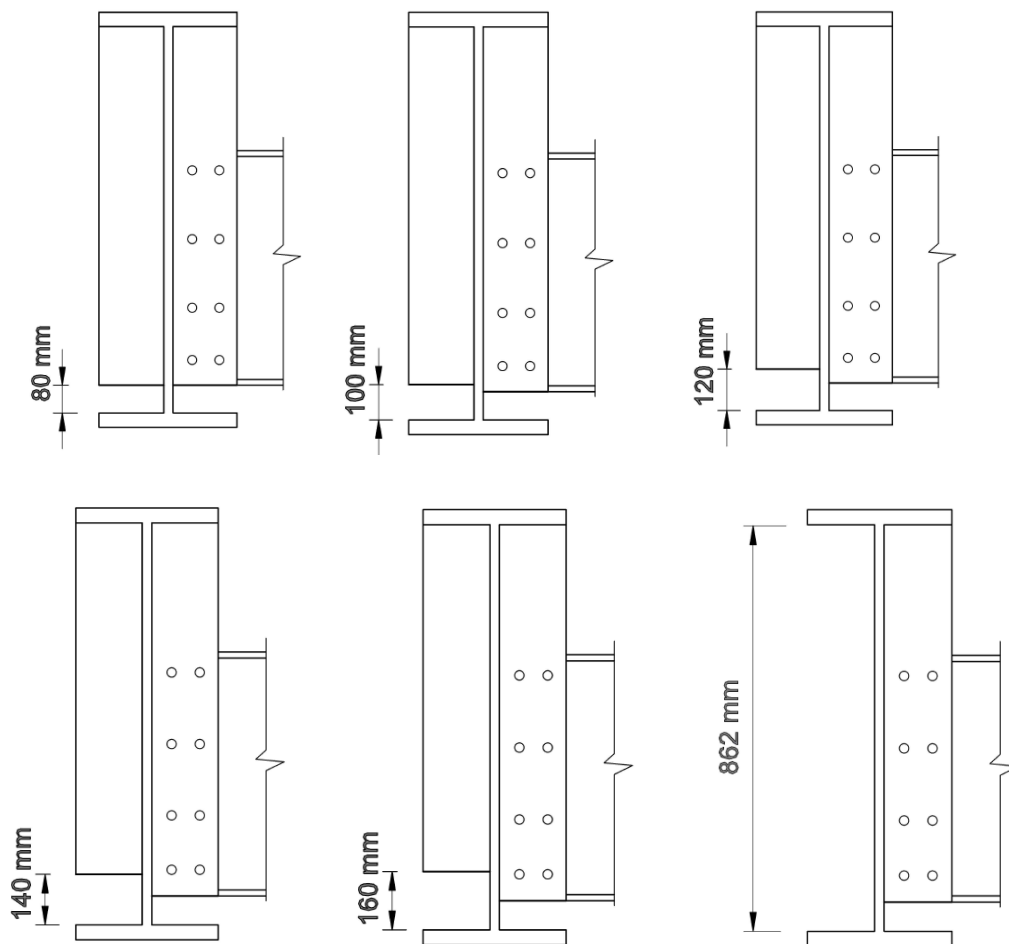
Figure 6.16 Cross section of steel I-beams with different web gap lengths.

The goal of the repair strategies was to reduce web-gap stresses to an acceptable level as recommended by ((EN 1993-1-9 2005) and AASHTO 2012)) in order to avoid the initiation of fatigue cracks. To understand the effects of the cut back on the rigidity of the web girder, parametric analysis of a numerical

model of the web panel was conducted. The numerical model is a simplified finite element model created using the ANSYS software package on the basis of the available engineering drawings for the bridge.

6.4.1 Numerical evaluation of the proposed retrofit

Two types of finite element analyses are performed for investigating lateral buckling of the web panel. The first is an eigenvalue analysis that estimates the buckling load from a linear buckling analysis. The second is a nonlinear buckling analysis that allows for large deformations and geometrical and material nonlinearities. It gradually increases loads on the structure to identify the load at which the structure becomes unstable. Using the nonlinear technique, the model can include features such as initial imperfections, plastic behaviour and large deflection response. An important point to note is that the application of nonlinear buckling analysis in conjunction with the cut back retrofit method is a novel contribution of this work.

Model of web panel

In studying the critical buckling stresses, researchers usually model one panel from the plate girder, but in this study, two panels are modelled to take into account the stiffener effect on the buckling shear stress. The web panels have length L = 1940 mm, height h = 890 mm and thickness t =19.5 mm. The stiffener on one side of the plate is modelled. The stiffener has a length of 810 mm and a thickness of 13 mm. Boundary conditions for the stiffened plate girder web panel and the applied loads are chosen such that results obtained are conservative according to NA to BS EN 1993-1-5 (BS NA EN 1993-1-5 2006) . The panel is

assumed to be pinned all along the boundary. The effects of the top and bottom flanges on the buckling strength and the elastic shear buckling strength are excluded herein. Also the stiffening effects of the two transverse stiffeners on either side of the web panel are not considered. Displacements are imposed to the plates edges nodes for shear stress calculations instead of concentrated loads to avoid excessive distortion of the elements. It should be noted that in the numerical simulations, the effect of 0.004 mm of imposed displacement is equivalent to that of 1 MPa of imposed shear stress. The boundary conditions and load application are illustrated in Figure 6.17. A pure shear stress state (τ_{xy}) is obtained in the plate by the application of displacements along the edge nodes as shown in Figure 6.18.
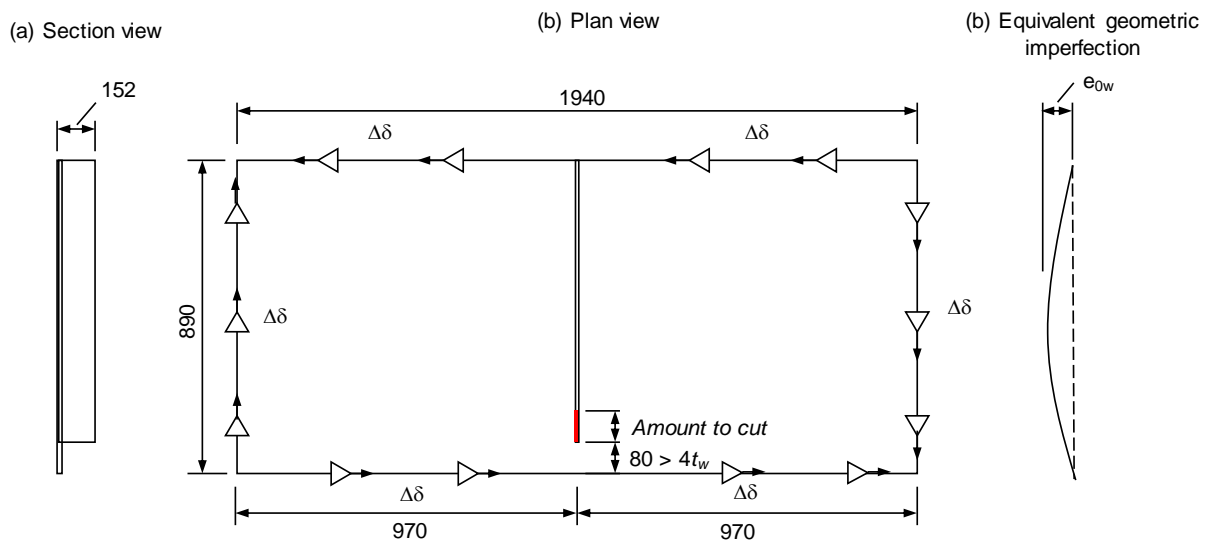
Figure 6.17 Girder web panel scheme modelling and loading for nonlinear parametric buckling analysis (units: mm).
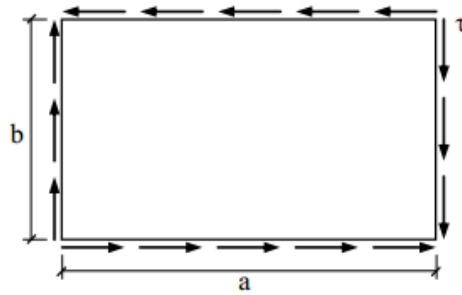
Figure 6.18 Schematic of pure shear stress τ_{xy}

The finite element model of the aforementioned web panel model is produced in ANSYS. Quadrilateral shell elements are used to construct the models for time efficiency. The elastic modulus and Poisson's ratio of steel are specified as 205 GPa and 0.3 respectively. The ANSYS model for web panel is shown in Figure 6.19.
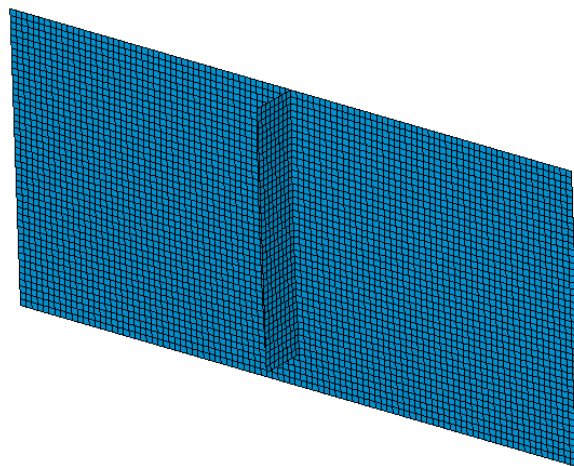
Figure 6.19 ANSYS prototype model.

Linear plate buckling analyses (Eigenvalue analysis)

First, eigenvalue buckling analysis is performed of the prototype web panel without a transverse stiffener. This is done as a reference study and does not consider any out of plan imperfections in the web nor any plasticity of the steel. This analysis predicts the theoretical buckling strength of an ideal linear elastic

237

structure. This method corresponds to the textbook approach to elastic buckling

analysis: for instance, an eigenvalue buckling analysis of a column will match the

classical Euler solution. In this study, the critical load factor is first obtained from

theory using equations below:

$$\tau_{cr} = \frac{k_\tau \pi^2 E}{12\,(1-v^2)} \left(\frac{t}{b}\right)^2 \tag{6.10}$$

$$k_t = 4.0 + \frac{5.34}{a^2} \quad , \qquad a \le 1 \tag{6.11}$$

$$k_t = 5.34 + \frac{4.0}{a^2} \quad , \qquad a > 1 \tag{6.12}$$

k_t is the buckling coefficient for shear buckling stress, a is length of the panel, b

is the width of the panel, E is the elastic modulus, v is Poisson ratio, t is the

plate thickness and τ_{cr} is the critical shear buckling stress.

Secondly, a special software package called EBPlate (Elastic Buckling of Plate)

(CTICM 2018) and ANSYS (ANSYS 2018) are used to evaluate the critical load

factors. A finite element mesh that provides accurate results within a reasonable

amount of computational time is identified using convergence studies. A mesh of

shell elements of approximately 1 mm x 1 mm size is seen to provide adequate

accuracy in the eigenvalue buckling analysis. The deformed shape and absolute

displacements as produced by the buckling analysis during the shear buckling

failure of the web panel without a transverse stiffener are shown in Figure 6.20

and Figure 6.21, respectively.
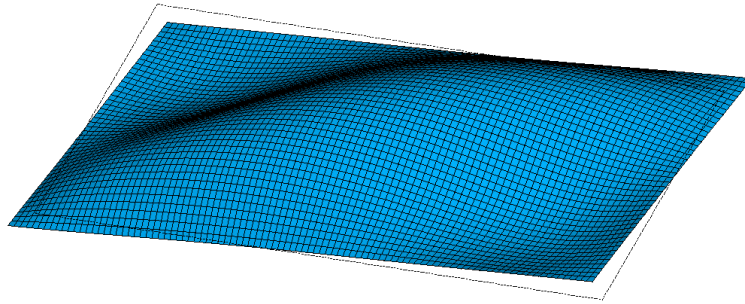
Figure 6.20 ANSYS buckle Analysis- deformed shape of unstiffened web panel.

| 1.30 | 1.89 | 2.47 | 3.05 | 3.64 | 4.22 | 4.81 | 5.40 | 5.98 | 6.56 |
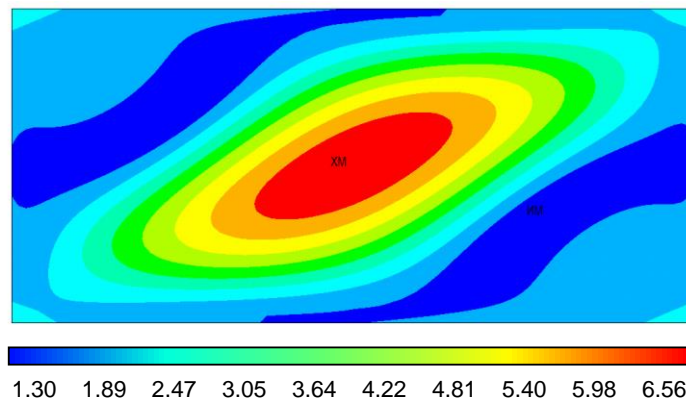
Figure 6.21 ANSYS buckle Analysis- absolute displacements. The blue represents no stress while red and orange represent an area of high stress (units: mm).

Results obtained through EBPlate program and ANSYS are checked by comparing them with results obtained through analytical models. Table 6.7 shows the theoretical critical load factor of the unstiffened plate obtained through linear eigenvalue buckling analysis. However, imperfections and nonlinearities prevent most real-world structures from achieving their theoretical elastic buckling strength. Thus, eigenvalue buckling analysis often yields un-conservative results that are not compatible with EN 1993-1-5 recommendations. Thus a nonlinear buckling analysis is performed that includes the plastic behaviour of the steel.

Table 6.7 Critical load factors for the web panel without transverse stiffener.

Method	Theoretical	EBPlate	ANSYS
Critical load factors (MPa)	563.25	575.61	557.31

6.4.2 Nonlinear plate buckling analyses

A nonlinear analysis of the ultimate shear loading capacity for the stiffened web panel plate is performed using ANSYS. Two ANSYS models – one representing the stiffened web panel plate without cut back (as built) and another with cut back of 80 mm, are created as shown in Figure 6.22 and Figure 6.23. The finite element analysis uses the full Newton-Raphson equilibrium iteration scheme and arc-length method to include geometric and material nonlinearities. The automatic time stepping features are activated to enhance the convergence. The method of automatic time stepping (or automatic loading) is one in which the time step size and/or the applied loads are automatically determined in response to the current state of the analysis under consideration.

The material is idealized to be elastic-perfectly plastic. It is modelled by adopting the true nonlinear stress strain curve considering the characteristics of S355 steel as outlined in the BS EN 1993-1-5: yield strength $F_{ty} = 345$ MPa for $t > 16\ mm,$ ultimate stress ($F_{tu} = 630$ MPa), Young modulus $E = 210$ GPa and strain at rupture ($\varepsilon_{max} = 22\%$).
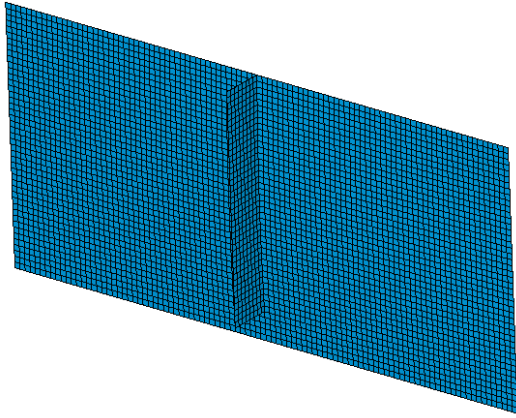
Figure 6.22 ANSYS stiffened prototype web panel model.
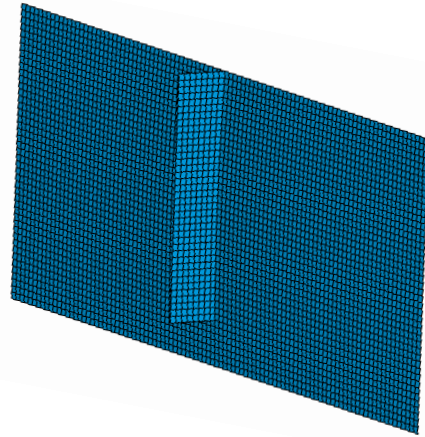
Figure 6.23 ANSYS stiffened prototype web panel model with cut back 80 mm.

Since the buckling analysis involves large inelastic strains, the nominal (engineering) static stress-strain curves are converted to true stress and logarithmic plastic true strain curves. The true stress (σ_{true}) and plastic true strain ε_{true} are calculated using equations:

$$\sigma_{true} = \sigma \, (1 + \epsilon) \tag{6.13}$$

$$\epsilon_{true} = ln \, (1 + \epsilon) \tag{6.14}$$

where σ and ϵ are the nominal (engineering) stress and strain values respectively. Figure 6.24 shows the true stress (σ_{true}) and plastic true strain ε_{true}.

An appropriate finite element mesh that provides accurate results in a reasonable amount of computational time is chosen by conducting convergence studies. It is found that a mesh of shell elements with approximately 2 mm x 2 mm size provides adequate accuracy.
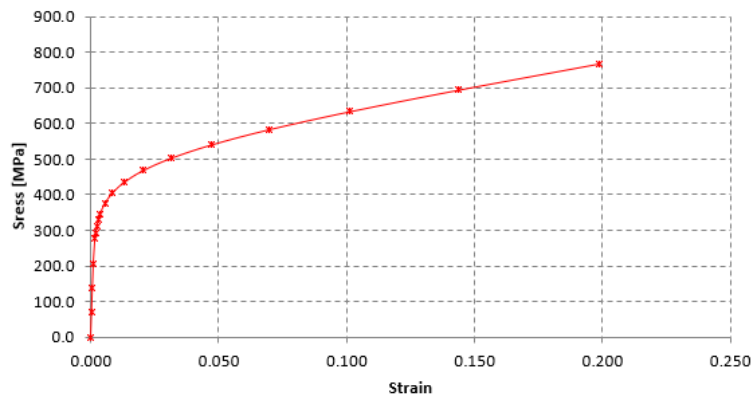
Figure 6.24 True stress-strain curve.

Initial imperfections are applied in the finite element models in order to initiate buckling in the nonlinear analyses. Eurocode (2003) suggests that out-of-plane imperfection of plates shall be taken as the smaller of a/200 and b/200, where a and b are the web panel length (Figure 6.17) and web height respectively. The deformed shape and absolute displacements resulting from the nonlinear buckling analysis for the web panels with and without cut back are shown in Figure 6.25 and Figure 6.26 respectively.

(a) as-built τ_{xy} obtained for the same element in the region of max. displacements
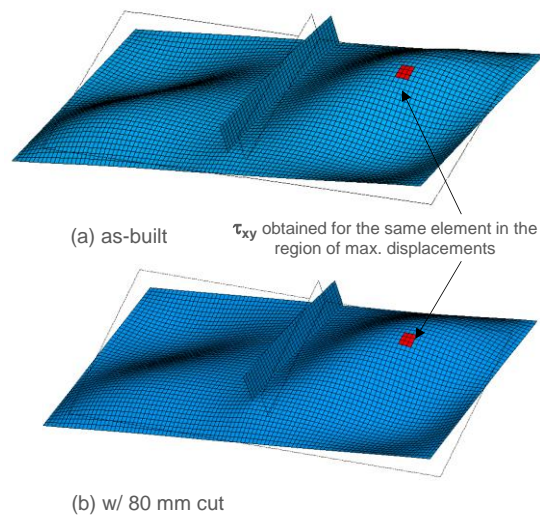
(b) w/ 80 mm cut

Figure 6.25 Deformed shape at buckling failure for (a) as-built and (b) with 80 mm cut back.
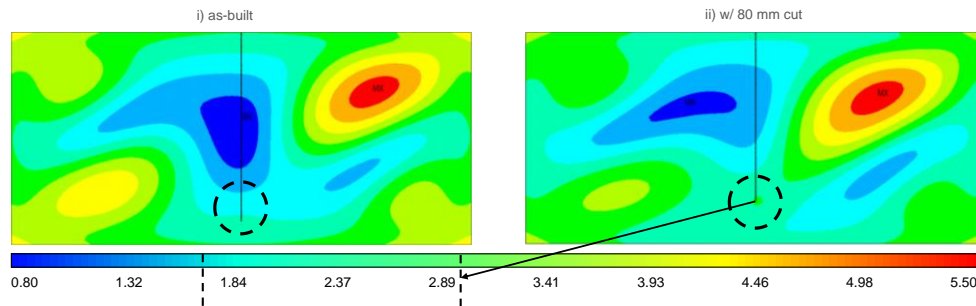
Figure 6.26 a) Absolute out-of-plane displacements during the step of shear buckling failure for (a) as-built and (b) with 80 mm cut (units: mm).

The effect of web gap length on the ultimate shear buckling resistance of the web girder is then studied using nonlinear finite element analysis. This is done by varying the magnitude of cut back length of stiffener of the web panel. Results from the nonlinear analysis of the web panels for different cut backs are presented in Figure 6.27. As the magnitude of cut back length is increased from 0 to 80 mm, the ultimate shear strength of plate girder decreases.
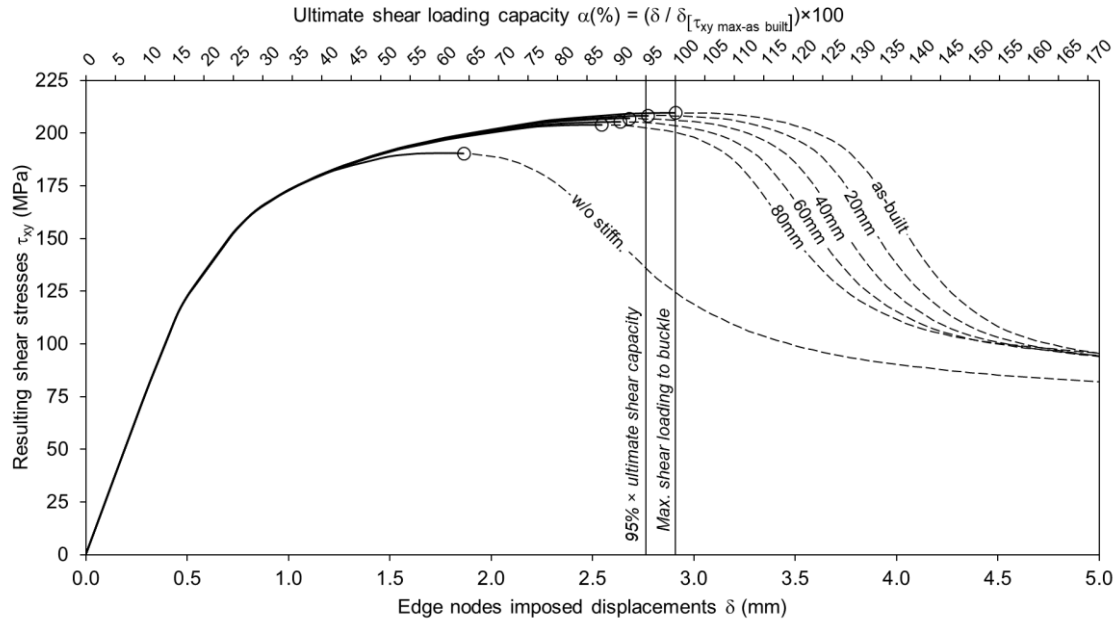
Figure 6.27 Results of the parametric nonlinear analysis for web panels with different configurations.

243

For a cut back length of 20 mm, the percentage decrease in maximum shear loading capacity is less than 5%. A decrease of 14% is observed for a cut back length of 80 mm. For an unstiffened web panel, the shear loading capacity is significantly reduced by 35%.

From the results it can be concluded that the ultimate shear load carrying capacity (for buckling of the web) is unnecessarily high. The web panel is likely to fail in compression well before reaching its shear buckling capacity. Hence there is definitely room for cut back of the web gap to increase the fatigue life of the detail. Therefore, a cut back length of 20 mm is adopted as a preventive retrofit that has the potential to significantly increase the fatigue life while reducing the ultimate shear load carrying capacity of web girder panel by only 5%.

6.4.3 Stress evaluation (Stress reduction effects)

To analytically verify the effectiveness of the proposed retrofit, stresses predicted at the critical detail before and after completion of the proposed retrofit are compared. To this end, the calibrated global FEM of the bridge is combined with the sub models for hot spot and effective notch stress (described in section 6.3.4 and 6.3.4). The maximum vehicle axle loads (240 kN) for fatigue considerations are applied at mid-span as shown in Figure 6.28.

The proposed retrofit softens the web gap and distributes the load transferred from the cross beam to a wider web area. Figure 6.29 shows a significant stress reduction within the web gap as a result of this repair technique. The tensile hot spot stress decreases by 30% from 46MPa before the retrofit to 32MPa after the retrofit.

(a) Global model static analysis result.

(b) Pumping effect.

i) Compression inside.

ii) Tension outside.
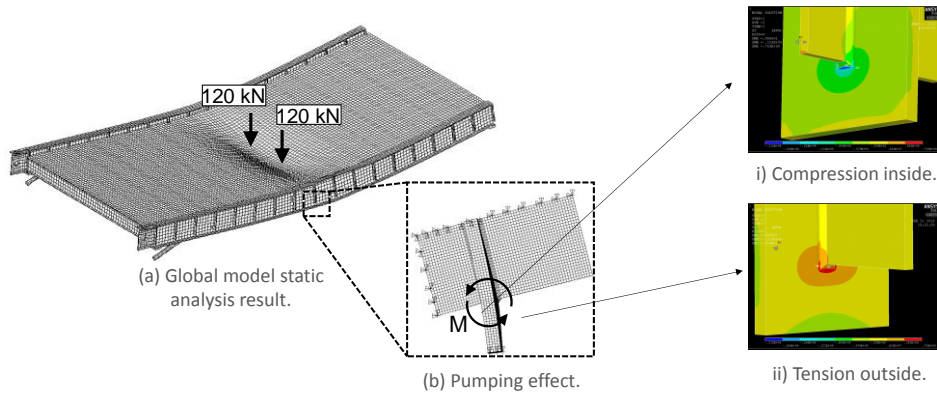
Figure 6.28 The deformed shape of the bridge predicted by the model when subject to the maximum truck axle load (240 kN).
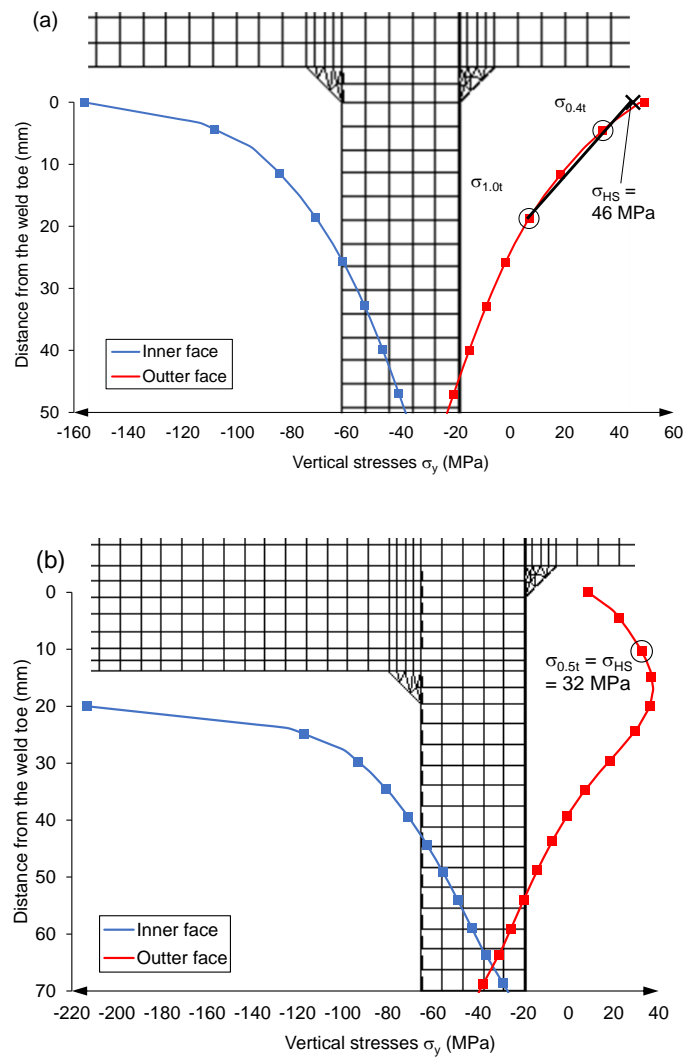
Figure 6.29 Comparison between the hot-spot stress estimations for a) the as-built condition and b) the retrofitted condition.

Effective notch stresses at the weld toe and weld root are calculated according to the IIW's guideline (Section 2.3) using the corresponding sub model of the web gap region. Figure 6.30 shows contours of the maximum principal stress in the web gap region of the critical connection.
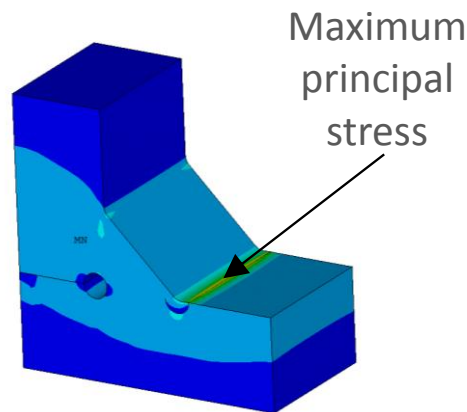
Figure 6.30 The contour of the maximum principle stress at weld toe.

The stresses before and after the retrofit are compared in Figure 6.31. A significant stress reduction within the web gap is observed as a result of this repair technique. The effective notch method shows a drastic 73% reduction (from 213.49MPa to 57.95MPa) of the maximum principal stress at the weld toe. As for the stress at the weld root, the evaluated effective notch stress for the as-built condition was 42% below the CAFT required for preventing fatigue crack initiation and growth. Therefore, the effective notch stress after retrofit is not evaluated.

A key observation from Figure 6.30 and Figure 6.31 is that the magnitude of out of-plane stress within the web gap region is significantly reduced by the 20 mm cut back. This technique reduces the stress concentrations to a level below the critical stress that is required to initiate fatigue cracks.

as-built		20 mm cut
Notch stress (MPa)		Notch stress (MPpa)
Weld toe	Weld root	Weld toe
213.49	66.12	57.95
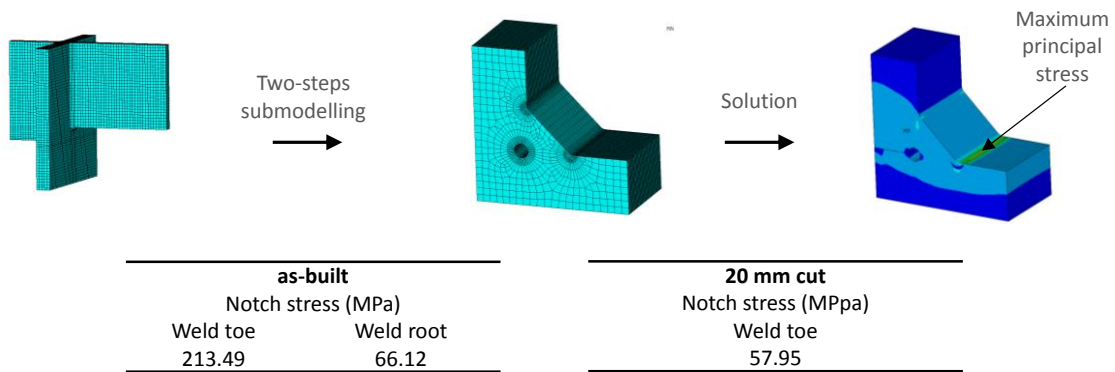
Figure 6.31 Comparison between the effect notch stress for the as-built and the retrofitted condition.

In the following sections fatigue analysis is performed to evaluate if this retrofit can increase the fatigue life of the bridge as computed using the hot spot stress method.

6.4.4 Fatigue life assessment using hot spot stress method

Using the S-N method, fatigue life and consequently remaining life of a retrofitted welded detail of the Bascule Bridge are calculated. Following the procedure described in section 6.3.5: *Fatigue damage based on Hot spot stress method*, the total damage D_d is obtained. The total annual damage for vehicles in fast and slow lanes are $1.8{\times}10^{-3}$ and $5.82{\times}10^{-5}$ respectively. The total annual damage for all vehicles is $1.85{\times}10^{-3}$. The corresponding remaining fatigue life, in years, of the bridge is calculated and presented in Table 6.8.

Table 6.8 Remaining fatigue life of the bridge.

Total Damage year	Bridge's life (years)	Total fatigue damage	Remaining fatigue life (years) considering $D_d = 0.5$
$1.85{\times}10^{-3}$	46	0.085	270

As can be seen, the calculated remaining fatigue life for this location was increased considerably (19 times of the value before retrofitting) - from 14 years to 270 years after the execution of retrofit. This improvement in fatigue life can be explained by the reduction in the hot-spot stress range provided by the cut back retrofit.

6.5   Summary & conclusions

A steel bridge (Bascule Bridge) is employed to address the study objectives (4-7) stated previously in Chapter 1. Hot spot stresses predicted by the proposed research methodology are used to predict the fatigue damage. The calibrated numerical model of the bridge is used to evaluate the web gap stresses at cross beam-main beam connection positions. A cost-effective and easy-to-implement retrofit method is proposed and implemented numerically for distortion-induced fatigue damage. The fatigue capacity of both as-built and retrofitted joints is assessed using the stress cycle (S-N curve) method.

This study results in the following observations and conclusions.

1. The remaining fatigue life of the Bascule Bridge at its mid span connection as determined by using nominal stress method is more than 400 years. In contrast, the remaining fatigue life of the bridge at the studied critical connection as determined by using hot spot stress method is less than 14 years. This result emphasizes the importance of treating distortion-induced fatigue on localized regions in the bridge.

2. The shear load carrying capacity of the web is significantly larger than its buckling capacity and this supports performing a cut back of the stiffener. A 20 mm cut back, which is recommended as the retrofit, reduces only 5% of the ultimate shear load carrying capacity of web girder panel.

3. Results show that a cut-back of 20 mm can contribute to a significant reduction of the out-of-plane stresses. Due to the retrofit, the stresses as evaluated using hot spot and effective notch stress methods are observed to reduce by 30% and 73% respectively.

4. The fatigue life of the detail with the presented retrofit is over 19 times higher than the fatigue life of the original detail, thus confirming the effectiveness of the proposed measure.

CHAPTER 7   Conclusions, and recommendations for future work

This thesis investigates the following hypothesis: detailed finite element models of fatigue-critical connections and in-service strain measurements that capture the shear, flexure, and axial demands of the modelled connections can be combined to estimate accurately the in-situ hot spot/nominal stresses. This enables much more reliable assessment of fatigue life than possible by current methods. Proving this hypothesis also permits expanding the approach for predicting hot spot/nominal stresses at uninstrumented connections by combining numerical models with real-time measurements from a few instrumented connections. The thesis specifically focuses on investigating this hypothesis for the fatigue-sensitive web-gap welded details in ladder-type bridge decks. However the presented ideas are applicable to riveted/bolted connections in this type of steel bridges.

7.1   Conclusions

The conclusions are structured within two areas: fatigue stress prediction methodology and fatigue life assessment.

7.1.1 Fatigue stress prediction methodology:

- The proposed methodology, which is based on combining numerical models with in-situ strain measurements from strain gauges placed further away from a welded detail, is shown to be an

effective approach for evaluating hot spot stresses relevant to fatigue damage assessment.

- The strains predicted by the local FEM of a connection upon using internal forces computed from measured strains is within 3% of the field measured strains for the Bascule Bridge and the Mineral Line Bridge. This demonstrates that the real stresses at fatigue critical details can be evaluated using the proposed methodology.

- The choice of boundary conditions plays an important role in the performance of the local FEM. Boundary condition *BC3*, which corresponds to partially fixed connections using spring elements at the ends of the main girder in the local FEM, leads to the best stress predictions.

- In the Bascule Bridge, the predicted stress at the weld region is mainly due to internal shear forces in the cross beam. The internal moment is found to have a negligible effect on the hot spot stress.

- The local FEM created using IIW recommendations for numerical modelling can predict hot spot stresses reliably while avoiding unnecessary complexity and computational effort.

- Although nonlinear behaviour is expected in the web-gap region due to the nature of the connections, the global FEM is still able to accurately predict strain response in this region using only a linear elastic model but with additional refinement of mesh at the connection.

251

- The field measurement campaigns on the railway bridges show that the proposed methodology can capture the stress cycles for each axle of the train which grate of important for stress range counting.

- The virtual sensing procedure is capable of predicting stress histories at uninstrumented locations by computing the peak stress ratios using global FEM and or directly from strain measurements.

- When deriving the stress peak ratio from a calibrated global FEM, there is a need to average all the peak ratio over a number of load scenarios to adjust for any loading related variations.

7.1.2 Fatigue life assessment

- The remaining fatigue life of the Bascule Bridge at its mid span connection as determined by using nominal stress method is more than 400 years. In contrast, the remaining fatigue life of the bridge at the studied critical connection as determined by using hot spot stress method is less than 14 years. This result emphasizes the importance of treating distortion-induced fatigue on localized regions in the bridge.

- The Mineral Line Bridge being relatively short (17.7 m in length) is subject to more major stress cycles than larger spans (Sorrenson 2003); the bridge experiences a stress cycle for nearly each axle of the train.

- The shear load carrying capacity of the web of the Bascule Bridge is significantly larger than its buckling capacity and this supports

performing a cut back of the stiffener. A 20 mm cut back, which is recommended as the retrofit, reduces only 5% of the ultimate shear load carrying capacity of web girder panel.

- Results show that a cut-back of 20 mm can contribute to a significant reduction of the out-of-plane stresses. Due to the retrofit, the stresses as evaluated using hot spot and effective notch stress methods are observed to reduce by 30% and 73% respectively.

- The results for vertical stiffener detail retrofit presented fatigue life value that is more than 19 times higher than the fatigue life of the original detail, thus confirming the effectiveness of the proposed preventive retrofitting measure.

7.2   Recommendations for future work

- This research is based on data collected from short monitoring periods. Further long-term field monitoring is essential to prove robustness of methodology and to identify the effects of seasonal variations in ambient conditions and loading.

- Future work in the field of service-life prediction of existing steel bridges should consider inclusion of environmental conditions and existing deterioration such as corrosion. Consideration of these conditions may improve both the quality and accuracy of remaining fatigue life assessments.

253

- Sophisticated modelling concepts that represent contact, friction between the connection elements parts and the clamping forces in the rivets/bolts need further investigation as they can improve the performance of a local FEM.

- Implementation of the proposed retrofit measure – i.e. the stiffener cut back, in the actual bridge and subsequent field evaluation in terms of changes in stress concentration would offer further support for the methodology and retrofit proposed in this study.

- Investigate the use of Theory of Critical Distances (TCD) in conjunction with proposed local FE, in order to estimate the fatigue damage and the remaining life. The hot spot stress method has been found to have certain limitations for 3D stress concentrations (Doerk et al. 2003) and it is far from straightforward to define the stress state at non-welded details.

Conference proceedings presented by the author

Kwad, J. et al., 2017. Fatigue assessment of an existing steel bridge by finite element modelling and field measurements. Journal of Physics: Conference Series, 843, p.012038.

Kwad, J. & Kripakaran, P., 2017. Fatigue evaluation in steel bridges: Integrating field measurements and numerical modelling within hot-spot stress approach. Structural Health Monitoring of Intelligent Infrastructure SHMII-8 (December 5-8, 2017) in Brisbane, Australia.

Journal paper prepared by the author

Kwad, J. & Kripakaran, P. Numerical and Experimental Techniques for Fatigue Life Prediction of Welded Connections in Bridges. Structure and Infrastructure Engineering, in communication.

Kwad, J. et al., 2017. Distortion induced fatigue repair measure of an old metallic bridge by local approaches. Under preparation.

References

Ahlborn, T.M. et al., 2010. The State-of-the-Practice of Modern Structural Health Monitoring for Bridges: A Comprehensive Review. *Burns*, 48105(734), p.70. Available at: http://www.mtri.org/bridgecondition/doc/State-of-PracticeSHMforBridges(July2010).pdf.

Aid, A. et al., 2011. Fatigue life prediction under variable loading based on a new damage model. *Materials and Design*, 32(1), pp.183–191. Available at: http://dx.doi.org/10.1016/j.matdes.2010.06.010.

Al-Emrani, M. & Aygül, M., 2014. *Fatigue design of steel and composite bridges*, Göteborg, Sweden.

Alampalli, S. & Lund, R., 2006. Estimating Fatigue Life of Bridge Components Using Measured Strains. *Journal of Bridge Engineering*, 11(6), pp.725–736.

Albrecht, P. & Lenwari, A., 2009. Variable-amplitude fatigue strength of structural steel bridge details: Review and simplified model. *Journal of Bridge Engineering*, 14(4), pp.226–237. Available at: http://dx.doi.org/10.1061/(ASCE)1084-0702(2009)14:4(226).

American Association of State Highway and Transportation Officials., 2017. *AASHTO LRFD bridge design specifications*,

American Association of State Highway and Transportation Officials, 2012. *AASHTO LRFD bridge design specifications*,

American Association of State Highway and Transportation Officials, 2010. *AASHTO LRFD bridge Design Specifications*,

ANSYS, 2018. Advanced Analysis Techniques Guide. Release 18.1

Documentation for ANSYS. ANSYS, Inc.

ASTM E1049 - 85, 2005. Standard Practices for Cycle Counting in Fatigue Analysis 1. *ASTM International, West Conshohocken, PA.*, 85(Reapproved 2011), pp.1–10.

Attanayake, U. & Aktan, H., 2015. First-generation ABC system, evolving design, and half a century of performance: Michigan side-by-side box-beam bridges. *Journal of Performance of Constructed Facilities*, 29(3), pp.1–14.

Attema, T. et al., 2017. Maintenance decision model for steel bridges: A case in the Netherlands. *Structure and Infrastructure Engineering, Taylor*, 13(2), pp.242–253.

Baptista, C., 2016. *Multiaxial and variable amplitude fatigue in steel bridges*. Phd thesis, EPFL.

Berglund, E.M. & Schultz, A.E., 2006. Girder Differential Deflection and Distortion-Induced Fatigue in Skewed Steel Bridges. *Journal of Bridge Engineering*, 11(2), pp.169–177. Available at: http://ascelibrary.org/doi/10.1061/%28ASCE%291084-0702%282006%2911%3A2%28169%29.

Bowman, M.D. et al., 2012. *Fatigue Evaluation of Steel Bridges*, Washington, D.C.: Transportation Research Board. Available at: https://www.nap.edu/catalog/22774.

Brownjohn, J.M.W., 2007. Structural health monitoring of civil infrastructure. *Philosophical Transactions of the Royal Society A: Mathematical, Physical and Engineering Sciences*, 365(1851), pp.589–622. Available at:

http://rsta.royalsocietypublishing.org/cgi/doi/10.1098/rsta.2006.1925.

Brownjohn, J.M.W., Xu, Y. & Hester, D., 2017. Vision-Based Bridge Deformation Monitoring. *Front. Built Environ*, 3(23). Available at: http://journal.frontiersin.org/article/10.3389/fbuil.2017.00023/full.

BS 5400, 1980. *Part 10 (1980). Steel, concrete and composite bridges. Part 10. Code of practice for fatigue. British Standards Institution.*, UK.

BS NA EN 1991-2, 2003. Eurocode 1: Actions on structures - Part 2: Traffic loads on bridges. *Technical report, European Committee for Standardization (CEN), Brussels.*

BS NA EN 1993-1-5, 2006. NATIONAL ANNEX UK National Annex to Eurocode 3 : Design of steel structures –.

BS NA EN 1993-1-9, 2005. UK National Annex to Eurocode 3: Design of Steel Structures: Fatigue strength of steel structures.

Cai, S. et al., 2017. Fatigue life assessment of large scale T-jointed steel truss bridge components. *Journal of Constructional Steel Research*, 133, pp.499–509. Available at: http://linkinghub.elsevier.com/retrieve/pii/S0143974X17300081.

Cardini, A. & DeWolf, J., 2009. Implementation of a long-term bridge weigh-in-motion system for a steel girder bridge in the interstate highway system. *Journal of Bridge Engineering*, (December), pp.418–423.

Chan, T.H.T., Li, Z.X. & Ko, J.M., 2001. Fatigue analysis and life prediction of bridges with structural health monitoring data — Part II: application.

International Journal of Fatigue, 23, pp.55–64. Available at: www.elsevier.com/locate/ijfatigue.

Chotickai, P. & Bowman, M.D., 2006. Truck models for improved fatigue life predictions of steel bridges. *Journal of Bridge Engineering*, 11(1), pp.71–80. Available at: http://dx.doi.org/10.1061/(ASCE)1084-0702(2006)11:1(71).

Chowdhury, F.H., Raihan, M.T. & Islam, G.M.S., 2015. Application of different structural health monitoring system on bridges : An overview. *IABSE-JSCE Joint conference on advances in bridge engineering-III; Dhaka, Bangladesh*, pp.978–984. Available at: http://www.iabse-bd.org/session/72.pdf.

Chung, H.-C. et al., 2004. Real-time visualization of bridge structural response through wireless MEMS sensors. *Proceedings of SPIE*, 5392, pp.239–246.

Clarke, T., 2009. *Guided wave health monitoring of complex structures*. Phd thesis, Imperial College London. Available at: https://spiral.imperial.ac.uk/handle/10044/1/5288.

Clough, R.W. & Penzien, J., 1995. *Dynamics of Structures*, Berkeley: Computers & Structures.

Coletti, D., Chavel, B. & Gatti, W., 2011. Challenges of Skew in Bridges with Steel Girders. *Transportation Research Record: Journal of the Transportation Research Board*, 2251(1), pp.47–56. Available at: http://journals.sagepub.com/doi/10.3141/2251-05.

Connor, R.J.. & Fisher, mJ. W.., 2006. Identifying effective and ineffective retrofits for distortion fatigue cracking in steel bridges using field instrumentation. *Journal of Bridge Engineering*, 11(6), pp.745–752. Available

References

at: http://www.scopus.com/inward/record.url?eid=2-s2.0-
33750122911&partnerID=40&md5=714660dd332e63f70cc3d17bc9f78985.

Connor, R.J. & Fisher, J.W., 2006. Identifying Effective and Ineffective Retrofits
for Distortion Fatigue Cracking in Steel Bridges Using Field Instrumentation.
Journal of Bridge Engineering, 11(6), pp.745–752.

Connor, R.J., Hodgson, I.C. & Bowman, C., 2005. *Field Testing and Fatigue
Evaluation of the I-79 Bridge over the Ohio River*, Center for Advanced
Technology for Large Structural Systems (ATLSS), Lehigh
University,Bethlehem, USA.

Connor, R.J. & Lloyd, J.B., 2017. *Maintenance Actions to Address Fatigue
Cracking in Steel Bridge Structures: Proposed Guidelines and Commentary*,
West Lafayette, IN: Purdue University. Available at:
http://docs.lib.purdue.edu/sbritereports/2/.

Cremona, C. et al., 2013. Improved Assessment Methods for Static and Fatigue
Resistance of Old Metallic Railway Bridges. *Journal of Bridge Engineering*,
18(11), pp.1164–1173. Available at:
http://ascelibrary.org/doi/10.1061/%28ASCE%29BE.1943-5592.0000466.

CTICM, 2018. EBPlate. Available at: www.cticim.com.

Cui, W., 2002. A state-of-the-art Review on Fatigue Life Prediction Methods for
Metal Structures. *Journal of Materials Science and Technology*, 7, pp.43–
56.

D'Attilio, P. et al., 2008. Structural health monitoring of bridges in the State of
Connecticut. *Earthquake Engineering and Engineering Vibration*, 7(4),
260

pp.427–437.

Dai, J. et al., 2013. Reliability risk mitigation of free air cooling through prognostics and health management. *Applied Energy*, 111, pp.104–112. Available at: http://dx.doi.org/10.1016/j.apenergy.2013.04.047.

Desjardins, S.L. et al., 2006. Reall-time data processing, analysis and visuafization for structural monitoring of the confederation bridge. *Advances in Structural Engineering*, 9(1), pp.141–157.

Dexter, R.J. & Ocel, J.M., 2013. Manual for Repair and Retrofit of Fatigue Cracks in Steel Bridges (FHWA-IF-13-020). , (March), p.134.

Doerk, O., Fricke, W. & Weissenborn, C., 2003. Comparison of different calculation methods for structural stresses at welded joints. *International Journal of Fatigue*, 25(5), pp.359–369.

Dong, P., 2001. A structural stress definition and numerical implementation for fatigue analysis of welded joints. *International Journal of Fatigue*, 23(10), pp.865–876.

Doornink, J.D. et al., 2006. Damage detection in bridges through fiber optic structural health monitoring. In *Conference on Photonic Sensing Technologies*. pp. U15–U26.

EN 1993-1-9, 2005. Eurocode 3: Design of steel structures - Part 1-9: Fatigue. *European Committee for Standardization (CEN), Brussels.*

Fasl, J., 2013. *Estimating the remaining fatigue life of steel bridges using field measurements*. PhD thesis, The University of Texas,Austin. Available at:

http://repositories.lib.utexas.edu/handle/2152/20693.

Fatemi, a. & Yang, L., 1998. Cumulative fatigue damage and life prediction theories: a survey of the state of the art for homogeneous materials. *International Journal of Fatigue*, 20(1), pp.9–34.

Fisher, J.W. & Roy, S., 2015. Fatigue damage in steel bridges and extending their life. *Advanced Steel Construction*, 11(3), pp.250–268.

Frangopol, D.M., Strauss, A. & Kim, S., 2008. Bridge Reliability Assessment Based on Monitoring. *Journal of Bridge Engineering*, 13(3), pp.258–270.

Fricke, W., 2003. Fatigue analysis of welded joints : state of development. *Marine Structures*, 16, pp.185–200.

Fricke, W., 2013. IIW guideline for the assessment of weld root fatigue. *Welding in the World*, 57(6), pp.753–791.

Fujino, Y., 2002. Vibration, control and monitoring of long-span bridges-recent research, developments and practice in Japan. *Journal of Constructional Steel Research*, 58(1), pp.71–97.

Ghahremani, K., 2015. Fatigue Assessment of Repaired Highway Bridge Welds Using Local Approaches. Available at: https://uwspace.uwaterloo.ca/handle/10012/9455.

Goulet, J.-A., Kripakaran, P. & Smith, I.F.C., 2010. Multimodel structural performance monitoring. *Journal of Structural Engineering*, 136(10), pp.1309–1318.

Guo Tong et al., 2008. Fatigue Life Prediction of Welded Joints in Orthotropic

Steel Decks Considering Temperature Effect and Increasing Traffic Flow. *Structural Health Monitoring*, 7(3), pp.189–202. Available at: http://shm.sagepub.com/cgi/content/abstract/7/3/189 [Accessed August 23, 2011].

Gurney, T., 2006. *Cumulative damage of welded joints*, Woodhead Publishing Limited: Woodhead Publishing Limited. Available at: http://www.sciencedirect.com/science/book/9781855739383.

Hajializadeh, D., OBrien, E.J. & O'Connor, A.J., 2017. Virtual structural health monitoring and remaining life prediction of steel bridges. *Canadian Journal of Civil Engineering*, 44(4), pp.264–273. Available at: http://www.nrcresearchpress.com/doi/10.1139/cjce-2016-0286.

Han, T., 2009. *AMBIENT MODAL IDENTIFICATION, FINITE ELEMENT MODEL UPDATING, AND SEISMIC ANALYSIS OF BRIDGES ON TRANS-CANADA HIGHWAY*. Master's thesis, THE UNIVERSITY OF BRITISH COLUMBIA.

Hassel, H.L., 2011. *AN ANALYTICAL EVALUATION OF DISTORTION-INDUCED FATIGUE IN STEEL BRIDGES*. Master's thesis, University of Kansas.

Heshmati, M., 2012. *Fatigue Life Assessment of Bridge Details Using Finite Element Method. Master's thesis*. Chalmers University of Technology.

Hobbacher, A., 1996. *Fatigue design of welded joints and components*, Woodhead Publishing Limited. Available at: http://www.sciencedirect.com/science/book/9781855733152.

Hobbacher, A., 2016. *Recommendations for Fatigue Design of Welded Joints*

and Components Second Edi., Cham: Springer International Publishing. Available at: http://link.springer.com/10.1007/978-3-319-23757-2.

Hobbacher, A.F., 2009. The new IIW recommendations for fatigue assessment of welded joints and components – A comprehensive code recently updated. *International Journal of Fatigue*, 31(1), pp.50–58.

Imam, B.M. & Righiniotis, T.D., 2010. Fatigue evaluation of riveted railway bridges through global and local analysis. *Journal of Constructional Steel Research*, 66(11), pp.1411–1421.

Jajich, D. et al., 2000. *Distortion-Induced Fatigue in Multi-Girder Steel Bridges*, University of Minnesota.

Jang, S. et al., 2010. Structural health monitoring of a cable-stayed bridge using smart sensor technology: deployment and evaluation. *Smart Structures and Systems*, 6(5–6), pp.439–459.

Jinping Ou & Hui Li, 2010. Structural Health Monitoring in mainland China: Review and Future Trends. *Structural Health Monitoring*, 9(3), pp.219–231.

Kashefi, K., Zandi, a. P. & Zeinoddini, M., 2010. Fatigue life evaluation through field measurements and laboratory tests. *Procedia Engineering*, 2(1), pp.573–582. Available at: http://linkinghub.elsevier.com/retrieve/pii/S1877705810000639 [Accessed December 7, 2014].

Kim, J.H. et al., 2017. Development of fatigue prediction model for steel bridges based on characteristics of variable stress spectra. *International Journal of Damage Mechanics*, 26(7), pp.951–967.

References

Kossakowski, P.G., 2016. Mechanical Properties of Late-nineteenth-century Bridge Steel at Low Temperature. *Procedia Engineering*, 156, pp.180–185.

Kreislova, K. & Geiplova, H., 2012. Evaluation of corrosion protection of steel bridges. *Procedia Engineering*, 40, pp.229–234. Available at: http://dx.doi.org/10.1016/j.proeng.2012.07.085.

Kwon, K. et al., 2012. Probabilistic Fatigue Life Estimation of Steel Bridges by Using a Bilinear S - N Approach. *Journal of bridge engineering (ASCE)*, 17(1), pp.58–70.

Larsson, T., 2009. *Fatigue assessment of riveted bridges*. PhD thesis, Luleå University of Technology.

Leander, J., 2008. Bro över Söderström: Stockholms C.-Älvsjö km 1+ 83: Rapport 1: Mätning och utvärdering map utmattning.

Lee, J.-M. et al., 2010. Comparison of hot spot stress evaluation methods for welded structures. *International Journal of Naval Architecture and Ocean Engineering*, 2(4), pp.200–210. Available at: http://linkinghub.elsevier.com/retrieve/pii/S2092678216302497.

Lee, Y.J. & Cho, S., 2016. Shm-based probabilistic fatigue life prediction for bridges based on fe model updating. *Sensors (Switzerland)*, 16(3).

Lenwari, A. & Chen, H., 2013. Finite element analysis of distortion-induced web gap stresses in multi-I girder steel bridges. *Engineering Journal*, 17(1), pp.95–108.

Li, Z., Li, A. & Han, X., 2009. Operational modal identification of suspension

bridge based on structural health monitoring system. *Journal of Southeast University (English Edition)*, 25(1), pp.104–107. Available at: http://www.scopus.com/inward/record.url?eid=2-s2.0-65349119988&partnerID=tZOtx3y1.

Liao, J., 2011. *Fatigue Damage in the Orthotropic Steel Deck with respect to the Trough-to-Deck Plate Joint in between the Crossbeams*. Delft University of Technology.

Liu, Y. & Mahadevan, S., 2007. Stochastic fatigue damage modeling under variable amplitude loading. *International Journal of Fatigue*, 29(6), pp.1149–1161.

Lotsberg, Inge and Sigurdsson, G., 2006. Fatigue design of plated structures using finite element analysis. *Journal of Offshore Mechanics and Arctic Engineering*, 128(4), pp.330–336.

Lotsberg, I., 2006. Fatigue design of plated structures using finite element analysis. *Ships and Offshore Structures*, 1(1), pp.45–54. Available at: http://www.tandfonline.com/doi/abs/10.1533/saos.2005.0006.

Luo, X., Luo, R. & Lytton, R.L., 2014. Energy-based mechanistic approach for damage characterization of pre-flawed visco-elasto-plastic materials. *Mechanics of Materials*, 70, pp.18–32. Available at: http://dx.doi.org/10.1016/j.mechmat.2013.11.008.

Manson, S.S., 1986. Re-examination of Cumulative Fatigue Damage Analysis — An Modifying Procedure for Including Mean Stress Effects. *Engineering FractureMechanics*, 25(5–6), pp.539–571.

266

References

Manson, S.S. & Halford, G.R., 1981. Practical implementation of the double linear damage rule and damage curve approach for treating cumulative fatigue damage. *International Journal of Fracture*, 17(2), pp.169–192.

Marques, F. et al., 2018. Fatigue analysis of a railway bridge based on fracture mechanics and local modelling of riveted connections. *Engineering Failure Analysis*, 94(January), pp.121–144. Available at: https://doi.org/10.1016/j.engfailanal.2018.07.016.

Marsh, G. et al., 2016. Review and application of Rainflow residue processing techniques for accurate fatigue damage estimation. *International Journal of Fatigue*, 82, pp.757–765. Available at: http://dx.doi.org/10.1016/j.ijfatigue.2015.10.007.

Mashiri, F.R. & Zhao, X.-L., 2005. Thickness effect in welded joints - A review. In *Proceedings of the International Offshore and Polar Engineering Conference*.

MATLAB, 2017. MATLAB the Language of Technical Computing. Version R2016b. Natick, MA: MathWorks Inc.

Miner M, 1945. Miner_Cumulative Damage in Fatigue.pdf. *Journal of Applied Mechanics*, 12(3), pp.A159–A164.

Mohammadi, J., Guralnick, A. & Polepeddi, R., 1998. Bridge Fatigue Life Estimation from Field Data. *Practice Periodical on Structural Design and Construction*, 3(August), pp.128–133.

Moy, S.S.J., Clark, J. & Clarke, H., 2004. The Strengthening Of Wrought Iron Using Carbon Fibre Reinforced Polymer Composites. In *Advanced Polymer*
267

Composites for Structural Applications in Construction: ACIC 2004. pp. 258–265.

Mufti, A.A., 2002. Structural Health Monitoring of Innovative Canadian Civil Engineering Structures. *Structural Health Monitoring*, 1(1), pp.89–103.

Museros, P., 2002. Advances in The Analysis of Short Span Railway Bridges for High-Speed Lines. *Computers & Structures*, 80(27–30), pp.2121–2132.

Nie, R., Huang, Y. & Li, S., 2018. in-Service Condition Assessment of Long-Span Bridges Based on Traffic Load Effects Using Monitoring Data. *Stavební obzor - Civil Engineering Journal*, 27(3), pp.450–457.

Niemi, E., Fricke, W. & Maddox, S.J., 2006. Fatigue analysis of welded components: Designer's guide to the structural hot-spot stress approach. *IIW Document*, 13, pp.1800–1819.

Nijssen, R.P.L., 2006. *Fatigue Life Prediction and Strength Degradation of Wind Turbine Rotor Blade Composites*. PhD thesis, Delft University.

Nishikawa, K., Murakoshi, J. & Matsuki, T., 1998. Study on the fatigue of steel highway bridges in Japan. *Construction and Building Materials*, 12(2–3), pp.133–141.

Norman Edward Frost, Kenneth James Marsh, L., 1974. *Metal Fatigue*, Oxford: Clarendon Press. Available at: https://books.google.co.uk/books?id=wlHwTcO68iYC&printsec=frontcover&source=gbs_ge_summary_r&cad=0#v=onepage&q&f=false.

Nussbaumer, A., Borges, L. & Davaine, L., 2011. *Fatigue Design of Steel and*

Composite Structures., ECCS, Wiley-Blackwell, Ernst & Shon.

Okelo, R., 2017. Fatigue life prediction for distortion-induced cracking of steel bridges. *International Journal of Steel Structures*, 17(2), pp.801–820.

Olofsson, I. et al., 2005. Assessment of European railway bridges for future traffic demands and longer lives – EC project "Sustainable Bridges." *Structure and Infrastructure Engineering*, 1(No.2), pp.93–100.

Park, J.Y. & Kim, H., 2014. Fatigue Life Assessment for a Composite Box Girder Bridge. *International Journal of Steel Structures*, 14(4), pp.843–853.

Pasquier, R. et al., 2016. Measurement, Data Interpretation, and Uncertainty Propagation for Fatigue Assessments of Structures. *Journal of Bridge Engineering*, 21(5), pp.4015087–13.

Phares, B.M. et al., 2003. Strengthening of steel girder bridges using FRP. In *Proc., 2003 Mid-Continent Transportation Research Symp.* pp. 1–12.

Poutiainen, I., Tanskanen, P. & Marquis, G., 2004. Finite element methods for structural hot spot stress determination—a comparison of procedures. *International Journal of Fatigue*, 26(11), pp.1147–1157.

Radaj, D., 1990. *Design and analysis of fatigue resistant welded structures* 1st Editio., Abington Hall; Abington; Cambridge CB1 6AH; England: Abington Publishing; Woodhead Publishing Ltd;

Radaj, D., Sonsino, C.M. & Fricke, W., 2006. *Fatigue assessment of welded joints by local approaches*, Woodhead Publishing Limited: Woodhead Publishing Limited. Available at:

http://www.sciencedirect.com/science/book/9781855739482.

Rahbari, R. et al., 2015. Structural identification of Humber Bridge for performance prognosis. *Smart Structures and Systems*, 15(3), pp.665–682.

Rakoczy, P., 2011. *WIM BASED LOAD MODELS FOR BRIDGE SERVICEABILITY LIMIT STATES b.* PhD thesis, University of Nebraska.

Rashidi, M. & Gibson, P., 2011. Proposal of a methodology for bridge condition assessment. *Australasian Transport Research Forum 2011 Proceedings*, (September), pp.1–15. Available at: http://ro.uow.edu.au/engpapers/1278/.

Rodriguez, G., Casas, J.R.. & Villalba, S., 2015. SHM by DOFS in civil engineering: a review. *Structural Monitoring and Maintenance*, 2(4), pp.357–382. Available at: http://koreascience.or.kr/journal/view.jsp?kj=E1TPK5&py=2015&vnc=v2n4&sp=357.

Russo, F. et al., 2016. *Design and Evaluation of Steel Bridges for Fatigue and Fracture REFERENCE MANUAL*, Michael Baker International, Moon Township.

Saberi, M.R. et al., 2016. Bridge Fatigue Service-Life Estimation Using Operational Strain Measurements. *Journal of Bridge Engineering*, 21(5), p.04016005.

Schumacher, A., 2003. *Fatigue behaviour of welded circular hollow section joints in bridges.* École Polytechnique Fédérale de Lausanne, Lausanne.

Schumacher, A. & Nussbaumer, A., 2006. Experimental study on the fatigue

behaviour of welded tubular K-joints for bridges. *Engineering Structures*, 28(5), pp.745–755.

Seo, J. et al., 2013. Use of structural health monitoring system for assessment of bridge load rating. *Forensic Engineering 2012*, pp.18–27.

Shen, W. et al., 2016. A method of determining structural stress for fatigue strength evaluation of welded joints based on notch stress strength theory. *International Journal of Fatigue*, 90, pp.87–98. Available at: http://dx.doi.org/10.1016/j.ijfatigue.2016.04.014.

Sorrenson, P.J., 2003. *An integrated methodology for stress-based fatigue assessment of steel railway bridges*. PhD thesis, University of Wollongong.

Tarries, D.J. et al., 2002. Bolt Loosening Retrofit to Inhibit Fatigue Cracking in Steel Girder Bridges. *Transportation Research Board*, (515), pp.1–25.

Terrence, B. et al., 1995. FATIGUE ASSESSMENT OF THROUGH PLATE GIRDER RAILWAY BRIDGES By Terrence W. Philbrick Jr.,1 Student Member, ASCE, George W. Zodo,2 Student Member, ASCE, and Scott D. Schiff,3 Member, ASCE. , 121(November), pp.1613–1619.

Tveiten, B.W.T., M, X.W. & V, S.B., 2007. Fatigue Assessment of Aluminum Ship Details by Hot-Spot Stress Approach. *ABS Technical Papers*, 135(November), pp.13–17.

Vasudevan, A.K., Sadananda, K. & Iyyer, N., 2016. Fatigue damage analysis: Issues and challenges. *International Journal of Fatigue*, 82, pp.120–133. Available at: http://dx.doi.org/10.1016/j.ijfatigue.2015.08.026.

References

Vičan, J., Jošt, J. & Gocál, J., 2014. Analysis of the Stringer-to-Cross-Beam Riveted Joints Behaviour. *Civil and Environmental Engineering*, 10(1), pp.51–61. Available at: http://content.sciendo.com/view/journals/cee/10/1/article-p51.xml.

Wong, K.Y.Y., 2007. Design of a structural health monitoring system for long-span bridges. *Structure and Infrastructure Engineering*, 3(2), pp.169–185.

Worden, K. & Dulieu-Barton, J.M., 2004. An Overview of Intelligent Fault Detection in Systems and Structures. *Structural Health Monitoring*, 3(1), pp.85–98.

Xiao, Zhi-Gang and Yamada, K., 2004. A method of determining geometric stress for fatigue strength evaluation of steel welded joints. *International Journal of Fatigue*, 26, pp.1277–1293.

Xu, Y.L., 2018. Making good use of structural health monitoring systems of long-span cable-supported bridges. *Journal of Civil Structural Health Monitoring*, 8(3), pp.477–497. Available at: https://doi.org/10.1007/s13349-018-0279-2.

Ye, X.W. et al., 2012. Statistical analysis of stress spectra for fatigue life assessment of steel bridges with structural health monitoring data. *Engineering Structures*, 45, pp.166–176. Available at: http://dx.doi.org/10.1016/j.engstruct.2012.06.016 [Accessed September 10, 2012].

Ye, X.W., Su, Y.H. & Han, J.P., 2014. A State-of-the-Art Review on Fatigue Life Assessment of. *Mathematical Problems in Engineering*, 2014, p.13.

Yen, C.S. & Dolan, T.J., 2007. *A CRITICAL REVIEW OF THE CRITERIA FOR*
272

NOTCH-SENSITIVITY IN FATIGUE OF METALS, University of Illinois. Available at: http://hdl.handle.net/2142/4249.

Yi, T.H., Li, H.N. & Gu, M., 2013. Wavelet based multi-step filtering method for bridge health monitoring using GPS and accelerometer. *Smart Structures and Systems*, 11(4), pp.331–348. Available at: http://www.scopus.com/inward/record.url?eid=2-s2.0-84877086599&partnerID=tZOtx3y1.

Yun, C.-B. et al., 2003. Recent R&D activities on structural health monitoring for civil infra-structures in Korea. *KSCE Journal of Civil Engineering*, 7(6), pp.637–651. Available at: http://link.springer.com/10.1007/BF02829136.

Zamiri Akhlaghi, F., 2009. *Fatigue life assessment of welded bridge details using structural hot spot stress method. Master's thesis*. Chalmers University of technology. Available at: http://publications.lib.chalmers.se/records/fulltext/132073.pdf.

Zhang, Q. & Zhou, Y., 2007. Investigation of the applicability of current bridge health monitoring technology. *Structure and Infrastructure Engineering*, 3(2), pp.159–168. Available at: http://www.tandfonline.com/doi/abs/10.1080/15732470600590762.

Zhang, W., Cai, C.S. & Pan, F., 2013. Fatigue Reliability Assessment for Long-Span Bridges under Combined Dynamic Loads from Winds and Vehicles. *Journal of Bridge Engineering*, 18(8), pp.735–747. Available at: http://ascelibrary.org/doi/10.1061/%28ASCE%29BE.1943-5592.0000411.

Zhang, W. & Yuan, H., 2014. Corrosion fatigue effects on life estimation of

deteriorated bridges under vehicle impacts. *Engineering Structures*, 71, pp.128–136. Available at: http://dx.doi.org/10.1016/j.engstruct.2014.04.004.

Zhao, Z., Haldar, l A. & Jr., and F.L.B., 1994. the American Association of State Highway and Transportation Officials ' (AASHTO) Guide Specifications for Fatigue Design of Steel Bridges (1989); *Journal of Structural Engineering*, 120(5), pp.1608–1623.

Zhou, T.Q. & Chan, T.H.T., 2007. Hot spot stress analysis of fatigue for Tsing Ma Bridge critical members under traffic using finite element method. *Progresses in Fracture and Strength of Materials and Structures, 1-4*, 353–358(3), pp.925–928.

Zhou, Y.E., 2006. Assessment of Bridge Remaining Fatigue Life through Field Strain Measurement. *Journal of bridge engineering (ASCE)*, 11, pp.737–744. Available at: http://ascelibrary.org/doi/abs/10.1061/(ASCE)1084-0702(2006)11:6(737) [Accessed February 28, 2014].

Zuo, F.J. et al., 2015. Fatigue life prediction under variable amplitude loading using a non-linear damage accumulation model. *International Journal of Damage Mechanics*, 24(5), pp.767–784.